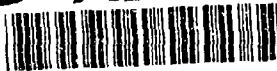


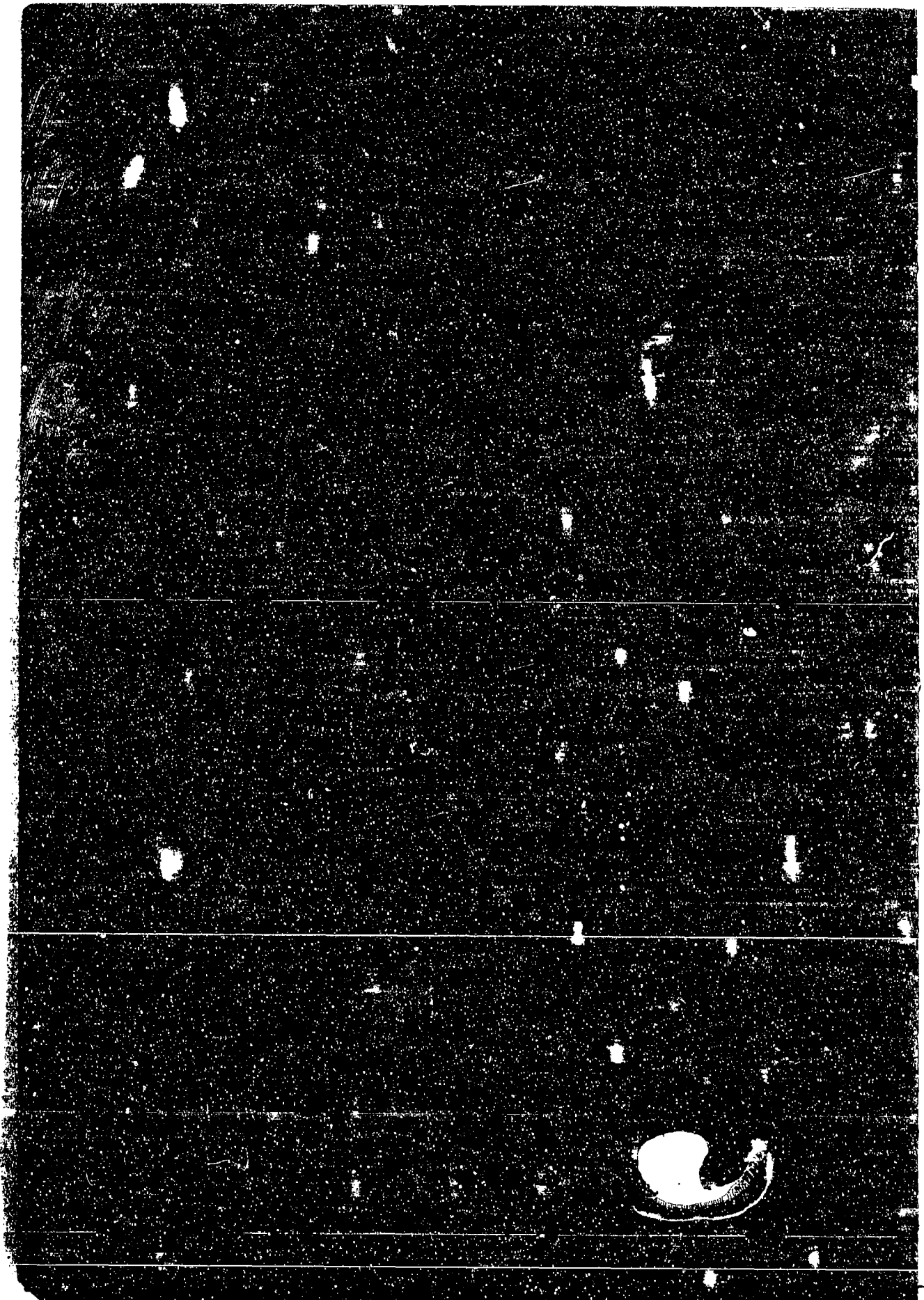
AD-A286 453



94-35559

19418





# DRAFT SF 298 . --.

1. Report Date (dd-mm-yy) 10 Oct 94	2. Report Type conference proceedings	3. Dates covered (from... to ) 29 June - 2 July 1994					
4. Title & subtitle  4th International Symposium on Stratified Flows		5a. Contract or Grant # N00014-94-J-9018					
		5b. Program Element #					
6. Author(s)  Emil Hopfinger, Bruno Voisin, Genevieve Chavand, editors		5c. Project # 5202					
		5d. Task # EUR					
		5e. Work Unit #					
7. Performing Organization Name & Address Laboratoire des Ecoulements Geophysiques et Industriels, Institut de Mecanique de Grenoble, B.P. 53 X - 38041 Grenoble Cedex 9 France			8. Performing Organization Report #				
9. Sponsoring/Monitoring Agency Name & Address  Office of Naval Research Europe PSC 802 BOX 39 FPO AE 09499-0700			10. Monitor Acronym ONREUR				
			11. Monitor Report #				
12. Distribution/Availability Statement A							
13. Supplementary Notes 4 volumes							
14. Abstract							
15. Subj' Terms  stratified flows							
Security Classification of					19. Limitation of Abstract	20. # of Pages	21. Responsible Person (Name and Telephone #)
16. Report Unclassified	17. Abstract Unclassified	18. This Page Unclassified	Unlimited		Mike Shear, 011-44-0171-514-4921		

## Saturday – July 2 – Morning

8:45 – 9:30

### General Session

Biomass production in stratified waters  
*A. Stigebrandt*

Accession For	
NTIS	CRA&I <input checked="" type="checkbox"/>
DTIC	TAB <input type="checkbox"/>
Unannounced <input type="checkbox"/>	
Justification _____	
By _____	
Distribution/ _____	
Availability Codes	
Dist	Avail and/or Special
A-1	

### Session A7 ENTRAINMENT & MIXING

### Session B7 OCEANIC PROCESSES : OBSERVATION & MODELS

9:30 Persistence theory of stratified entrainment – 97 <i>A. J. Cotel, R. E. Breidenthal</i>	9:30 Turbulence produced by internal waves in the oceanic thermocline at mid and low latitudes – 88 <i>M. C. Gregg, D. P. Winkei, T. B. Sanford, H. Peters</i>
9:45 Dyapycnal mixing: fluxes and energetics – 112 <i>K. B. Winters, P. N. Lombard, J. J. Riley, E. A. d'Asaro</i>	9:45 Geostrophic adjustment: frontogenesis and energy conversion – 56 <i>W. Blumen, R. Wu, R. T. Williams</i>
10:00 Turbulent penetration and mixing at an interfacial layer in a wind tunnel – 25 <i>Jayesh, Z. Warhaft</i>	10:00 Laboratory experiments with mid-latitude circulation in a two-layer ocean – 120 <i>R. W. Griffiths, P. Cornillon</i>
10:15 Direct measurements of the mutual-entrainment velocity at a density interface – 242 <i>K. Kan, N. Tamai</i>	10:15 Manifestations of bottom topography on the ocean surface: the physical mechanism and solution of direct and inverse problems on a beta-plane – 165 <i>V. I. Shnir, S. Yu. Annenkov</i>

10:30 – 11:00

### COFFEE BREAK

11:00 The importance of internal waves for mixing in a stratified tidal flow – 235 <i>R. Uittenbogaard, J. Imberger</i>	11:00 Cylindrical co-ordinate system and large scale ocean circulation – 261 <i>R. Schopp, A. Colin de Verdier</i>
11:15 The evolution of a turbulent mixed patch in a stratified shear flow – 207 <i>G. Hughes</i>	11:15 Turbulence decay in stratified and homogeneous marine layers – 133 <i>I. D. Lozovatski</i>
11:30 Efficiency of mixing by a turbulent jet in a stably stratified fluid – 106 <i>M. Larson, L. Jönsson</i>	11:30 Observations of internal wave reflection and mixing at a seamount – 151 <i>C. C. Eriksen</i>
11:45 Large-scale percolation and diffusion in free and layer turbulent stratosphere – 13 <i>A. Bershadskii, H. Branover, M. Nagomy</i>	11:45 Numerical simulations of the flow of a stratified fluid over topography – 264 <i>J. W. Rottman, D. Broutman, R. Grimshaw</i>

12:00 – 1:00

### Closing Lecture

Processes in the surface mixed layer of the ocean  
*C. Garrett*

# PRODUCTION OF ORGANIC MATTER IN STRATIFIED WATER

by

Anders Stigebrandt

Department of Oceanography

Göteborg university

P.O. Box 4038

S-40040 Göteborg, Sweden

## Abstract

Some aspects of the role of stratification for the biological production in aquatic systems are reviewed. First is presented some elementary knowledge about organic matter and processes producing and decomposing organic matter in aquatic systems, including the roles played by light and nutrients for plant production. Next I discuss a necessary condition on the maximum depth of well-mixed surface layers for phytoplankton growth. This can be used to predict the time for onset and offset of phytoplankton growth in an arbitrary region of the sea. High-frequency cycles of stratification-destratification of the surface waters may enhance plant production. The perhaps best example of this may be found at tidally forced shelf fronts which execute a fortnightly seaward-landward oscillation. It is also shown that thin surface layers promote small phytoplankton. Reasons for deep phytoplankton maxima in stratified water in summer are discussed. The global production in the sea is ultimately determined by external sources and internal sinks. However, the production is not evenly distributed. Areas of upwelling and areas having high-frequency cycles of destratification-stratification are particularly productive.

## 1. Introduction

The stratification of natural water bodies is a result of external forcing by winds, thermohaline processes and tides. The time-scale for the accompanying vertical circulation ranges from one year in temperate lakes to hundreds of years in the ocean. Usually turbulence is absent or occurs only sporadically in the major part of the water body. It is only a thin layer of varying thickness close to the sea surface that is fully turbulent most of the time. The optical properties of water are such that light penetrates only a relatively thin layer at the sea surface. Biota encounter in natural water bodies a physical environment that is very different from that encountered on land. As a result biological evolutionary processes have developed species of biota and whole ecosystems which differ much between aquatic and terrestrial environments.

## 2. Organic matter

Organic matter is composed of carbon and some additional essential elements of which the so-called plant nutrients nitrogen and phosphorus are the most interesting since shortage of one of these usually limits the production of organic matter. Through different biogeochemical processes matter is transferred between organic and inorganic states. Photosynthesis is the process by which illuminated plants produce organic matter from inorganic compounds with light as the energy source. Almost neutrally buoyant

microscopic phytoplankton is the dominant producer of organic matter in aquatic systems. Phytoplankton reproduces extremely fast, if conditions are favourable the number of plants and the biomass of a population may double in one day. This kind of plant is apparently very competitive in aquatic environments. Large, slowly growing anchored plants, which are the completely dominating type of plant on land, occur only on shallow, illuminated bottoms.

Animals (zooplankton, fish, etc.), bacteria and sponges consume organic matter. Some of the metabolized organic matter is used to build up new organisms while the rest is broken down to inorganic constituents that are excreted and then again available for plant production. Zooplankton that directly graze phytoplankton, so-called herbivores, are also quite small. Herbivores are in turn eaten by larger zooplankton and other animals. The system of primary producers and decomposers, which also involve bacteria, is quite complex and web-like and therefore often denoted the food web.

There is an extremely great manifold of living and dead organic matters occurring in both dissolved and particulate forms. One very important property of particulate organic matter in aquatic systems is that it is usually denser than water why it sinks. The sinking speed of particles depends on their specific weight, size and form. The smallest particles have negligible sinking speeds while large particles, like faecal pellets from zooplankton and fish, may have sinking speeds of hundreds of metres per day. The sinking implies that organic matter is vertically dispersed from the zone of production close to the sea surface.

### 3. The growth and respiration of phytoplankton

The growth of phytoplankton in a unit volume may be written in the following comprehensive way (Kremer & Nixon, 1978)

$$\text{Growth} = \text{NUTLIM} \cdot \text{LTLIM} \cdot \text{GMAX} \cdot \text{PON} \quad (1)$$

where PON is the concentration of phytoplankton and the rate constant is split in three factors. The first two factors NUTLIM and LTLIM, attaining values between zero and one, describe possible limiting effects on the growth by shortage of nutrients or light respectively. The magnitude of these factors is thus determined by external, environmental conditions. When nutrients and light do not limit the growth these factors attain the value one and the growth is determined by the intrinsic maximal growth rate of phytoplankton GMAX. The value of GMAX is typically  $0.5 \text{ day}^{-1}$  which implies a daily doubling of the biomass. GMAX varies between species and increases with temperature.

The function LTLIM is often described using the following function suggested by Smith (1936)

$$LTLM = \frac{I/I_k}{\sqrt{1 + (I/I_k)^2}} \quad (2)$$

Here  $I$  is the light intensity at the actual depth and  $I_k$  is a light sensitivity factor for phytoplankton. The latter vary from species to species and may also vary for a specific species due to so-called photoadaptation, see e.g. Kirk (1983).

Nutrient uptake by phytoplankton is according to so-called Michaelis-Menten kinetics which implies that NUTLIM should be described by

$$NUTLIM = \frac{DIN}{K_N + DIN} \quad (3)$$

Here DIN is the concentration of the actual nutrient (i.e. inorganic compounds of nitrogen or phosphorus) and  $K_N$  is the so called half saturation constant for the actual nutrient.  $K_N$  has different values for phosphorus and nitrogen, e.g. Kremer & Nixon (1978). It is assumed that the nutrient having the lowest value of NUTLIM limits the production (Liebigs minimum law).

Within phytoplankton there is an ongoing metabolism (so-called dark respiration) by which primary products from the photosynthesis are processed to fats and proteins. The respiration, which for some species (flagellates) also may include energy requirements for swimming, may be parameterized in the following way

$$Resp = -r \cdot GMAX \cdot PON \quad (4)$$

According to Kirk (1983)  $r \approx 0.1$  but there is large variation between different species. It is typical for models of biological processes that rate constants and parameters vary much. This is probably a result of the ability of living matter to adapt to changing external conditions. When the rules for adaption are known it should be possible to include these in the models.

The depth where the local production and respiration are of equal magnitude ( $Growth + Resp = 0$ ) is called the compensation depth  $H_c$ . Under stratified conditions the zone close to the sea surface where plant production may occur, the euphotic zone, is delimited downwards by the compensation depth. It should be noted that since Growth, see equation (1), depends on the availability of both nutrients and light there is in a specific water column a possibility for more than one compensation depth and a partition of the euphotic zone in thinner layers, see example in Fig. 3. Under well mixed conditions the situation is a bit different as discussed below.

The thickness of the euphotic zone when  $NUTLIM = 1$  depends on the optical properties of water which may be described by the vertical attenuation coefficient  $c$  defined by  $dI/dz = -cI$ , where  $I$  is the light intensity and  $z$  is the depth. A rule of thumb says that the

compensation depth  $H_c$  is where the light intensity is 1% of the surface value. In the open "blue" sea  $c \sim 0.05 \text{ m}^{-1}$  and  $H_c \sim 100 \text{ m}$ . In "green" coastal waters  $c$  is usually appreciably greater and the euphotic zone is accordingly thinner, often in the range 10-30 m. It should be noted that high concentrations of phytoplankton give significant contributions to  $c$  and this is actually the reason why coastal waters often are "green".

#### 4. Conditions for phytoplankton growth in well-mixed surface layers

During late autumn and winter, with a deepening mixed surface layer, the water column is replenished with nutrients right up to the sea surface.  $\text{NUTLIM}$  by that often attains a value close to one. However, at least at higher latitudes, the light at the sea surface is weak due to short days and low sun height. Phytoplankton, passively advected around in the deep mixed layer, will therefore stay in darkness most of the time. The average of  $\text{LTLIM}$  over the mixed layer will be small and the integral of  $\text{Growth} + \text{Resp}$  over the mixed layer is negative. In spring the seasonal pycnocline retreats whereby the thickness of the mixed layer decreases. This, together with the increasing illumination of the sea surface, drastically increases the average of  $\text{LTLIM}$  over the mixed layer. A phytoplankton population starts to grow (bloom) when the integral over the mixed layer of  $\text{Growth} + \text{Resp}$  becomes positive. There is a certain depth for which the vertical integral from the sea surface to that depth of  $\text{Growth} + \text{Resp}$  is zero. This depth, the critical depth, gives the upper limit for the thickness of a well-mixed surface layer with positive phytoplankton production (Sverdrup, 1953). Clearly, the critical depth for a well-mixed layer is deeper than the depth of the euphotic zone.

In Fig. 1 are shown computations of annual cycles of mixed-layer depths and critical depths for the Baltic proper and Kattegat. The Baltic proper has a seasonal pycnocline that varies from  $\sim 60 \text{ m}$  depth in winter to  $\sim 10 \text{ m}$  in summer (e.g. Stigebrandt, 1985) while Kattegat has a very strong halocline at about 15 m depth all the year. In order to facilitate a comparison of model results with observations the critical depth in Fig. 1 is defined slightly different than above. It was defined such that the integral from the sea surface to the critical depth of  $\text{Growth} + \text{Resp}$  is equal to the integral over the same water column of  $\text{Growth}/2$ . This definition should ensure that the phytoplankton population really grows when the mixed layer depth becomes equal to the critical depth. In order to demonstrate the effect of daily variations of light conditions the critical depth was computed for both cloudy and cloudless conditions.

The computations predict that spring bloom should start in February in Kattegat and in April in the Baltic proper (Fig. 1) which is in accordance with observations (Fig. 2). According to the computations cloudless conditions give a tendency for an early spring bloom. The computations also show that due to the shallow halocline phytoplankton production should last about one month longer in Kattegat than in the Baltic proper. However, the prediction for the autumn may be uncertain since the assumption  $\text{NUTLIM}=1$  used in the computation of the critical depth may be invalid at the end of the production season.

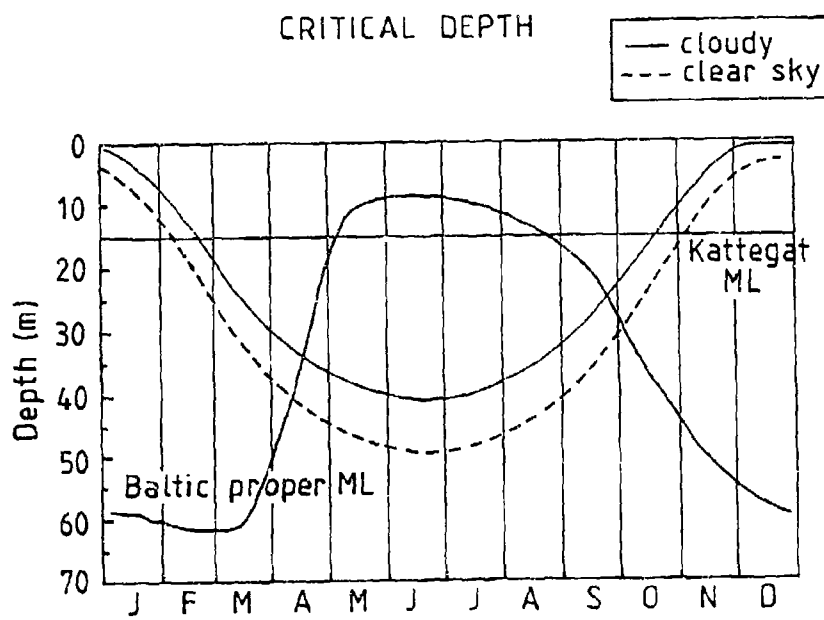


Fig. 1 The annual cycle of mixed layer depth and critical depth in Kattegat and the Baltic proper. For the computations of the critical depth the following parameter values were used:  $c=0.25 \text{ m}^{-1}$ ,  $I_k=30 \text{ W m}^{-2}$ ,  $\text{NUTLIM}=1$ ,  $r=0.1$ .

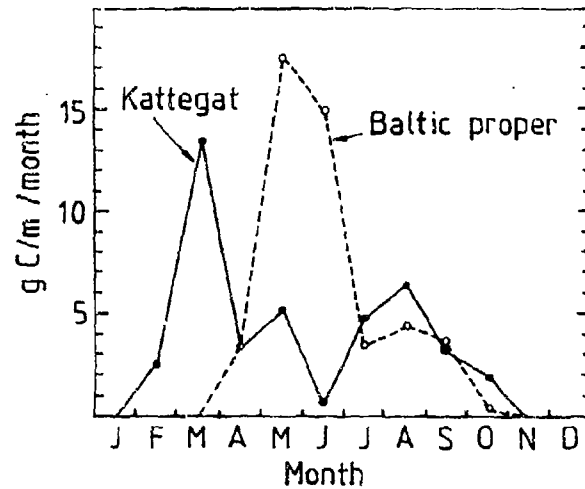


Fig. 2 The annual cycles of net production in Kattegat and the Baltic proper (redrawn from Stigebrandt, 1991).

The computations presented above demonstrate that a simple but realistic model for growth and respiration of phytoplankton can be used to compute the critical depth for well-mixed surface layers with respect to phytoplankton production. The latter takes place only when the depth of the mixed layer is less than the critical depth. If one knows the annual cycle of the seasonal pycnocline, either from measurements or from computations using a proper model, it is thus possible to predict the time for onset and offset of phytoplankton production. Computations similar to those presented here were first undertaken by Sverdrup (1953).

In addition to respiration grazing by zooplankton acts as a sink process for phytoplankton. For well-mixed surface layers one also has to consider the loss of phytoplankton sinking through the bottom of the layer. The sinking speed of living phytoplankton is in the range 0-30 m day<sup>-1</sup>. From Stoke's law for the settling speed of small particles one expects a positive correlation between sinking speed and plankton diameter. A complicating factor is that some species are able to swim. Large flagellates may swim with speeds 2-20 m day<sup>-1</sup>, e.g. Valiela (1984). If  $w_p$  is the sinking speed the flux of phytoplankton out of a mixed layer is  $w_p PON$ , where PON is the phytoplankton concentration in the layer.

If the effect of swimming is included the rate of change of the phytoplankton concentration in a well-mixed surface layer of thickness H is

$$\frac{dPON}{dt} = Growth + Resp - \frac{w_p}{H} PON \quad (5)$$

where LTLM in Growth is averaged over the layer. Using equations (1) and (4) one obtains

$$\frac{dPON}{dt} = [(NUTLIM \cdot LTLM - r) GMAX - \frac{w_p}{H}] PON \quad (6)$$

With  $NUTLIM \leq 1$ ,  $LTLM \leq 1$ ,  $r=0.1$  and  $GMAX=0.7$  one finds that a phytoplankton population may grow only if

$$\frac{w_p}{H} \leq 0.6 \quad (7)$$

This shows that large phytoplankton with high sinking speeds require thick well-mixed layers to grow. In thin well-mixed surface layers, often found in estuaries and close to coasts, one expects to find small phytoplankton with low sinking speeds or swimming flagellates.

## 5. The importance of cycles of destratification-stratification for plant production

The description in the previous section of effects of the seasonal variation of the mixed layer depth upon phytoplankton production demonstrates that a varying mixed layer depth is essential for the production. The deepening of the mixed layer by entrainment of underlying water with usually high nutrient concentrations in autumn and winter is important for the replenishment of the surface waters with nutrients. The stratification of the surface water in spring by the retreat of the mixed layer to depths shallower than the critical depth is usually necessary to start plant production.

Sequences of destratification-stratification also occur on higher frequencies, for instance forced by varying tidal currents. Legendre et al. (1986) give a number of examples of enhanced production due to such sequences. The perhaps most well-known examples of enhanced biological production due to high frequency cycles of stratification-destratification may be found on continental shelves with strong tides. Pingree (1978) shows that there is an enhanced biological production coupled to the fortnightly excursion of shelf fronts in the North Sea. He also used fishery statistics to show that fishing intensity decreases rapidly with distance from frontal areas.

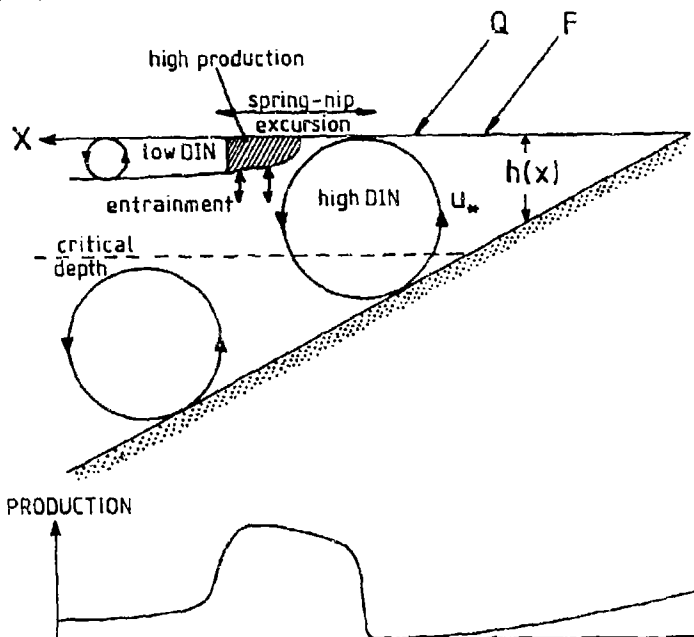


Fig. 3      Idealized vertical cross-section through a shelf front. Q and F denote fluxes of heat and freshwater respectively. The long-term mean production of organic matter along the cross-section is sketched in the lower figure.

A sketch of an idealized summer situation in a vertical cross-section from the open sea and through a shelf front is shown in Fig. 3. Due to strong tidal currents the turbulent bottom boundary layer surfaces on the landside of the front. On the seaward side the

stratification may be described as two superposed turbulent mixed layers, mechanically forced by winds and tides respectively, which exchange water by entrainment, see Stigebrandt (1981). Thus, there is a wind-driven supply of nutrients from the lower to the upper layer. This is strongest close to the front where plant production accordingly is high (cf. Fig. 3). However, in addition to this effect production in the frontal area should also be enhanced by the seaward-landward oscillation of the front in the fortnightly spring-neap tidal cycle. This oscillation imposes a cycle of stratification-destratification in the excursion area which should strongly increase the phytoplankton production. The expected variation of the long-term production along the section is sketched in Fig. 3. For a recent paper on the dynamics of shelf fronts including biological aspects, see Bo Pedersen (1994).

#### 6. The summer submerged phytoplankton maximum

In summer the surface mixed layer is usually shallow with low concentrations of nutrients and NUTLIM has a value close to zero. However, below the euphotic zone nutrient concentrations are often rather high. Vertical diffusion will then transport nutrients towards the euphotic zone by which the value of NUTLIM increases. Close to the bottom of the euphotic zone the product LTLIM times NUTLIM may attain a maximum then. At that depth one often finds a sub-surface phytoplankton maximum, see the idealized example in Fig. 4. In this example there are two compensation depths restricting the euphotic zone (production layer) to the upper part of the nutricline. The actual form of the phytoplankton concentration depends on a number of factors like vertical diffusivity, sinking speed of phytoplankton and rates of grazing and mineralization.

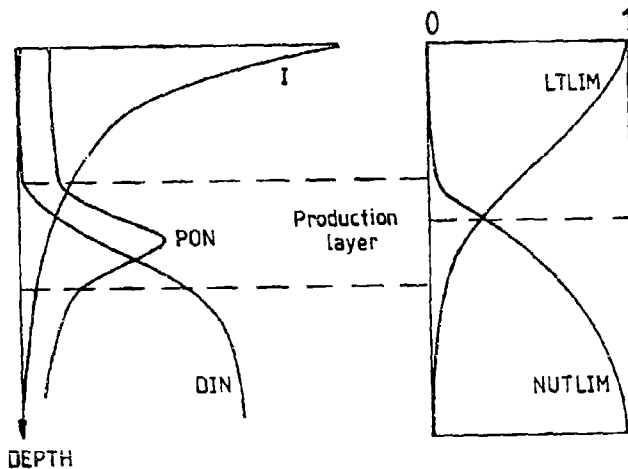


Fig. 4 Typical vertical profiles of light (I), nutrients (DIN) and phytoplankton (PON). Also shown are NUTLIM and LTLIM. The density profile, not shown, is parallel to the DIN profile.

A lot of papers have been published on observations and modelling of sub-surface phytoplankton maxima in stratified water. Taylor et al. (1986) presented an instructive

one-dimensional plankton model where the vertical diffusivity may vary vertically. The model was used to study the difference between shelf systems, with strong turbulence beneath the pycnocline, and deep ocean systems, with weak turbulence beneath the pycnocline. They also studied the sensitivity of the model to certain assumptions about respiration (mortality) and the magnitude of the half-saturation constant for nutrient uptake. The importance of daily variations of the intensities of light and turbulence was also studied.

#### 7. Large-scale circulation of plant nutrients and nutrient control by sinks

The vertical flux of sinking particulate organic matter from the euphotic zone, the net or export production, decreases and changes character with increasing depth. The reason for this is of course a continuous consumption (pelagic mineralization) which implies that particles are physically and biochemically broken down at the same time as new particles in the form of faeces are produced. The vertical flux of sinking particulate organic matter is called the biological pump. The biological pump tends to decrease concentrations of biochemically active substances, e.g. carbon and nutrients, in the surface layers and increase concentrations at greater depths.

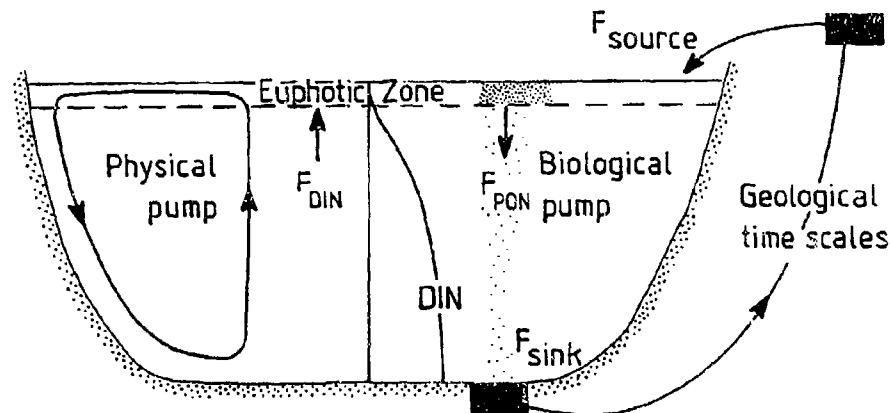


Fig. 5 The biological and physical pumps and the resulting vertical profile of nutrients.

In the ocean there should be a vertical sinking-diffusion/advection balance of nutrients, with nutrients transported vertically downwards by the biological pump and advected and diffused upwards by currents and turbulence (the physical pump). The vertical concentration profiles of nutrients should be determined by the combined action of these pumps (Fig. 5).

The steady-state total content of nutrients in an aquatic system is dependent on external

sources and internal sinks. Nutrient sinks are usually associated to bottom sediments. Due to pelagic mineralization the fraction of the net production that reaches the bottom should be less in a deep than in a shallow system. If it is assumed that nutrient sinks are proportional to the flux of organic matter reaching the bottom it follows that deep aquatic systems should attain higher nutrient concentrations than shallow systems, provided that all other factors are equal.

Simple and efficient empirical nutrient models have been developed for temperate lakes, e.g. Peters (1986). These models predict the lake nutrient concentration for a given strength of the nutrient source. The "secret" behind the success of these models is the parameterization of the sinks which in essence is taken proportional to the winter surface concentration of nutrients (phosphorus).

#### 8. Horizontal variability of plant production in the sea

In the previous section it was demonstrated that the overall nutrient state of an aquatic system is determined by a balance between sources and sinks. The time-constant of this balance is about 50,000 years in the ocean. The availability of nutrients just below the productive layer in a certain area of the sea depends on the combined action of the biological and physical pumps. The physical pump operates on time-scales which increase vertically, from 1 year close to the sea surface to 100-1000 years in the deep ocean. When and how available nutrients are introduced in the production layer depends on local mixing processes in the uppermost part of the sea. As already told, the latter are governed by weather forced processes at the sea surface and, in shallow areas, also tides. Close to coasts the production layer may in addition obtain nutrients from the continents.

The pattern of biological production in the sea is strongly typed by the pattern of vertical transports of nutrients into the euphotic zone (Berger et al., 1988). A global map of nutrient concentrations just beneath the production layer quite much resembles a map of the net production of organic matter, e.g. Najjar (1992). Particularly great production occurs in areas of wind-driven upwelling, e.g. along the subtropical eastern margins of the oceans. This is manifested by great fisheries at the coasts of Peru and California in the Pacific Ocean and at the southwest and northwest coasts of Africa in the Atlantic Ocean. As already discussed great production also occurs at shelf fronts.

#### 9. Conclusions

In this paper I have tried to explain how stratification influences production of organic matter in aquatic systems. The influence spans wide ranges in time and space. The largest scales involve the source-sink balance regulating the nutrient content of the system while the shortest scales are of interest for understanding local production.

Certainly a lot of interesting topics are missing from the presentation others are only covered in a rudimentary way. One of the missing topics is the practice to use existing stratification in natural water bodies to interleave sewage water containing nutrients beneath the euphotic zone in order to prevent local plant production. It would have been

interesting to discuss under what circumstances this may work and, in particular, to discuss circumstances when it does not work.

#### References

Berger, W.H., Fisher, K., Lai, C. and Wu, G., 1988: NOAA Natl. Under-sea Res. Progr. res. Rep. 88-1. pp- 131-176.

Bo Pedersen, Fl., 1994: The oceanographic and biological tidal cycle succession in shallow sea fronts in the North Sea and the Englisg Channel. Estuarine, Coastal and Shelf Science, 38, 249-269.

Kremer, J.N. and Nixon, S.W., 1978: A coastal marine ecosystem. Springer Verlag. 217 pp.

Kirk, J.T.O., 1983: Light and photosynthesis in aquatic ecosystems. Cambridge Univ. Press. 401 pp.

Legendre, I., Demers, S. and Lefavre, D., 1986: Biological production at marine ergoclines. p. 1-29 in Marine Interfaces Ecohydrodynamics (J.C.J. Nihoul, ed.). Elsevier Oceanography Series, 42. Elsevier.

Najjar, R.G., 1992: Marine biochemistry. p. 241-282 in Climate System Modeling (K.E. Trenberth, ed.). Cambridge Univ. Press.

Peters, R.H., 1986: The role of prediction in limnology. Limnol. Oceanogr., 31, 1143-1159.

Pingree, R.D., 1978: Mixing and stabilization of phytoplankton distributions on the northwest european continental shelf. pp. 181-220 in Spatial Pattern in Phytoplankton Communities (J.H. Steele, ed.). Plenum Press, New York.

Stigebrandt, A., 1981: Cross thermocline flow on continental shelves and the location of shelf fronts. p. 51-65 In Ecohydrodynamics (J.C.J. Nihoul, ed.). Elsevier.

Stigebrandt, A., 1985: A model for the seasonal pycnocline in rotating systems with application to the Baltic proper. J. Phys. Oceanogr., 15, 1392-1404.

Stigebrandt, A., 1991: Computations of oxygen fluxes through the sea surface and the net production of organic matter with application to the Baltic and adjacent Seas. Limnol. Oceanogr., 36, 444-454.

Sverdrup, H.U., 1953: On conditions for vernal blooming of phytoplankton. J. Cons. Perm. Int. Exp. Mer., 18, 287-295.

Taylor, A.H., Harris, J.R.W. and Aiken, J., 1986: The interaction of physical and biological processes in a model of the vertical distribution of phytoplankton under stratification. p. 313-330 in Marine Interfaces Ecohydrodynamics (J.C.J. Nihoul, ed.). Elsevier Oceanography Ser. 42. Elsevier.

Valiela, I., 1984: Marine ecological processes. Springer Verlag. 546 pp.

# Persistence Theory of Stratified Entrainment

A. J. COTEL and R. E. BREIDENTHAL

Department of Aeronautics and Astronautics

University of Washington, Seattle, Washington, 98195, USA

Turbulent entrainment is discussed in a variety of stratified flows. In general, the entrainment rates decrease as the stratification increases. Different entrainment laws have been observed, usually the entrainment rate is proportional to  $Ri^{\beta/2}$ , where  $\beta$  can be 0, 1, 2, 3 and  $Ri$  is the Richardson number based on the large eddies. For some flow regimes, the entrainment rate does not depend on the Richardson number, but on the Schraadt and Reynolds numbers. To explain the full spectrum of entrainment rates, a new parameter the persistence has been introduced. This parameter separates the flows into persistent and nonpersistent cases, depending on the number of rotations one eddy makes in one position. Each regime is discussed on the basis of its definition, conditions of existence, and physical example. A distinction is also made between thick and thin stratified interfaces.

---

## 1. Introduction

Entrainment affects the structure of the atmosphere and the ocean. It is important to understand the process of entrainment in geophysical flows and in the laboratory. If we take as a particular example a momentum-driven jet interacting with a stratified interface, a different entrainment rate is observed depending on the position of the jet with respect to the interface. If the jet is vertical, impinging on the stratified interface (Cotel & Breidenthal 1994), then the entrainment rate is proportional to  $Ri^{1/2}$ , but if the jet is horizontal below the interface (Schneider 1980), it is proportional to  $Ri^{-3/2}$ . If the jet is horizontal and at the interface (Fernando 1993), the entrainment rate is now proportional to  $Ri^{-1}$ .

The Reynolds, Schmidt, and Richardson numbers can be the same in all three of the configurations, but the entrainment rates are different. What tells nature to choose one process over another? There must be another parameter which determines the entrainment process. It has been proposed that the other parameter is the vortex persistence  $T$ , defined as the number of vortex rotations before a vortex has moved its own diameter.

A detailed explanation of each regime for  $Sc > 1$ ,  $Sc < 1$  and the thick interface case is given. The Richardson number is defined to be  $Ri = \frac{g\delta}{w_1^2}$ ,

where  $\delta$  is the width of the jet at the interface, and  $w_1$  is the incident jet velocity at the interface.

The Reynolds number is  $Re = \frac{w_1 \delta}{\nu}$  and the Schmidt number is  $Sc = \frac{\nu}{D}$ , where  $\nu$  is the kinematic viscosity and  $D$  is the molecular diffusivity.

Each entrainment rate is derived from the ratio of the appropriate length scale and time scale. The reasoning for the choice of these scales is given in the following sections.

## 2. Thin stratified interface with $Sc > 1$

### - Regime I: Unstratified

Regime I occurs when the Richardson number based on the large eddies is less than one, so that even the largest eddies are unstratified. Then Taylor's entrainment hypothesis sets the entrainment rate, which is proportional to the incident velocity. The entrainment velocity can be defined as proportional to  $\frac{\delta}{\tau}$ , where  $\delta$  is the size of the large eddies of the turbulent flow studied, and  $\tau$  is the rotation period of these same eddies. Such a regime is seen for a turbulent jet in a homogeneous environment, or a vertical jet impinging on a very weak interface.

### - Regime II: The largest eddies are stratified and persistent.

A physical example is a vertical jet impinging on a stratified interface. The flow is persistent, because the lateral vortices doing most of the entrainment and mixing stay in one position. So  $T$ , the number of rotations one vortex makes in one position before it moves its own diameter, is very large.

In this case, the important length scale is the dome height  $\delta_m$  of the jet, which is proportional to the size of the lateral vortex. The other choices of length scales would be  $\delta$ , the width of the impinging jet and  $\delta_r$ , the rebound eddy size (Linden 1973). There is no rebound in this case, so  $\delta_r$  is not relevant, and since the entrainment is controlled by the lateral vortices, the jet vortices do not entrain directly, so  $\delta$  drops out of the problem. There are only two time scales in the problem: one based on the jet,  $\tau$ , i.e. the rotation period of the jet vortices, and one buoyancy time scale  $\tau_b$  defined to be

$$\left(\frac{\delta}{g}\right)^{1/2}.$$

Since buoyancy is controlling the lateral vortices, the buoyancy time scale is chosen.

Therefore, the entrainment velocity is  $\frac{\delta_r}{\tau_r}$ , which gives an entrainment rate proportional to  $Ri^{-1/2}$ .

- Regime III: Entraining eddies become nonstationary

When the largest eddies become nonstationary, then another entrainment mechanism is observed. An example is the impingement of a vortex ring on an interface or entrainment due stirring grid turbulence with salt stratification. Entrainment has been modeled by a rebound mechanism (Linden 1973).

Here the entrainment velocity is  $\frac{\delta_r}{\tau_r}$ , because the important length scale is the rebound length scale, and the time scale still has to be the buoyancy time scale yielding an entrainment rate proportional to  $Ri^{-3/2}$ . The transition from regime II to regime III must occur at some value of  $T$  which depends on  $Ri$ . It has been proposed that the transition is at  $Ri=T$ .

- Regime IV: Diffusion across Taylor layers

If the stratification becomes very strong then molecular diffusion comes into play. The flow is still nonstationary. Such a regime is encountered for stirring grid experiments with heat stratification.

The entrainment velocity is here equal to  $\frac{(Dt_r)^{1/2}}{\tau_{\lambda_r}}$ ,

where the numerator is the Taylor layer diffusion length during a rebound global time and the denominator is the rebound Kolmogorov microscale time. Assuming a Kolmogorov cascade,  $\tau_{\lambda_r} = \tau_r (Re_r)^{-1/2}$ , where  $Re_r$  is the rebound Reynolds number based on  $\delta_r$  and  $w_r$ , the rebound length scale and velocity respectively. This gives an entrainment rate proportional to  $Sc^{-1/2} Ri^{-1}$ .

In the atmosphere,  $Sc \approx 1$  and  $T \approx 1$ . The model would predict an entrainment rate proportional to  $Ri^{-1}$ .

- Regime V: Nonstationary flat interface

When the Richardson number of the smallest eddies is equal to or greater than one,  $Ri$  drops out of the problem. The interface is flat. If the flow is nonstationary, there can be at any point or within an eddy size an accumulation of a scalar in time, so the rate limiting process is set by the eddies with the lowest velocity, which are the smallest eddies. Then the Batchelor layer thickness is the characteristic length scale, so the entrainment velocity becomes

$$w_e = \frac{(D(\lambda_0^2/v_{\lambda_0}))^{1/3}}{\tau_{\lambda}}$$

The exponent 1/3 comes from boundary layer theory for  $Sc > 1$  (Schlichting 1960), because the thickness of the vorticity gradient is bigger than the thickness of the concentration gradient. The entrainment rate is then proportional to  $Sc^{-1/3} Re^{-1/4}$ .

#### Regime VI: Stationary flat interface

In this regime, the flow is stationary, so that there cannot be any accumulation or increase of scalar concentration in time. The rate-limiting process in the steady sequence of events is set by the eddies with the longest rotation period, the largest eddies.

The entrainment velocity is

$$w_e = \frac{(D(\delta^2/w_1))^{1/3}}{\tau}$$

and the entrainment rate is then  $Sc^{-1/3} Re^{-1/2}$ .

Figure 1 illustrates the entrainment regimes for thin interfaces for  $Sc > 1$ . The double lines represent a discontinuous jump between regimes and the single lines a continuous transition.

#### 3. Thin stratified interface with $Sc < 1$

The Schmidt number is always less than 1, so regime III disappears. For the flat interface region, the dependence on  $Sc$  is changed. The thickness of the vorticity gradient is smaller than the thickness of the concentration gradient, so from boundary layer theory the Schmidt number exponent is now -1/2.

#### 4. Thick Interface Case

When the interface is no longer sharp, then the vorticity does not impinge on the interface but resides imbedded within it. Thus the entrainment mechanism is changed. In the absence of impingement, the controlling eddies are no longer the largest or the smallest, but intermediate eddies of particular size  $\lambda^*$ , which have a unity Richardson number. The largest eddies cannot engulf fluid and the smallest are less efficient at pulling down tongues of fluid than the critical  $\lambda^*$  eddies.

This case is observed for a stratified shear layer (Fernando 1993). The eddies are

moving along at the interface, so  $T=1$ . For  $Re>1$  and  $1 < Ri < Re^{1/4}$ , the entrainment velocity is proportional to the rotation speed of the eddy of size  $\lambda^*$ ,  $Ri_{\lambda^*} = 1$ . Assuming a Kolmogorov spectrum,

$$\frac{v_{\lambda^*}}{\Delta U} = \left( \frac{\lambda^*}{\delta} \right)^{1/3}.$$

It follows that the entrainment rate is proportional to  $Ri^{-1}$ .

For  $Re>1$  and  $Ri>Re^{1/4}$ , the regime is unchanged from before, as that the entrainment rate is proportional to  $Sc^{-1/3}Re^{-1/4}$  for  $Sc>1$ , and is  $Sc^{-1/2}Re^{-1/4}$  for  $Sc<1$ .

### 5. Comparison with experiments

Table 1 gives a summary of some experiments on entrainment, the complete references of which can be found in Cotel and Breidenthal (1994). The model and the experiments are in accord, except for a few.

For example, Nokes (1988) found an entrainment rate proportional to  $Ri^{-1.2}$  using Turner's experimental data for a stirring grid with salt stratification. Pedersen (1980) observed a -2 exponent.

Most of the shear-driven experiments obtained a -1 exponent. That would correspond to the thick interface case, since the vorticity is created at the surface rather than arriving by impingement, and the interface can no longer be considered thin if  $Ri>1$ .

The entrainment rate of an impinging plume is proportional to  $Ri^{3/2}$  (Baines 1975, Kumagai 1984) in contrast to that of an impinging jet ( $Ri^{-1/2}$ ). Evidently this is due to the relatively high fluctuations of a plume. In comparison, a jet is more steady. Therefore, the jet is considered persistent, while the plume is not.

Fernando and Long (1975) observed an entrainment rate proportional to  $Ri^{-7/4}$  for stirring grid experiments. So their results do not agree with the model presented here.

Not many experiments have been done in the range  $Ri \rightarrow \infty$ . However, a comparison can be made with heat transfer on a flat plate. When the boundary layer is laminar, then the small scale turbulence doesn't affect the heat transfer, but when the boundary layer is turbulent, heat transfer is enhanced by the small scales (Schlichting 1960). This would be analogous to the persistence effect on the entrainment rate. At the same  $Sc$  and  $Re$ , the non-stationary entrainment rate is higher than the stationary one.

### 6. Conclusion

A new model for stratified entrainment has been proposed, and it seems to agree with most experiments. More experiments need to be done to fully test for the effect of the per-

sistence parameter, while keeping the other parameters constant.

Internal waves have not been mentioned here, since the purpose is to use new arguments to explain entrainment. The breaking of internal waves may be important for entrainment, which presumably can be modeled by nonstationary vortices. That would correspond to Regime III or IV depending on the Schmidt number.

### 7. Acknowledgement

This research was supported by NSF ATM-8611225A02.

### 8. Bibliography

A.J. Cotel and R.E. Breidenthal, "Persistence effects in stratified jet entrainment", submitted to *Phys. Fluids*.

H-H. Schneider, "Laboratory experiments to simulate the jet-induced erosion of pycnoclines in lakes," *Proc. Int. Stratif. Flows, 2nd, Trondheim*, Trondheim: Nor. Inst. Technol. (1980).

H.J.S. Fernando, "Migration of density interfaces subjected to differential turbulent forcing," *Bulletin Am. Phys. Soc. Ann. Meet. Div. Fluid Dyn.*, **38**(12):2254 (1993).

P.F. Linden, "The interaction of a vortex ring with a sharp density interface: a model for turbulent entrainment," *J. Fluid Mech.* **60**:467-480 (1973).

H. Schlichting, *Boundary layer theory*, 6th Ed., McGraw-Hill, New York, 300 (1960).

R.I. Nokes, "On the entrainment rate across a density interface," *J. Fluid Mech.* **188**:185-204 (1988).

F.B. Pedersen, "A monograph on turbulent entrainment and friction in two-layer stratified flow, Ser. Pap. No 25, Inst. Hydrodyn. Hydraul. Eng. Tech. Univ. Den., Copenhagen (1980).

W.D. Baines, "Entrainment by a plume or a jet at a density interface," *J. Fluid Mech.* **68**:309-320 (1975).

M. Kumagai, "Turbulent buoyant convection from a source in a confined two-layer region," *J. Fluid Mech.* **147**:105-131 (1984).

H.J.S. Fernando and R.R. Long, "The growth of a shear-free mixed layer in a linearly stratified fluid," *Phys. Fluids* **28**(10):2999-3003 (1985).

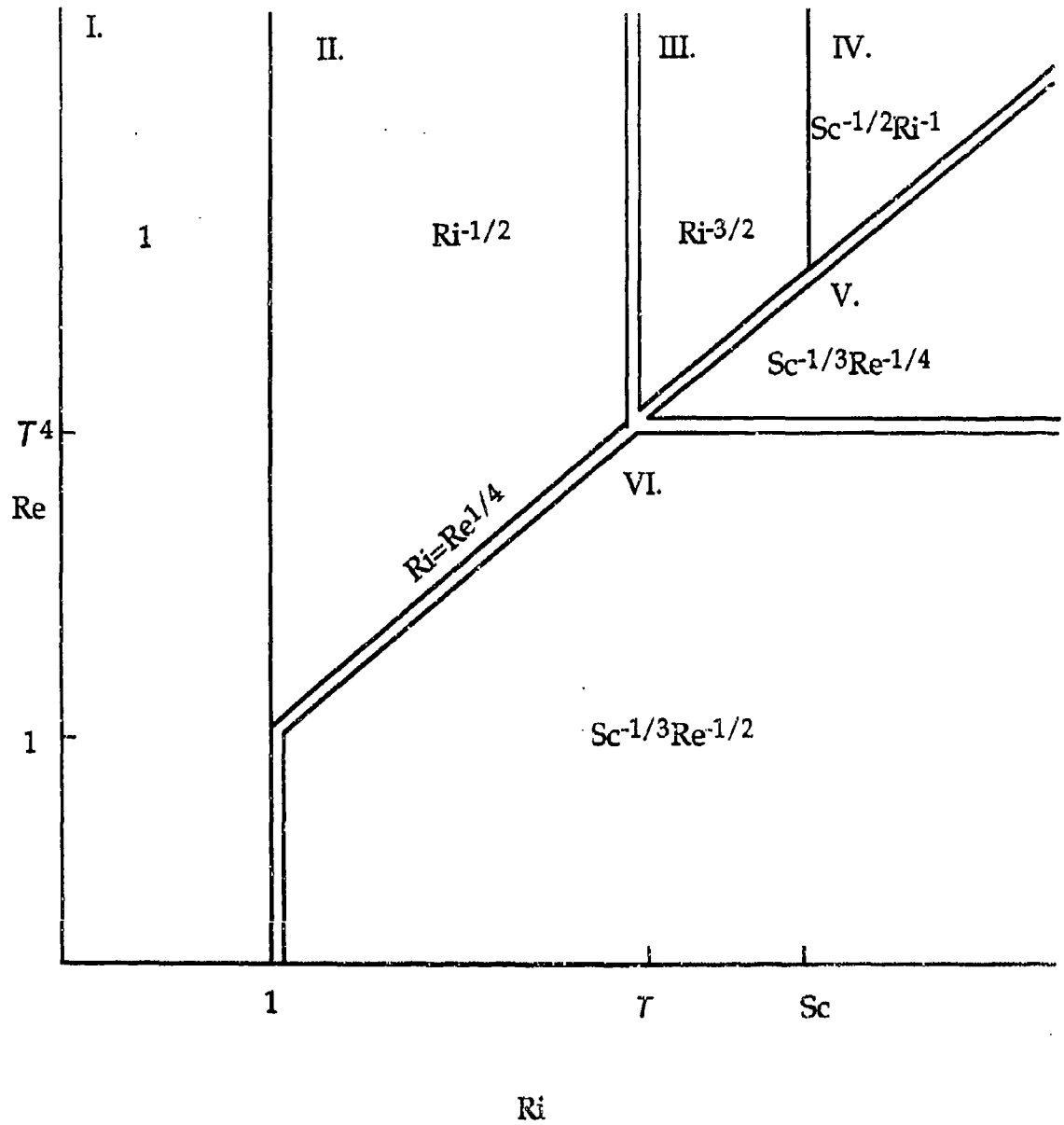


Figure 1: Entrainment regimes of impinging vorticity for  $Sc > 1$

Table 1:

Reference	Type of experiment	Richardson number exponent	Regime
Kato & Phillips 1969	Surface stress (screen), salt	-1 (-1/2 Price 1979)	II
Kit et al 1980	Surface stress (screen), salt	-3/2	III
Jones & Mulhearn 1983	Surface stress (screen), salt	-2	
Deardorff & Yoon 1984	Surface stress (screen), salt	-3/2	III
Monismith 1986	Surface stress (moving surface belt)	-1	IX
Chai 1989	Surface stress (screen)	-1.8	
Turner 1969	Surface stress (field), ocean	-1	IX
Denman & Miyake 1973	Surface stress (field), ocean	-1	IX
Halpern 1974	Surface stress (field), ocean	-1	IX
Kullenberg 1977	Surface stress (field), ocean	-1	IX
Price et al 1978	Surface stress (field), ocean	-1	IX
Dillon & Powell 1979	Surface stress (field), Lake Tahoe	-1	IX
Wu 1973	Surface stress (wind), salt	-1	IV
Kranenburg 1984	Surface stress (wind), salt	-1/2	II
Buch 1980	Buoyant overflow (field), salt	-1	IX
Pedersen 1980	Buoyant overflow	-1	IX
Moore & Long 1971	Counterflow, salt	-1	IX
Piat & Hopfinger 1981	Entrainment into a boundary layer	-1/2	II
Narimousa & Fernando 1987	Odell-Kovasznay tank, salt	-1	IX
Schneider 1980	Horizontal jet, salt	-3/2	III
Kumagai 1984	Plume, salt	-3/2	III
Baines 1975	Vertical jet or plume, salt	-3/2	III
Nokes 1988	Grid, salt	-1.2	
Kantha et al 1977	Surface stress (screen), salt	-1 (-1/2 Price 1979)	II
Fernando & Long 1985	Grid, salt	-7/4	
Turner 1968	Grid, salt, heat	-3/2, -1	III, IV
Shy 1990	Grid+buoyancy reversal	-3/2	III
Deardorff & Willis 1982	Surface stress (screen)	$R_t^{-1/2} R_v^{-1.4}$	II, III
Narimousa et al 1986	Odell-Kovasznay tank, salt	-1/2, -1, -3/2	II, IX, III
Fernando 1987	Grid+stabilizing buoyancy flux, salt	-1	
Linden 1973	Vortex ring impingement, salt	-3/2	II
Hopfinger & Toly 1976	Grid, salt	-3/2	III
Hannoun & List 1988	Grid, salt	-3/2	III

# Diapycnal Mixing: Fluxes and Energetics

Kraig B. WINTERS<sup>\*†</sup>, Peter N. LOMBARD<sup>\*</sup>,

James J. RILEY<sup>\*†</sup> AND ERIC A. D'ASARO<sup>\*†</sup>

The energetics and fluxes associated with diapycnal mixing in a density-stratified Boussinesq flow are discussed. The concept of gravitational available potential energy is used to formulate an energy budget in which the evolution of the background potential energy, *i.e.* the minimum potential energy attainable through adiabatic motions, can be explicitly examined. For closed systems, *i.e.* those with no advection across the boundaries, the background potential energy can only change as a result of diabatic processes. Changes in the background potential energy provide a direct measure of the potential energy changes due to diabatic mixing. The analysis is generalized to allow treatment of open boundaries and can be applied to either transient or steady state flows. It is particularly appropriate for evaluation of diabatic mixing rates in numerical simulations of turbulent flows. The energetics of a shear-driven mixing layer and an internal wave instability at a critical level are used to illustrate the analysis.

## 1. INTRODUCTION

In this paper, we discuss the energetics of diapycnal mixing in density-stratified Boussinesq fluids. We use the term diapycnal mixing to describe the process through which the potential energy of a fluid volume is irreversibly increased through molecular diffusion. The rate of diapycnal mixing is significantly enhanced if the fluid flow is turbulent rather than laminar. The mixing rate is thus a fundamental descriptor of a density-stratified, turbulent flow. This rate, however, is notoriously difficult to measure, whether in the laboratory, in the field or, more surprisingly, in numerical simulations. Most measurement strategies are based on a Reynolds averaged theory assuming a steady-state, production equals dissipation, turbulent energy balance. As not all flow fields of interest satisfy this assumption, a more general approach is desirable.

In this discussion, we will consider isolated, small-scale turbulent mixing events within a larger-scale stable stratification, such as those that occur frequently in the ocean. We will consider the time dependent energetics within a fixed volume  $V$  enclosing the mixing event with the aim of determining the instantaneous rate of diapycnal mixing. First, we review the Osborn-Cox (1972) (OC) approach to determining the mixing rate from microstructure measurements, *i.e.* dissipation rate of density variance. We then introduce a more general approach, based on the theory of available potential energy. We show that using this approach, instantaneous rates of diapycnal mixing can be unambiguously determined. Analyses of numerical simulations of transient mixing events will be used to illustrate the discussion.

## 2. OSBORN-COX BALANCE

In this section we briefly review the theoretical basis of the OC method for determining diapycnal fluxes from microstructure measurements, emphasizing the underlying assumptions.

<sup>\*</sup>Applied Physics Laboratory, <sup>†</sup>Department of Applied Mathematics, <sup>\*</sup>Department of Mechanical Engineering, <sup>†</sup>School of Ocean and Fishery Sciences

### 2.1. Diapycnal Flux

The Osborn-Cox analysis (Osborn and Cox, 1972) begins with the equation for temperature; we will use the Boussinesq density equivalent.

$$\frac{\partial \rho}{\partial t} + \bar{u} \cdot \nabla \rho = \kappa \nabla^2 \rho \quad (1)$$

Here  $\kappa$  is the coefficient of diffusivity and is assumed constant. Define a linear averaging operator  $\langle \rangle$  such that all fields can be decomposed into mean and fluctuating parts, i.e.  $\rho = \langle \rho \rangle + \rho'$  with  $\langle \rho' \rangle = 0$ . The specification of the averaging operator  $\langle \rangle$  will be denoted assumption  $\mathcal{A}$ . For horizontally homogeneous turbulence, with mean fields that vary only in the vertical (assumption  $\mathcal{B}$ ), Eq. (1) can be used to obtain

$$\begin{aligned} \frac{\partial}{\partial t} \langle \frac{1}{2} \rho'^2 \rangle + \langle w' \rho' \rangle \frac{d}{dz} \langle \rho \rangle = \\ -\kappa \langle |\nabla \rho'|^2 \rangle \end{aligned} \quad (2)$$

Assuming further that the flow is steady in time (assumption  $\mathcal{C}$ ) gives

$$\langle w' \rho' \rangle = -\kappa \langle |\nabla \rho'|^2 \rangle \left[ \frac{d}{dz} \langle \rho \rangle \right]^{-1} \quad (3)$$

The OC assumptions  $\mathcal{ABC}$  result in a balance between the buoyancy flux and the diapycnal flux. Note that the diapycnal flux is positive definite for stable mean density gradients.

### 2.2. Energetics

It is useful to relate the fluxes in Eq. (3) to the time rate of change of potential energy. Averaging Eq. (1)

$$\frac{\partial}{\partial t} \langle \rho \rangle = -\frac{\partial}{\partial z} \langle w' \rho' \rangle + \kappa \frac{\partial^2}{\partial z^2} \langle \rho \rangle \quad (4)$$

The total potential energy  $E_p$  is

$$E_p = g \int_V \rho z \, dV \quad (5)$$

and using the mean state  $\langle \rho \rangle$  and (4) yields

$$\frac{d}{dt} \langle E_p \rangle = g \int_V \langle w' \rho' \rangle \, dV \quad (6)$$

where we have further assumed that the mean density gradient is fixed at the upper and lower

surfaces of  $V$ . This assumption is for convenience only, diffusive boundary terms can easily be carried along in this and the subsequent analysis. From the previous section, assuming  $\mathcal{B}$  and  $\mathcal{C}$ , the buoyancy flux can be replaced by the diapycnal flux, i.e.

$$\begin{aligned} \frac{d}{dt} \langle E_p \rangle = \\ -\kappa g \int_V \langle |\nabla \rho'|^2 \rangle \left[ \frac{d}{dz} \langle \rho \rangle \right]^{-1} \, dV \end{aligned} \quad (7)$$

Using the OC analysis, we reach the following conclusion. Provided that assumptions  $\mathcal{A}$ ,  $\mathcal{B}$  and  $\mathcal{C}$  are valid, i.e. provided an averaging operator  $\langle \rangle$  can be chosen such that the averaged fields are horizontally homogeneous and steady in time, the irreversible rate of increase of mean potential energy can be obtained by measuring the dissipation rate of density variance, the mean density gradient and integrating over the volume of interest. Many flows of interest do not satisfy these assumptions, particularly the assumption of steady-state.

### 2.3. Scaling Eq. (2) for the ocean thermocline

Suppose we were to choose  $\langle \rangle$  to be a 100m average taken along vertical profiles of the ocean thermocline. The density variance would be dominated by vertical displacements induced by the internal wavefield. Assuming a Gaussian distribution of internal waves with an rms displacement of about 3m and a correlation time scale of a few hours (Levine et al (1985), Briscoe (1977)), the first term in Eq. (2) is of the order of  $10^{-3} \text{ m}^2/\text{s}$  for  $n=1$  profile. The diffusive term on the right hand side of (2) is of the order of  $10^{-5} \text{ m}^2/\text{s}$  (Gregg, 1989). We can estimate then, that in order to neglect the time dependence in (2), spatial averaging over many ( $n = O(10^4)$ ) profiles is required. If the averaging is insufficient, time dependence cannot be neglected and, in particular, the irreversible result (7) will not hold. If the averaging is seriously deficient, Eq. (2) will be well approximated by a strictly adiabatic or reversible balance.

Further insight into the role of the averaging operator can be obtained by considering Eq. (3). Both ocean measurements (McPhee

(1992), Moum (1990)) and numerical simulations (Ramsden and Holloway (1992), Itsweire and Helland, (1989)) of stratified turbulence show that the buoyancy flux on the left hand side of (3) is dominated by scales of motion significantly larger than the diffusive scales and that at small scales, the buoyancy flux is often counter-gradient. The diapycnal flux, however, occurs only at small scales. Thus, in order for (3) to hold, the average  $\langle \rangle$  must include both "large" and "small" scales. We have already seen that, if internal wave scales are to be included, then time dependence cannot be neglected without heavy averaging. The amount of averaging required depends on the statistics of motions with scales much larger than those responsible for diffusion. In effect, the OC analysis requires the use of an averaging operator  $\langle \rangle$  that filters out reversible, adiabatic processes. In practice, we observe that scale-selective averaging, either temporal or spatial, is not a particularly effective way of accomplishing the separation. The underlying difficulty is that reversible and irreversible processes overlap in both spatial and temporal scale. The practical difficulties are particularly severe in the ocean thermocline where reversible processes occur over a broad range of scales and the turbulent mixing events are often initiated by internal wave instabilities.

### 3. EXAMPLE: A TRANSIENT MIXING EVENT

We now illustrate the difficulties inherent in applying the OC analysis to an isolated, wave-driven mixing event in a stratified fluid. Results from a three-dimensional, large-eddy simulation of a wave instability at a critical level are shown. A more complete analysis of this simulation can be found in Winters and D'Asaro, (1994). The simulation describes the time evolution of a downward propagating internal wave packet, a vertically varying horizontal shear flow and a small amplitude, broad-banded "noise" field. The analysis volume  $V$  encloses the known location of the critical level. The wave packet enters  $V$  from above and propagates toward the critical level, interacting with the ambient shear as it does so. The wave energy density increases and an instability develops, leading

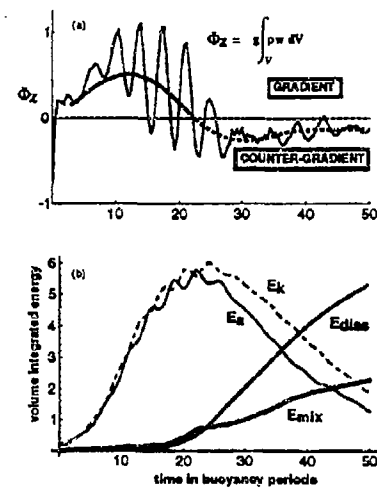


Fig. 1. (a) Volume integrated buoyancy flux during a transient mixing event. (b) Time histories of available potential energy ( $E_a$ ) and the increase in background potential energy due to mixing ( $E_{\text{mix}}$ ). Also shown are the volume integrated, fluctuating kinetic energy ( $E_k$ ) and the kinetic energy dissipation rate ( $E_{\text{diss}}$ ).

to turbulent mixing and dissipation.

Figure (1a) shows the volume integrated vertical buoyancy flux  $\Phi_z$  as a function of time. The horizontal extent of  $V$  coincides exactly with the horizontal wavelength of the incident wave packet. Early in the evolution  $\Phi_z > 0$ , increasing the potential energy  $E_p$ . Prior to about  $t = 18$ , when the wave instability begins, the effective balance in Eq. (2) is between the first two terms, with the diffusive term of negligible importance. Physically, fluid parcels are displaced from their equilibrium positions, increasing the potential energy of the fluid. After about  $t = 18$ ,  $\Phi_z < 0$  and the potential energy decreases. It is during this time, however, that all of the diffusive mixing occurs. Energetically, the restratification associated with the collapsing internal waves dominates the small increase in potential energy associated with irreversible diffusive mixing. At no time during this process does the steady state balance (3) hold. Spatial averaging alone is insufficient to filter out the reversible, wavelike contributions to the buoyancy flux and permit the use of Eq. (7).

If, in addition to spatial averaging, the flow is also averaged over the lifetime of the event, Eq. (3) becomes valid and the *average* rate of irreversible mixing can be determined using (6) or (7). This result is somewhat unsatisfactory. Mixing may not happen uniformly during transient events and we would like to be able to determine the rate of irreversible mixing on an instantaneous basis. This can be accomplished using the concepts of available and background potential energy.

#### 4. AVAILABLE POTENTIAL ENERGY AND DIAPYCNAL MIXING

We now exploit the theory of available potential energy to derive an expression for the instantaneous rate of diapycnal flux. The key element in the theory of available potential energy is the reference or background state. The background state is defined as that state, obtained through adiabatic redistribution of fluid elements, that minimizes potential energy (see e.g. Lorenz, 1955; Lombard, 1989). Available potential energy is the difference between the potential energy of the actual fluid state and the potential energy of the background state. Because the background state can be represented mathematically as a function of a single sorting coordinate (see Section 4.1), we often refer to it as the background or sorted-state profile.

For a fixed volume with no boundary fluxes, i.e. for a fixed mass of fluid, the background profile will change in time if and only if diffusive mixing occurs. Since changes in the energetics of the background profile can be ascribed to diapycnal mixing (Winters et al 1994), we can interpret the time rate of change of the background state in terms of a diapycnal flux. Our development is generalized to include open systems, i.e. fixed spatial volumes within which the mass is not necessarily conserved. As we will see, the concepts of available and background potential energy are ideally suited to the study of irreversible mixing in a stratified flow.

In Section 4.1 we introduce the spatial sorting coordinate  $z_*$ . We then derive an evolution equation for the background density pro-

file  $\rho(t, z_*)$ . In 4.2, the time rate of change of the background state is integrated to give an expression for the instantaneous rate of diapycnal flux. The energetics of diapycnal mixing are then discussed in 4.3.

##### 4.1. The sorting coordinate $z_*$

Consider a Lagrangian description of a Boussinesq fluid flow in a fixed spatial volume  $V$ . Each fluid element is uniquely identified by its initial location  $\vec{x}_0$  and the time  $t$ . For a given velocity field  $\vec{u}$ , the properties of interest for each element include the position  $\vec{x}(\vec{x}_0, t)$  and the density  $\rho(\vec{x}_0, t)$ . We will introduce an additional property  $z_*(\vec{x}_0, t)$ , defined as follows:

$$z_*(\vec{x}_0, t) = \frac{1}{A} \int_V H(\rho(\vec{x}, t) - \rho(\vec{x}_0, t)) dV. \quad (8)$$

Here  $A$  is the horizontal area of  $V$  and  $H$  is the Heaviside step function satisfying

$$H(\rho(\vec{x}, t) - \rho(\vec{x}_0, t)) = \begin{cases} 0, & \rho(\vec{x}, t) < \rho(\vec{x}_0, t) \\ 1/2, & \rho(\vec{x}, t) = \rho(\vec{x}_0, t) \\ 1, & \rho(\vec{x}, t) > \rho(\vec{x}_0, t). \end{cases}$$

The analysis can be generalized to irregular volumes by letting  $A = A(z)$  and moving it into the integrand. We will limit our discussion to regular domains for which  $A$  is independent of depth. The property  $z_*$  has dimensions of length and can be interpreted as a statistically stable ordering of the fluid elements, with  $z_*(\vec{x}_1, t) < z_*(\vec{x}_2, t)$  when  $\rho(\vec{x}_1, t) > \rho(\vec{x}_2, t)$ . The function  $z_*(\vec{x}_0, t)$  has the same value at all points on a given isopycnal surface and so  $z_*$  can be considered a unique function of density  $\rho$ . Consequently, we will sometimes use the notation  $z_*(\rho)$ .

The evolution equations for position and density are simply

$$\frac{d}{dt} \vec{x}(\vec{x}_0, t) = \vec{u}(\vec{x}, t) \quad (9)$$

$$\frac{d}{dt} \rho(\vec{x}_0, t) = \kappa \nabla^2 \rho(\vec{x}, t) \quad (10)$$

where  $\frac{d}{dt}$  is the material derivative following the motion of a given element. The corresponding equation for  $z_*$  can be derived from the pre-

ceding equations. Taking the time derivative of Eq. (8) and using Eqs. (9) and (10) gives

$$\frac{d}{dt} z_*(\vec{x}_0, t) = \frac{1}{A} \int_V \delta(\rho(\vec{x}', t) - \rho(\vec{x}, t)) \times [\kappa \nabla^2 \rho(\vec{x}', t) + \nabla \rho \cdot \vec{u} - \kappa \nabla^2 \rho(\vec{x}, t)] dV' \quad (11)$$

where  $\delta$  is the Dirac delta function. Note that

$$\nabla H(\rho(\vec{x}, t) - \rho(\vec{x}_0, t)) = \delta(\rho(\vec{x}, t) - \rho(\vec{x}_0, t)) \nabla \rho. \quad (12)$$

Isopycnally averaging Eq. (11), i.e. averaging over those points  $\vec{x}_0$  comprising an isopycnal surface, and using the incompressibility relation  $\nabla \cdot \vec{u} = 0$  gives

$$\frac{d}{dt} \langle z_* \rangle_\rho = \frac{1}{A} \int_S H(\rho(\vec{x}', t) - \rho(\vec{x}, t)) \vec{u} \cdot \hat{n} dS' \quad \text{or} \quad \frac{d}{dt} z_*|_\rho = T_S(t, z_*), \quad (13)$$

where  $S'$  is the surface bounding  $V$  and  $\hat{n}$  is the outward facing unit vector normal to  $S'$ .  $T_S$  is the rate of advective transport of fluid heavier than a specified density across  $S'$ .

Eq. (10) can also be averaged over an isopycnal surface. Since  $z_*$  has the same value for all elements on an isopycnal surface, we write

$$\frac{d}{dt} \rho|_{z_*} = \kappa \langle \nabla^2 \rho \rangle_{z_*}. \quad (13)$$

Since there is a one-one mapping between  $z_*$  and  $\rho$  at any time  $t$ , we can express  $\rho = \rho(t, z_*)$  and write a differential equation for the time rate of change of the sorted-state or background profile.

$$\begin{aligned} \frac{d}{dt} \rho(t, z_*) &= \frac{d}{dt} \rho|_{z_*} + \frac{d\rho}{dz_*} \frac{d}{dt} z_*|_\rho \\ &= \kappa \langle \nabla^2 \rho \rangle_{z_*}(t, z_*) + \frac{d\rho}{dz_*} T_S(t, z_*) \quad (14) \end{aligned}$$

Equation (14) describes the time evolution of the adiabatically rearranged state of minimum potential energy. As expected, the background profile is insensitive to adiabatic motions unless these motions result in a net mass flux into  $V$ . The background density profile changes in time as a result of diffusive fluxes across isopycnal surfaces.

#### 4.2. Diapycnal Flux

We can now express the diffusive term in (14) as the gradient of a diapycnal flux  $\phi_d$ . Let

$$\kappa \langle \nabla^2 \rho \rangle_{z_*}(t, z_*) = -\frac{1}{g} \frac{d}{dz_*} \phi_d(t, z_*). \quad (15)$$

Integrating with respect to  $z_*$  gives

$$\phi_d(t, z_*) = -\kappa g \int^{z_*} \langle \nabla^2 \rho \rangle_{z_*'}(t, z_*') dz_*'. \quad (16)$$

Consider a spatially isolated turbulent mixing event that occurs within  $V$ . The volume integrated, instantaneous rate of diapycnal flux  $\Phi_d$  is

$$\Phi_d(t) = A \int_{z_1}^{z_2} \phi_d(t, z_*) dz_* \quad (17)$$

where  $z_1$  and  $z_2$  are the lower and upper bounds on the range of  $z_*$  obtained via Eq. (8). Assuming that  $V$  is chosen so that the diffusive flux is negligible at the bounding surface  $S$ ,  $\Phi_d$  can be written as

$$\Phi_d(t) = A \kappa g \int_{z_1}^{z_2} \langle z_* \nabla^2 \rho \rangle_{z_*}(t, z_*) dz_* \quad (18)$$

Eqs. (16) and (18) show that the diapycnal flux can be expressed in terms of the local rate of diffusion, averaged isopycnally, and integrated with respect to the  $z_*$  coordinate. In the absence of molecular diffusion,  $\Phi_d = 0$ .

These results can be recast slightly for comparison with oceanic microstructure measurements. Distributing the divergence operator, and noting that  $\nabla z_* = \frac{dz_*}{d\rho} \nabla \rho$ , gives

$$\begin{aligned} \Phi_d(t) &= -A \kappa g \int_{z_1}^{z_2} \frac{dz_*}{d\rho} |\nabla \rho|^2 \langle z_* \rangle_{z_*} dz_* \\ &\quad + A \kappa g \int_{z_1}^{z_2} \langle \nabla \cdot z_* \nabla \rho \rangle_{z_*} dz_*. \quad (19) \end{aligned}$$

The second term reduces to  $A \kappa g (z_* \frac{d\rho}{dz_*})|_{z_1}^{z_2}$ . Note that when  $\nabla \rho = \frac{d\rho}{dz} = \text{constant}$ , the two terms on the right hand side of (19) cancel and  $\Phi_d = 0$ .

Eq. (19) shows that the volume integrated, instantaneous rate of diapycnal flux can be obtained by making measurements of  $\rho$  and  $\nabla \rho$ , sorting, and integrating spatially. Eq. (19) is very similar to the Osborn-Cox recipe for di-

adiabatic diffusivity (Gregg, 1987; Osborn and Cox, 1972) when formulated in terms of density rather than temperature. In contrast to the Osborn-Cox formulation, however, Eq. (19) does not require the flow to satisfy a steady state, production equals dissipation, density variance balance. Thus, microstructure profiles taken from isolated turbulent mixing events, not necessarily in steady state, can be interpreted directly in terms of a diapycnal flux.

#### 4.3. Energetics

In this section we neglect advective fluxes across  $S$ , letting  $\vec{u} \cdot \hat{n} = 0$ , and show that the diapycnal flux  $\phi_d$  results in an irreversible increase in background potential energy  $E_b$ . A more complete discussion of the rates of energy transfer between kinetic, available potential and background potential energies, allowing for more general boundary conditions, is given in Winters et al (1994). Within a fixed volume  $V$ , the background potential energy is defined as

$$E_b(t) = g \int_V z_* \rho(\rho) \rho(\vec{x}, t) dV = Ag \int_{z_1}^{z_2} z_* \rho(t, z_*) dz_* \quad (20)$$

where  $z_*$  and  $\rho$  are related via Eq. (8). Taking the time derivative and neglecting advection across  $S$ , we obtain

$$\frac{d}{dt} E_b = Ag \int_{z_1}^{z_2} z_* \frac{d}{dt} \rho|_z dz_* \quad (21)$$

The time derivative in the integrand can be rewritten using Eqs. (13) and (15). Thus,

$$\frac{d}{dt} E_b = -A \int_{z_1}^{z_2} z_* \frac{d}{dz_*} \phi_d(z_*) dz_* \quad (22)$$

which can be integrated by parts to give

$$\frac{d}{dt} E_b = A \int_{z_1}^{z_2} \phi_d(z_*) dz_* = \Phi_d(t) \quad (23)$$

assuming that diffusion across the bounding surface  $S$  is negligible. Thus, diapycnal mixing, which occurs at the instantaneous rate  $\Phi_d(t)$  irreversibly increases the background potential energy  $E_b$ .

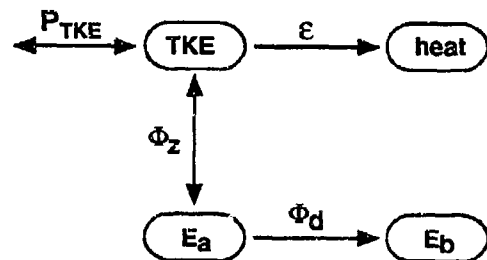


Fig. 2. Energy transfers in a diffusive, density-stratified flow. Double sided arrows indicate reversible energy exchanges, single sided arrows indicate irreversible energy transfers.

Denoting the available potential energy  $E_a$ , and noting that the total potential energy  $E_p$  is the sum of  $E_a$  and  $E_b$ ,

$$\frac{d}{dt} E_p = \int_V g \rho w dV + \Phi_i = \Phi_z + \Phi_i \quad (24)$$

$$\frac{d}{dt} E_a = \Phi_z + \Phi_i - \Phi_d \quad (25)$$

where  $\Phi_z$  is the spatially integrated, (negative) vertical buoyancy flux and  $\Phi_i$  is the rate of exchange between internal and potential energy. For the Boussinesq Eq. (1), this rate is nonzero but extremely small compared with turbulent exchange rates and will be henceforth ignored.

Neglecting  $\Phi_i$ , Eqs. (23)-(25) are summarized in a simple energy diagram in Figure 2. The energy components represent spatially integrated quantities and the transfer rates are generally time dependent. Energy is input via turbulent production  $P_{TKE}$ . Turbulent kinetic energy (TKE) can then be irreversibly dissipated at rate  $\epsilon$  or converted to available potential energy at rate  $\Phi_z$ . Available potential energy is then exchanged with TKE, at rate  $\Phi_z$ , or irreversibly converted to background potential energy at rate  $\Phi_d$ .

The time dependent, wave driven mixing previously discussed can now be easily diagnosed. The time rate of change of  $E_b$  can be computed, as can the contributions resulting from mass fluxes across the bounding surface  $S$ . Alternatively, Eq. (19) can be used directly, independent of whether mass is conserved. In Figure (1b), the quantity  $E_{mix}$  is the background

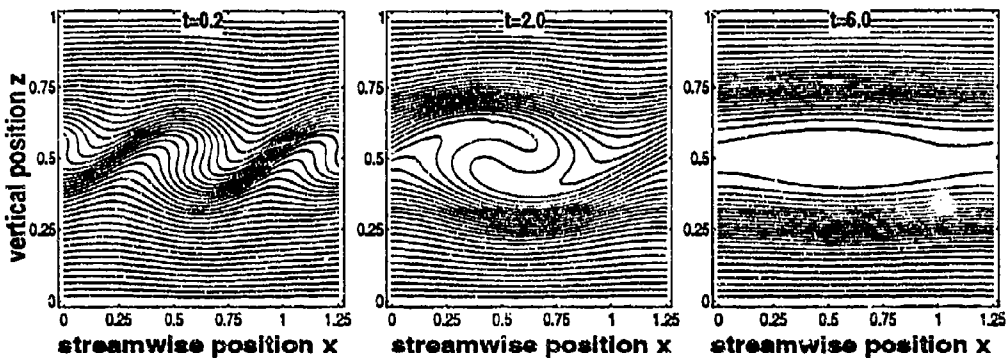


Fig. 3. Density contours from a low  $Re$  shear-driven mixing event.

potential energy, compensated for changes due to mass fluxes across  $S$ . Note that prior to the wave instability,  $E_{\text{mix}}$  remains small as the rate of diffusion is negligible. During this time, the available potential energy  $E_a$  increases as the wave propagates into  $V$ , displacing the initially quiescent isopycnals. As the wave collapses and restratification occurs,  $E_a$  decreases. At the same time, diapycnal mixing begins as evidenced by the increase in  $E_{\text{mix}}$ . Partitioning the potential energy between available and background components allows the adiabatic and the diabatic processes to be examined separately.

##### 5. TIME DEPENDENT DIAPYCNAL FLUX

We now consider a second numerical example. Figure 3 shows isopycnals from a low  $Re$  simulation of a shear-driven mixing layer at several instants in time. The isopycnals were initially flat. At each time shown, the instantaneous value of potential energy  $E_p(t)$  is greater than the initial value  $E_p(0)$ . To what extent the cumulative increase in  $E_p$  at any given time is due to adiabatic, reversible buoyancy flux or to diabatic, irreversible mixing cannot be determined using simple potential energy arguments.

Using the developments presented in the previous section, however, the time dependent rate of diapycnal mixing, as a function of density (or  $z_*$ ) can be examined. Figure 4 shows contours of the reference density field  $\rho(t, z_*)$  for the flow corresponding to Figure 3. If no di-

apycnal mixing were to occur, the isopycnals would remain flat. Spreading isopycnals indicate the formation of a mixed layer. The diapycnal flux responsible for the mixing is shown in (4b). The flux can be calculated via Eq. (16) or by assuming the observed time rate of change of the density field results from the gradient of a flux and integrating numerically to find the flux. Though the volume integrated flux  $\Phi_d$  is a positive definite quantity, Eq. (16) places no sign constraint in the local values of  $\phi_d$ ;  $\langle \nabla^2 \rho \rangle_{z_*}$  can be of either sign. Figure 4(b) shows two distinct regions where  $\phi_d < 0$ . The regions of negative flux correspond to fluid for which the background density gradient increases. These negative fluxes are purely diffusive, they do not indicate counter-gradient fluxes in the usual (adiabatic) sense.

##### 6. SUMMARY AND CONCLUSIONS

The concepts of available and background potential energy are extremely well suited for the analysis of the energetics of diapycnal mixing in density-stratified fluids. The sorting operations inherent in these ideas can be expressed mathematically and used to derive evolution equations for the reference state, the instantaneous flux and the rate of change of both background and available potential energy. The results presented show that instantaneous mixing rates can be calculated for a turbulent, stratified flow even if the flow is not steady and in the presence reversible internal waves.

The diapycnal flux rate in a fixed volume  $V$

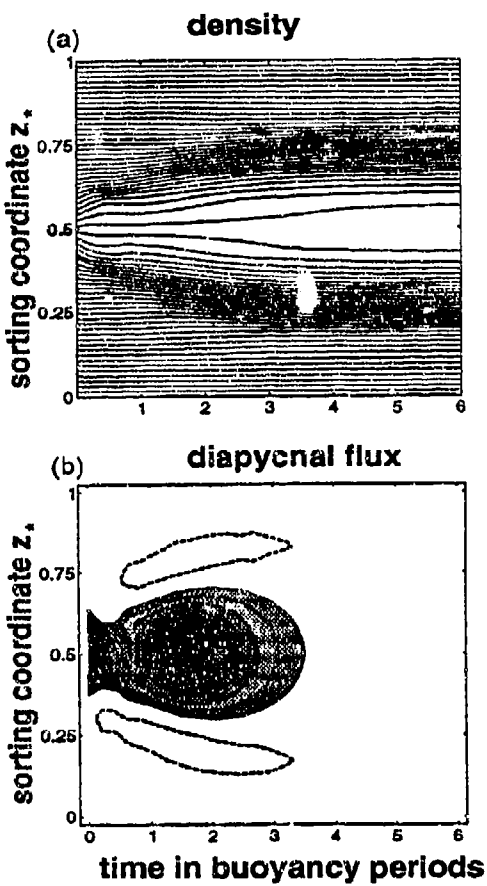


Fig. 4. (a) Density contours from in the  $(t, z^*)$  plane. Diapycnal mixing produces diverging isopycnals. (b) Diapycnal flux  $\phi_d$ . Darker shading indicates larger positive values. Dashed contours indicate (slightly) negative values.

that encloses a turbulent region of interest can be obtained directly from measurements of  $\rho$  and  $\nabla \rho$ . These quantities are commonly measured in the ocean using vertical microstructure profilers, but have only been formally related to the desired diapycnal flux when ensemble averaged to justify a steady-state, production equals dissipation energy balance.

*Acknowledgments.* The authors are indebted to Derek Stretch and Chantal Staquet for the many

discussions that led to the formulation of these ideas. We also appreciate the insightful comments of Frank Henyey, Harvey Seim and Mike Gregg. This work was supported by the National Science Foundation and the Office of Naval Research.

## 7. REFERENCES

Briscoe, M. G., 1977: Gaussianity of internal waves. *J. of Geophys. Res.*, **82**, 2117-2126.

Gregg, M. C., 1989: Scaling turbulent dissipation in the thermocline. *J. of Geophys. Res.*, **94**, 9686-9698.

Itsweire, E. C. and K. N. Helland, 1989: Spectra and energy transfer in stably stratified turbulence. *J. Fluid Mech.*, **207**, 419-452.

Levine, M. D., Paulson, C. A., and J. H. Morison, 1985: Internal waves in the Arctic Ocean: Comparison with lower-latitude observations. *J. Phys. Oceanogr.*, **15**, 800-809.

Lombard, P. N., 1989: Energetics of a stably stratified turbulent flow, Masters thesis, Department of Mechanical Engineering, University of Washington.

Lorenz, E. N., 1955: Available potential energy and the maintenance of the general circulation. *Tellus*, **7**, 157-167.

McPhee, M. G., 1992: Turbulent heat flux in the upper ocean under sea ice. *J. of Geophys. Res.*, **97**, 5365-5379.

Moum, J., 1990: The quest for  $K_p$ : preliminary results from direct measurements of turbulent fluxes in the ocean. *J. Phys. Oceanogr.*, **20**, 1980-1984.

Osborn, T. R., and C. S. Cox, 1972: Oceanic fine structure. *Geophys. Fluid Dyn.*, **3**, 321-345.

Ramsden, D. and G. Holloway, 1992: Energy transfers across the internal wave-vortical mode spectrum. *J. of Geophys. Res.*, **97**, 3659-3668.

Winters, K. B. and E. A. D'Asaro, 1994: Three-dimensional wave instability near a critical level. *To appear J. Fluid Mech.*

Winters, K. B., Lombard, P. N., Riley, J. J. and E. A. D'Asaro, 1994: Available potential energy and mixing in density-stratified fluids. *Submitted to J. Fluid Mech.*

# Turbulent Penetration and Mixing at an Interfacial Layer in a Wind Tunnel

Jayesh and Z. Warhaft

Sibley School of Mechanical & Aerospace Engineering  
Ithaca, New York 14853

## 1 Introduction

The transport of heat, pollutants,  $CO_2$ , moisture and other trace gases is affected by stable stratification, both in the ocean (particularly at the thermocline) and atmosphere, (particularly at the top of the boundary layer, where there is an inversion cap, and at the tropopause). Under some conditions the stable stratification, in which the temperature increases (density decreases) with height, dampening turbulence and sometimes completely suppressing it, persists for long periods allowing the pollution concentration to increase to intolerable levels, such as can occur in Los Angeles when warm air from the sea over-rides cooler air at ground level. The broad concepts are well understood: the decrease in density inhibits the overturning of the turbulent eddies by extracting their kinetic energy and converting it into potential energy. The dynamics are discussed in the standard texts, e.g. Turner (1973). The diffusivity of turbulence is many orders greater than that of laminar flow and if it is suppressed, so is the mixing and transport of pollutants, trace gases and particles. However, in order to design new power-stations and smoke stacks as well as write new legislation, and litigate against transgression of existing law, there are details of the scalar mixing and transport that must be understood. We must know, for example, the probability density function (pdf) of the fluctuations, and how it varies with stability. It is not enough to know the mean concentration of a toxic pollutant if there is a reasonable chance of a fluctuation hundreds of times greater occurring, killing a human or animal who happens by chance to take a breath. This implies that we must have a deeper understanding of the higher order moments, joint moments and joint pdf's and so on. *In situ* measurements are difficult, if not impossible because of the very large sampling times needed to supply stable higher order statistics (Wyngaard, 1973). The stirred tank experiments carried out over the past thirty years (Turner 1973, Hopfinger 1987, Fernando, 1992), while supplying detailed information on entrainment rates under controlled conditions, are inherently non-stationary and thus here too there is insufficient time to gain reliable higher order statistics.

In the experiment described here we have used a wind tunnel, with the air in the upper portion heated, to produce an inversion or interfacial layer (Figure 1). Moreover we have induced a much greater level of turbulence below the inversion

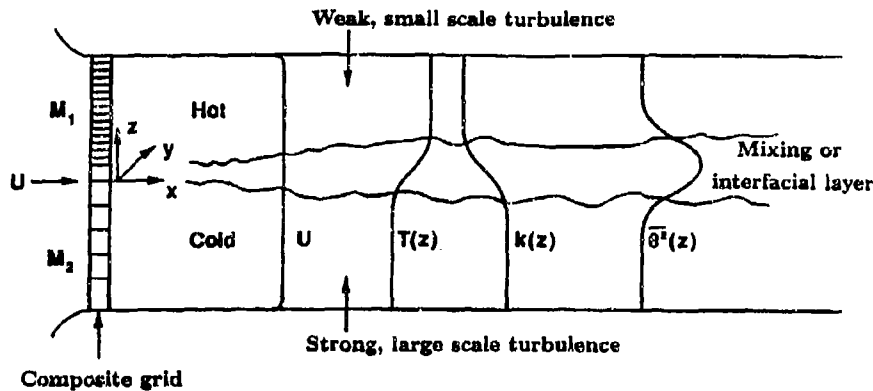


Figure 1. A sketch of the test section of the stratified wind tunnel showing vertical profiles of  $U$ ,  $T(z)$ ,  $k(z)$  and  $\langle \theta^2 \rangle(z)$ . The composite grid (Veeravalli & Warhaft 1989) generates large scale turbulence at the bottom, and small scale turbulence above, in the absence of mean shear. The temperature step is generated to the left of the grid in the plenum chamber by means of a number of horizontal heating rods, the bottom half of which are turned off (Yoon & Warhaft 1990). The profiles of mean temperature, kinetic energy and temperature variance in the mixing or interfacial layer are similar to those observed in the atmospheric boundary layer, at the capping inversion.

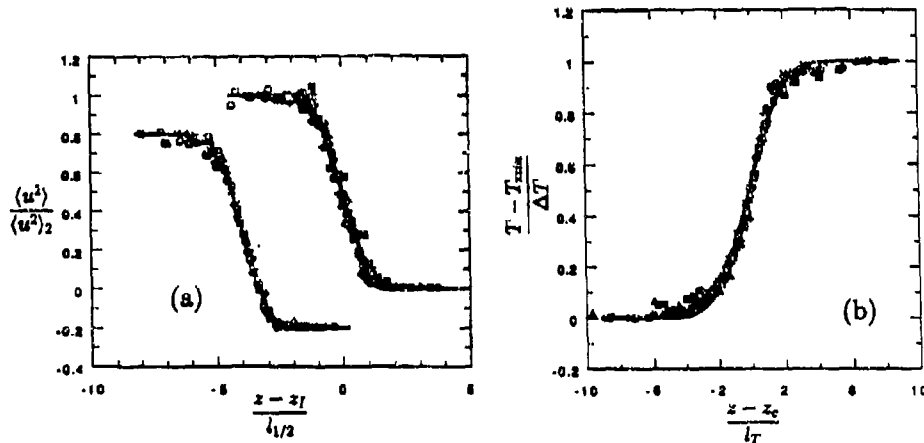


Figure 2. (a). Horizontal velocity variance profiles, without stratification (left hand side) and with stratification (right hand side).  $\langle u^2 \rangle_2$  is the velocity variance in the strong turbulence side of the layer,  $l_{1/2}$  is the velocity half width of the layer and  $z_i$  is the inflection height of the velocity variance profile. Solid line, best fit error function. The profile on the left has been shifted  $-4$  non dimensional units to the left and down by  $-0.2$  units. The various symbols represent different downstream distances. (b). Mean temperature profiles normalized by the temperature step,  $\Delta T$ .  $T_{min}$  is ambient temperature in the large scale turbulence region. The height  $z$  is normalized by the mean thermal half width  $l_T$ .  $z_c$  is the center line height of the mean temperature profile. The various symbols represent different downstream distances.

by means of a grid of large mesh ( $M_2$ ). Above the layer we have used a fine mesh ( $M_1$ ) which while causing turbulence in its close proximity, decays very rapidly. Thus there is turbulent penetration of the almost quiescent inversion from below, such as occurs below, say the inversion cap of the planetary boundary layer (although in that case, we note, the turbulence is convectively, as well as mechanically driven). Notice that for this set-up the flow is statistically stationary; the evolution occurs in space (downstream), not in time as for the atmosphere and grid stirred tank experiments. Thus we are able to measure the statistics of the fluctuations with great accuracy. Furthermore our grid has been designed so that there is no shear and thus we are able to study the details of the transport process (Veeravalli and Warhaft 1989).

The experimental set-up is a combination of the earlier work of Jayesh, Yoon and Warhaft (1991) in which there was stable temperature step in conventional grid turbulence and the turbulence mixing grid of Veeravalli and Warhaft (1989) in which the velocity was generated in the same way as in the present work, but there was no stratified temperature step. A full account of the present work will appear in Jayesh and Warhaft (1994). What follows here is a summary.

## 2 Apparatus and Flow Conditions

We performed the experiment in our large ( $.91 \times .91 \text{ m}^2$  and  $9.1 \text{ m}$  long) open circuit, low turbulence level suction wind tunnel designed specially to study stratified flows, (Figure 1 and Yoon & Warhaft (1990)). A grid with two different mesh sizes on top and bottom but the same solidity throughout was used to create turbulence of the nature described in the Introduction. The grid design was essentially that of Veeravalli & Warhaft (1989) but was rescaled to fit the stratified horizontal tunnel used in our present experiment. On the top half of the flow (i.e., the low turbulence region) a rectangular wire mesh screen (wires in both vertical and horizontal direction) of mesh size  $3.175 \text{ mm}$  and wire-diameter  $1.19 \text{ mm}$  with open area of 70.2% (or solidity of 29.8%) was used; on the bottom, horizontal parallel adjustable bars of width  $11.11 \text{ mm}$  were used. Here too the solidity was 29.8%. Thus the ratio of the large to small scale mesh sizes,  $M_2/M_1$  was 12.6, a value higher than in our previous work. The overall change in  $U$  was less than 5% across the flow, comparing favorably with that observed by Veeravalli & Warhaft (1989). The turbulence intensity profiles will be discussed below. Heating elements at the entrance of the plenum (Yoon & Warhaft (1990)) were employed to produce the desired temperature step. Measurements were made for nominal values of  $\Delta T = 10^\circ\text{C}$ , and  $20^\circ\text{C}$  and a mean velocity of approximately  $4 \text{ m/s}$ . The mean velocity, fluctuating velocities and fluctuating temperature were measured using an X-wire in conjunction with a cold wire. Wollaston wires of  $5.08 \mu\text{m}$  diameter were used for the X-wire with the length to diameter ratio approximately 200, and the over heat ratio 1.95. A platinum resistance wire of  $1.27 \mu\text{m}$  with length to diameter ratio of 400 was used for the cold wire.

### 3 Results

As the flow evolves downstream, buoyancy effects become more pronounced since the turbulence decays and thus has less energy to work against the restraining (negative) buoyancy forces of the temperature step. The Bulk Richardson number,  $Ri_B$ , which we define as

$$Ri_B \equiv (g/T_0)(\Delta T/\ell_T)/(\langle u_2^2 \rangle/L_u^2)$$

where  $\Delta T$  is the temperature step,  $T_0$  is a reference temperature,  $\ell_T$  is the half width of the temperature step  $\langle u_2^2 \rangle$  is the velocity variance in the high turbulence side below the layer and  $L_u$  is the length scale of the turbulence below the layer, varied from zero, close to the grid, to 82 far downstream. In spite of the pronounced effects on the evolution of the layer thickness and the transport (see below) the variation in  $Ri_B$  did not have a striking effect on the form of the velocity variance profiles or the mean temperature profiles, which are close to an error function with or without stratification (Figure 2).

On the other hand the higher order moments were strongly affected by the stratification. Figure 3(a) shows the vertical velocity time series, at the interface, with and without stratification. For the unstratified case bursts of high velocity are evident; with stratification the bursts are suppressed and there is no sign of intermittency. Veeravalli and Warhaft (1989) show much of the thickening of the layer (in the neutral case) is due to the large scale bursting at the interface of the strong and weak turbulence. The qualitative effects of Figure 3(a) are manifested in the pdf of  $w$ . In Figure 3(b) we have plotted the fourth moment (kurtosis) of  $w$ , as a function of vertical height through the layer. On either side of the layer in the kurtosis has the Gaussian value of 3. With no thermal stratification it has a high value in the layer, reflecting the intermittency, but when the stratification is applied, the kurtosis is 3 throughout. The full pdf's show Gaussian behavior throughout the layer with stratification, while they are strongly skewed, with broad tails for the neutral case.

The suppression of large scale mixing by the stratification inhibits the growth of the layer. Figure 4(a) shows the evolution of the half width of the mean temperature profile as a function of  $x/M_2$  and Figure 4(b) shows the evolution of the temperature variance profiles as a function of  $Ri_B$ , which increases with  $x/M_2$ . For both cases the layer first thickens, as would be expected for a passive temperature step, and then due to the stabilizing effect of the layer, it becomes thinner. The same phenomenon was observed in Jayesh et al. 1991 for the symmetrical case (of turbulence of the same intensity above and below the layer). For this case however most of the layer development (thickening and thinning) is due to the bottom part of the layer, where the turbulence is strongest.

The effect of the stratification on the transport processes within the layer, is clearly shown in the vertical profiles of heat flux  $\langle \theta w \rangle$ , kinetic energy flux,  $\langle kw \rangle$ , where  $k \equiv \frac{1}{2}(u^2 + v^2 + w^2)$ , and the vertical flux of temperature variance,  $\langle \theta^2 w \rangle$ , Figures 5a, b, c, respectively. These figures contrast the various quantities at  $x/M_2 = 32 (Ri_B = 0.8)$  where the stratification is insignificant, to those at  $x/M_2 = 146 (Ri_B = 63)$  where the stratification is so strong that the heat flux has collapsed and has reversed sign (counter gradient) in the upper part of the layer (Figure 5a). Notice that the kinetic energy flux (Figure 5(b)) also changes sign in the upper part

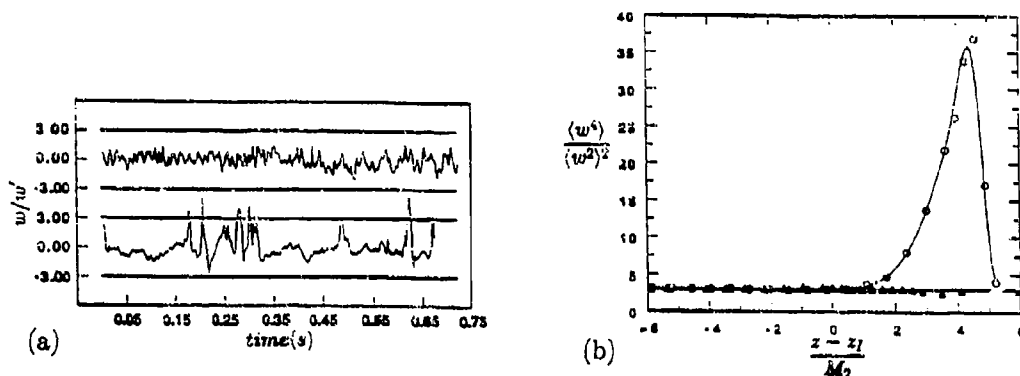


Figure 3. (a). Time series of the vertical velocity fluctuations with stratification (upper series) and without stratification (lower series) at  $x/M_2 = 146$ ;  $z/M_2 = 17.1$  and  $z/M_2 = 16.8$  respectively. The straight solid lines are  $\pm 3$  standard deviations from the mean. (b). The profiles of the kurtosis of the vertical velocity fluctuations at  $x/M_2 = 146$ , with ( $\Delta$ ) and without ( $\bigcirc$ ) stratification ( $\Delta T = 20.2^\circ C$ ).

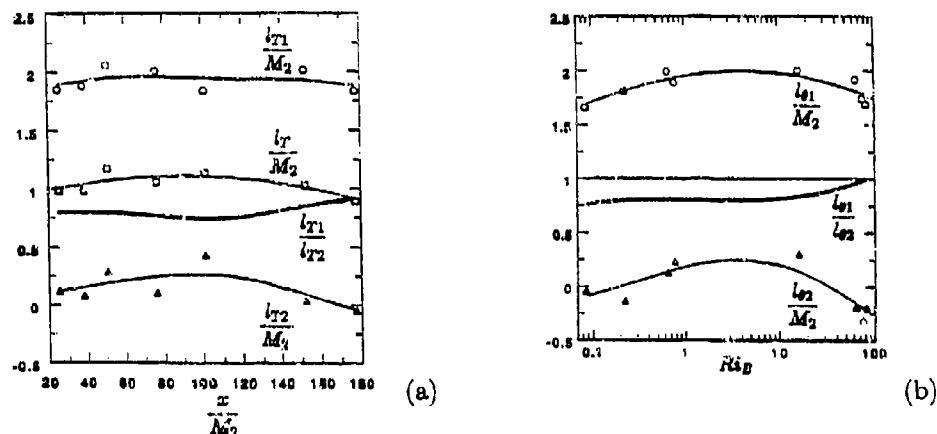


Figure 4. (a). Downstream evolution of the half width of the mean temperature profile,  $l_T$ , and its partition for the upper part of the layer,  $l_{T1}$ , and lower part,  $l_{T2}$ , as well as their ratio,  $l_{T1}/l_{T2}$ .  $M_2$  is the mesh length of the large grid bars.  $\square$ ,  $l_T$ ;  $\bigcirc$ ,  $l_{T1}$ ;  $\triangle$ ,  $l_{T2}$ ; thick line,  $l_{T1}/l_{T2}$ .  $l_{T1}$  has been shifted up by 1.0 and  $l_{T2}$  has been shifted down by 1.0 on the vertical axis. (b). The half width of the temperature variance profiles plotted as a function of  $Ri_B$ .  $l_{\theta 1}$  ( $\bigcirc$ ) is the half width of the upper portion of the profile and  $l_{\theta 2}$  ( $\triangle$ ) is the half width of the lower portion. The solid line is the ratio,  $l_{\theta 1}/l_{\theta 2}$ .  $l_{\theta 1}$  has been shifted up by 1.0 and  $l_{\theta 2}$  has been shifted down by 1.0.

of the layer, when the stratification becomes strong, as does transport of temperature variance: at  $x/M_2 = 32$ ,  $\langle \theta^2 w \rangle$  is positive above the location where  $\langle \theta^2 \rangle$  is maximum, and negative below, indicating the variance is carried away from its peak towards the edges of the layer, while the reverse holds further downstream in the region of counter gradient heat flux (Figure 5(c)). A more detailed analysis of these profiles is given in Jayesh and Warhaft (1994) where the gradients (and fluxes) of the quantities shown in Figure 5 are discussed.

In order to further investigate the effects of buoyancy we determined the conditional heat flux, i.e. the heat flux conditioned on its particular value of temperature. Assuming joint normality between  $w$  and  $\theta$  it can be shown (Jayesh and Warhaft 1994) that the normalized conditional heat flux,  $\xi$  is an inverted parabola, i.e.

$$\xi \equiv \frac{\langle w\theta | \theta \rangle}{|\langle w\theta \rangle|} = -\frac{\theta^2}{\langle \theta^2 \rangle} \equiv (-\alpha^2)$$

The joint normal assumption is sound for a passive scalar (Tavoularis and Corrsin 1981). Here we study the nature of the departure from joint normality, for stratified flows. Figure 6(a) shows  $\xi$  for a passive profile and for a stable stratification (both linear temperature profiles) taken from the data of Yoon and Warhaft (1990) in conventional grid turbulence. For the passive case  $\xi$  is indeed an inverted parabola, but when the stratification becomes significant,  $\xi$  curls up for large  $\alpha$ . Figure 6(a) clearly shows that in the mean sense, the intense fluctuations are affected by the buoyancy whereas the weaker fluctuations are still acting as if they were a passive scalar.

The conditional heat flux, for the present work is shown in Figure 6(b), far downstream in the strongly stable region. In this inhomogeneous field the departure from joint normality is strong, as would be expected, and the strongest departure is for the low energy turbulence. This plot provides a quantitative relationship between the stratification and the intensity of the fluctuations, indicating, for example, that for positive  $\theta$  its effects are small unless the fluctuations exceed approximately one standard deviation.

In summary, our results have much in common with our previous study of a stratified layer in a conventional grid turbulence (Jayesh et al. 1991), where we also found that the heat flux collapsed, resulting in a small but significant depletion of the vertical velocity variance within the layer. However, because the flow was close to homogeneous, there was relatively little large scale intermittency in the velocity field. Here, on the other hand, the velocity field above the layer was deliberately suppressed by means of the grid construction. Thus intermittency was *a priori* a principal method of transport for the passive case (the other mode being turbulent diffusion, Veeravalli & Warhaft 1989). For this configuration our experiment has clearly shown that the stratification completely suppresses the large scale intermittency and that transport is only by turbulent diffusion, be it up or down the gradient.

We thank the U.S. Department of Energy, Basic Energy Sciences, for their support.

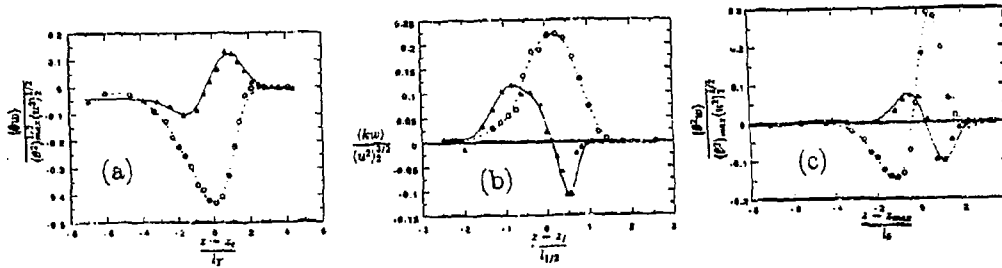


Figure 5. (a). The normalized heat flux profiles  $\langle \theta w \rangle / (\langle \theta^2 \rangle_{\max}^{1/2} \langle u^2 \rangle_2^{1/2})$ , at two downstream locations;  $x/M_2 = 32$  (passive) and  $x/M_2 = 146$  (strongly stable).  $\circ$ ,  $x/M_2 = 32$  ( $Ri_B = .8$ );  $\triangle$ ,  $x/M_2 = 146$  ( $Ri_B = 63$ ).  $z_c$  is the height where the mean temperature is  $T_{\min} + (T_{\max} + T_{\min})/2$ . Other symbols have been previously defined. (b). The normalized vertical flux of kinetic energy,  $\langle kw \rangle / \langle u^2 \rangle_2^{3/2}$ . (c). Vertical profiles of the normalized flux of temperature variance,  $\langle \theta^2 w \rangle / (\langle \theta^2 \rangle_{\max} \langle u^2 \rangle_2^{1/2})$ . The circles and triangles are at  $x/M_2 = 32$  and 146 respectively.

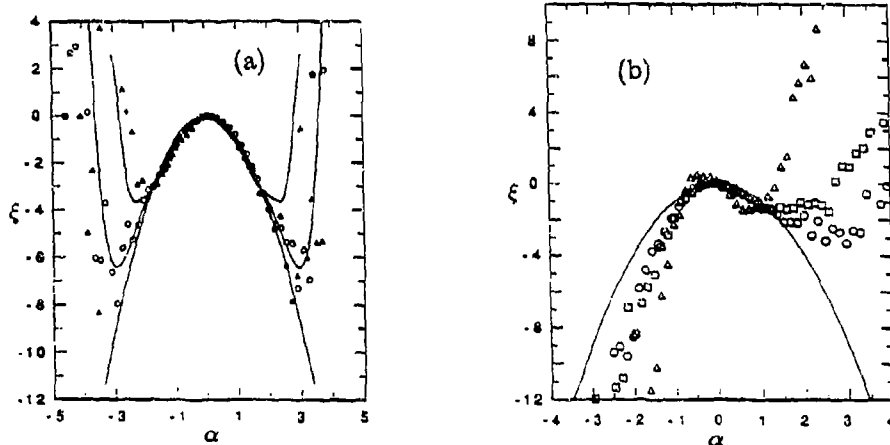


Figure 6. (a).  $\xi$  vs.  $\alpha$  for data of Yoon & Warhaft (1990) where the flow is strongly stable.  $\circ$ ,  $U = 2.8$  m/s,  $\partial T / \partial z = 55^\circ C$ ,  $x/M = 116.5$ ,  $\rho = -.39$ ;  $\triangle$ ,  $U = 3.6$  m/s,  $\partial T / \partial z = 50^\circ C$ ,  $x/M = 196.5$ ,  $\rho = -.16$ . The value of  $\xi$  for the passive case is the inverted parabola. A symmetric smooth curve has been drawn along the data points. (b). The normalized conditional heat flux  $\xi$  as a function of  $\alpha$  for the present experiment. The data is at  $x/M_2 = 146$  in the strongly stable region.  $\circ$ ,  $z/M_2 = 12.04$ ;  $\square$ ,  $z/M_2 = 12.67$ ;  $\triangle$ ,  $z/M_2 = 13.0$ . The curve shown in solid line is for the passive case.

## 4 References

Fernando, H.J.S. 1992 Mixing in stratified fluids. *Ann. Rev. Fluid Mech.* **23**, 455-493.

Hopfinger, E.J. 1987 Turbulence in stratified fluids: A review. *J. Geophys. Res.* **92**, 5287-5303.

Jayesh, Yoon, K. & Warhaft, Z. 1991 Turbulent mixing and transport in a thermally stratified interfacial layer in decaying grid turbulence. *Phys. Fluids A* **3**, 1143-1155.

Jayesh & Warhaft Z. 1994 Turbulent penetration of a thermally stratified interfacial layer in a wind tunnel. Submitted to *J. Fluid Mech.*

Tavoularis, S. & Corrsin, S. 1981 Experiments in nearly homogeneous turbulent shear flow with a uniform mean temperature gradient. Part 1. *J. Fluid Mech.* **104**, 311-347.

Turner, J.S. 1973 *Buoyancy effects in fluids* Cambridge U.P., Cambridge.

Veeravalli, S. & Warhaft, Z. 1989 The shearless turbulence mixing layer. *J. Fluid Mech.* **207**, 191-229.

Wyngaard, J.C. 1973. On surface layer turbulence. In *Workshop on micrometeorology* (ed. D.A. Haugen), pp 101-149.

Yoon, K. & Warhaft, Z. 1990 The evolution of grid-generated turbulence under conditions of stable thermal stratification. *J. Fluid Mech.* **215**, 601-638.

# Direct measurements of the mutual-entrainment velocity at a density interface

By K. Kan\* and N. Tamai\*\*

\*Dept. of Civil Eng., Shibaura Inst. of Tech.; and

\*\*Dept. of Civil Eng., Univ. of Tokyo; Japan

Through experiments for horizontally homogeneous shearing flow, characteristics of mutual entrainments are observed. The velocity fluctuations near the density interface became relatively large. This shows that the mutual entrainment toward the upper- and lower- layer directions were caused simultaneously near the interface by shear instability. With visualization technique it is observed that the mutual interactions between the vortex shear layer and the gravity wave play a dominant role on the interfacial mixing. The characteristics of the mutual entrainments are also analyzed considering the interaction between the dynamic property of vortex shear layer and gravity wave.

## 1 Introduction

The characteristics of mixing phenomena vary from one case to another, depending on what causes them to happen. Turbulence on water surface caused by winds plays a dominant role in the behavior of stratified layers in reservoirs. While at the density interface in a saline wedge, shear force is dominant in the interfacial mixing process. In case of thermal stratification, thermal effect on the interface plays an important role. To establish a model for these interface mixing phenomena and examine them experimentally, it is necessary to have suitable facilities which can simulate turbulence generating that controls the real mixing processes. For the case of a saline wedge which is originated from the instability of the shear layer, an apparatus which can generate the shear flow is necessary, and one that creates both the upper- and lower- layers of the stratified flows has generally been used. However, in past experiments, emphasis has often been on measuring the entraining layer, not the layer being entrained.

In case of a saline wedge, with different combinations for the velocities in the upper- and lower- layers, mixing at the interface is complicated. Hence it is necessary to conduct experiments by bearing on mind the mutual-entrainment phenomenon. In mixing caused by internal waves and the instability of the shear layer, it is normally considered that mixing advances to the upper and the lower layer, leading to mutual entrainment. To understand this phenomenon, it is necessary to measure both the upper- and lower- layers, including the interface in between. A circulating flume in which horizontally homogeneous flows can be realized, without the influences of the flume's two ends, is easy to handle and can improve the measurement precision. There are also secondary flow problems. It has also been pointed out that secondary flows damp the inner side's turbulence intensity, force toward the inner side the intermediate density layer generated by the mutual entrainment, thus reducing the entrainment area. A circulating flume in which secondary flows' influences are minimized has been made to measure directly the mutual-entrainment phenomenon under shear-flow conditions, and to shed more light on the characteristics of the mutual-entrainment phenomenon. By changing the upper and lower layers' velocities, we have directly measured the fluid transport at the interface,

visualized the interface, explained its original causes, and examined the suitability of the mutual-entrainment conception.

## 2 Experiments

In Fig.1 is shown the circulating flume used in the experiments. It is made of acrylic, and is elliptic, being composed of a straight part and a semi-circle part, both of which are 1.5m long. Shear flow is generated by belts installed on the bottom and the surface of the flume's one straight part. On the belts were attached roughness elements. Measurements were conducted on the other side. Since there is no obstacle, homogeneous shear flow is generated in the measuring part of the flume, and good precision can be expected from the bottom to water surface. In order to get rid of secondary flow's influences, vertical sheets were installed in the curved part, and grids in the connecting part between the curved and straight ones, guaranteeing thus a homogeneous shear flow in the straight part. The belt at the bottom is double layered so as to eliminate influences from the motor, and horizontal sheets were installed to minimize the mutual interference between the surface and the bottom belts.

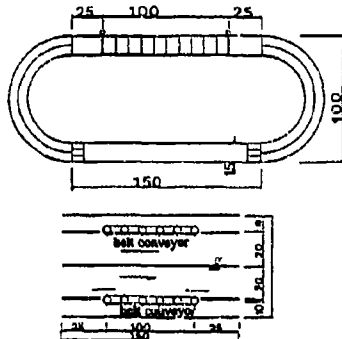


Fig.1 Experimental setup

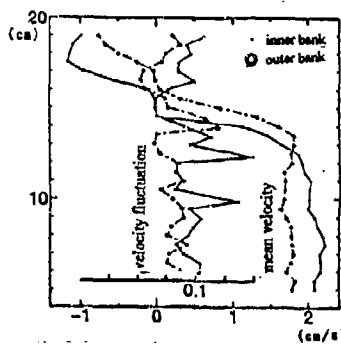


Fig.2 Distributions of the average velocity and velocity fluctuations

In Fig.2 are shown the vertical distributions of the average velocity as well as the fluctuating velocity's RMS. It is seen that a rather homogeneous shear flow exists, though there is also weak turbulence on the inner side. To obtain the relative velocity in the experiments, the upper and lower layers were moved to the opposite directions. Longitudinal and vertical velocity components were measured with a two-component hot-film probe, while density was taken by a hand-made miniature density probe which is 3mm wide and has a 0.1mm electrode.

In order to measure continuously the density variations, density probes were installed every 5mm at 6 points, and displaced in accordance to the interface's displacement, such that the probes can always cover the interface. To measure the density flux at the interface, a two-component hot-film probe and a density probe were placed closely (3mm apart) for the measurements.

## 3 Interface and Its Instability

Using aluminium powder, density interface in case where the upper- and lower- layers move in the opposite directions was visualized. Though in the past researches about interface's stability has been much studied, little is known about the case when instability occurs. While it is possible to determine the unstable wave period, it is not to discuss about whether this will

lead to breaking, which dominates interfacial mixing. Here the large eddy model proposed by Scorer is used in the following discussion.

When the upper- and lower- layers move in the opposite directions, and the velocity difference (thus the shear) is small, the interface is stable, and there is no structural internal wave. The eddy structure at the interface starts to change once the velocity difference becomes larger. At this stage there are no breakers accompanying eddy movement. When the velocity difference becomes still larger, instability appears, together with the eddys' deformation. Vortices gather in the eddys, leading to billow. This is shown in Photo 1, where the bright part corresponds to this engrossment. With this the eddys deform, which leads to gravitational instability, absorbing the upper- and lower- layers' fluids into the eddy's center, and subsequently it dissipates, part of which goes into the upper- or lower- layer, as shown in Photo 2. Corresponding to vortex engrossment, part of the eddy's inclination increases, then the crest is broken away by the upper- and lower- layer, and entrained into their respective mutual-entrainment layers.

In this way, mutual entrainment occurs when both the upper and lower layers move. The time variations of the interface position depend on this mutual entrainment. Vortex engrossment in this eddy layer, as well as the mutual entrainment thereof are considered in the following, using Scorer's method.

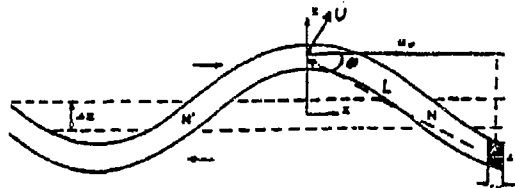


Fig.3 Eddy's vibration



Photo 1 Visualization of the interface  
(vortex engrossment)

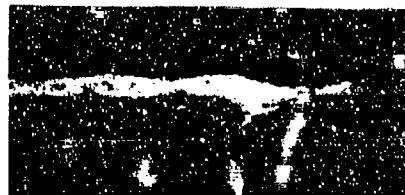


Photo 2 Visualization of the interface  
(eddy layer's deformation)

The vibration of the eddy layer caused by velocity difference is described by gravitational wave (Fig.3)  $\xi = A \cos kx$ . Due to this vibration, vortices are distributed along the wave, and new flow appears inside the eddy layer. The velocity,  $u_0$ , at the crest, and due to the circulation  $\eta \delta x \delta z$  inside the volume  $\delta x \delta z$ , with a distance of  $x$  from the crest, can be deduced as in the following. Let the distance between the crest and the circulation be  $L$ , and the vertical velocity component which is perpendicular to  $L$  as  $u$ , one from the conservation of circulation has:

$$u 2\pi L = \eta \delta x \delta z \quad (1)$$

Let the angle in Fig.3 be  $\theta$ , the horizontal component is  $u'_0 = u \sin \theta$ . When  $\theta$  is small enough,  $L=x$ ,  $\sin \theta = A (1 - \cos kx)/x$ , and:

$$u_0 = \frac{\eta \delta x \delta z A (1 - \cos kx)}{2\pi x} \quad (2)$$

Integrating the above equation, we obtain the new velocity at the crest as:

$$u_0 = \int_{-\infty}^{\infty} \frac{\eta \delta x \delta z A (1 - \cos kx)}{2\pi x} dx = \frac{1}{2} \eta A k \delta z \quad (3)$$

by which the vortices are transported and amassed at N in Fig.3. Assume that horizontal velocity variation is given by  $u_0 \cos kx$ , the increase is  $-\eta \delta z du/dx$ . Further, vortices generated by gravitational force due to eddy's deformation are given by  $\beta g \delta z d\xi/dx$ , which restricts eddy's deformation. The total of this effect and that from the vortex engrossment is given as  $\sin kx$ . When this is positive, vortices increase at N in Fig.3, while decreases at N', and becomes unstable as shown in Fig.5. Thus the condition for instability is :

$$k > k_c = 2g\beta/\eta^2 \delta z \quad (4)$$

where  $\beta$ ,  $\eta$  are defined in  $\Delta U = \eta \delta z$ ,  $\Delta \rho = \beta \rho \delta z$ . If Richardson number  $R_i = g\beta/\eta^2$ , the relation between Richardson number and the ratio of the unstable eddy layer's thickness  $\delta z$  to wave length  $L$  (about the wave's inclination) is:

$$\pi \delta z / L > R_i \quad (5)$$

The results from visualization are shown in Fig.4, where  $\bullet$  stands for the case when vortices gather and dissipate (Photo 1), and  $\circ$  represents the stable case when the wave is long. In the present experiments,  $R_i$  varies around 0.75, which separates the stable zone from the unstable zone, and Eq.5 is thought to give the approximate critic value.

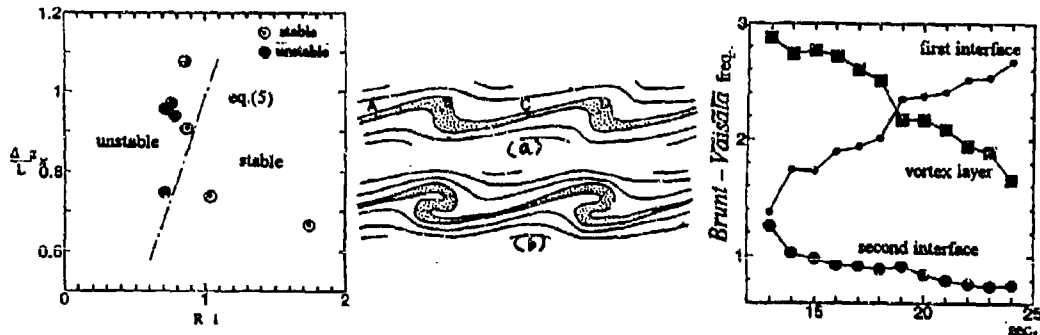


Fig.4 Eddy layer's stability Fig.5 Eddy layer's deformation Fig.6 Brunt-Vaisala frequency

Due to eddy deformation, vortices gather to B, D in Fig.5(a), lead to gravitational instability as in Fig.5(b), and create mixing. In this way the processes from eddy layer's increasing instability to break waves may be modelled. And it can be considered that mixing is generated

simultaneously in both the upper- and lower- layer. The velocity with which mixing enters into the two layers is called mutual-entrainment velocity. Figure 6 shows Brunt-Vaisala frequency's variation, with which mixing expands when the lower layer's speed is relatively large. The results calculated by using the density gradient at the interface with the upper layer (interface I), with the lower layer (interface II), and the average density gradient in the eddy layer, are drawn with symbols  $\circ$ ,  $\bullet$ , and  $\blacksquare$ , respectively. Horizontal coordinate stands for time, and vertical coordinate for Brunt-Vaisala frequency. Interfaces I and II's variations also show the density distributions' variations due to mixing along the interfaces, and demonstrate that mixing occurs at the interfaces. Also, Brunt-Vaisala frequency's decrease in the eddy layer shows the mixing in it, and that the eddy layer serves as a medium through which mixing occurs in the upper- and lower- direction.

#### 4 Velocity Variations

In the above, we have introduced the concept mutual entrainment to the shear layer instability in case where both the upper and lower layers are in movement. Here we determine the interface's shape by using statistic values from the velocity variations. The average velocity and the RMS of the velocity fluctuations are given in Fig.7, which shows that the velocity fluctuation is strong along the interface. The RMS of the vertical velocity component is shown in Fig.8, and Reynolds stress distribution in Fig.9. The maximum Reynolds stress and the maximum velocity fluctuation appear at the same position, in which part exists strong shear stress. It is predicted that at these positions the instability due to shear stress becomes larger.

In Fig.10 is shown the velocity fluctuation spectral at 5mm below the interface. Figure 10(a) shows the case of higher stability, where the peak appears at low wave number of 0.2-0.4. This is considered as the gravitational wave which corresponds more or less to the Brunt-Vaisala frequency of the middle layer in Fig.6. Fig.10(b) is for the case with relative unstable interface.

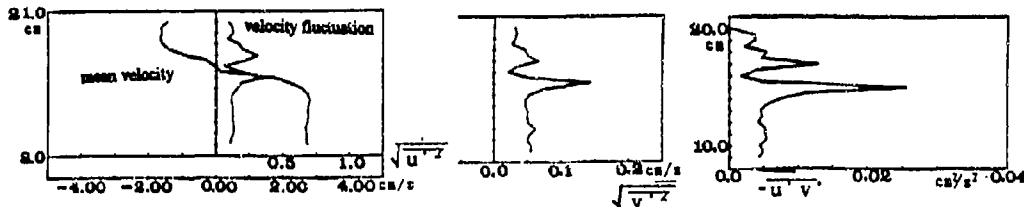


Fig.7 Longitudinal velocity and its fluctuation

Fig.8 Vertical velocity's fluctuation

Fig.9 Reynolds stress distribution

With increasing instability due to vortex engrossment, peak appears at a wave number of 0.8-1.0, which corresponds to billow-type vibration. Thus, in case of higher stability gravitational wave dominates; in case of lower stability eddy layer's deformation leads to instability, and billow's wave number dominates. However, both exist. Subsequently, mixing becomes stronger, billow gets smaller and broken, leading to breakers of higher wave number.

#### 5 Density Variations and Density Contours

In order to measure density variations in mixing, density probes were used at every 5mm, including the interface. And the time series were taken. The spectral of the density variations at the interface is given in Fig.11. Similar to what is shown in Fig.10, peak appears at billow's wave number. Because of the mixing by breakers, there exists the part with a frequency of 1-2Hz.

Contours are drawn (Image 1, 2) for the time series obtained by 6 density probes which measured across the interface. Vertical coordinate shows the probes' positions, horizontal coordinate is time. At a fixed point, one can observe the phenomenon through the density variations.

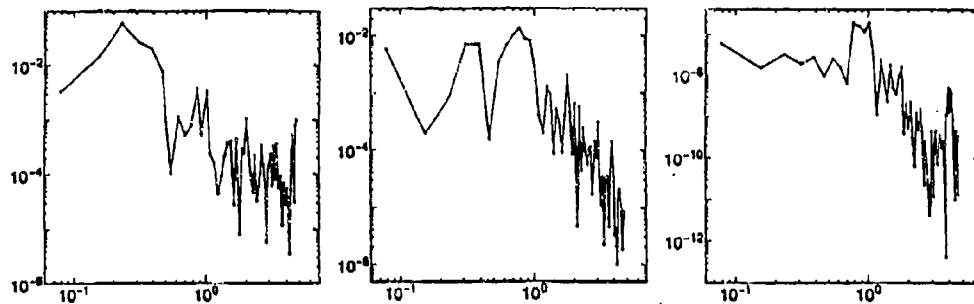


Fig.10(a) Fluctuation velocity's  
spectral

(b) Fluctuation velocity's  
spectral

(c) Density-vari: tion  
spectral



Image 1 Density contours in the  
lower layer

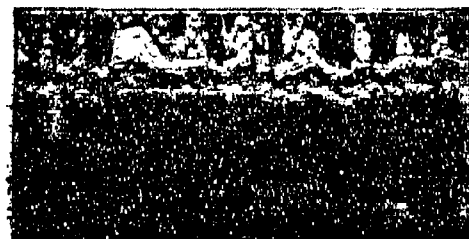


Image 2 Density contours in the  
upper layer

Fig. 11

In Image 1 are drawn the contours below the interface. The band shows the interface, below which is eddy shaped and of which the density is higher, with the surrounding density being lower. This shows that the mutual entrainment moves the fluid in the middle or the upper layer to the lower layer. Image 2 gives the contours for the upper layer, and shows that the upper part is of high density, while high density fluids from the middle- and lower- layers are transported into the upper layer. However, direct, large scale transport from the lower to the upper layer was not observed. It is through the middle layer that the upper and lower layer generate mutual entrainment. In this mutual-entrainment processes, eddy layer's vortex deformation plays the dominant role.

## 6 Density-flux Measurement and Mixing inside the Large Eddy

Since the large eddys play an important role in the mutual entrainment to the shear layer, it is necessary to examine the mixing process by directly measuring the density flux. Though velocity and density measurements were not taken at the same points (being 3mm apart), the results are considered as from the same points, since visualization shows that the eddy scale is larger than 3mm. Density flux in the vertical direction is shown in Fig.12, through the presentation of the vertical velocity component  $v'$  and density fluctuation  $\rho'$  in quadrants. Vertical coordinate shows the vertical velocity component (upward is positive), horizontal one stands for density fluctuation. Fig 12(a), (b) and (c) show the density fluxes below the shear layer, in the middle of the shear layer, and above the shear layer, respectively. At the borders of the shear layer, density flux can also be observed outside the I, II quadrants, showing complex mixing. At the center of the shear layer, due to density effect and zero velocity, density fluctuation is large though velocity fluctuation is limited. This shows active mixing of the upper- and lower- layers.

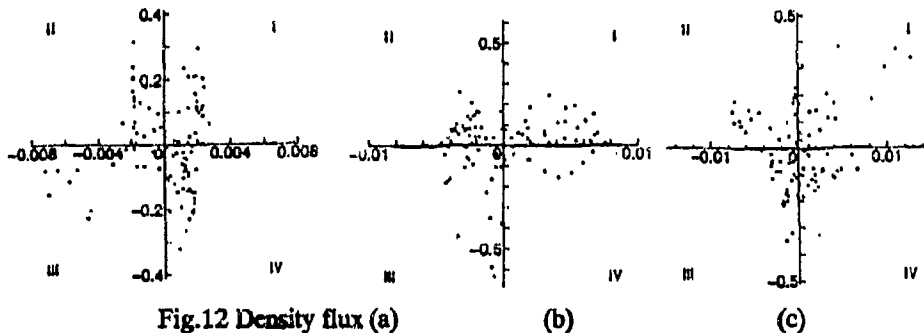


Fig.12 Density flux (a)

(b)

(c)

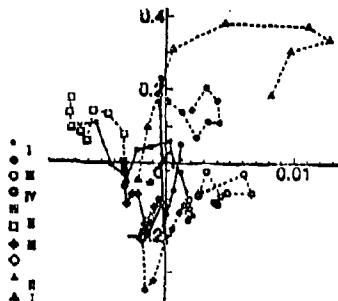


Fig.13 Density flux's variations

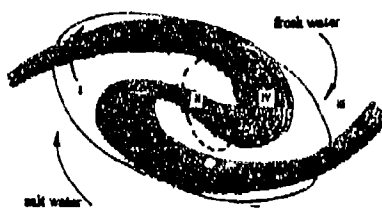


Fig.14 Mixing inside the large eddy

Further, to examine the mixing process by tracing the density flux, the time series (one sample per second) of the density flux in the large eddy are presented in Fig.13. Corresponding to image processing, transport inside the eddy is sketched in Fig.14, in the order of I  $\rightarrow$  III  $\rightarrow$  IV  $\rightarrow$  II  $\rightarrow$  III  $\rightarrow$  II  $\rightarrow$  I quadrant. And in Fig.15 are given Reynolds stress's time series (twice per second). Since Reynolds stress is calculated when it appears in each quadrant, Reynolds stress is zero if the number of appearance is zero. Horizontal coordinate shows time, and vertical one stands for dimensionless Reynolds stress  $-u'v' / \sqrt{u'^2 v'^2}$ . The order in which Reynolds stress appears in the quadrants is III  $\rightarrow$  IV  $\rightarrow$  I  $\rightarrow$  IV  $\rightarrow$  III  $\rightarrow$  II, from which eddy's rotating direction is shown in Fig.16. Figure 14, which was obtained by tracing density flux, agrees rather well with Fig.16 that was obtained by tracing Reynolds number. As shown by the arrow in Fig.14, it is possible to model the mixing inside the eddy. Similar to Image 1, the

large eddy in Fig.14 is sketched in Fig.17, in which the heavily drawn part stands for lower density, while less heavily drawn is for higher density. It agrees quite well with Image 1.

The mixing phenomenon inside the large eddy, as well as the fact that the shear layer draws its surrounding fluids to this large eddy, have been clarified. Due to the mixing fluids' intermittent release, the fluid in the upper (lower) layer is transported to the lower (upper) layer through the shear layer. The resulting density flux is dispersed to the whole layer by the mutual-entrainment layer's turbulence, and the mutual-entrainment process is completed.

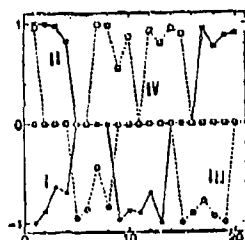


Fig.15 Time variations of the Reynolds stress

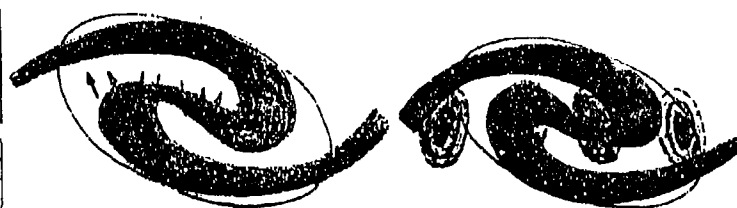


Fig.16 Reynolds stress distribution

Fig.17 Eddy seen through density contours

## 7 Conclusions

Interface phenomenon in shear flows as well as the mutual-entrainment processes have been investigated using a circulating flume. The following conclusions may be drawn:

- 1) Vertical sieves were installed in the flume's curved part. This avoids the effects by secondary flows, and generates quasi homogeneous shear flow in the flume's straight part.
- 2) By considering vortex engrossment due to eddy's deformation, it is possible to explain the interface's deformation and the transition to instability. This agrees well with the stability of billow-type interfacial wave obtained by visualization.
- 3) At the interface co-exist gravitational wave as well as billow whose wave number is slightly smaller. Together they dominate the interfacial mixing.
- 4) Density flux at the interface was measured, and it is found that transports to the upper- and lower- layers occur simultaneously. This can also be understood from 2). However, structural mixing that jumps across the middle layer was not observed.
- 5) The eddy layer's instability plays an important role.

## Acknowledgement

We thank fourth-year students at Shibaura Institute of Technology, Kitagishi and Koto, for their helps in the experiments and data processing.

## References

- 1) Scranton, D.R. and W.R. Lindberg (1983): *Phys. in Fluids*, **26**(5), pp.1198-1205.
- 2) Nishida, S. and S. Yoshida (1983): *Proc. Hydr. Eng., JSCE*, vol.27, pp.549-553.
- 3) Yoshida, S. (1978): *Report of JSCE*, No.273.
- 4) Scorer, R.S. (1978): *Environmental Aerodynamics*, Ellis Horwood Ltd., Ch.6.
- 5) Kan, K. and N. Tamai (1983): *Proc. Hydr. Eng., JSCE*, vol.27, pp.543-548.

## THE IMPORTANCE OF INTERNAL WAVES FOR MIXING IN A STRATIFIED TIDAL FLOW

Rob UITTENBOGAARD (+) Jörg IMBERGER (\*)

(+) DELFT HYDRAULICS, P.O. Box 2600 MH Delft, The Netherlands.  
(\*) Centre for Water Research, Nedlands, Western Australia 6009.

### Abstract

Analysis of turbulence as well as internal wave observations in a tidal stratified flow supports the following statement. Subgrid internal gravity waves in computations of stably stratified, free surface flows are a significant source of turbulence production unknown in applied turbulence models.

### 1. Introduction and goal

Usually, in feasible three dimensional computation of mass transport of shallow coastal seas and estuaries, the horizontal mesh size  $\Delta x$  exceeds the water depth. Thus, irrespective of the number of computational layers, we actually average small scale vertical mixing phenomena over layer areas of several horizontal grid boxes and timesteps. Hence, in view of the relevant scale ratios, the implied subgrid surface-averaging and time-averaging in large-scale free-surface simulations approximates ensemble-averaging of 3D turbulence. Consequently, we may apply "standard" 3D-turbulence models as subgrid models in the computation of large-scale free-surface flows. However, the large anisotropy of the 3D-computational mesh as well as of the stratified flow proper leaves, in terms of subgrid models, a spectral gap between stratified 3D-turbulence and the resolved horizontal circulation. We expect that internal gravity waves occupy this part of the subgrid spectrum. In addition, we infer that these internal waves play a role in momentum transfer as well as energy transfer to 3D-turbulence.

The present paper explores the necessity of the proposal (Uittenbogaard and Baron, 1989) through analysis of our field observations in the Rotterdam harbour. In the context of this paper we define the **macrostructure** as the computationally resolvable part of a stratified tidal flow in nature, say beyond horizontal length scales of 100 [m]. Further, we define the **microstructure** as the subgrid range of length and time scales of nearly isotropic stratified 3D turbulence below the Ozmidov length scale. As an example we take the  $k\cdot\varepsilon$  turbulence model to represent vertical mixing by 3D-turbulence. Finally, the **mesostructure** contains the subgrid flow at scales occupied by anisotropic turbulence and, at larger subgrid scales, internal gravity waves.

### 2. The site

We will only discuss our observations in the Rotterdam Waterway. This is a tidally forced, mainly salinity stratified channel connected to the North Sea. Several kilometres in upstream as well as downstream direction of our site the sand/silt bed at 22 m depth is straight, horizontal and smooth. Not this section of the channel nor its groins did notably create lee waves. However, through 100 kHz echo sounding, we occasionally monitored long, ship-generated internal waves in the macrostructure range. Then we stopped our mesostructure internal wave observations. During the six hours of our measurements the flood increased from practically zero velocity at the bed to maximal 1.8 [m/s] six hours later (Fig.1). The current maintained a stable density stratification of 15  $\text{kg/m}^3$  between the fresh water top layer going seaward and the landward flow of seawater in the bed layer. The density differences were mainly due to differences in salinity content and occurred over an interval of 3-5 [m] around a depth of 10 [m].

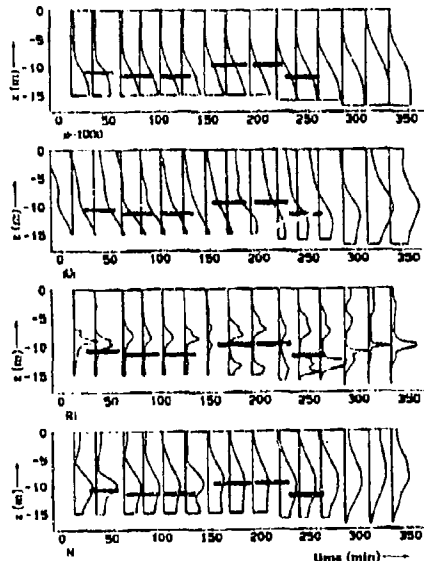


Fig.1. Vertical macrostructure  
Rotterdam Waterway

#### 4. Instrumentation

We simultaneously deployed the following three groups of instruments, each designated to record at various ranges of vertical ( $\lambda_v$ ) or horizontal ( $\lambda_h$ ) wavelengths the microstructure, the mesostructure and the macrostructure. We observed the microstructure at  $2 < \lambda_v < 500$  [mm] with CWR's free falling fine-scale CTD probe sampling at 1 [mm] vertical intervals (see also Fig. 4a). This probe was deployed from a freely drifting ship.

Secondly, on fixed levels and in 30 minute series the mesostructure ( $0.1 < \lambda_h < 100$  [m]), was sampled at 20 Hz using a platform (3 vel. comp.+cond.+temp.) suspended from an anchored vessel. Correspondingly, we define time-averages, say  $u$  of signal  $u$ , as 30 minutes averages i.e. 1/25 of the  $M_2$  tidal cycle. Incidentally, the 3D-velocity vector was measured with two 2-component electromagnetic current meters of 40 [mm] diameter tested in a towing tank and checked against LDA. In addition, the platform motions were recorded and the perturbed flow signals were corrected by transfer functions calibrated on-line. In this manner the final flow signals have become linearly independent of the recorded platform motions. This method has been checked separately and works very satisfactory.

Thirdly, to observe the macrostructure, we deployed the Elmar, which is a torpedo-shaped container suspended from an anchored vessel and equipped with a CTD probe, electronic compass and Ott mill (velocity magnitude). The macrostructure was observed by 2 minute averages per level on fixed levels 0.5 or 1 [m] apart. In this manner one macrostructural observation of the vertical profile took about 25-30 minutes and yields as vertical resolution of 2 [m], see also Fig. 4b. We took 15 macrostructure profiles, 6 mesostructure measurements of 30 minutes each near 10 [m] depth and 44 drops for the microstructure. In the following we present and discuss our findings.

#### 5. Macrostructure

Given the orthogonal horizontal velocity components  $u$  and  $v$  and vertical coordinate  $z$ , positive against gravity, we define the gradient Richardson number  $Ri$ , the buoyancy frequency  $N$  and mean shear rate  $S$  as follows:

$$Ri = \left(\frac{N}{S}\right)^2 ; N^2 = -\frac{g}{p} \frac{\partial p}{\partial z} ; S^2 = \left(\frac{\partial u}{\partial z}\right)^2 + \left(\frac{\partial v}{\partial z}\right)^2 . \quad (5.1)$$

These macrostructural parameters are computed and smoothed using 3rd order Ausgleich splines (Fig. 4b). Fig. 1 shows qualitatively the evolution of the vertical macrostructure where  $Ri$  is truncated to maximal 10. During the first 150 min. the fresh water top layer above 5 [m] depth is nearly unstratified. Along the depth-time platform path of the mesostructural observations we derived  $N=0.12-0.18$  [rad/s] while  $Ri=0.5-2.2$ . In particular  $Ri$  is very sensitive to smoothing. The velocity magnitude varies between 0.5-1.5 m/s at  $S=0.1$  [1/s] without a notable veering of the horizontal velocity vector. Hence, we study a flow at moderate stratification and with the only nonzero shear rate in a streamwise vertical plane.

#### 6. Microstructure.

Below we define state parameters of the microstructure which are closely related to the measuring technique and data processing described by (Imberger and Boashash, 1986) and (Ivey and Imberger, 1991). Near a fixed horizontal position  $(x, y)$  the vertical microstructure along a stationary interval  $\Delta z$  at time  $t$  are observed and subsequently defined at the interval centre  $z$ . In essence are used: (1) the local buoyancy frequency  $N_g(z, t)$  (2) the centred displacement scale  $L_C(z, t)$  and

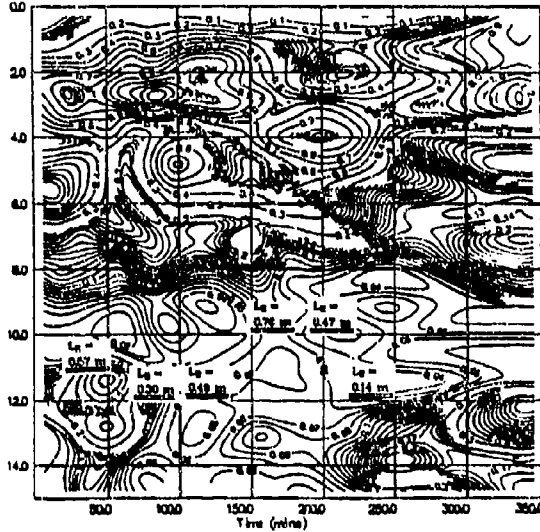


Fig. 2. Centred displacement scale  $L_C$  [m].

(3) the turbulence dissipation rate  $\epsilon_0(z, t)$ .

The local buoyancy frequency follows from re-ordering the observed density profile into a monotonous one while  $L_C$  equals twice the vertical displacement between the observed and re-ordered density profile and averaged over  $[z \Delta z(z)]$ . In absence of overturning events  $L_C = 0$  and thus  $L_C$  is a practically unbiased signature of a turbulence mixing length. Moreover, Itzeaere (1984) showed the good accordance between  $L_C$  and twice the rms Thorpe scale for grid-generated stratified turbulence. Finally, the energy dissipation rate follows from fitting Batchelor's spectrum to spectra derived from the observed temperature gradient fluctuations along  $[z \Delta z(z)]$ . Actually, from the independent parameters  $N$  and  $\epsilon_0$  follow the local Kolmogorov length scale  $L_R$ , the local Ozmidov length scale  $L_K$ . These three length scales

define the turbulent Reynolds number  $Re_T$ , the local activity parameter  $Fr_T$  and shear Froude number  $Fr_y$ :

$$L_R = \left(\frac{\epsilon_0}{N^3}\right)^{1/4}; L_K = \left(\frac{v^3}{\epsilon_0}\right)^{1/4}; Re_T = \left(\frac{L_C}{L_K}\right)^{4/3}; Fr_T = \left(\frac{L_R}{L_K}\right)^{2/3}; Fr_y = \left(\frac{L_R}{L_K}\right)^{2/3} \quad (6.1)$$

The CTD drops were deployed from a vessel drifting along the anchored vessel for the remaining observations. To match the low resolution of the macrostructure the fine-scale parameters (6.1), have been smoothed vertically as well as in time. For the purpose of this paper we can only show some results. Fig. 2, with the same reference time as Fig. 1 and with the dotted line of platform, shows that in the region of significant buoyancy,  $L_C$  hardly exceeds 100 [mm]. There also holds  $Fr_T \approx 1$  which implies that  $L_C$  nearly equals Ozmidov length scale. In the nearly unstratified top layer above 5 [m] for the first 150 min.  $L_C$  yields 500-1000 [mm]. In addition, Fig. 3 shows in the stratified region below 5 [m] that  $\epsilon = 1-10$  [ $\text{mm}^2/\text{s}^3$ ] irrespective of the variations in the underlying velocity and density profiles. This is a relatively high energy dissipation rate, actually belonging to an unstratified channel flow! However, the small mixing length reduces the vertical eddy diffusivity in the stratified region to only 10-50 [ $\text{mm}^2/\text{s}$ ]. Further, we estimated  $Re_T > 100$  and  $Fr_y > 20$  in the stratified region. This implies the application of large-Reynolds-number turbulence models without direct effect of buoyancy on the energy dissipation range and thus on the evolution equation for  $\epsilon$ .

#### 7. Diagnosis with k- $\epsilon$ turbulence model

Instead of a 3D-computation we use the observed macrostructure shear rate  $S(z)$  and buoyancy frequency  $N(z)$  as input to the k- $\epsilon$  turbulence model. Here we compare the model's results with the observed microstructure. We will neglect the weak horizontal gradients as well as advection and assume a quasi-steady state of turbulence. Then we apply the following 1DV version of the k- $\epsilon$  turbulence model where instead of  $k$  we use  $q^2$  for turbulent kinetic energy:

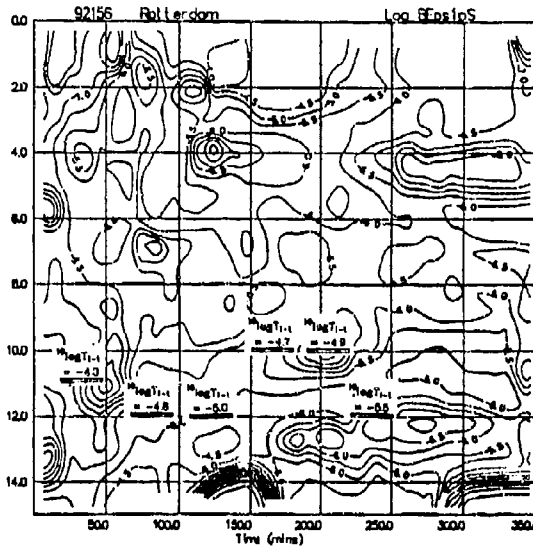


Fig. 3. Energy dissipation rate  $\epsilon$  [ $\text{m}^2/\text{s}^3$ ].  
(isoclines of  $10 \log \epsilon$  are shown)

$$\frac{\partial q^2}{\partial t} = \frac{\partial}{\partial z} \left\{ \frac{v_T}{\sigma_k} \frac{\partial q^2}{\partial z} \right\} + v_T \cdot \left\{ S^2 - \frac{N^2}{\sigma_p} \right\} - \epsilon + T ; \quad v_T = c_\mu \cdot \frac{q^4}{\epsilon} \quad (7.1)$$

$$\frac{\partial \epsilon}{\partial t} = \frac{\partial}{\partial z} \left\{ \frac{v_T}{\sigma_\epsilon} \frac{\partial \epsilon}{\partial z} \right\} + c_{1\epsilon} v_T \cdot \left\{ \frac{\epsilon}{q^2} \right\} \cdot \left\{ S^2 - c_{3\epsilon} \frac{N^2}{\sigma_\epsilon} \right\} - c_{2\epsilon} \frac{\epsilon^2}{q^2} , \quad (7.2)$$

$$c_\mu = 0.09 ; \sigma_q = 1.0 ; \sigma_p = 0.7 ; \sigma_\epsilon = 1.3 ; c_{1\epsilon} = 1.44 ; c_{3\epsilon} = 0.0 ; c_{2\epsilon} = 1.92.$$

Here is  $v_T$  the eddy viscosity and  $\sigma_\epsilon$  the turbulent Schmidt to estimate the eddy diffusivity  $\sigma_\epsilon/v_T$ . In (7.2) we have assumed  $c_{3\epsilon} = 0$  because  $Fr_y > 20$ . For each vertical macrostructural profile

we solved (7.1) and (7.2) until steady state.

In the stratified region the results yield a practical laminar response: a mixing length less than 1 [mm] and  $c = 0.01$   $\text{mm}^2/\text{s}^3$ . This is a consequence of the value of  $v_T$  which sets a critical  $Ri$ -value for laminar response. Similar laminar results were obtained when  $\sigma_\epsilon$  was increased to 1.3. Instead, we could apply empirical damping functions for  $\sigma_\epsilon = \sigma_\epsilon(Ri)$ , however, we

prefer to add more hydrodynamic knowledge to the turbulence model. Actually, in the next section we will pursue the suggestions made by G.I. Taylor (1931) on internal wave modes. These modes are not obvious from Fig. 4 and require a different set-up of instruments and a different analysis.

We aim at the following improvement of (7.1). In (7.1) we have added an unspecified transfer term  $T$  which is the sum of the energy transfer from internal waves to turbulence and vice versa, see (Uittenbogaard and Baron, 1989). In section 9 we motivate the additional turbulence source  $T(i-t)$  which should improve estimates with (7.1) and (7.2).

#### 8. Mesoscale with random internal waves

We have included in Fig. 1 the Ellison scale:  $L_E = 2 \cdot |\rho'| \left( \frac{\partial \rho}{\partial z} \right)^{-1}$  (8.1)

derived from the rms value  $|\rho'|$  of density fluctuations observed on the platform. Here  $\rho'$  is defined as the deviation of density  $\rho$  from its least square fit of sections each lasting 7 min. and taken from one 30 min. series. With 50% overlap these 7 min. sections, each containing 8,092 samples, also served as input to spectral analysis. Fig. 1 shows that the Ellison scale (8.1) is 0(5) times larger than the centred displacement scale along the depth-time path of the platform. This indicates large non-overturning particle motions which exceed the 3D-turbulence excursions and is supported by echosoundings (Fig. 5).

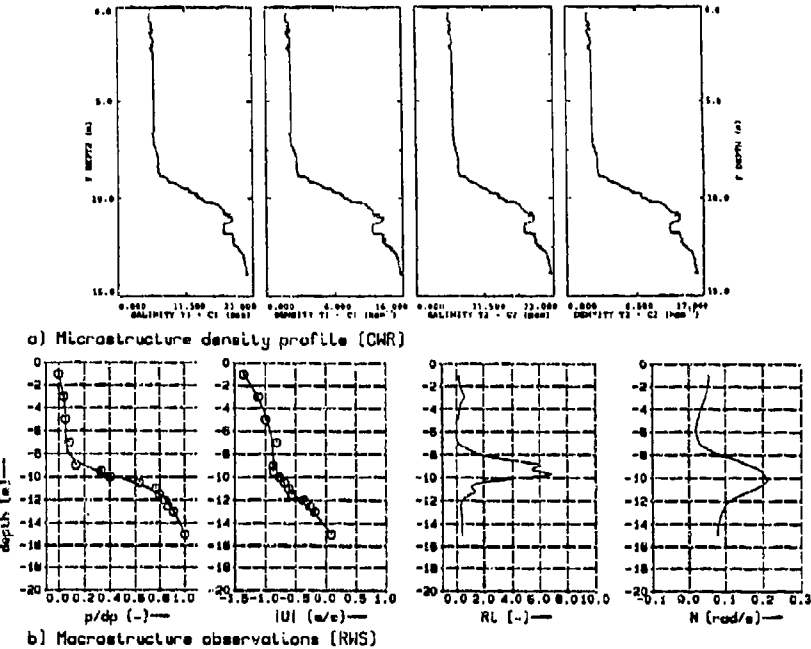


Fig. 4. Vertical microstructure (a) underlying macrostructure (b).

The non-overturning density perturbations are not observable with the methods underlying Fig. 4a+b but require a platform suspended from an anchored vessel. Incidentally, in Fig. 5 we attempted to follow the wave patterns with a pencil and we found they consist of only a few periods, which indicates to short wave groups with different properties.

We want to detect whether the mesostructure in the stratified flow can be considered as linear, random internal gravity waves. In addition, we would like to quantify their energy content and other properties or limitations.

For that purpose we considered the following. Similar to the formulation of the Taylor Goldstein equation we assume that the large wavelength part of the mesostructure field satisfies the following linearized equations for a stratified shear flow:

$$\vec{v} \cdot \vec{u}' = 0 ; \frac{\partial p'}{\partial t} + w' \frac{\partial p}{\partial z} = 0 ; \frac{\partial u'}{\partial t} + w' \frac{\partial u}{\partial z} + \frac{1}{\rho} \vec{v} \cdot \vec{p}' - \frac{\rho'}{\rho} g = 0 ; \frac{\partial}{\partial t} = \left( \frac{\partial}{\partial t} + \bar{u}(z) \cdot \frac{\partial}{\partial x} \right) \quad (8.2)$$

We decompose solutions to (8.2) into elementary harmonics or modes which depend on the vertical Cartesian coordinate  $z$ , the horizontal streamwise wavenumber  $k$  in  $x$ -direction where  $\bar{u}(z)$  is the streamwise velocity ( $v_m=0$ ) and the transverse wavenumber  $\ell$  in  $y$ -direction. In (8.2) we substitute for the vertical velocity of a single mode  $(k, \ell)$ :

$$w(x, t; k, \ell) = F(z) \exp\{i[k(x - \bar{u}t) + \ell y + \phi(z) - \Omega t]\}, \quad (8.3)$$

with intrinsic angular frequency  $\Omega$ , growth rate  $\delta$  and unknown amplitude  $F(z)$ . Using WKB expansion the vertical wavenumber  $m(z) = \pm \text{Re}(d\phi/dz)$  follows from the phase function  $\phi(z)$ ; the horizontal wavenumber magnitude reads  $k_h^2 = (k^2 + \ell^2)$  and the total wavenumber magnitude  $|k|^2 = (k^2 + \ell^2 + m^2)$ . Consequently, the intrinsic frequency yields:

$$\Omega = [N \cos \theta(k, \ell)] \{ \delta + (1 + \delta^2)^{1/2} \} ; \delta = \frac{k}{k_h |k| N} \cdot \frac{d^2 u}{dz^2} ; \cos \theta(k, \ell) = \frac{k_h}{|k|}. \quad (8.4)$$

Here the basis of the wavenumber vector  $k$  coincides with the spatial Cartesian system and  $\theta$  is the angle between  $k$  and the horizontal plane  $m=0$ . However, in the spirit of the WKB-approximation  $\delta$  must be negligible small because the vertical wavelength  $(2\pi/m)$ , hidden in the magnitude  $|k|$  is assumed to be much smaller than the vertical length scale over which  $\bar{u}(z)$  varies. However, in a shear flow with significant shear rate, but with negligible velocity curvature, the well-known dispersion relation  $\Omega = N \cos \theta$  for internal waves in uniform flow still holds. The vertical fluid particle excursions possess modes belonging to  $(k, \ell)$  with real-valued amplitude  $Z(k, \ell)$ . In comparison with internal waves on a uniform flow now the streamwise variance is augmented with  $\frac{1}{2} \langle Z^2 \rangle (d\bar{u}/dz)^2$  so that the kinetic energy of each internal wave mode reads:

$$\frac{1}{2} \langle \bar{u} \cdot \bar{u} \rangle = \frac{1}{2} \langle Z^2(k, \ell) \rangle \cdot N^2 \{ 1 + \text{Ri}^{-1} \} \quad (8.5)$$

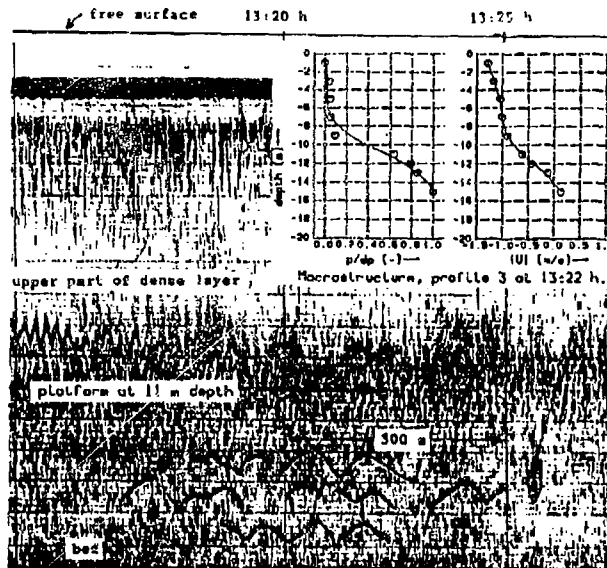


Fig. 5. Echosounding indicating internal waves.  
(some lines are enhanced with a pencil)

Here, the brackets  $\langle \dots \rangle$  mean averaging per wavenumber vector  $\mathbf{k}$  so that we expressed (8.5) into spectral energy densities. Fortunately, (8.5) does not explicitly depends on  $\mathbf{k}$ . Hence, given the spectral energy density of  $Z'$  we integrate (8.6) directly over the relevant bandwidth. We apply two estimators for the variance of  $Z'$  and we argue that they serve as upper and lower bounds. We define the upper bound estimator simply by assuming all density variations are induced by linear internal waves so that:  $\langle p' \rangle = \langle Z' \rangle \cdot |\frac{\partial p}{\partial z}|$ . (8.6)

Hence, from the vertical macrostructure and the density variations recorded by the platform's instruments follow the spectrum of  $Z'$  and through (8.5) the spectrum of IWE (Internal Wave Energy). Actually, (8.6) serves as upper-bound estimator because we consider all density variations as wave-induced.

Next we define a lower-bound estimator using the assumption that stationary internal waves have a  $+/ - 90^\circ$  phase difference between density and vertical velocity. Actually, if we regard the quadratures  $\text{Im}(\langle p u_i^{\text{cc}} \rangle)$  with  $(\dots)^{\text{cc}}$  complex conjugates and  $i=(1,2,3)$  as orthogonal components of a vector then, for  $\delta=0$  in (8.6), the magnitude of this vector reads

$$\{\text{Im}(\langle p u_1^{\text{cc}} \rangle) \cdot \text{Im}(\langle p u_1^{\text{cc}} \rangle)\}^{\frac{1}{2}} = N \langle Z' \rangle \cdot \{1 + \mu^2\}^{\frac{1}{2}} \cdot \frac{\partial \bar{Z}}{\partial z}; \mu = \{4\Omega |\mathbf{k}| \cdot \langle Z' \rangle^2\}^{-1} \frac{\bar{D}}{Dt} \left[ \frac{d \langle Z^2 \rangle}{dz} \right] \quad (8.7)$$

Parameter  $\mu$  vanishes, either because the variance is independent of  $z$  or, more likely in practice, its mean material derivative is negligible. Hence, for  $\mu=0$  we can estimate the variance of  $Z'$  from the quad spectra between  $p'$  and  $u'$ . However, if in two separate observations wave groups pass with opposite phase shifts then their contribution to the mean quad spectra is partly cancelled. For that reason we take the mean of absolute quad spectra, which we define as  $\langle |\text{Im} p u_i^{\text{cc}}| \rangle$ , at the expense of adding noise as well as some turbulence contributions to this estimator. Finally, the coincidence spectra of shear stress  $-\langle u' w' \rangle$  and of buoyancy flux  $\langle p' w' \rangle$  induced by waves satisfying (8.2) yield:

$$\text{Re} \langle u w^{\text{cc}} \rangle = - \frac{1}{2} \frac{\bar{D} \langle Z^2 \rangle}{Dt} \cdot \frac{d \bar{u}}{dz} - \frac{k \cdot m}{k^2 + \omega^2} \cdot \{ \Omega^2 + \beta^2 \} \cdot \langle Z' \rangle; \text{Re} \langle p w^{\text{cc}} \rangle = - \frac{1}{2} \frac{\bar{D} \langle Z^2 \rangle}{Dt} \cdot \frac{d \bar{p}}{dz} \quad (8.8)$$

From the 30 min. time series of the platform instruments we derived all raw energy densities, coherence, phase etc.. However, Fig. 5 reveals the random nature of the wave group with only a few coherent cycles. Therefore we applied, to the raw averaged complex-valued Fourier spectra, a convolution filter with a width increasing proportionally with frequency. The factor of proportionality is chosen such that the equivalent box-car function, moving over the time record, contains four wave periods for the frequency/wavelength of interest. In this manner we did not de-correlated our data. Finally, the spectra are truncated beyond frequency  $(\bar{u}/L_R)$  because of instrument limitations as well as the definition of the mesostructure range. Fig. 6 is a typical, and not the best, example of our mesostructure observations in the Rotterdam Waterway. This particular observations started a few minutes after the echosoundings of Fig. 5. In Fig. 6 the hump at a (apparent) wavelength of about 3 m is likely surface wave-induced energy at that frequency. For  $\lambda > 5$  [m] we observe in this particular case a fair coherence as well as a  $-90^\circ$  phase shift. This phase shift means waves travelling in the direction of the main flow or opposite to the flow with a phase speed exceeding the flow velocity. However, in other series we observed a phase shift between  $p'$  and  $w'$  that with decreasing wavelengths jumped from  $-90^\circ$  to  $+90^\circ$ , the latter belongs to internal waves travelling opposite the flow at phase speed smaller than the flow velocity. In Fig. 6 we compare the energy spectra for total kinetic energy (Total KE) with those for upper bound (IWE- $p'$ ) derived from  $p'$  in (8.6) and lower bound (IWE- $p' u'$ ) derived from (8.7). Here both kinetic IWE estimates practically coincide and yield  $60\% \pm 5\%$  of the total kinetic energy. We have converted frequency into streamwise wavelength  $\lambda$  using the observed macrostructure velocity while assuming a frozen wave field. The validity of this assumption is disputable for  $\lambda$  exceeding  $O(30)$  [m] if  $\Omega = N$ , however, this implies  $\theta = 0^\circ$  which is geometrically impossible in water with 22 [m] depth.

In Fig. 6 we have plotted  $\pi_{uw}^{\text{ow}}$  and  $\pi_{uw}^{\text{nw}}$  which are the co-spectra (8.7) normalized by the square roots of the energy spectra of  $u', w'$  and  $p'$ .

For Fig. 6, at  $Ri=0.43$ , the mean shear rate dominates in (8.8) the shear spectrum of  $(u'w')$ . Indeed, Fig. 6 shows opposite changes in sign between  $\pi_{uw}$  and  $\pi_{ww}$ . Firstly, this behaviour indicates that linear theory (8.8) may be applicable. Secondly, Fig. 6 shows that the waves may extract energy from the macrostructure but may also return their energy at other bandwidths.

#### 9. Discussion

From Fig. 6 and similar ones for the other mesostructure observations we conclude that indeed beyond  $\lambda_h=5$  [m] at the site investigated we can describe the mesostructure fluctuations as random internal waves using linear theory. We have estimated the kinetic energy of the microstructure from  $L_c$  and  $c$  and applied the connection given in (Ivey and Imberger, 1991) to grid-generated stratified turbulence. Then we arrive at ratios of  $O(20)$  between kinetic mesostructure energy and microstructure energy. However, the computed mesostructure buoyancy flux and mesostructure shear stress are negligible and of the same order as those estimated from the microstructure eddy diffusivity. The latter is derived from the fine-scale CTD drops and the procedure given in (Ivey and Imberger, 1991). Thus at our site the random internal waves, in the mesostructure range, transfer energy from the macrostructure towards the microstructure without significant changes in energy in the meantime. Hence, internal waves, in the mesostructure range, serve as practically inert steps on the energy cascade not yet accounted for in turbulence models.

We infer that at the high wavenumber part of the mesostructure range internal waves break and in this way transfer their energy to 3D turbulence. Firstly, this point of view follows from

theoretical considerations on critical layer formation in a shear flow. Secondly, all fine-scale density profile, such as Fig. 4a, show overturning or the remnants of wave breaking. We have analysed that wave breaking due to convective overturning i.e.  $(\partial p'/\partial z) > 0$  occurs prior to the shear instability with locally  $Ri < 1$ . In other words: at the smallest mesoscale wavelength we expect that internal waves break by convective overturning if locally  $\{(\partial p'/\partial z) + (\partial p/\partial z)\} > 0$ . If the spectral shape for  $p'$  is given then its constant of proportionality follows from the observed variance of  $p'$ . Finally, we can compute the rms-value  $|\partial p'/\partial z|$  by integration from the largest scale to the smallest mesostructure scale. Then we expect, for sinusoidal waves, that near overturning holds  $|\partial p'/\partial z| = -0.7(\partial p/\partial z)$ . Hence, we put

$$|\frac{\partial p'}{\partial z}| = -C^{\frac{H}{2\pi L_R}} \frac{\partial p}{\partial z} ; \langle p'^2 \rangle = \alpha \cdot m^{-3} ; C = \alpha \cdot \ln\left(\frac{H}{2\pi L_R}\right) . \quad (9.1)$$

In (9.1) we computed the variance of  $p'$  from an assumed a  $(-3)$  power vertical wavenumber spectrum and integrated this spectrum from the largest vertical wavelength  $\lambda_v$ , which we set equal to the waterdepth  $H$ , to the smallest vertical mesostructure wavelength  $2\pi L_R$ , as we defined earlier. This yields for the "internal-wave-induced Cox number"  $C=0.56 \pm 0.25$  and  $C < 0.92$  from our six mesostructure measurements at the

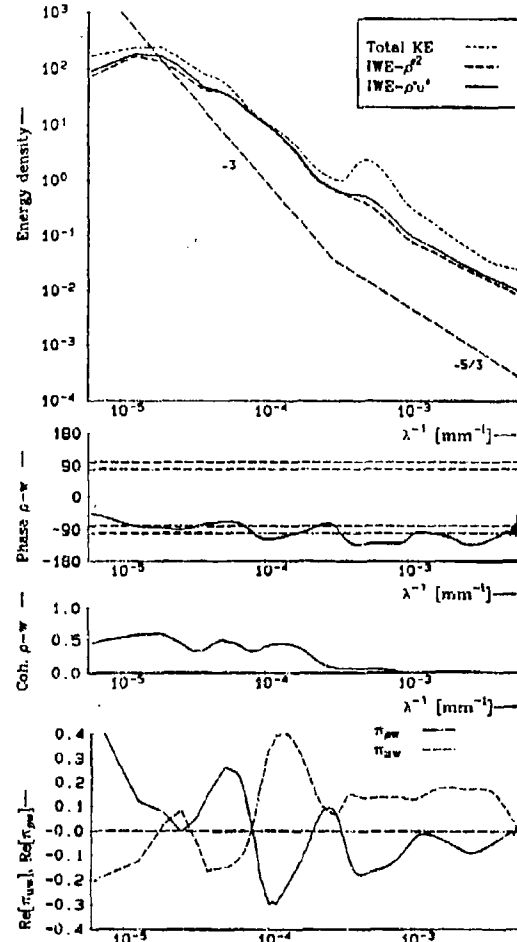


Fig.6. Spectral analysis of random internal waves at  $Ri = 0.43$ ;  $N=0.15$  rad/s.

site investigated. These properties of C support our point of view that at the large wavelength range of the mesostructure internal waves do not break. Next we derive the energy transfer to 3D turbulence by wave breaking. The loss  $L_e$  of kinetic IWE by convectional overturning of waves, initially with amplitude  $\%L_E$  and reduced by  $\%L_C$  after breaking, yields

$$L_e = \%N^2 L_E^2 - \%N^2 (L_E - L_C)^2 = \%N^2 (L_E \cdot L_C) \cdot (1 - \frac{\%L_C}{L_E}). \quad (9.2)$$

In addition, we propose the time scale  $\tau_c$  during which an internal wave is deformed until the critical layer state with  $\theta$  in (8.4) nearly  $90^\circ$ . Here we suppose that the Richardson number is small enough so that the mean shear rate dominates over the wave-induced shear. Then we apply the refraction equation for solitary wave groups to estimate the rate of change of  $\theta$  along a ray. For small vertical wavelengths but gradual vertical changes in buoyancy frequency the typical time scale  $\tau_c$  to increase the magnitude of  $\tan\theta$  by  $\Delta\theta = 0(5-10)$  reads:  $\tau_c = \Delta\theta / |\frac{du}{dz}|$ . Hence, the ensemble averaged effect of the process of growing and breaking waves equals the following (rate of energy) transfer  $T_{i+t}^{br}$  from IWE to TKE, solely by wave breaking:

$$\text{for } L_C \leq L_E : \quad T_{i+t}^{br} = \frac{L_e}{\tau_c} = \{\% \Delta\theta^{-1} \cdot N^2 (L_E \cdot L_C) \cdot (1 - \frac{\%L_C}{L_E})\} \cdot |\frac{du}{dz}|; \quad \Delta\theta = 5-10. \quad (9.3)$$

This turbulence production term should be included in (7.1). The part of (9.3) between  $\{\dots\}$  is an additional shear stress in the momentum equations for the macrostructure. Further, apart from  $\Delta\theta$ , the energy transfer (9.3) can be estimated along the depth-time path of the platform and it should at least balance against  $\epsilon$  in (7.1).

#### Conclusions

The main conclusion of this paper is the comparison in Fig.3 along the depth-time path of the platform between  $\epsilon$  and the energy transfer (9.3) to the microstructure: it varies between  $3-50$  [ $\text{mm}^2/\text{s}^3$ ] for  $\Delta\theta = 5$ . Moreover, we added to (7.1) the source (9.3) based on averages of the observed  $L_C$  and  $L_E$ . Then the results of (7.1) and (7.2) with (9.3) clearly improve: the computed mixing length and dissipation rate are certainly within the same order of Fig. 2 and 3. Thus energy transfer by wave breaking should be included in the proposal (Uittenbogaard and Baron, 1989). Further analysis (Uittenbogaard, 1993) reveals that the IWE estimates follow well the observed vertical velocity spectrum in the mesostructure range. However, the spectrum of the observed horizontal velocity components is usually underestimated. Hence, the latter findings suggest the variable contribution of quasi-2D turbulence as described by (Métais and Herring, 1989).

#### Acknowledgements

The measurements in this paper were performed as part of long term research project for the Netherlands' Ministry of Transport, Public Works and Water Management/Tidal Water Division. The first author wants to thank prof. F.T.M. Nieuwstadt of Delft University for his stimulating interest in this work.

#### References

- IMBERGER, J. & BOASHASH, B. 1986 Application of the Wigner-Ville distribution to temperature gradient microstructure: A new technique to study small-scale variations. *J. Phys. Oceanogr.*, 16, pp. 1997-2012.
- ITSWEIRE, E.C. 1984 Measurements of vertical overturns in a stably stratified turbulent flow. *Phys. Fluids*, Vol. 27, No. 4, 764-766.
- IVEY, G. & IMBERGER, J. 1991 On the nature of turbulence in a stratified fluid. Part I: the energetics of mixing. *J. Phys. Oceanogr.*, 21, May, pp. 650-658.
- METTAIS, O. & J.R. HERRING 1989 Numerical simulation of freely evolving turbulence in stably stratified fluids. *J. Fluid Mech.*, vol. 202, pp. 117-148.
- TAYLOR, G.I. 1931 Internal waves and turbulence in a fluid with variable density, *Rapports et procès-verbaux des réunions du Conseil Permanent International pour l'Exploration de la Mer*, vol. LXXVI, pp. 35-42.
- UITTENBOGAARD, R.E. & BARON, F. 1989 A proposal: extension of the  $k-\epsilon$  model for stably stratified flows with transport of Internal Wave Energy, paper 18.4 in *7th Turbulent Shear Flows Symp.*, Stanford, August 21-23.
- UITTENBOGAARD, R.E. 1993 The importance of internal waves for mixing in a stratified estuarine tidal flow. DELFT HYDRAULICS, report Z-722, October.

# The Evolution of a Turbulent Mixed Patch in a Stratified Shear Flow

Graham Hughes

Department of Applied Mathematics and Theoretical Physics

University of Cambridge

Silver Street

Cambridge CB3 9EW

England

Telephone: +44 223 337911; Facsimile: +44 223 337918;

Email: goh10@amtp.cam.ac.uk

## Abstract

The collapse of a turbulent patch in a stratified shear flow has been considered experimentally. A region of fluid in a linear stratification is stirred and allowed to collapse in the presence of a constant imposed velocity shear. These experiments are a model for the collapse behaviour which follows mixing events in stratified environments such as the ocean and the atmosphere.

Measurements are presented showing how the dimensions of the patch evolve over time. Initially the patch expands in the horizontal direction under the action of buoyancy forces in a similar manner to that found by Wu (1969). However the imposed shear profile soon reestablishes itself in the patch and begins to play an important, yet subtle role in the ensuing collapse. The ambient shear may be able to supply the turbulence in the patch with energy from the mean flow, but it also enhances the horizontal spreading rate of the patch, whereupon buoyancy forces act more effectively to damp the turbulence. In the range of turbulent Reynolds numbers and Richardson numbers investigated the latter effect is observed to dominate, leading to the decay of turbulent energy.

## 1 Introduction

It is widely recognised that the generation of a mixed region and its subsequent gravity-driven spread into a stratified medium has an important role to play in the ocean and the atmosphere. Mixed regions can form following the interaction of the flow with an obstacle. Overturning in the wake behind an object and the breaking of mountain lee waves are among the examples given in the review by Lin & Pao (1979). Another important generation mechanism identified by Wu (1969) is the shear instability induced by strong internal waves. Turner (1973) and Barenblatt (1978) describe in detail how these waves can generate sufficiently large velocity gradients to become locally unstable to a Kelvin-Helmholtz type mode. As the instability develops, the overturning creates a mixed region which subsequently collapses under gravity. Such processes are thought to account for some of the observed oceanic microstructure (Turner (1973)).

The need for a better understanding of these mechanisms in the atmosphere and ocean has motivated many studies and a summary of these is given in §2. In most cases, however, the effects on the gravitational collapse arising from an ambient shear flow and from the turbulence generated in the mixed region by the initial overturning have been neglected. The importance of these effects needs to be assessed. The current experimental work and results are described in §3 and §4, followed by the conclusions in §5.

## 2 Background

Many previous studies of mixed region collapse have considered how a quiescent patch spreads horizontally into an ambient stratification. The experiments of Wu (1969) identified three regimes for this process – the ‘initial’, ‘principal’ and ‘final’ stages of collapse.

In the initial collapse regime, a transfer in the mixed region of excess potential energy to kinetic energy is assumed to occur. This transfer is described for a two-dimensional mixed region by

$$(l - l_0)/l_0 \sim (Nt)^2, \quad Nt \lesssim 2, \quad (1)$$

where  $N$  is the buoyancy frequency of the stratification,  $t$  is the time and  $l$  and  $l_0$  are the current and initial horizontal extents of the mixed region (Wu (1969), Hartman & Lewis (1972), Kao (1976) and Amen & Maxworthy (1980)).

The transition to the principal collapse regime was found to occur when significant internal wave radiation results in a ‘loss of energy’ from the vicinity of the mixed region (Kao (1976), Manins (1976) and Barenblatt (1978)). The corresponding buoyancy–inertia balance applied at this stage gives

$$l/l_0 \sim (Nt)^{1/n}, \quad 2 \lesssim Nt \lesssim 25, \quad (2)$$

where  $n = 2$  for a two-dimensional mixed region and  $n = 3$  in an axisymmetric collapse.

Barenblatt (1978) and Zatespin et al. (1978) found a viscous–buoyancy balance to apply in the stage of ‘final’ collapse, given by

$$l/l_0 \sim (Nt)^{1/n}, \quad Nt \gtrsim 25, \quad (3)$$

where  $n = 6$  for a two-dimensional mixed region and  $n = 10$  for the axisymmetric case.

When the ambient conditions for the gravitational collapse of the mixed region discussed above are extended to include a velocity shear, the dependence on the Richardson number,

$$Ri = \frac{N^2}{\gamma^2}, \quad (4)$$

must be considered. Here the shear is parameterised by  $\gamma = dU/dz$ . The experiments of Itsweire et al. (1993) and Rohr et al. (1987, 1988) demonstrate that a stratified shear flow with  $Ri < Ri_{cr}$  (where  $Ri_{cr} \sim 0.25$ ) can maintain or enhance the level of turbulence within the flow due to shear instabilities. In contrast, ambient turbulence was always observed to decay in flows when  $Ri > Ri_{cr}$ .

In this paper we shall restrict attention to the case where the shear is relatively weak,  $Ri \gg Ri_{cr}$ , as is typical of many oceanic and atmospheric flows. Although  $Ri > Ri_{cr}$  and turbulence cannot be maintained throughout the ambient flow, it is apparent that a mixing event will generate a patch with a low local Richardson number. The question to

be answered is, whether for sufficiently low  $Ri$  in the finite volume patch, the turbulence can be maintained in the patch as it undergoes gravitational collapse. Some theoretical models of this problem have been proposed.

Avdeyeva & Maderich (1987) model a turbulent patch as consisting of a turbulent core region surrounded by an entrainment layer through which the level of turbulence decreases to zero, so as to merge with the ambient fluid. A calculation of the energy fluxes through these regions is undertaken in order to identify the important mechanisms providing energy transfer. In the absence of external shear, the dominant terms in the energy budget were turbulent dissipation, the conversion of potential energy to kinetic energy, the radiation of internal waves and the smoothing of buoyancy fluctuations by diffusion. As the external shear is increased from zero the turbulent energy extracted from the mean shear and the energy flux associated with entrainment of ambient fluid were found to become important only for  $Ri < 0.25$ .

However the analysis by Barenblatt (1990) suggests the possibility of different types of behaviour. A turbulent patch was considered in its later stage of collapse, where its thickness is much less than the horizontal spread. Consequently the ambient shear profile is assumed to have become established across the patch, unaffected by the patch turbulence, which is taken to be small-scale and self-similar. The subsequent evolution of the turbulence in the mixed region is found using a semi-empirical  $\kappa - \epsilon$  turbulence model together with a time-varying turbulent viscosity. Two cases of interest were then examined. In the first case, the ambient shear profile through the patch was assumed constant in time and it was found, that for sufficient initial turbulent energy, the turbulent intensity increases in the patch. Once the turbulence has grown sufficiently to modify the assumed shear profile in the patch, this analysis becomes invalid. The second case then becomes appropriate, where a constant turbulent shear stress is assumed to exist in the patch. Sudden increases in the level of turbulence are found to be possible from this state and Barenblatt (1990) suggests this as a mechanism for obtaining a 'turbulent burst' from a patch of relatively weak 'fossilised' turbulence.

### 3 Experimental Apparatus

The mixed region collapse experiments described below were conducted in the stratified shear flow tank detailed by Redondo (1989) and similar to that used by Koop (1981) and Koop & McGee (1986). The shear flow tank consists of a closed circuit channel, shaped like a race-track, around which the fluid is driven by a special pump, as first suggested by Odell & Kovasznay (1971). The pump consists of two stacks of thin horizontal disks which, when rotated about a vertical axis, drive the fluid by friction in the horizontal direction while causing a minimum of vertical disturbance to the stratification. Each stack consists of two layers, one on top of the other in the stack, which may be driven independently of the other at different speeds, so as to produce a shear velocity profile over the tank depth.

In these experiments a linear stratification of depth 25cm was set up in the tank, with the buoyancy frequency  $N$  typically in the range  $0.9 - 2 \text{ s}^{-1}$ . Although vertical disturbance and subsequent mixing in the flow is minimised by the use of this horizontal disk pump, the stratification is inevitably eroded over time. At the slowest speeds the stratification is maintained over an hour or more, but this time is reduced to about ten minutes when the individual layers are driven at the maximum speed (approximately  $3 - 4 \text{ cm/s}$ ) in

opposite directions.

For all of our experiments the two sets of disks in each stack were counter-rotated so as to produce a zero velocity level at mid-depth. Advantage was taken of this to generate a mixed region centred about the level of zero velocity and have it evolve in the stationary laboratory frame.

A turbulent patch was produced using a spindle fitted with a row of nylon bristles or plastic strips in a single plane and supported horizontally across the flow. Once a shear flow was established, generation of the mixed region was achieved by using a stepper motor to rotate the spindle rapidly back and forth about its mean horizontal position. Providing this mixing process was achieved on a timescale less than or comparable to both the buoyancy period  $N^{-1}$ , of the stratification and the shear timescale  $\gamma^{-1}$ , the initial mixed region was well approximated by a two-dimensional horizontal cylinder of turbulent fluid lying across the tank. Shadowgraph images or fluorescein injected into the vicinity of the spindle prior to mixing, with illumination by a light sheet from below, proved to be an effective means of visualising the collapse. Video footage was taken of each experiment allowing subsequent analysis and data to be collected from the tapes.

#### 4 Observations and Results

Two general regimes were observed in all of the patch collapse experiments conducted. These are broadly defined as 'symmetric' and 'antisymmetric' collapse about a vertical axis through the patch midpoint. Symmetric collapse was always observed first, proceeding under the action of buoyancy forces as seen by Wu (1969). As the patch evolved, a transition was observed where the ambient shear became the dominant driving force for the collapse, leading to an antisymmetric deformation of the mixed region.

With an externally imposed shear profile, horizontal spreading of the mixed region is achieved much more rapidly than that which occurs for a collapse under buoyancy alone. Buoyancy forces remain important at all times in the shear-driven case, however, causing vertical contraction of the patch. In the antisymmetric stage of collapse the combination of horizontal spreading by shear and vertical collapse under buoyancy results in the patch assuming a thin pancake-like shape, slightly inclined to the horizontal.

In experiments conducted without shear, Wu (1969) observed that the motion of the patch boundary generates large amplitude internal waves while the mixed region collapses. Observations of the collapse process when ambient shear is introduced show particularly violent internal wave activity, with the large amplitude vertical oscillations being strongly sheared in the horizontal. This induces wave-breaking, overturning and mixing events on the patch boundary, with a subsequent increase in the rate at which energy is lost from the patch.

Barenblatt (1990) suggested that in the presence of ambient shear, energy can be drawn from the mean flow to maintain or even enhance the level of turbulence within the patch. In our experiments turbulence was generated on the patch boundary by the internal wave-shear interaction events described above, but nevertheless strong damping of all turbulence in the patch was observed soon thereafter. The reason seems to be that when the patch is spread horizontally by the shear the largest eddy, which scales on the vertical dimension of the patch, is decreasing. Hence the Reynolds number for the turbulence becomes smaller and smaller until a viscous coupling is established across the

patch. This conjecture is supported by observations that dye crystals dropped through the collapsing patch indicated the existence of a smooth linear variation in velocity within the patch.

Following the decay of turbulence in the patch there is very little mixing apparent between the mixed region and the ambient fluid. Therefore if the mixed region volume is assumed to remain constant in this regime the spreading behaviour of the patch may be predicted. The model geometry for the collapsing region is shown in Figure 1. For large aspect ratio  $l/h$ , we take the patch to be approximately rectangular, with area  $A$ , where

$$A = hl. \quad (5)$$

Observations have shown that the shear is the dominant process driving the collapse during this stage. The mixed region fluid is seen to travel at a horizontal speed matching that of the local shear velocity, except at the extremities of the mixed region where buoyancy gradients are high, forcing a local vertical adjustment to maintain gravitational stability. A transfer of fluid from the section of patch above the zero velocity level to that below will therefore occur as shown, but because of the assumed symmetry this is exactly balanced by a return flow from the lower to upper portions at the other end. Hence the net volume flow rate  $Q$  available to lengthen either the upper or lower sections of the patch is just that transported by the linear shear profile,

$$Q = \frac{1}{2}\gamma h^2 = h \frac{dl}{dt}, \quad (6)$$

where  $dl/dt$  is the rate at which the rectangular patch lengthens.

Combining equations (5) and (6) we obtain,

$$\frac{dh}{dt} = -\frac{\gamma h^3}{2A}, \quad (7)$$

the solution of which yields,

$$\frac{h}{h_0} = \left(1 + \frac{h_0}{l_0}\gamma t\right)^{-1/2}, \quad (8)$$

$$\frac{l}{l_0} = \left(1 + \frac{h_0}{l_0}\gamma t\right)^{1/2}, \quad (9)$$

where  $h_0$  and  $l_0$  are the initial patch dimensions at time  $t = 0$ . Thus equations (8) and (9) predict that as time passes the patch dimensions should vary as  $h \sim t^{-1/2}$  and  $l \sim t^{1/2}$ .

A graph of the patch length  $l/l_0$  versus the non-dimensional time  $Nt$  for these experiments is shown in Figure 2. A relatively narrow range of Richardson numbers, well beyond those for shear instability have been considered here, including three runs without shear. The exponent for the collapse data seems to be slightly less the 1/2 predicted by equation (9), however the collapse needs to be studied for a longer time to avoid being unduly biased by initial collapse behaviour.

Although a transition is observed experimentally between what we have termed the symmetric and antisymmetric stages of collapse, a break point in the spreading rate is not evident on this plot. This is because the transition to a shear-driven collapse, given in equation (9), usually takes place in the principal collapse regime, described by equation (2). As both regimes predict  $l \sim t^{1/2}$ , the transition is smooth and finding it requires a

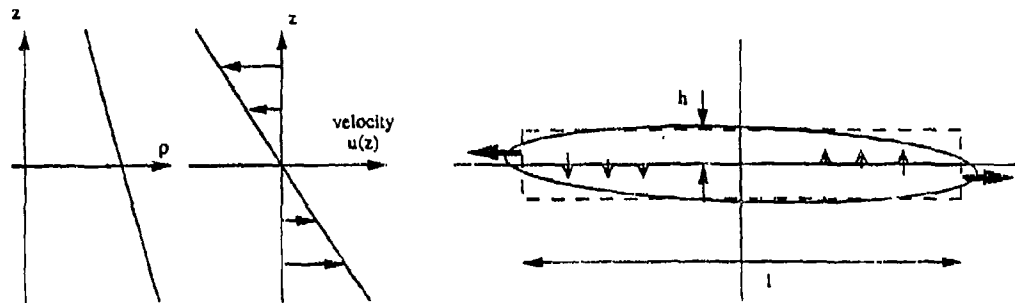


Figure 1: Idealised geometry for collapsing mixed region. The ambient density and velocity profiles are also shown.

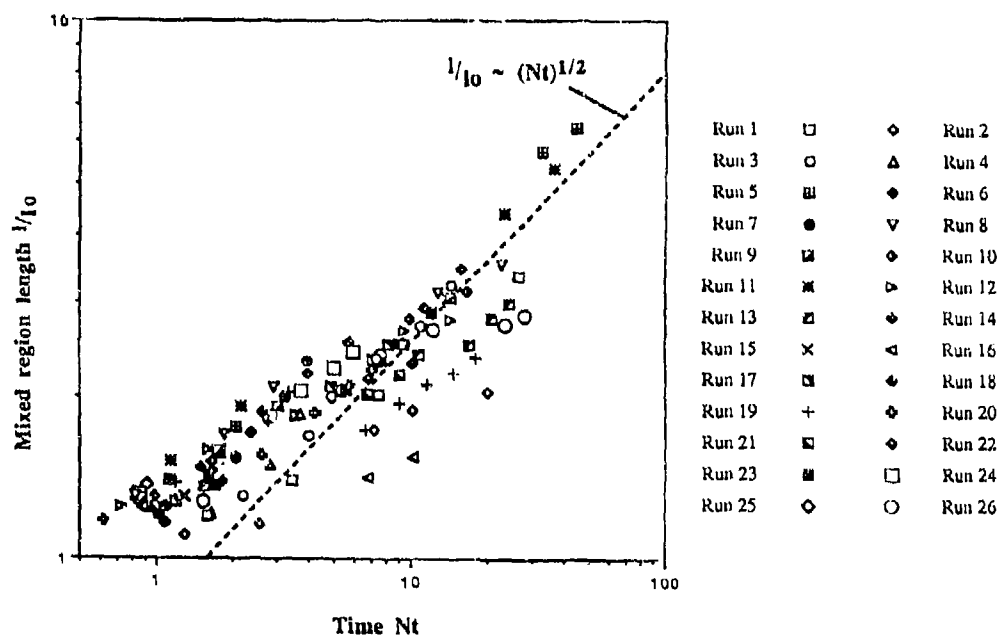


Figure 2: Plot of the measured length of the collapsing mixed region as a function of the non-dimensional time  $Nt$ . The approximate values of  $Ri$  for the experiments are:  
 $Ri \sim 1000$ : Runs 1-11, 13-20  
 $Ri \sim 1250$ : Runs 23, 24  
 $Ri \sim 2500$ : Run 26  
 $Ri \sim 5000$ : Run 25  
 $Ri \rightarrow \infty$ : Runs 12, 21, 22

comparison with control experiments conducted without shear. Over a longer measurement period the difference is clear between the spreading rate predicted by equation (9) in shear and by equation (3) for the viscous collapse stage, as can be seen in Figure 2 for the runs without shear.

## 5 Conclusions

An experimental method has been described which is able to generate a turbulent patch in a stratified shear flow. It has been used to conduct preliminary experiments on a class of problems that are directly applicable to flows in the ocean and atmosphere. Results to date would suggest that the turbulent regions generated by mixing events in these stratified environments will spread out to a large horizontal extent under the action of the applied shear flow. Simple scaling laws predict that the horizontal extent of the patch increases as  $t^{1/2}$  in the collapse regime dominated by shear. This seems to be in general agreement with the experimentally observed behaviour.

Any turbulence in the patch appears to be strongly damped as buoyancy forces decrease the vertical length scale during the collapse. We are now looking at simultaneous velocity and density measurements in an effort to confirm this behaviour. A complex and very active internal wave field is also generated by the collapse; this too requires further study.

The author is grateful to The Association of Commonwealth Universities for their financial support during the course of this work, and also to Dr P.F. Linden and Dr S.B. Dalziel for their helpful suggestions and comments.

## 6 References

AMEN, R. & MAXWORTHY T. 1980 The gravitational collapse of a mixed region into a linearly stratified fluid. *J. Fluid Mech.* **96**, 65.

AVDEYEVA, I.Y. & MADERICH, V.S. 1987 Energetics of turbulent patches in a stably stratified ocean. *Oceanology* **27**, 133.

BARENBLATT, G.I. 1978 Dynamics of turbulent spots and intrusions in a stably stratified fluid. *Izv., Atmos. Oceanic Phys.* **14**, 139.

BARENBLATT, G.I. 1990 Evolution of turbulence in a stably stratified shear flow. *Izv., Atmos. Oceanic Phys.* **26**, 928.

HARTMAN R.J. & LEWIS, H.W. 1972 Wake collapse in a stratified fluid : linear treatment. *J. Fluid Mech.* **51**, 613.

ITSWEIRE, E.C.; KOSEFF, J.R.; BRIGGS, D.A. & FERZIGER, J.H. 1993 Turbulence in Stratified Shear Flows: Implications for Interpreting Shear-induced Mixing in the Ocean. *J. Phys. Oceanogr.* **23**, 1508.

KAO, T.W. 1976 Principal stage of wake collapse in a stratified fluid : Two-dimensional theory. *Phys. Fluids* **19**, 1071.

KOOP, C.G. 1981 A preliminary investigation of the interaction of internal gravity waves with a steady shearing motion. *J. Fluid Mech.* **113**, 347.

KOOP, C.G. & MCGEE, B. 1986 Measurements of internal gravity waves in a continuously stratified shear flow. *J. Fluid Mech.* **172**, 453.

LIN, J.T. & PAO, Y.H. 1979 Wakes in stratified fluids. *Ann. Rev. Fluid Mech.* **11**, 317.

MANINS, P.C. 1976 Mixed-region collapse in a stratified fluid. *J. Fluid Mech.* **77**, 177.

ODELL, G. & KOVASZNAY, L. 1971 A new type of water channel with density stratification. *J. Fluid Mech.* **50**, 535.

REDONDO, J.M.R. 1989 Internal and External Mixing in a Stratified-Shear Flow. *Advances in Turbulence 2* Fernholz, H.H. & Fiedler, H.E., Eds, Springer-Verlag 198.

ROHR, J.J.; HELLAND, K.N.; ITSWEIRE, E.C. & VAN ATTA, C.W. 1987 Turbulence in a Stably Stratified Shear Flow: A Progress Report. *Fifth Symp. on Turbulent Shear Flows* F. Durst et al. Eds, Springer-Verlag 67.

ROHR, J.J.; HELLAND, K.N.; ITSWEIRE, E.C. & VAN ATTA, C.W. 1988 Growth and decay of turbulence in a stably stratified shear flow. *J. Fluid Mech.* **195**, 77.

TURNER, J.S. 1973 *Buoyancy Effects in Fluids* Cambridge University Press.

WU, J. 1969 Mixed region collapse with internal wave generation in a density stratified medium. *J. Fluid Mech.* **35**, 531.

ZATESPIN, A.G.; FEDEROV, K.N.; VOROPAYEV, S.I. & PAVLOV, A.M. 1978 Experimental study of the spreading of a mixed region in a stratified fluid. *Izv., Atmos. Oceanic Phys.* **2**, 170.

# Efficiency of Mixing by a Turbulent Jet in a Stably Stratified Fluid

Magnus Larson<sup>1</sup> and Lennart Jönsson<sup>2</sup>

**ABSTRACT:** Mixing in a two-layer stably stratified fluid by a turbulent jet was studied through a laboratory experiment. A non-swirling jet was discharged vertically downwards in a confined fluid system consisting initially of a top layer of fresh water and a bottom layer of salt water. In total, 16 experimental cases were performed where the diameter and exit velocity of the jet were varied together with the density difference between the top and bottom layer. Vertical density profiles were determined from conductivity measurements. A three-layer density structure developed in all cases with an intermediate layer that grew in size with time elapsed as fresh and salt water were mixed. The mixing efficiency, defined as the percentage of the supplied kinetic jet energy that is used for increasing the potential energy of the fluid system, was related to a densimetric Froude number based on the intermediate layer depth. Overall, the calculated jet mixing efficiency displayed higher values than comparable efficiencies for destratification with air-bubble plumes.

## Introduction

Artificially induced circulation is a useful technique for improving water quality in for example reservoirs, harbors, and small lakes. In such water bodies, a stable density stratification may develop that prevents vertical exchange of water, resulting in stagnant zones with inferior water quality. Conventional methods for destratification are mainly based on air injection techniques; however, an alternative method with technical and economical advantages involves submersible mixers (Suter and Kilmore 1990, Jönsson and Rissler 1991, Stephens and Imberger 1993). A mixer consists essentially of a propeller (diameter up to 2.5 m), which generates a swirling jet that penetrates through the water column and induces vertical water exchange. The theory for describing jets created by mixers and their interaction with a stratified, confined water body is not well-developed. Furthermore, both laboratory and field studies on this subject are scarce.

When comparing different techniques for destratification the efficiency  $\eta$  of the mixing process is a key parameter. For a fixed time period,  $\eta$  may be defined as the percentage of the total mechanical energy input that is used for increasing the potential energy of the fluid system. Asaeda and Imberger (1988) and Zic et al. (1992) presented values on the mixing efficiency for air-bubble plumes, where a maximum  $\eta$  of about 12% was obtained.

<sup>1</sup>Department of Civil Engineering, University of Tokyo, Bunkyo-ku, Tokyo 113, JAPAN (Associate Professor on leave from Department of Water Resources Engineering, University of Lund).

<sup>2</sup>Associate Professor, Department of Water Resources Engineering, University of Lund, Box 118, S-221 00 Lund, SWEDEN.

Stefan and Gu (1992) studied mixing by selective withdrawal and jet reinjection at a different depth, and experimentally found values on  $\eta$  between 12 and 33%. Stephens and Imberger (1993) performed laboratory experiments to determine the efficiency of mixers in destratification and obtained a maximum  $\eta$  of 12%. It should be stressed that the values on  $\eta$  reported by Stephens and Imberger (1993) are based on the energy input to the impeller and that this  $\eta$  is not directly comparable to the values given in Stefan and Gu (1992) or in the present study. The kinetic energy flux in the swirling jet generated by the propeller will be lower than the energy input to the impeller because of losses in the generation of the jet motion; thus, an  $\eta$  based on the energy input to the impeller will be lower than if the kinetic energy flux in the jet is employed in the definition of  $\eta$ .

This study focusses on the density profile evolution in a confined region with a stably stratified fluid, where mixing is induced by a circular, non-swirling turbulent jet. The efficiency of the mixing process was determined from consecutive density profiles derived from conductivity measurements. A non-swirling jet was employed as a first approximation to reproduce the effect of a mixer in the far-field; the flow pattern in swirling and non-swirling jets displays marked similarities, although the rate of entrainment is enhanced in a swirling jet.

## Laboratory Experiment

Larson and Jönsson (1994) performed a laboratory experiment to investigate the mixing in a stably stratified, confined fluid system induced by a turbulent jet. A two-layer stable stratification was created in a rectangular container by using water and sodium chloride, and the jet water was withdrawn from the top layer (fresh water) and discharged vertically down into the bottom layer (salt water). The container had an inside bottom area of  $0.98 \times 0.98 \text{ m}^2$ , a height of 0.65 m, and the exit of the jet was located 0.43 m above the bottom. During all experimental cases a water depth of 0.55 m was employed in the container, where the bottom layer was initially made approximately 0.30 m thick. The jet was generated using a variable-speed pump with a maximum capacity of 2.5 l/min.

A measurement system was developed that could sample conductivity readings from at most 16 probes through a predetermined scanning sequence, and each of these probes could be located arbitrarily in the container. The conductivity data were sampled using a personal computer and stored on disk together with the absolute probe location, which was recorded with a potentiometer, and measurements of the exit jet flow. The salinity was determined from the measured conductivity through calibration, and the density was derived from the salinity using standard tables (all densities given in this paper refer to 20 degrees). The measurements were performed either at fixed locations during jet action or while transversing the vertical with the probes when the jet was turned off. Only the latter measurements will be discussed in this paper. Figure 1 illustrates the experimental setup.

In total 16 experimental cases were performed encompassing different combinations of salinity in the bottom layer ( $S$ ), mean jet exit velocity ( $V_o$ ), and jet exit diameter ( $d_o$ ). Two different jet diameters (8.3 and 10.2 mm) were investigated with  $S$  ranging from 0.1-1.52% and  $V_o$  from 0.14-0.51 m/sec. The corresponding ranges for the densimetric Froude ( $Fr_o$ ) and the Reynolds ( $Re_o$ ) number, computed based on the jet conditions

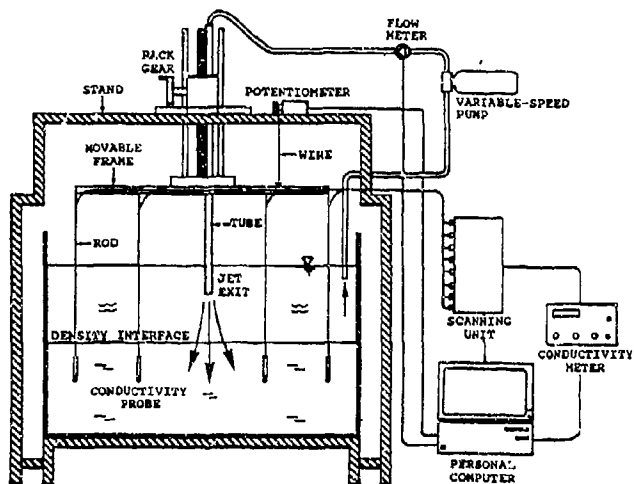


Figure 1: Experimental setup.

at the exit and using  $d_o$  as the representative length scale, were  $11.5 \leq Fr_o \leq 44.4$  and  $1200 \leq Re_o \leq 4200$ . Most of the generated jets were in the turbulent range already at the exit, although laminar flow prevailed immediately downstream the exit for a few cases where  $d_o = 10.2$  mm. Each of the experimental cases involved 10-60 min of effective jet action, during which the jet was turned off 2-9 times for measurements along the vertical. The conditions always stabilized quickly after jet turn-off, and during the measurements along the vertical the conductivity displayed no variation in the horizontal plane. Thus, only density profiles based on measurements from one probe are presented here.

## Results

### Density profile evolution

A three-layer density structure developed during all experimental cases encompassing a top, intermediate, and bottom layer. The top and bottom layers consisted of the original fresh and salt water respectively, and the intermediate layer, which grew in thickness with time elapsed, was formed by mixed water from the two layers. In the earlier stages of an experimental case, when the intermediate layer was thin, the density distribution in this layer was almost linearly decreasing with height. However, with increasing thickness of the intermediate layer the density became more and more homogenized in the bulk of the layer with sharp density gradients at the transitions to the top and bottom layers (an upper and lower interface, respectively; see Figures 2 and 3).

Initially, the jet was of a pure momentum type as fresh water was discharged into the top layer. The water flow in the jet increased with distance from the jet exit due to entrainment of fresh water from the top layer, in accordance with well-known jet theory. Provided the jet momentum was large enough, the jet would penetrate the upper interface thus entering the intermediate layer with further entrainment of water from this layer.

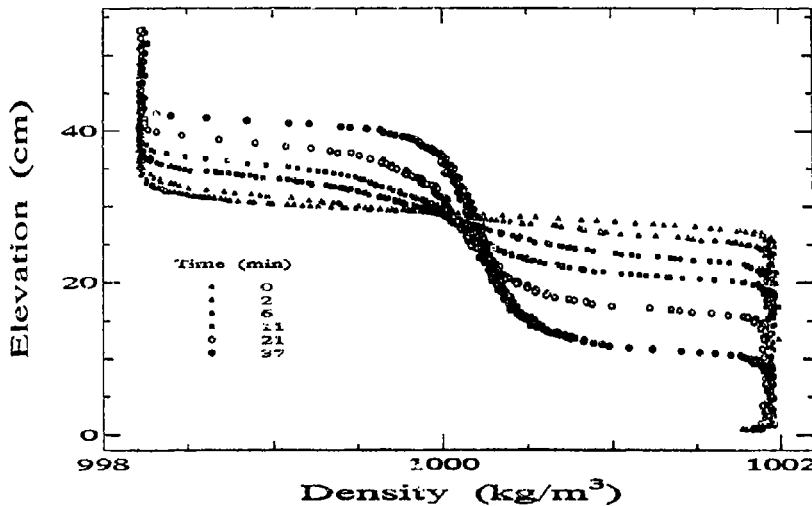


Figure 2: Density profile evolution with time elapsed ( $S=0.51\%$ ).

Passing through the intermediate layer, the jet experienced a buoyancy effect that slowed down the jet. In the experiment the jet passed the intermediate layer in all cases studied, penetrating a certain distance into the bottom layer of salt water, where the increased buoyancy stopped the downward motion altogether; a lower ceiling level was reached depending on the downward-directed momentum of the jet. After reversal, the jet water rose in a plume-like manner penetrating the lower interface of the intermediate layer as it moved upwards, simultaneously surrounding the downward directed jet. A part of the plume water was entrained into the downward moving jet and the rest rose to reach an upper ceiling level somewhere in the intermediate layer, after which the plume spread horizontally towards the container walls.

Figure 2 and 3 present selected density profiles measured during two different experimental cases with the  $s\tau \rightarrow$  jet parameters ( $d_o=8.3$  mm,  $V_o=0.34$  m/sec), but with a salinity of 0.51 and 1.51% in the bottom layer, respectively. The development of the three-layer density structure is clearly seen in the figures together with the homogenization of the conditions in the intermediate layer with time elapsed. The weaker stratification in Figure 2 allows the jet to penetrate deeper down into the bottom layer before reversal as compared to Figure 3; thus, the jet causes a considerably larger portion of the water volume to be mixed for the lower salinity during a specific time period.

#### Intermediate layer growth

The growth of the intermediate layer was most rapid during the initial phase of its development and slowed down as the distance from the jet exit to the lower interface increased. The vertically discharged jet transported fresh water downwards into the intermediate layer, where the added freshwater volume depended on the amount of water that was entrained into the jet before it penetrated the upper interface. In terms of destratification it is desirable to promote a pronounced intermediate layer growth, creating a well-mixed

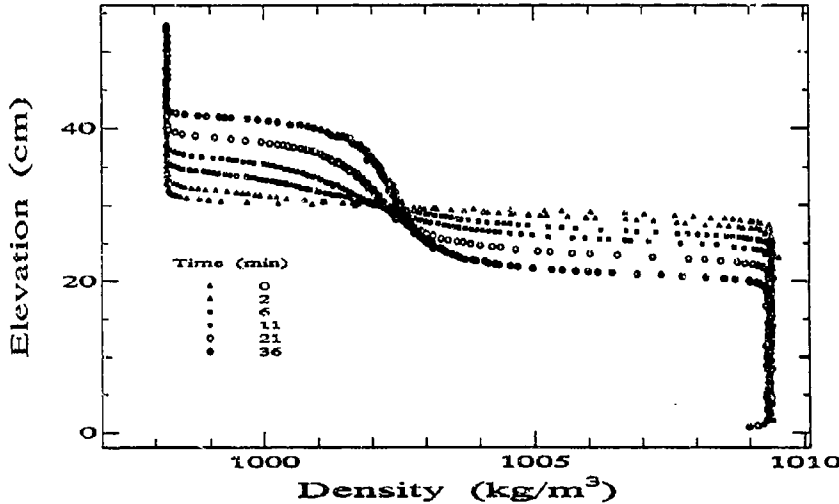


Figure 3: Density profile evolution with time elapsed ( $S=1.52\%$ ).

water body where the interface towards the bottom layer is displaced downwards. The thickness of the intermediate layer  $l$  was determined for the measured density profiles from the location of the upper and lower interface. Figure 4 displays typical time evolutions of the intermediate layer depth expressed in non-dimensional quantities for six selected cases ( $d_o=8.3$  mm; other experimental parameters given in the figure).

The layer depth was normalized with the total water depth in the container  $h_o$  and the non-dimensional time represents the ratio between the water volume discharged at the jet exit during a certain time  $t$  and the total water volume in the container. Thus, the curves in Figure 4 express the amount of water that must be supplied to achieve a specific intermediate layer depth for different jet parameters in terms of the total water volume to be mixed. The  $Fr_o$ -dependence of the curves is also implied in the figure; curves with comparable  $Fr_o$  numbers show similar time evolution of the layer depth. By introducing the  $Fr_o$  number as a multiplier for any of the non-dimensional quantities in Figure 4 (e.g.,  $Fr_o t Q_o / Ah_o$ ), the curves in the figure could be well represented by one single curve in the early phase of the layer development, whereas larger scatter was obtained at greater times.

The relative contribution to the intermediate layer growth from the discharge of fresh water through the upper interface was determined using the theory for a pure momentum jet and the measured layer growth. The average percentage  $\delta$  of the volume growth of the intermediate layer attributed to this jet discharge varied typically between 20 and 50% for the experimental cases studied. A larger jet exit velocity or smaller density difference implied that a smaller percentage of the growth of the intermediate layer was due to the freshwater volume supplied by the jet. The quotient  $\delta$  could be well correlated with  $Fr_o$ , showing a dependence of the power  $-2/3$ . Thus, a large  $Fr_o$ -value implied intermediate layer development with relatively smaller contribution from the fresh water discharge through the upper interface as compared to a small value on  $Fr_o$ .

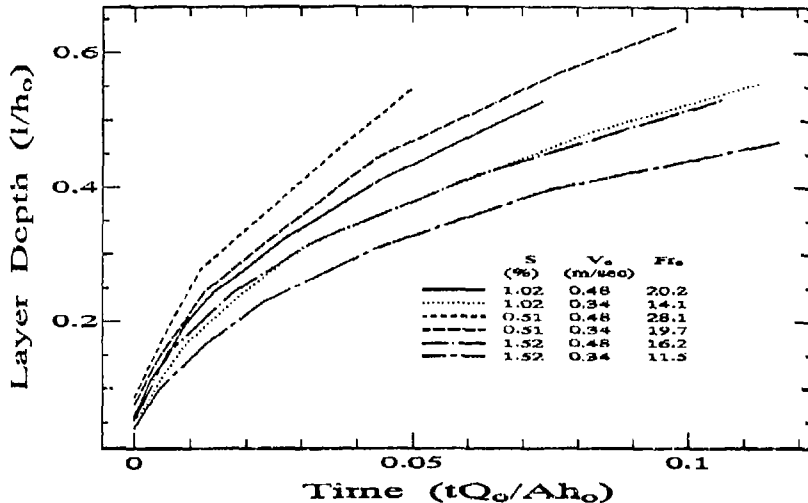


Figure 4: Time evolution of the intermediate layer depth.

### Mixing efficiency

The energy efficiency is of primary interest in practical applications regarding mixing in density-stratified water bodies. Thus, the objective should be to use as much as possible of the kinetic energy in the jet to increase the potential energy of the fluid system. When mixing a stably density-stratified fluid system, fluid with a higher density is lifted up and mixed with lighter fluid, which increases the potential energy of the system. A large portion of the kinetic energy supplied by the jet will be expended through the generation of turbulence that is eventually dissipated into heat. An efficiency factor  $\eta$  may be defined expressing how much of the kinetic energy per unit time  $\Delta K$  supplied to the fluid by the jet that is used for increasing the potential energy of the system per unit time  $\Delta P$ ,

$$\eta = \frac{\Delta P}{\Delta K} = \frac{\Delta P}{\frac{1}{2}\rho\alpha Q_o V_o^2}$$

where  $\rho$  is the jet water density,  $Q_o$  the jet flow at the exit, and  $\alpha$  a correction factor for the shape of the velocity profile (for laminar flow  $\alpha=2.0$  and for turbulent flow  $\alpha$  was derived from the velocity profile for smooth turbulent pipe flow as given by Schlichting (1968)). The increase in potential energy per unit time between two consecutive density profile measurements may be written,

$$\Delta P = \frac{\Delta m \Delta z g A}{\Delta t}$$

where  $\Delta m$  is the net mass of fluid that was moved as the density profile changed,  $\Delta z$  is the corresponding vertical displacement of the mass center for  $\Delta m$ ,  $A$  the cross-sectional area of the container,  $g$  the acceleration of gravity, and  $\Delta t$  the time period of jet action between the density profile measurements (see Larson and Jönsson 1994 for further details on how  $\eta$  was determined).

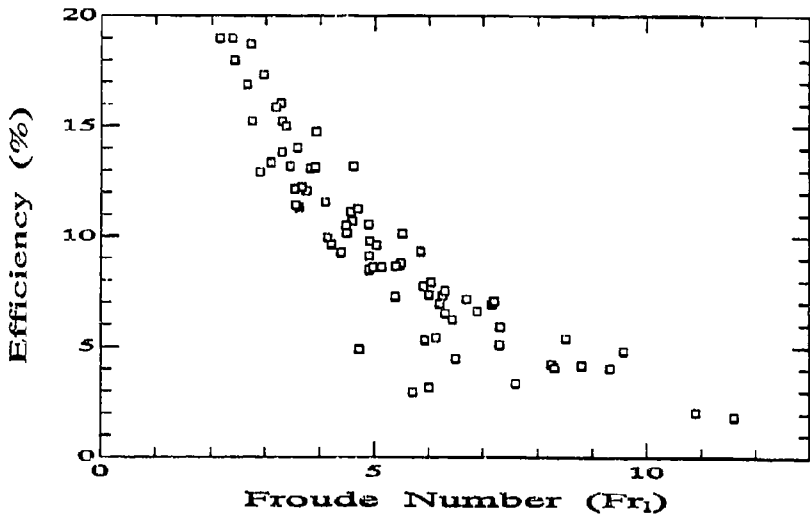


Figure 5: Mixing efficiency as a function of a densimetric Froude number.

All the measured density profiles from the 16 experimental cases were employed to determine the mixing efficiency, using consecutive density profiles in time to evaluate  $\Delta P$ . The mixing efficiency varied approximately between 5 and 20% for the cases studied, and there was a tendency for  $\eta$  to increase with time within a specific case as the intermediate layer grew. In Figure 5 is  $\eta$  plotted against a Froude number  $Fr_l$  defined based on the jet exit velocity, intermediate layer depth, and density difference between the top and bottom layer. The largest values on  $\eta$  was obtained for the smallest values on  $Fr_l$ , and  $\eta$  drops of approximately as  $Fr_l^{-1}$ . Even though the trend of the data points in Figure 5 indicates a continuous growth in  $\eta$  as  $Fr_l$  decreases,  $\eta$  typically became a constant or even decreased in some cases towards the end of a specific experiment.

### Concluding Remarks

In general, the calculated efficiency was significantly higher than what Zic et al. (1992) found for air-bubble plumes, bearing in mind that Zic et al. used the submergence depth of the diffusor to quantify the energy input when defining  $\eta$ , whereas the velocity head of the jet at the exit was used instead in the present study. However, the calculated  $\eta$ :s should be comparable since in both cases the net inflow of energy to the fluid system is used to define  $\eta$ . Thus, it should be possible to achieve a higher mixing efficiency with a jet than with an air-bubble plume. This observation pertains only to the net energy supplied to the fluid system, and an overall evaluation should also involve friction losses in pipe systems and pump efficiencies. The maximum  $\eta$  of about 20% for the jet was also higher than what has been observed for air-bubble plumes, where a maximum value of 12% was determined by Asaeda and Imberger (1988) from experimental data.

An additional experiment has been carried out with the same setup as for the jet but using a small propeller instead to initiate the mixing (compare Stephens and Im-

berger 1993); these experimental cases are presently being analyzed to determine  $\eta$ . Also, detailed LDV measurements are being performed in a homogeneous fluid to determine the velocity field immediately downstream a propeller, which will be helpful in order to understand the mixing process in the near field. Another topic of interest concerns the horizontal spreading of the intermediate layer. In the cases presented in this paper the horizontal and vertical length scale are of the same order of magnitude, which causes the mixing to be quite uniform in the container. A few preliminary tests have been performed in a flume with a length much greater than the depth to study the horizontal spreading of the intermediate layer; these tests have not yet been fully evaluated.

**ACKNOWLEDGEMENTS:** Support from the Japan Society for the Promotion of Science for the research visit of ML to the University of Tokyo is gratefully acknowledged, as well as the assistance from members of the Coastal Engineering Laboratory during his stay. This study was supported by the Swedish Technical Science Research Council (TFR) under contract 262/91-37. Lennart Grahn and Lars Landen provided valuable assistance during the laboratory experiment.

## References

Asaeda, T. and Imberger, J. (1988). "Structures of Bubble Plumes in Stratified Environments," Environmental Dynamics Report ED-88-250, Center for Water Research, University of Western Australia, Nedlands, WA.

Jönsson, L. and Rissler, S. (1991). "The Use of Mixers for Improving Water Quality in Reservoirs, Lakes, and Harbors," Proceedings of the European Conference on Advances in Water Resources Technology, Balkema, Rotterdam, Netherlands, pp 407-416.

Larson, M. and Jönsson, L. (1994). "Mixing in a Two-Layer Stably Stratified Fluid by a Turbulent Jet," Journal of Hydraulic Research (in press).

Schlichting, H. (1968). "Boundary-Layer Theory," McGraw-Hill Book Company, New York, NY.

Stefan, H.G. and Gu, R. (1992). "Efficiency of Jet-Mixing of Temperature-Stratified Water," Journal of Environmental Engineering, Vol 118, No. 3, pp 363-379.

Stephens, R. and Imberger, J. (1993). "Reservoir Destratification via Mechanical Mixers," Journal of Hydraulic Engineering, Vol 119, No. 4, pp 438-457.

Suter, P.J. and Kilmore, G. (1990). "Mechanical Mixers: An Alternative Destratification Technique, Myponga Reservoir, South Australia," Journal of the Australian Water and Wastewater Association, February, pp 32-35.

Zic, K., Stefan, H.G., and Ellis, C. (1992). "Laboratory Study of Water Destratification by a Bubble Plume," Journal of Hydraulic Research, Vol 30, No. 1, pp 7-27.

# Large-scale percolation and diffusion in free and layer turbulent stratosphere

*A.Bershanskii\*, H.Branover\*\*, and M.Nagorny\*\**

*\*P.O.Box 39953, Ramat - Aviv 61398, Tel - Aviv, Israel*

*\*\*Center for MHD - Studies, Ben - Gurion University, Beer - Sheva, Israel.*

## Abstract

A simple model analyzing the properties of fast components of turbulent diffusion is proposed in order to explain two different regimes of large scale transfer of passive scalar observed in the stratosphere. It is argued that these fast components are directly related to percolation of passive scalar in a turbulent fractal and there exist two spectral power laws for fluctuations of passive scalar concentration: the "-4/3" law and the "-7/3" law. These two laws correspond to different percolation regimes: free and layer. The first regime is controlled by the topological instabilities of two-dimensional turbulence in the three-dimensional space, while the second regime occurs with layer-type restriction of these instabilities. The fractal dimension of passive scalar cluster at the layer percolation  $D_V = 9/4$  and the fractal dimension of its perimeter  $D_p = 7/4$  (for the free quasi two-dimensional turbulent percolation  $D_p = 5/3$ ). A good correspondence is found between the spectral and the fractal scaling laws and the atmospheric, numerical and laboratory experimental data.

## 1 Introduction

In [1], (see also [2]-[4]) a simple model analyzing the properties of fast components of turbulent diffusion is proposed. It is argued that these fast components are directly related to critical phenomena in turbulence and relationship

$$\nu D_V = \frac{2}{3 - \gamma} \quad (1)$$

connecting critical exponent  $\nu$ , fractal dimension of the passive scalar cluster  $D_V$ , and passive scalar spectral exponent  $\gamma$ , is obtained. Using the topological condition:

$$\min [D_\sigma \text{ or } D_V] = D_\sigma + D_V - d \quad (2)$$

(where  $D_\sigma$  is the fractal dimension of passive scalar surface, [...] means the integer part of a number,  $d$  is the topological dimension of the space) and the Vassilicos relationship [5],[6]

$$3 - \gamma = D_p = D_\sigma - 1 \quad (3)$$

(where  $D_p$  is fractal dimension of perimeter of the passive scalar cluster) the two conjectured regimes for quasi two-dimensional turbulence can be obtained:

$$\gamma^{(1)} = 5/3, \quad D_V^{(1)} = 5/3, \quad D_p^{(1)} = 4/3, \quad (4)$$

and

$$\gamma^{(2)} = 4/3, \quad D_{\nabla}^{(2)} = 4/3, \quad D_p^{(2)} = 5/3. \quad (5).$$

In order to make a comparison with observational evidence in Fig. 1 (adapted from [7]) we show the horizontal spectra of atmospheric traces (ozone) measured in the stratosphere. The straight lines are drawn for comparison with the relations (4) and (5). It is seen that the relation (4) for  $\gamma$  is observed in small scales and is replaced by (5) at large scales. The Fig. 2 (which has been adapted from [8]) allows to find the value of  $D_p$  for atmospheric clouds. We have drawn in this Figure too the straight lines corresponding to the relations (4) and (5). Again, the same tendency can be seen in Fig. 2 - the relation (4) for  $D_p$  is valid in small scales, while in large scales holds the relation (5).

In this situation the critical exponent  $\nu$  appears to be remarkably close to its universal value in the *three-dimensional* percolation ( $\nu \approx 0.9$ ) rather than to the one for *two-dimensional* case ( $\nu = 4/3$ ) [9].

For understanding this phenomenon and its limitations let us introduce the concepts of free and layer quasi two-dimensional turbulence.

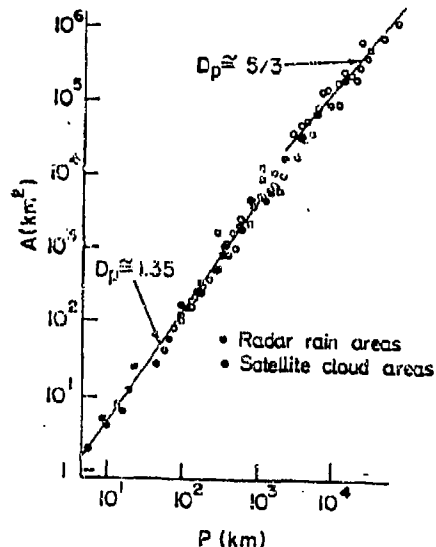
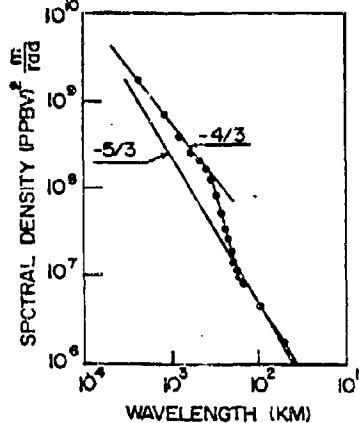


Figure 1 Horizontal spectra of atmospheric traces (ozone). Adapted from [7].

Figure 2 Scaling relations of area ( $A$ ) vs perimeter ( $P$ ) for atmospheric clouds, allowing to obtain the dimension  $D_p$ . Adapted from [8].

## 2 Free quasi two-dimensional turbulence

In [10] the topological instabilities of two-dimensional turbulence in three-dimensional space has been suggested as a basis to understand the properties of quasi two-dimensional turbulence. The instabilities will primarily manifest themselves by exciting helical travelling waves which bend the two-dimensional motion planes. Input of helicity into these waves is the main physical (topological) process for this phenomenon and the parameter  $\langle |dh/dt| \rangle$  replaces the Kolmogorov parameter  $\langle \varepsilon \rangle = \langle |du^2/dt| \rangle$  as governing parameter in corresponding interval of scales (cf. also with [11] and [12]). In the classic theory of Corrsin-Obuchov [13] scaling spectrum of passive scalar concentration,  $c$ , has the form

$$E_c \propto \langle N \rangle \langle \varepsilon \rangle^{-1/3} k^{-5/3} \quad (6)$$

( $N = |dc^2/dt|$ ), while in the free quasi two-dimensional turbulence the scaling spectral law for  $E_c$  is

$$E_c \propto \langle N \rangle \langle \left| \frac{dh}{dt} \right| \rangle^{-1/3} k^{-4/3} \quad (7)$$

It is clear that the percolation regime (5),(7) is controlled by these *three-dimensional* topological instabilities and three-dimensional value of  $\nu \simeq 0.9$  (see Introduction) can be understand as a consequence of this fact.

For experimental verification of the *universality* of this phenomenon for quasi two-dimensional turbulence we used a laboratory quasi two-dimensional turbulence, created in flow of mercury in external (transversal) magnetic field [14],[15].

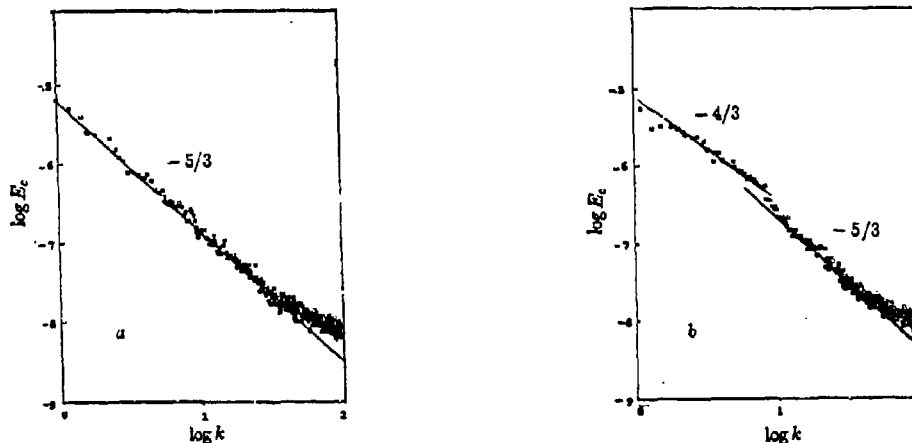


Figure 3a,b Spectra of passive scalar (temperature) fluctuations in the flow of mercury a) without magnetic field, b) with external magnetic field  $B \simeq 0.2T$  (arbitrary units).

In this experiment turbulence has been generated by the honeycomb ( $Re \simeq 5 \cdot 10^4$ ). Detailed description of the experimental installation used can be found in [15]. Since the mercury is a well electrically conducting fluid, external magnetic field transforms the original (without magnetic field) three-dimensional turbulence into quasi two-dimensional one [10],[14],[15]. The temperature has been used as a passive scalar in our experiment. The temperature spectrum,  $E_c$ , obtained in the flow without magnetic field is shown in Fig. 3a while the temperature spectrum obtained in the flow with external magnetic field ( $B \simeq 0.2T$ ) is shown in Fig. 3b. The straight lines are drawn for comparison with scaling laws (6) and (7) (cf. also with atmospheric spectrum in Fig. 1).

### 3 Layer turbulence

Another approach has been suggested in the paper [14]. The travelling waves, which bend the original two-dimensional motion planes, will bring about fluctuations of turbulent energy dissipation  $\varepsilon$ . In the corresponding interval of scales average rate of space  $\varepsilon$ -fluctuations, i.e a value  $\langle |d\varepsilon/dz| \rangle$  (where  $z$  is the co-ordinate perpendicular to two-dimensional turbulence plane) replaces  $\langle \varepsilon \rangle$  as a governing parameter [14].

Dimensions of both governing parameters  $\langle |dh/dt| \rangle$  and  $\langle |d\varepsilon/dz| \rangle$  are the same, and kinetic energy spectrum obtained from dimensional considerations [10],[14]

$$E_u \propto \langle \left| \frac{dh}{dt} \right| \rangle^{2/3} k^{-7/3} \quad \text{and} \quad E_u \propto \langle \left| \frac{d\varepsilon}{dz} \right| \rangle^{2/3} k^{-7/3} \quad (8)$$

has the same exponent '-7/3' in both these cases.

However, these situations are essentially different in the case of passive scalar. In the last case spectral law (7) must be replaced by

$$E_c \propto \langle \left| \frac{dN}{dz} \right| \rangle \langle \left| \frac{d\varepsilon}{dz} \right| \rangle^{-1/3} k^{-7/3} \quad (9)$$

because of space fluctuations of  $N$ . This quasi two-dimensional turbulence has a layer nature and the Vassilicos considerations [5],[6] as well as his relationship (3) are not valid in the case. However, for the layer turbulence we can use the two-dimensional value of  $\nu = 4/3$  [9] to obtaining the fractal dimensions (see also Discussion). Then from (1) and (9) we obtain for layer turbulence:

$$D_\nabla = 9/4 \quad (10)$$

and from the topological condition (2)

$$D_p = 7/4 \quad (11)$$

Fig. 4 shows one of the spectra of the temperature (and energy) fluctuations observed in stratosphere [16] and follows (9) (and (8)). Note that within the uncertainty of measurement it is difficult to determine from Fig. 2 whether  $D_p = 5/3$  (5) or  $D_p = 7/4$  (11) is observed at the large scales. In this sense, the numerical simulation of cloud formation by a cellular automaton model (which turns out to have a strong resemblance to percolation-based growth models) [3] is very useful. In Fig. 5 (taken from [3]) the crossover from isotropic growth of clouds to restricted growth in a layer is shown (cf. with Fig. 2). The dotted line gives  $D_p = 4/3$  at small scales while the solid line gives  $D_p = 7/4$  at large scales. The effective dimension of the large-scale cloud perimeter obtained in [3] for layer  $D_p = 1.74 \pm 0.05$ .

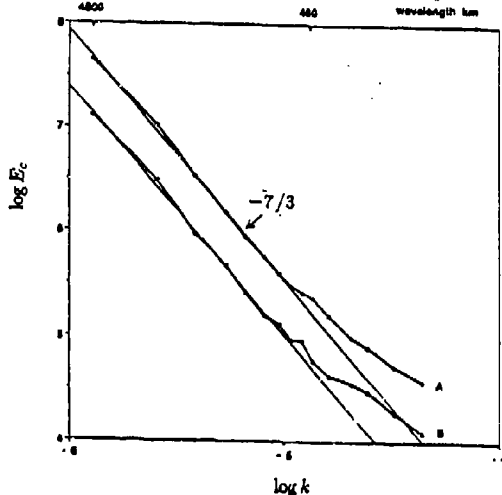


Figure 4. Temperature and kinetic energy spectra from GASP flights in stratosphere: A-kinetic energy, B - temperature. Adapted from [16].

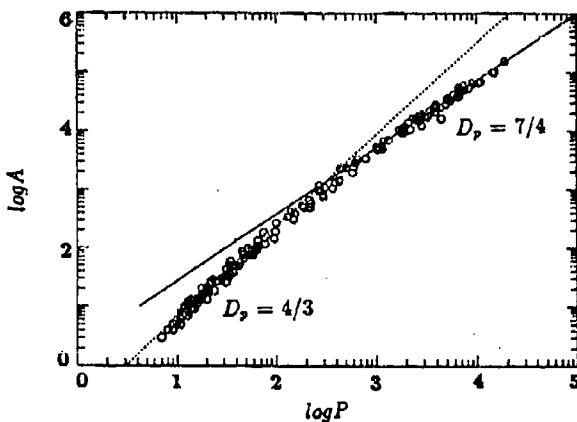


Figure 5. The crossover from isotropic cloud growth to restricted growth in a layer

(cf. with Fig. 2). Adapted from [3].

## 4 Discussion

The differences in the properties of free and of layer turbulent percolation cannot be understood without taking into account the differences in their topology. For three-dimension percolation clusters, due to the *multiconnected topology* of their external boundary, it was argued in [17],[18] that the fractal dimensions of the cluster and its external *hull* are the same. On the other hand, for two-dimensional percolation cluster these fractal dimensions are different. In the last case the fractal dimension of the hull  $D_h = 1 + 1/\nu$  [19], i.e for  $\nu = 4/3$   $D_h = 7/4$ . Thus, the topological restriction in layer (with  $D_\nabla < 9/4$ ) suppresses the topological instabilities (Section 2) and leads to coincidence of  $D_\nabla$  for layer percolation and  $D_h$  for two-dimensional percolation.

Following this logic, one may expect that increasing of the external magnetic field (the topological restriction in our experiment with mercury, see above), should lead to transition from spectrum (7) (Fig. 3b,  $B \simeq 0.2T$ ) to spectrum (9). Indeed, Fig. 6 shows the spectrum of temperature fluctuations at strong magnetic field ( $B \simeq 1T$ ) in the experiment and straight line is drawn for comparison with (9).

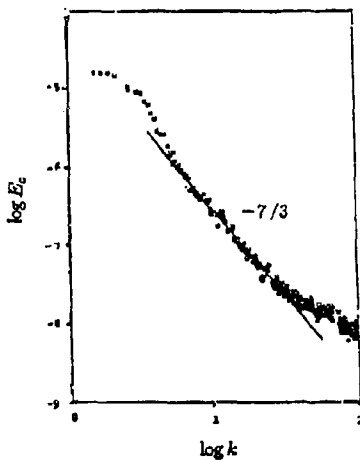


Figure 6. Temperature spectrum for the same flow as in Fig. 3a,b in strong magnetic field  $B \simeq 1T$  (strong restriction).

Authors are grateful to A.J. Chorin, and K.R. Sreenivasan for encouragement.

## References

- [1] A.Bershanskii, Sov. Phys. Usp., **33** (1990) 1073.
- [2] A.J.Chorin, J. Stat. Phys., **69** (1992) 67.
- [3] K.Nagel and E.Raschke, Physica A, **182** (1992) 519.
- [4] M.Schneider and T.Wohlke, Physica A, **189** (1992) 1.
- [5] J.C.Vassilicos, In "Advances in turbulence", **2**, eds. H.H.Fernholz and H.E.Fiedler, 404 (Springer, Berlin, 1989).
- [6] J.K.Vassilicos and J.C.R.Hunt, Proc. Roy. Soc., A, **435** (1991) 505.
- [7] G.D.Nastrom, W.H.Jasperson, and K.S.Gage, J. Geophys. Res., D, **91** (1986) 13201.
- [8] S.Lovejoy, Science, **216** (1982) 185.
- [9] D.Stauffer, and A.Aharony, Introduction to Percolation Theory, (Taylor and Francis, London 1992).
- [10] A.Bershanskii, E.Kit and A.Tsinober, Proc.Roy. Soc. A, **441** (1993) 147.
- [11] A.Bershanskii, and A.Tsinober, Phys. Rev. E, **48** (1993) 282.
- [12] H.K.Moffatt, and A.Tsinober, Annu. Rev. Fluid Mech., **24** (1992) 281.
- [13] A.S.Monin, and A.M.Yaglom, Statistical Fluid Mechanics, bf 2, (MIT Press, Cambridge, 1975).
- [14] H.Branover, A.Bershanskii, A.Eidelman, and M.Nagorny, Boundary-Layer Meteorology, **62** (1993) 117.
- [15] H.Branover, and S.Sukoryansky, Progr. in Astro. and Aeronautics, **112** (1988) 87.
- [16] K.S.Gage, and G.D.Nastrom, J. Atm. Sci., **43** (1986) 729.
- [17] D.Stauffer, Phys. Rep., **54** (1979) 2.
- [18] P.N.Strenski, R.M.Bradley and J.M.Debierre, Phys. Rev. Lett., **66** (1991) 1330.
- [19] H.Saleur and B.Duplantier, Phys. Rev. Lett., **58** (1987) 2325.
- [20] A.G.Bershanskii, Atm. and Oceanic Physics, **27** (1991) 475.
- [21] A.Bershanskii, and A.Tsinober, Phys. Lett. A, **165** (1992) 37.

## Appendix

It is very difficult to measure the fractal characteristics of the passive scalar in the mercury. However, we can use the measurements of probability distributions to obtain these characteristics. Indeed, it has been introduced in [20] (see also [21]) the probability density distribution,  $\rho(l)$  ( $l = r/R$ ), of active turbulent regions of scale  $r$  ( $R$  is external scale). The perimeter of the active turbulent subregions takes the form

$$P = \int_{\eta/R}^1 l \rho(l) dl. \quad (12)$$

If  $\rho(l) \propto l^{-x}$ , then (12) gives (for  $x > 2$ ):  $P \propto (R/\eta)^{x-2}$ . We can relate  $D_p$  to exponent  $x$  using well known relationship  $P \propto (R/\eta)^{D_p-1}$ :  $x = D_p + 1$ . On the other hand, one can estimate the scaling for large concentration of energy dissipation  $\epsilon$  using  $D_p$  [21]:  $\epsilon(l) \propto l^{2-D_p}$  and relate the probability density distributions  $p(\epsilon)$  and  $p(l)$ :  $p(\epsilon) \propto |dl/d\epsilon| \rho(l) \propto \epsilon^{-a}$ , where

$$a = 1 + \frac{D_p}{2 - D_p}. \quad (13)$$

The Fig. 7 shows probability distribution  $Pr(\epsilon) = \int_{\epsilon}^{\infty} p(\epsilon) d\epsilon \propto \epsilon^{a-1}$  obtained in the same experiment as Fig. 3b. We infer from the Fig. 7:  $a \approx 6$ , i.e.  $D_p \approx 5/3$  (13) (cf. with sections 1 and 2).

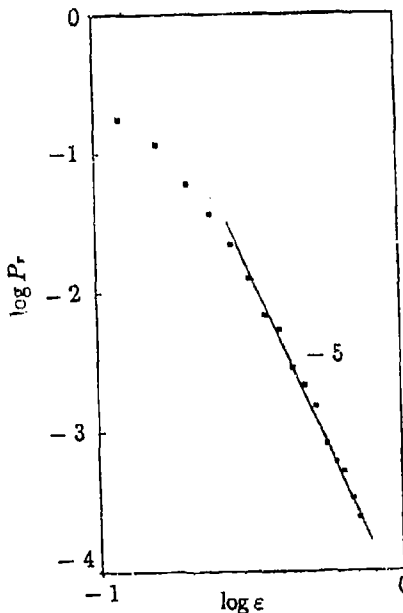


Figure 7. Probability distribution of  $\epsilon$  for the same flow as in Fig. 3b. ( $B \approx 0.2T$ ).

# Turbulence Produced by Internal Waves in the Oceanic Thermocline at Mid and Low Latitudes

M. C. GREGG, D. P. WINKEL, T. B. SANFORD

*University of Washington, Seattle, WA, USA*

H. PETERS

*State University of New York at Stony Brook, Stony Brook, N.Y., USA*

When mid-latitude internal waves are at the background state modeled by *Garrett and Munk* [1975], wave-wave interactions produce weak turbulence compared to buoyant restoring forces. Consequently, high wavenumber spectra contain only the viscous decay portion of the universal turbulent spectrum. Increases in low-wavenumber shear above background produce proportionately more intense turbulence, which can result in well-developed inertial subranges. The wave and turbulent regions of the vertical spectrum are separated by a  $k_3^{-1}$  rolloff that does not vary with the amplitude of low-wavenumber shear, indicating that the wave field is saturated. At low latitudes, internal wave shear is generally more intense than at mid latitudes, but the turbulence is similar to that found with mid-latitude waves at background. Kinematically, this anomaly results from steeper slope in the rolloff range.

## OBSERVATIONS AND ANALYSIS

The Multi-Scale Profiler (MSP) carries three sets of sensors -- electromagnetic, acoustic, and airfoil -- to measure eastward,  $u$ , and northward,  $v$ , velocities over wavelengths from 1000 m to 10 mm. Before calculating spectra, we subtract the ensemble average profiles,  $\bar{u}(x_3)$  and  $\bar{v}(x_3)$ , and apply the Hann filter. Velocity spectra,  $\Phi_{VEL}(k_3) \equiv \Phi_u(k_3) + \Phi_v(k_3)$ , are converted to shear spectra and normalized to form spectra of the gradient Froude number,  $\Phi_{Fr}(k_3) \equiv (2\pi k_3)^2 \Phi_{VEL}(k_3) N^{-2}$ . Vertical wavenumber,  $k_3$ , is the reciprocal of wavelength in cycles per meter (cpm), and  $N$  is the buoyancy frequency.

Integration gives the cumulative shear variance,

$$Fr^2(k_3) \equiv \int_{k_0}^{k_3} \Phi_{Fr}(m) dm. \quad (1)$$

Term  $\delta$  the Froude function,  $Fr^2 = 4$  when the rms gradient Richardson number is  $1/4$ .

Profiles of the viscous dissipation rate,  $\epsilon$ , are calculated by integrating spectra taken over successive blocks of 50 kPa or 100 kPa (0.5 m or 1 m). For transverse velocities assumed to be isotropic,

$$\epsilon = 7.5\nu \int_{k_0}^{k_u} (2\pi k_3)^2 \Phi_{VEL}(k_3) dk_3 [W kg^{-1}], \quad (2)$$

where  $k_0 = 1$  cpm or 2 cpm, and  $k_u$  is determined empirically where the spectrum is either resolved or noisy.

As a reference for background internal waves, we use the *Garrett and Munk* [1975] modification known as GM76 and described by *Gregg and Kunze* [1991]. Except for small changes in shape at low wavenumber, the Froude form of GM76 is independent of  $N$ . When internal waves are the only process affecting the profile, the strain spectrum is  $\Phi_{St}(k_3) \equiv (2\pi k_3)^2 \Phi_{\sigma\theta}(k_3) / (\partial\sigma\theta/\partial x_3)^2$ , where  $\sigma\theta$  is potential density. At all wavenumbers,  $\Phi_{St}^{GM76} = \Phi_{Fr}^{GM76}/3$ ,

consistent with a free wave with a frequency  $1.4f$ .

For high wavenumbers we use the turbulent velocity spectra of Nasmyth (published by Oakey [1982]) and of Panchev and Kesich [1969]. The shear form of the velocity spectrum peaks at  $0.16k_\nu$ , where  $k_\nu \equiv (2\pi)^{-1}(\epsilon/\nu^3)^{1/4}$  is the viscous, or Kolmogorov, wavenumber in cyclic units. For the turbulent scalar spectrum we use Batchelor [1959].

#### THE MID-LATITUDE BACKGROUND STATE

During PATCHEX in October 1986, we observed internal waves close to GM76 at  $34^\circ\text{N}$ ,  $127^\circ\text{W}$  in the eastern north Pacific [Gregg and Sanford, 1988]. Turbulence occurred intermittently in thin patches and is averaged over 0.05 MPa (5 m) in Figure 1 and subsequent profiles.

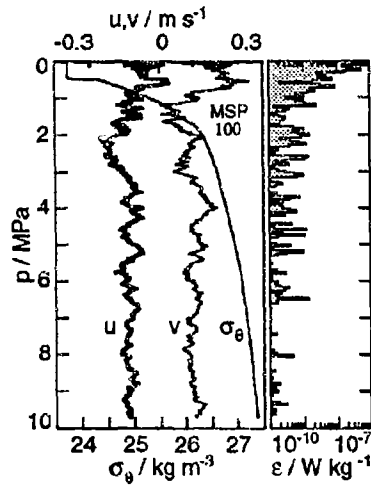


Fig. 1. Typical PATCHEX profile. Zero velocity is arbitrary in this and other profiles except TH 2.

Averaging the ensemble of 28 profiles gives

$$\bar{\epsilon} \equiv 7 \times 10^{-10} N^2 N_0^{-2} [\text{W kg}^{-1}], \quad (3)$$

very close to Henyey *et al.* [1986], who calculated the average energy flux from low to high wavenumbers in a random field of large-scale waves having the background spectrum formulated by Munk [1981]. Ray tracing followed the evolution of intermediate-scale test waves until their wavenumber grew to 0.2 cpm, when their energy was treated as irreversibly headed

for dissipation. Henyey *et al.* [1986] also developed an analytical model as a check on the numerical calculations. Both models predict  $\epsilon \propto N^{-2}$ , as does a separate calculation by McComas and Müller [1981]. The Henyey *et al.* [1986] amplitude also agrees with (3) when referenced to GM76 instead of Munk [1981]. Munk's formulation decreases the shear variance by  $\pi/2$  relative to GM76, a consequence that was not intended and is not called for by observations [W. Munk, personal communication 1990].

Osborn [1980] estimates diapycnal diffusivity as

$$K_\rho \leq 0.2\epsilon N^{-2} [\text{m}^2 \text{s}^{-1}]. \quad (4)$$

Using (3) for  $\epsilon$  gives  $K_\rho \leq 5 \times 10^{-6} \text{ m}^2 \text{s}^{-1}$ , constant with depth and 30 times  $\kappa_T$ , the molecular diffusivity. The North Atlantic Tracer Release Experiment (NATRE) seems to be confirming (4) by comparing it with diffusivity

from the thickening of thin tracer layers. The most recent results are  $K_\rho = 1.1 \times 10^{-5} \text{ m}^2 \text{s}^{-1}$  from the tracer [Ledwell *et al.*, 1994] and the microstructure survey [Schmitt *et al.*, 1994].

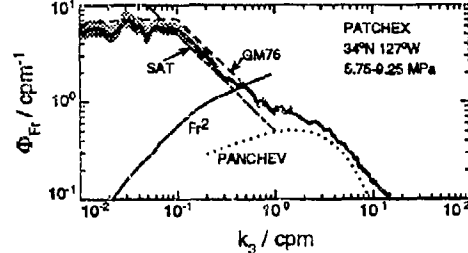


Fig. 2. Froude spectrum for PATCHEX.

The average PATCHEX spectrum is nearly flat for  $k_3 < 0.1 \text{ cpm}$  (Fig. 2). A slope of  $k_3^0$  is consistent with a shear field of many uncorrelated waves. In spite of thermohaline intrusions dominating higher wavenumbers, strain spectra can be formed at low wavenumbers and are very close to the GM76 shear-to-strain ratio. The internal wave spectrum cuts off at  $k_C = 0.1 \text{ cpm}$  and then decreases as  $k_3^{-1}$  until 1 cpm. The inflection near 1 cpm corresponds to the largest overturning scales and is the beginning of the turbulent range. The av-

Data	$10^3 N$ $s^{-1}$	$\epsilon$ $W kg^{-1}$	$K_p$ $m^2 s^{-1}$
P	3.0	$1.7 \times 10^{-10}$	$3.9 \times 10^{-6}$
Pn	3.2	$1.9 \times 10^{-9}$	$3.9 \times 10^{-5}$
FS1	12.5	$1.1 \times 10^{-8}$	$1.4 \times 10^{-5}$
FS2	5.4	$2.9 \times 10^{-8}$	$2.0 \times 10^{-4}$
FS3	4.3	$5.8 \times 10^{-9}$	$6.1 \times 10^{-5}$
FS4	5.0	$5.0 \times 10^{-9}$	$4.0 \times 10^{-5}$
FS5	5.0	$5.0 \times 10^{-9}$	$4.0 \times 10^{-5}$
FS6	5.5	$3.8 \times 10^{-9}$	$2.6 \times 10^{-5}$
FS7	4.5	$1.0 \times 10^{-8}$	$1.0 \times 10^{-4}$
TH11.4°N	2.9	$8.0 \times 10^{-11}$	$1.9 \times 10^{-6}$
TH2°N	2.7	$1.3 \times 10^{-10}$	$3.5 \times 10^{-6}$
TH1°N	2.8	$7.0 \times 10^{-11}$	$1.8 \times 10^{-6}$
TH0°	2.9	$2.2 \times 10^{-10}$	$5.8 \times 10^{-6}$
C1.7°S	2.8	$2.2 \times 10^{-10}$	$5.8 \times 10^{-6}$
C0°	2.8	$1.7 \times 10^{-10}$	$4.4 \times 10^{-6}$
C3°N	2.9	$7.0 \times 10^{-11}$	$1.7 \times 10^{-6}$

TABLE 1. Stratification and turbulence.

verage  $\epsilon$  in Table 1 gives 14.1 cpm for  $k_v \equiv (2\pi)^{-1}(\epsilon/\nu^3)^{1/4}$ , the viscous, or Kolmogorov, wavenumber in cyclic units. The universal shear spectrum peaks at  $0.16k_v = 2.3$  cpm.

The  $k_3^{-1}$  rolloff is close to the internal wave rolloff in the stratosphere. Rather than being broadband and random like oceanic internal waves, stratospheric waves usually have very narrow bandwidth in frequency and wavenumber. Generated at the top of the troposphere, they propagate upward, increasing in amplitude as the air thins. Two explanations have been advanced for the uniform rolloff at  $k_3 > k_C$ . The saturated hypothesis holds that the waves become unstable at  $k_C$  and break by shear instability and convective overturning at higher wavenumbers [Dewan and Good, 1986]. For a single wave, Smith *et al.* [1987] model the saturated spectrum as  $\Phi_{Fr}^{SAT} = 0.5k_3^{-1}$ , which is shown on our spectra. Fritts [personal communication, 1991] believes that the waves begin to lose energy at  $k_C$ , but breaking begins at higher numbers, perhaps  $2\pi k_C$ . The second explanation is advanced by Hines [1991a], who argues that the waves do not become unstable at  $k_C$ . Instead, energy is shifted to higher wavenumbers by strong Doppler shifting until the waves eventually break. Hines [1991b] develops a spectrum that asymptotically approaches  $k_3^{-1}$ .

Plotted in Figure 2,  $Fr^2 = 0.52-0.64$  for  $k_C$

= 0.09-0.11 cpm. Thus, there is no reason to suspect widespread shear instability at the cut-off wavenumber. Forming the probability distribution of  $Fr^2$  by first-differencing velocity profiles over 10 m and using constant  $N^2$  gives only 0.2% with  $Fr^2 > 4$  [Gregg *et al.*, 1993]. Owing to many thermohaline intrusions, we cannot directly compute overturning scales,  $l$ . Other observations [Dillon, 1982; Peters *et al.*, 1988], are consistent with  $l = (\epsilon/N^3)^{1/2}$ , the scaling developed by Ozmiodov [1965] for overturns limited by stratification. Using (3) gives  $l = 0.07(N/N_0)^{-1/2} = 0.094$  m. The  $\epsilon$  distribution is approximately lognormal and thus highly skewed. Consequently, the larger  $\epsilon$ 's are produced by overturns exceeding 0.1 m, but visual inspection shows about 1 m as the largest overturning scale. Because the form of saturation producing the rolloff does not produce significant wave breaking, we conclude that Hines's approach is more likely than the instability models to explain oceanic spectra.

#### MID-LATITUDE ANOMALIES

The PATCHEX north profiles were taken at 42°N, 126°W in a coastal jet off California. Although the jet was above 1 MPa, velocity and dissipation are larger than PATCHEX throughout the profile (Fig. 3). For example, the av-

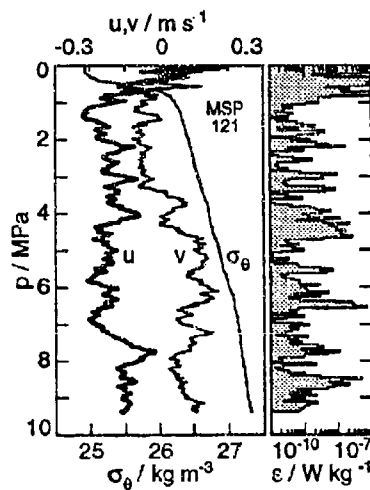


Fig. 3. Typical PATCHEX north profile.

erage  $\epsilon$  is more than ten times PATCHEX, giv-

ing  $K_p = 3.9 \times 10^{-5} \text{ m}^2 \text{ s}^{-1}$ . (Tbl. 1). Using PATCHEX north as the most energetic example, Gregg [1989] expressed the average dissipation rate in terms of the increased shear as

$$\epsilon = 7 \times 10^{-10} (N^2/N_0^2) (S_{10}^4/S_{10GM76}^4) . \quad (5)$$

$S_{10}$  is the 10-m first-difference shear corrected for attenuation by the first-difference filter. The expression is adapted from Henyey *et al.* [1986] to use shear, which is measured well by MSP, instead of kinetic energy, which is not measured well.

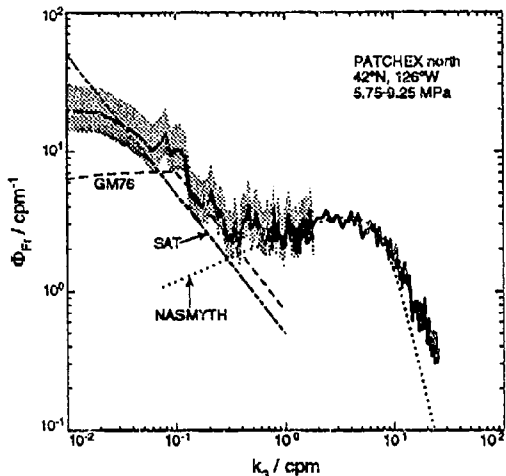


Fig. 4. Froude spectrum for PATCHEX north.

The Froude spectrum for PATCHEX north is 5 GM76 at 0.01 cpm and slopes steadily downward until it intersects an extension of the  $k_3^{-1}$  GM76 rolloff somewhat below 0.1 cpm (Fig. 4). Owing to the irregular shape, the beginning of the rolloff cannot be defined visually. For GM76,  $k_C = 0.1 \text{ cpm}$  and  $Fr^2(k_C) = 0.7$ . For PATCHEX north the closest estimate to  $Fr^2 = 0.7$  gives  $k_C = 0.04 \text{ cpm}$ . The turbulent spectrum begins at 0.4 cpm, where  $Fr^2 = 2.5$ , and is moderately well-developed with a distinct inertial subrange.

To observe internal waves in strong mean shear and near topography, in June 1990 we took stations across the Florida Strait at 27°N (Fig. 5). The Gulf Stream was centered on Stn. 3 near 0.5 MPa. At each station we took

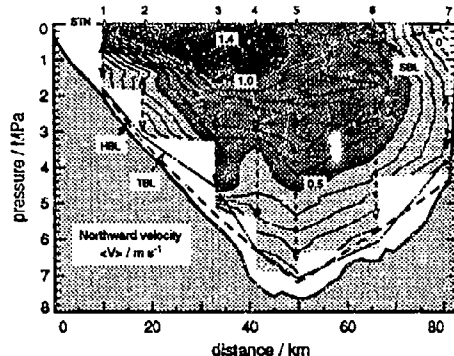


Fig. 5. Florida Strait stations, June 1990. Contours show average northward velocity in  $\text{m s}^{-1}$ . Labeled dashed lines are the maximum depth of the surface boundary layer (SBL) and the maximum heights of the homogenous bottom layer (HBL) and the turbulent bottom layer (TBL). Vertical dashed lines show where the spectra were taken.

about 10 profiles, each to within 5 m of the bottom. Most drops ended in sections of continuous strong turbulence much thicker than the homogenous bottom boundary layer (Fig. 7).

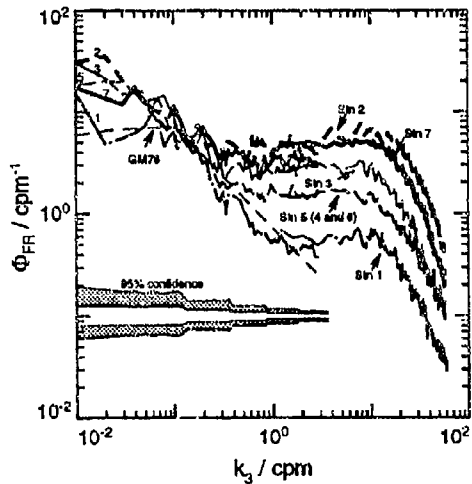


Fig. 6. Froude spectra from the Florida Straits.

Spectra taken below the core of the stream vary by factors of 2-3 at low wavenumbers and 10 at high wavenumbers (Fig. 6). All except Stn. 1 lie well above GM76 and cutoff where they intersect the GM76  $k_3^{-1}$  rolloff extended to lower wavenumbers. Considering the different circumstances, the similarity of the rolloff

to those of PATCHEX and PATCHEX north demonstrates that it is a very robust feature. The rolloff follows GM76 until the beginning of

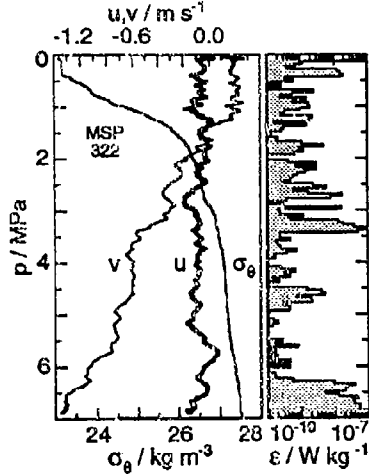


Fig. 7. Profile at Florida Strait Stn. 4. High  $\epsilon$  at the bottom extends well into the stratified section above the homogenized bottom boundary layer.

the turbulent range.

Stations 2 and 7 are the most energetic at low wavenumbers and have inertial subranges spanning a decade. Their strong turbulence produces  $K_\rho = (1-2) \times 10^{-4} \text{ m}^2 \text{ s}^{-1}$ . Observed  $\epsilon$ 's are within a factor of two of (5) in the center of the strait, but are factors of 5-10 times higher near the sides. Correcting with the shear-to-strain ratio as proposed by Polzin [1993] does not help. It appears, therefore, that the elevated  $\epsilon$  is not simply related to the shear variance.

#### LOW-LATITUDE ANOMALIES

During TROPIC HEAT 2 we profiled between  $11.4^\circ\text{N}$  and  $0^\circ$  near  $140^\circ\text{W}$ . Shears were several times GM76 but much less than predicted by Munk [1981]. At  $140^\circ\text{W}$  the internal waves are superimposed on 'deep jets' below the undercurrent (Fig. 8). The jets have magnitudes of  $\pm 0.1 \text{ m s}^{-1}$  and are about 150 m thick.

As a function of vertical wavenumber and frequency,  $\Phi_{Fr}^{\text{GM76}}(k_3, \omega)$  is proportional to  $f\omega^{-3}$  ( $\omega^2 - f^2)^{1/2}$ , where  $f$  is the Coriolis parameter. Integrating over  $\omega$  from  $f$  to  $N$  removes

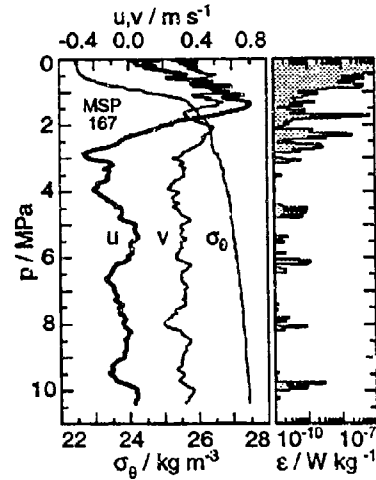


Fig. 8. TROPIC HEAT 2 profile on the equator. The Equatorial Undercurrent is centered at 1.5 MPa.

the  $f$  dependence, making  $\Phi_{Fr}^{\text{GM76}}(k_3)$  independent of  $f$ . To account for decreased coherences observed near the equator, Munk [1981] made  $\Phi_{Fr}^{\text{M81}}(k_3, \omega)$  proportional to  $(\omega^2 - f^2)^{1/2}\omega^{-3}$ , so that integrating makes  $\Phi_{Fr}^{\text{M81}}(k_3) \propto f^{-1}$ . Munk, therefore, predicts shear variances of 14 GM76 at  $2^\circ$  and 29 GM76 at  $1^\circ$ .

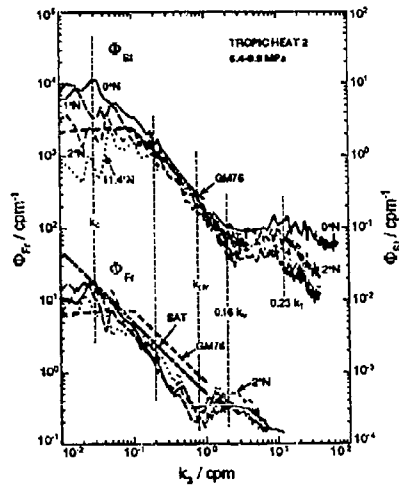


Fig. 9. TROPIC HEAT 2 spectra.

TROPIC HEAT 2 Froude spectra from  $11.4^\circ\text{N}$ ,  $2^\circ\text{N}$ ,  $1^\circ\text{N}$ , and  $0^\circ\text{N}$  differ less than a factor of two at all wavenumbers (Fig. 9). At low

wavenumbers they are 1.5–2 GM76, much less than predicted by *Munk* [1981]. The spectra are also more peaked than mid-latitude spectra, indicating that the wave field may have a narrower bandwidth. For  $k_3 > k_C \approx 0.03$  cpm, the spectra rolloff along  $\Phi_{Fr}^{SAT}$  or slightly below. Near 0.2 cpm the slope steepens to approximately  $k_3^{-1.4}$ . The steep rolloff produces a more distinct rise into the turbulent range. The dissipation rates give  $K_p$  within a factor of two of PATCHEX (Table 1).

Because these profiles lack thermohaline intrusions, strain can be obtained from temperature. For  $k_3 < k_C$ , the strain spectra are approximately flat and vary in amplitude from 3 GM76 at 11.4°N to 1/3 GM76 at 0°N (Fig. 9). If one wave frequency dominates the low wavenumbers, as seems likely owing to the peaked spectra, the shear-to-strain ratios correspond to average frequencies of 1.10f at 11.4°N, 1.27f at 2°N, and 1.7f at 1°N. *Eriksen* [1993] obtains a similar latitudinal variation in average frequency from calculations of the response of the equatorial ocean to rapidly moving wind bursts.

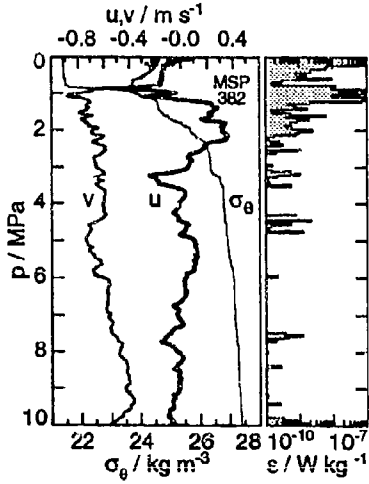


Fig. 10. COARE 3 profile at 0°. The Equatorial Undercurrent is centered at 2.5 MPa.

Changes in slope of  $\Phi_{St}$  match features in  $\Phi_{Fr}$ . Between  $k_C$  and 0.2 cpm, where  $\Phi_{Fr}$  follows  $\Phi_{Fr}^{SAT}$ , the strain spectra transition to the rolloff. At 0.2 cpm, where the  $\Phi_{Fr}$  rolloff steepens,  $\Phi_{St}$  rolls off close to GM76 but with

slightly steeper slope. The strain rolloff ends at 0.16  $k_\nu$ , the peak of the turbulent range in  $\Phi_{Fr}$ . The turbulent range approximates the scalar spectrum derived by *Batchelor* [1959].

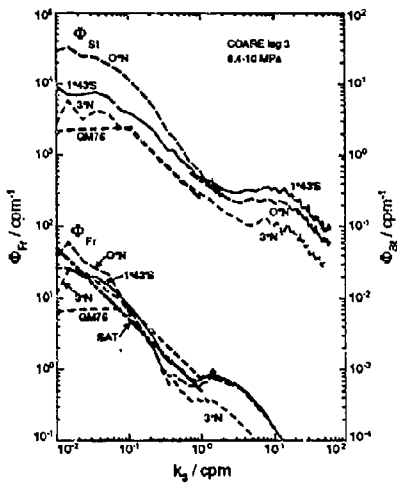


Fig. 11. Froude spectra for COARE 3.

During COARE 3 we profiled along 156°E. The profiles are roughly similar to those at 140°W (Fig. 10). At low wavenumbers the Froude spectra are more energetic than those from 140°W, and their rolloffs begin at higher wavenumbers, closer to the GM76 rolloff extended to low wavenumbers than to  $\Phi_{Fr}^{SAT}$  (Fig. 11). Otherwise the rolloff and turbulent ranges are similar to those for TROPIC HEAT 2, so that  $K_p$  again is no larger than PATCHEX.

The COARE 3 strain spectra are elevated even more than  $\Phi_{Fr}$ , particularly at 0°, where the rolloff remains twice GM76. *C. Eriksen* [personal communication, 1994] predicted preferential elevation of  $\Phi_{St}$  compared to  $\Phi_{Fr}$  as a consequence of the  $\beta$  effect on near-equatorial responses to wind forcing.

## DISCUSSION

Variations in turbulent production result from changes in wave-wave interactions with variations in spectral amplitude and shape. The present procedure for mid latitudes requires assuming that  $\epsilon$  depends only on total shear variance, presumably to  $k_C$ , and perhaps with correction for shifts in the average frequency of

the wave field. These are empirical results that breakdown when extended from mid to low latitudes, as shown vividly in Figures ?? and 13.

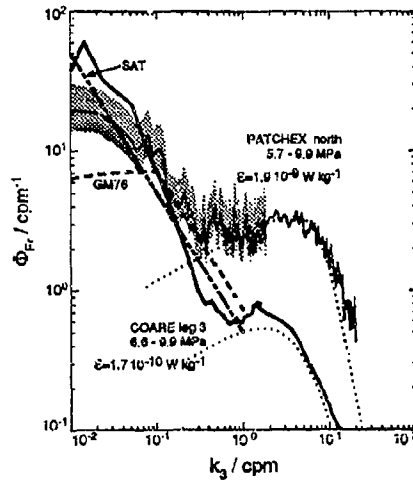


Fig. 12. Froude spectra for PATCHEX north and COARE3 0°N.

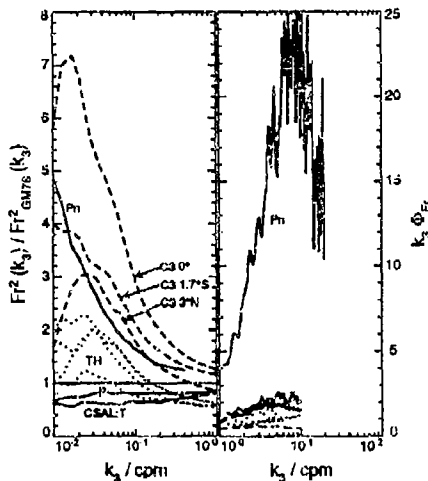


Fig. 13. Froude functions normalized by GM76 are shown on the left, and variance-preserving dissipation spectra are on the right.

In the former, COARE 3 drops from 2-3 times PATCHEX north for  $k_3 < 0.1$  cpm to 1/5 in the turbulent range. One possibility is that the COARE 3 internal wave field may contain only a few dominant waves rather than continuous distributions in wavenumber and frequency. If so, the steep rolloff may simply be envelope

of the narrowband distribution, and  $\epsilon$  may be lower because there are fewer and weaker interactions. In Figure 13 several other curves are closer to unity at 0.01 cpm and peak between 0.02-0.03 cpm, indicating that this may be a general condition at low latitudes. In any event if shear variance is the sole factor responsible for producing turbulence, it does not work in the same way everywhere or there would not be essentially two dissipation spectra on the right for such a varied range on the left.

These anomalous results also reveal the limitations of statistical approaches to wave-wave interactions. Our ensemble-averages were obtained by sampling sites for one to twelve days. The data are relatively stationary because at most places the internal wave field evolves slowly, allowing time for adequate sampling. In addition to lacking the three-dimensional structure of the wave field, we have not observed the evolution of internal wave field. Only then will we really be able to understand the dynamics producing turbulence. In the interim, calculations of interaction rates with altered spectra would be helpful. Henyey *et al.* [1986] simulated variations in wave energy level by changing the dimensionless energy density in Munk [1981] while retaining the canonical shape. A good start would be to do similar calculations with varied shapes, including narrow band fields that are not separable, i.e. ones with wavenumber distributions varying with frequency.

*Acknowledgments.* The Office of Naval Research and the National Science Foundation funded the collection and analysis of these observations.

#### REFERENCES

- Batchelor, G. K., Small-scale variation of convected quantities like temperature in turbulent fluid, *J. Fluid Mech.*, **5**, 113-139, 1959.
- Dewan, E. M., and R. E. Good, Saturation and the 'universal' spectrum for vertical profiles of horizontal scalar winds in the atmosphere, *J. Geophys. Res.*, **91**, 2742-2748, 1986.
- Dillon, T. M., Vertical overturns: A comparison of Thorpe and Ozmidov length scales, *J. Geophys. Res.*, **87**, 9601-9613, 1982.
- Eriksen, C. C., Equatorial ocean response to rapidly translating wind bursts, *J. Phys. Oceanogr.*, **23**, 1208-1230, 1993.
- Gargett, C. J. R., and W. H. Munk, Space-time scales of internal waves: A progress report, *J.*

*Geophys. Res.*, 80, 291-297, 1975.

Gregg, M., Scaling turbulent dissipation in the thermocline, *J. Geophys. Res.*, 94, 9686-9698, 1989.

Gregg, M., and E. Kunze, Shear and strain in Santa Monica Basin, *J. Geophys. Res.*, 96, 16,709-16,719, 1991.

Gregg, M., and T. Sanford, The dependence of turbulent dissipation on stratification in a diffusively stable thermocline, *J. Geophys. Res.*, 93, 12,381-12,392, 1988.

Gregg, M., H. Seim, and D. Percival, Statistics of shear and turbulent dissipation profiles in random internal wave fields, *J. Phys. Oceanogr.*, 23, 1777-1799, 1993.

Henyey, F. S., J. Wright, and S. M. Flatté, Energy and action flow through the internal wave field, *J. Geophys. Res.*, 91, 8487-8495, 1986.

Hines, C. O., The saturation of gravity waves in the middle atmosphere. Part I: Critique of linear-instability theory, *J. Atmos. Sci.*, 48, 1348-1359, 1991a.

Hines, C. O., The saturation of gravity waves in the middle atmosphere. Part II: Development of Doppler-spread theory, *J. Atmos. Sci.*, 48, 1360-1379, 1991b.

Ledwell, J. R., A. J. Watson, and C. S. Law, Tracer dispersion during the North Atlantic Tracer Experiment (NATRE), *Eos*, 75S, 121, 1994.

McComas, C. H., and P. Müller, The dynamic balance of internal waves, *J. Phys. Oceanogr.*, 11, 970-986, 1981.

Munk, W. H., Internal waves and small-scale processes, in *Evolution of Physical Oceanography*, edited by B. A. Warren and C. Wunsch, 264-291, MIT Press, Cambridge, MA, 1981.

Oakey, N. S., Determination of the rate of dissipation of turbulent energy from simultaneous temperature and velocity shear microstructure measurements, *J. Phys. Oceanogr.*, 12, 256-271, 1982.

Osborn, T. R., Estimates of the local rate of vertical diffusion from dissipation measurements, *J. Phys. Oceanogr.*, 10, 83-89, 1980.

Ozmidov, R. V., On the turbulent exchange in a stably stratified ocean, *Izv., Atmos. Oceanic Phys.*, 1, 853-860, 1965.

Panchev, S., and D. Kesich, Energy spectrum of isotropic turbulence at large wavenumbers, *Comptes rendus de l'Académie bulgare des Sciences*, 22, 627-630, 1969.

Peters, H., M. Gregg, and J. Toole, On the parameterization of equatorial turbulence, *J. Geophys. Res.*, 93, 1199-1218, 1988.

Polzin, K. L., *Observations of turbulence, internal waves and background flows: An inquiry into the relationships between scales of motion*, Ph.D. thesis, Woods Hole Oceanog. Inst./MIT, 1993.

Schmitt, R. W., K. L. Polzin, and J. M. Toole, A comparison of direct turbulence measurements with tracer dispersion in the North Atlantic Tracer Release Experiment, *Eos*, 75S, 130, 1994.

Smith, S. A., D. C. Fritts, and T. E. VanZandt, Evidence for a saturated spectrum of atmospheric gravity waves, *J. Atmos. Sci.*, 44, 1404-1410, 1987.

## Geostrophic Adjustment: Frontogenesis and Energy Conversion

WILLIAM BLUMEN

Astrophysical, Planetary and Atmospheric Sciences Department  
University of Colorado  
Boulder, CO 80309

RONGSHENG WU

Department of Atmospheric Sciences  
Nanjing University  
China

R. T. WILLIAMS

Department of Meteorology  
Naval Postgraduate School  
Monterey, CA 93943-5114

### ABSTRACT

Nonlinear geostrophic adjustment is examined with a Boussinesq model. The motion is restricted to a two-dimensional channel in the horizontal and vertical  $x, z$  plane; the fluid is in uniform rotation, is stably stratified, inviscid and incompressible. The flows considered fall under two classes: zero and uniform potential vorticity flows. Steady geostrophic flow fields are determined from initial mass imbalances, represented by an antisymmetric density anomaly that varies along the  $x$ -axis. The distinguishing characteristic of the solutions is the development of a front, defined as a zero-order discontinuity in both density and geostrophic velocity at both vertical boundaries. The condition for a front to form is expressed in terms of a Rossby number, based on the spatial gradient of the initial density anomaly, and on a Froude number.

The relative amounts of kinetic  $\Delta KE$  and potential energy  $\Delta PE$  partitioned to the geostrophic flow field by the redistribution of mass is represented by  $\gamma = \Delta KE / \Delta PE$ . Zero potential vorticity flow is characterized by  $\gamma = 1/2$ , and there is a smooth transition from  $\gamma = 1/2$  to  $\gamma = 1/3$  for uniform potential vorticity flow, when the initial mass imbalance approaches a step function distribution.

## 1. Introduction

The adaptation of an unbalanced mass and/or momentum distribution in rotating fluid to a state of geostrophic balance is referred to as *the geostrophic adjustment problem*. The prototype for this process was formulated by Rossby (1937, 1938), who examined the adaptation of the sea surface following a wind gust that imparted an initial momentum imbalance by a surface stress. Ou (1984) later demonstrated that a by-product of the geostrophic adjustment of an initial mass imbalance is the formation of zero-order discontinuities at level boundaries-fronts in both the density and velocity fields.

The present talk focuses on two aspects of geostrophic adjustment: frontogenesis and partition of energy between kinetic and potential energies of the balanced state. A front may only occur if the gradient of the initial density anomaly is sufficiently large. The critical value may be expressed in terms of a Rossby number and a Froude number. These nondimensional numbers are, in effect, measures of the respective horizontal and vertical gradients of the initial density field. Although the relative amount of kinetic  $\Delta KE$  and potential  $\Delta PE$  energy partitioned to the balanced flow also depends on the initial mass distribution, perhaps a more distinctive characteristic of the fluid that determines the magnitude of  $\gamma = \Delta KE / \Delta PE$  is the potential vorticity of the flow. This distribution is emphasized by examination of both zero and uniform potential vorticity flow.

## 2. Model

The fluid is incompressible and stably stratified; the constant rotation rate is  $f/2$ , where  $f$  is the coriolis parameter; and the motion is assumed to vary only in the  $(x, z)$  plane, where  $x$  is horizontally directed and  $z$  is directed upward antiparallel to gravity  $g$ . This model has been examined by Ou (1984) in the context of the geostrophic adjustment problem. The basic equations may be expressed by three conservation principles, potential vorticity, linear momentum, incompressibility:

$$\frac{d}{dt} \left[ \left( f + \frac{\partial v}{\partial x} \right) \frac{\partial \rho}{\partial z} - \frac{\partial v}{\partial z} \frac{\partial \rho}{\partial x} \right] = 0, \quad (1)$$

$$\frac{d}{dt} (fx + v) = 0, \quad \frac{d \rho}{dt} = 0. \quad (2), (3)$$

Here  $d/dt = \partial/\partial t + u\partial/\partial x + w\partial/\partial z$ , where  $t$  denotes time,  $(u, w)$  are  $(x, z)$  velocity components, while  $v$  is directed cross-stream. The Boussinesq approximation has been introduced, and  $\rho$  is a nondimensional density defined as the ratio

$$\frac{\rho_{ref} - \rho(0)}{\rho(0)} = \rho, \quad (4)$$

where  $\rho_{ref}$  is the density and  $\rho(0)$  is a constant reference value. The fluid is assumed to be unbounded in  $|x|$  with rigid level surfaces at  $z = 0$  and at  $z = h$ .

It is possible to by-pass the initial-value problem to determine the final geostrophic state by making use of the conservation principles (1), (2) and (3). The tacit assumption, used by several investigators following Ro by's approach, is that the final state can be uniquely determined from the imposed initial state. There may, however, be situations when the *inviscid* conservation principles cannot be applied in this manner. The initial imbalance will generate gravity waves, for example, that may form hydraulic jumps where a local dissipative region occurs, or waves may overturn and dissipate energy. The conditions for these events to occur will not be examined in the present investigation.

It is convenient to use the scaling provided by Ou (1984), since his results will be rederived and compared with another class of flow. The nondimensional quantities are defined as:  $x = \lambda x'$ ,  $z = hz'$  and  $v = (g^* h)^{1/2} v'$ , where  $g^* = g \Delta \rho / \rho(0)$  denotes "reduced gravity",  $\Delta \rho$  is the characteristic amplitude of the density anomaly and  $\lambda = (g^* h)^{1/2} f^{-1}$  is the internal deformation radius.

The potential vorticity  $q_0$  is defined in (1), and there are three classes of flow that may be considered:

- 1) zero potential vorticity,  $q_0 = 0$
- 2) uniform potential vorticity,  $q_0 = \text{constant}$
- 3) nonuniform potential vorticity,  $q_0 = q_0(x_0, z)$ .

Only the first two classes will be investigated here. The method of solution is presented by Blumen and Wu (1994). The initial density anomaly is antisymmetric, and given by

$$\rho_0(x_0) = -\epsilon \text{Erf}(ax_0), \quad (5)$$

where  $\text{Erf}$  denotes the error function,  $\epsilon$  is an amplitude to be specified, the subscript denotes the initial state and the nondimensional inverse length scale is

$$a = (g^* h)^{1/2} / f a_D^{-1}. \quad (6)$$

The quantity  $a_D^{-1}$  is the dimensional length scale of the density anomaly and  $a$  in (6) may be associated with a Rossby number based on a velocity scale  $(g^* h)^{1/2}$ . The distribution represented by (5) is displayed in Figure 1 for  $\epsilon = 1/2$ .

Finally, the steady flow is both geostrophic and hydrostatic, and satisfies thermal wind balance

$$\partial_1 \partial_2 \cdots \partial_n \partial_1$$

17

### 3. Frontal formation

#### a. Zero potential vorticity flow

The zero potential vorticity solution is that of Oa (1964), but the initial density anomaly is (5). The geostrophic flow is given by

$$v = \left( \frac{1}{\epsilon} \right)^{1/2} \epsilon \frac{\partial \phi}{\partial y} \quad (8)$$

The transformation to  $(x, z)$  space is found from (2) and (8), expressed as

$$x = x_0 - \alpha z, \quad (9)$$

where  $\alpha$  is defined by (6). With  $\epsilon = 1/2$ , a front forms when  $\alpha = 2.03$ . The fields of  $(p, v)$  are displayed in Figure 2. Smaller values of  $\alpha$  would not lead to frontal formation; larger values would lead to a multi-valued density distribution. This latter situation, which would occur after frontal formation on the boundaries, is not a valid steady-state solution.

#### b. Uniform potential vorticity flow

This case is distinguished by  $q_0 = -1$ , with an initial state

$$p_0 = -z + p_0^*(x_0). \quad (10)$$

The quantity  $p_0^*(x_0)$  is also represented by (5), but in this case  $\epsilon = 1/4$ . The initial state and final state, when a front has formed, is displayed in Figure 3. The presence of stable stratification introduces a new parameter  $N$ , the Brunt-Väisälä frequency. The uniform potential vorticity solution is then characterized by two nondimensional parameters, the Rossby number (6) and the froude number

$F = (g^* h)^{1/2} / Nh$ . The solution presented in Figure 3 is characterized by  $F = 1$ . This case bears a closer resemblance to atmospheric fronts that are characterized by cold dense air that extends a few kilometers above the surface, although the upper boundary front would be absent in the atmosphere. Further details in the development of this solution are presented by Blumen and Wu (1994).

### 4. Energy ratios

The redistribution of the initial unbalanced density anomaly lowers the center of mass, and provides energy to transient and stationary motions. The quantity

$$\gamma = \Delta KE / \Delta PE \quad (11)$$

represents the ratio of the kinetic to potential energy partitioned to the stationary geostrophic solutions. The quantity  $\gamma$  has been determined for various model solutions, exhibiting an upper limit of 1/2, and a lower limit of 1/3 when the initial state exhibits a first-order discontinuity, e.g., Gill (1982). Blumen and Wu (1994) show that the potential vorticity framework provides a relatively simple way to connect diverse results that have appeared in the literature. Ou's (1986) demonstration that  $\gamma = 1/2$ , independent of  $a$ , applies only to the zero potential vorticity model. The solution presented by Blumen and Wu (1994), for uniform potential vorticity flow, is used to evaluate  $\gamma$ . It is shown that for large scales ( $a \rightarrow 0$ ),  $\gamma \rightarrow 1/2$ . [The same result would apply by letting the vertical density stratification vanish.] There is a monotonic decrease to  $\gamma = 1/3$  as  $a \rightarrow \infty$ , which is the limiting value for a discontinuous initial density distribution. An unusual aspect of this problem is the fact that the zero potential vorticity result  $\gamma = 1/2$  is independent of scale, while the energy ratio associated with uniform potential vorticity flow is both shape and scale dependent.

### 5. Remarks

There are a number of unanswered questions associated with the present results. These are associated with the time-dependent adaptation of the fluid, associated with inertia-gravity waves. The time evolutions are obtained by numerically integrating the model which is described by Williams *et al.* (1992). In the zero potential vorticity numerical experiments, a strong inertial oscillation is found in the horizontal velocity components. With the error function initial condition (5) in the density field, a discontinuity forms on the upper and lower boundaries whenever  $a \geq 2.03$ , which agrees with the steady state analysis in section 3. In addition, discontinuities are found for values of  $a$  as low as  $a = 1.6$ .

The stable stratification that exists in the uniform potential vorticity case does permit waves to propagate away indefinitely. A steady state could be realized, but the wave influence on frontal formation as a function of the Rossby and Froude numbers is being explored.

*Acknowledgements.* Financial support for this investigation for W. Blumen and R. Wu has been provided by the National Science Foundation under Grants INT-9113566 and ATM-9393111. R. Wu also acknowledges support by the National Science Foundation of China and Nanjing University. Financial support for R. T. Williams has been provided by the National Science Foundation under Grant ATM-9208751.

## REFERENCES

Blumen, W., and R. Wu, 1994: Geostrophic adjustment: Frontogenesis and energy conversion. *J. Phys. Oceanogr.*, under revision.

Gill, A. E., 1982: *Atmosphere-Ocean Dynamics*. Academic Press, 662 pp.

Ou, H. W., 1984: Geostrophic adjustment: A mechanism for frontogenesis. *J. Phys. Oceanogr.*, **14**, 994-1000.

\_\_\_\_\_, 1986: On the energy conversion during geostrophic adjustment. *J. Phys. Oceanogr.*, **16**, 2203-2204.

Rossby, C.-G., 1937: On the mutual adjustment of pressure and velocity distribution in simple current systems., 1. *J. Mar. Res.*, **1**, 15-28.

\_\_\_\_\_, 1938: On the mutual adjustment of pressure and velocity distribution in simple current systems., 2. *J. Mar. Res.*, **1**, 239-263.

Williams, R. T., M. S. Peng and D. A. Zankofski, 1992: Effects of topography on fronts. *J. Atmos. Sci.*, **49**, 287-305.

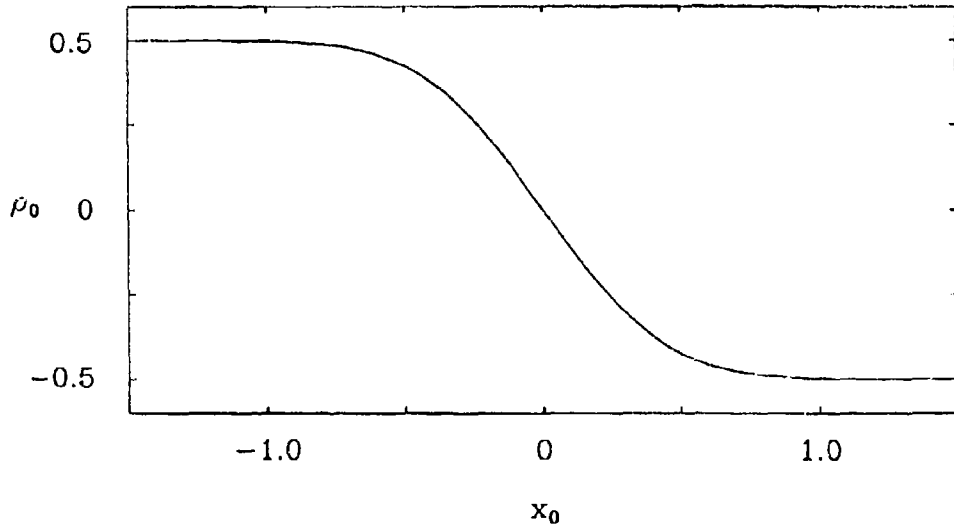


Figure 1. Initial density distribution  $\rho_0(x_0)$ , defined by (5), for  $\epsilon = 1/2$  and  $\alpha = 2.03$ .

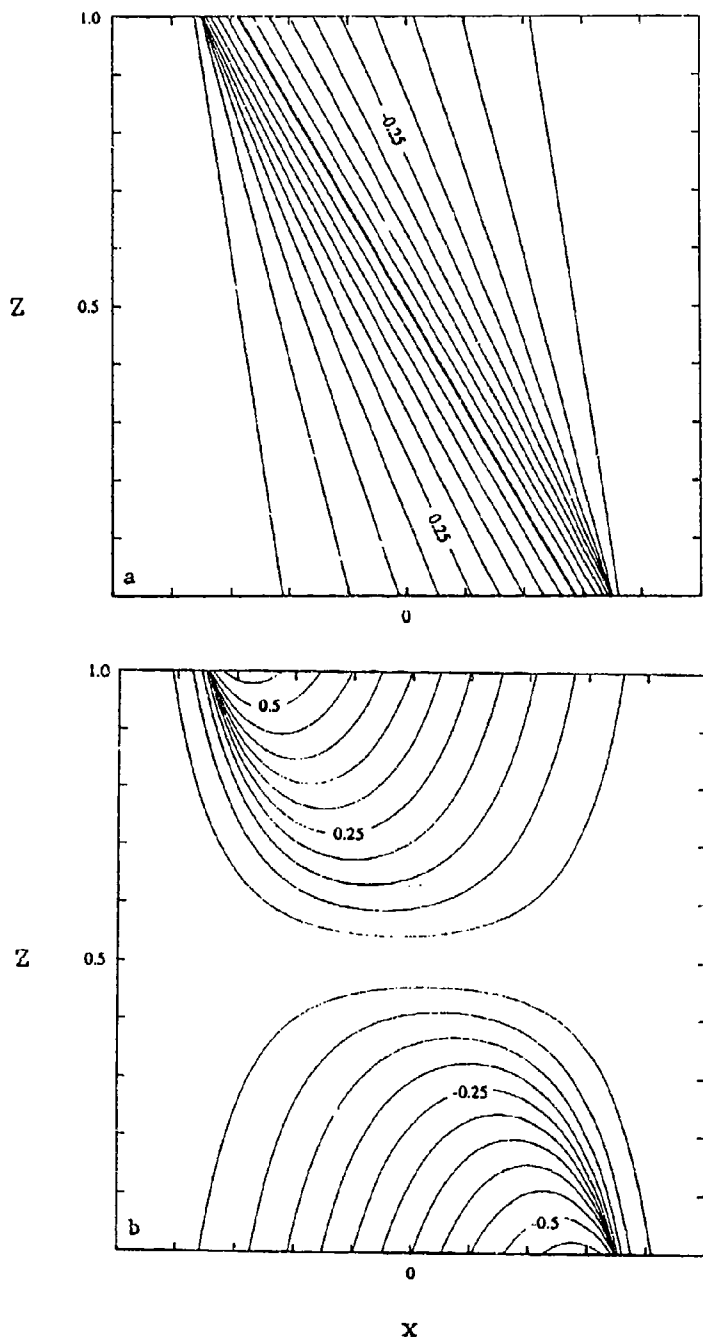


Figure 2. Cross sections of the final state for zero potential vorticity flow that corresponds to  $\rho_0(x_0)$  in Figure 1. Increments along the axes are  $\Delta x = 0.2$  and  $\Delta z = 0.1$ . a. Density distribution with  $\Delta \rho = 0.05$ . b. Geostrophic velocity  $v$ , with  $\Delta v = 0.05$ .

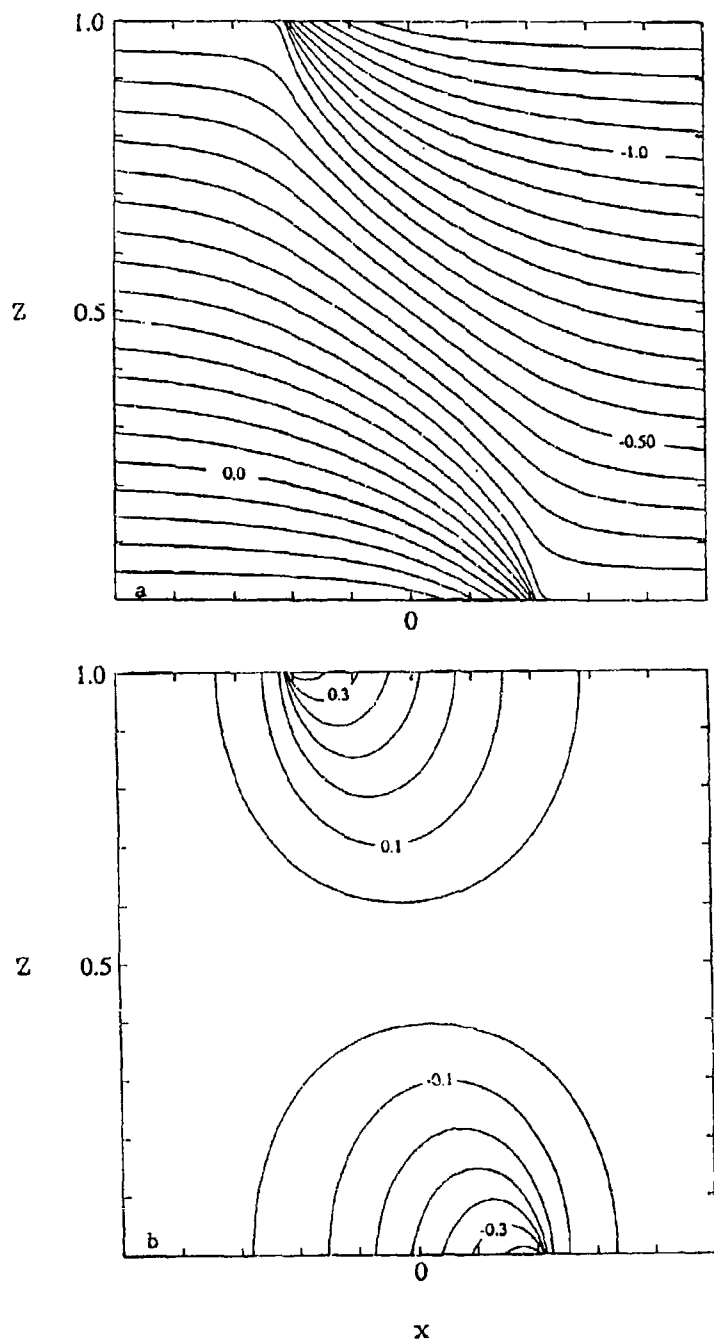


Figure 3. As in Figure 2, except for uniform potential vorticity flow. The initial density field is defined by (10) and (5) with  $\epsilon = 1/4$  and  $\alpha = 6.00$ . a. Density distribution with  $\Delta \rho = 0.05$ . b. Geostrophic  $\nabla \times \mathbf{v} = \Delta \mathbf{v} = 0.05$ .

## LABORATORY EXPERIMENTS WITH MID-LATITUDE CIRCULATION IN A TWO-LAYER OCEAN

Ross W. Griffiths<sup>a</sup> and Peter Cornillon<sup>b</sup>

<sup>a</sup>Research School of Earth Sciences, Australian National University, Canberra 0200, ACT, Australia.

<sup>b</sup>Graduate School of Oceanography, University of Rhode Island, Narragansett, RI 02882-1197, USA.

### Abstract

A laboratory  $\beta$ -plane model is being used to examine aspects of wind-driven ocean circulation at mid-latitudes, including effects of stratification. The model is a 'sliced cylinder' with a surface stress exerted by differential rotation of the lid and is similar to that used by Beardsley (1969) in his experiments with a homogeneous fluid. However, a much wider cylinder and two sloping boundaries are required to extend the results to the two-layer case. New results from this wider basin are given also for the homogeneous case and reveal significant differences from previous data. In two-layer flow separation of the western boundary current from the western wall is found to coincide with outcropping of the lower layer to the surface, but the position of separation is almost independent of conditions and lies only a little farther upstream than in the one-layer case. In contrast, an energetic current extension flowing across the interior of the basin and still coincident with the outcropping front (as predicted by Parsons, 1969) follows a mean path that is strongly dependent on both the magnitude of the  $\beta$ -effect and the ratio of surface forcing to buoyancy. Eddies are shed from an adjustment region between the separating boundary current jet and the interior flow.

### 1. Introduction

There remain many uncertainties in our understanding of mid-latitude ocean circulation. The causes of western boundary current separation and the factors affecting the position of separation are still being questioned; the dynamics and path of the energetic current extension are difficult to model; and the dynamical connections between the sub-tropical and sub-polar gyres are unclear.

Parsons (1969) suggested that boundary current separation corresponds to surfacing of the thermocline in the region of anticyclonic wind stress curl. By requiring that the 'equatorward' longitudinally-integrated wind-driven Ekman flux is equal to the net 'poleward' geostrophic flow in the upper layer across any latitude he showed that outcropping will occur when the value of a forcing parameter  $\lambda = L\tau_m/\delta\rho d_1^2$  exceeds a critical value, where  $L$  is the basin width,  $\tau_m$  is a scale for the surface stress,  $\delta\rho$  is the density difference between layers and  $d_1$  is the mean depth of the upper layer. In this model the lower layer is assumed stationary. The critical value for outcropping in a rectangular basin with a cosine wind stress is  $\lambda_c = 0.26$ . For supercritical forcing the latitude at which outcropping should occur is given in terms of the upper layer depth on the eastern boundary, the reduced gravity and the applied wind stress. Veronis (1973) added to this model a cyclonic sub-polar gyre and the possibility of a net 'poleward' flux out of the basin. Numerical solutions by Huang & Flierl (1987) show how the model predicts a sub-tropical warm pool isolated to the south of the basin for sufficiently large forcing, and even to the southwest after separation from the eastern boundary under extreme forcing ( $\lambda_c > 5.3$ ).

The Parsons-Veronis hypothesis was formulated in terms of an assumption that surface stress acts as a body force on the whole depth of the upper layer. The theory also neglected transport or mixing between the layers. Thus the boundary current extension was expected to follow the isopycnal outcropping. This simple model predicts an outcropping front extending eastward and 'poleward' across the ocean, with the lower layer surfacing

in the northwest (in the northern hemisphere). Pedlosky (1987) extended the model by considering the wind stress as applied only to the surface Ekman layer. He also allowed transport in the Ekman layer to cross the outcropping density front. Hence some lower-layer water is carried into the upper layer, where it was assumed to be converted into upper layer water by warming. This modification resulted in a significant change in the global circulation pattern, in which outcropping of the interface is no longer associated with a separated boundary current flowing along the outcropping front. Pedlosky appealed instead to the local vorticity dynamics of the boundary current as the cause of separation. The Ekman flux across the outcropping line also provides a driving mechanism for deep circulation.

Little attempt has been made to explore stratified  $\beta$ -plane circulation using laboratory experiments. Beardsley (1969) investigated homogeneous flow forced by a differentially rotating lid in the 'sliced cylinder' geometry, and his study has been followed by further experimental, analytical and numerical studies (Pedlosky & Greenspan, 1967; Beardsley & Robbins, 1975; Becker & Page, 1990). These have been very successful in modelling some aspects of the mid-latitude circulation, particularly the interior Sverdrup balance closed by an intense western boundary current. However, even in this simple model there remains uncertainty over the mechanism responsible for separation of the western boundary current (Becker & Page, 1990). The only previous experiments with two-layer models (Krishnamurti & Na, 1978) were attempted in a somewhat different geometry in which the  $\beta$ -effect was simulated by a conical slope on both base and lid of a cylinder. Radial barriers served as meridional boundaries. Surfacing of the lower layer against the (differentially rotating) lid at the radial western boundary was observed, but little quantitative information on separation and outcropping was obtained.

In new experiments in a planar  $\beta$ -plane model we examine the circulation in both one- and two-layer cases. Both base and lid are sloping in order to apply a  $\beta$ -effect in each layer, and the flow has a much smaller aspect ratio than those used previously in order that the internal deformation radius be much smaller than the width of the basin. In particular, we aim to test the Parsons-Veronis hypothesis and modifications introduced by Pedlosky (1987), including the position of separation of the western boundary current, the behaviour of any current extension flowing into the interior of the basin, and the location of lower layer outcropping.

## 2. Apparatus and method

Experiments are carried out in a large rotating cylindrical tank of diameter  $L = 1.0\text{m}$ . The north-south gradient of planetary vorticity is simulated by a variation of the depth of each layer produced by planar sloping top and bottom boundaries. In the experiments reported here the base slope  $\alpha_2$  has been set at either  $\tan\alpha_2 = 0.05$  or  $0.10$ , while the lid has been set to a number of slopes between zero and  $\tan\alpha_1 = 0.10$ . However, the preferred conditions for two-layer runs are  $\tan\alpha_2 = 0.10$  and  $\tan\alpha_1 = 0.05$ , with the ratio of upper to lower layer depths  $d_1/d_2 \approx 1/2$ , in order to impose similar values of  $\beta = (2\Omega/d_i)\tan\alpha_i$  in each layer. The lid rotates relative to the cylinder about an axis normal to the lid slope. The total mean depth of water,  $D$ , is either  $15.0\text{cm}$  or  $12.5\text{cm}$ . Hence the aspect ratio is  $D/L = 0.128$  or  $0.154$ , which are much smaller than the aspect ratios used by Beardsley (1969) ( $D/L = 0.502$ ) and Becker & Page (1990) ( $D/L = 1.17$ ). In our two-layer runs the ratio of mean depth-to-width of the upper layer  $d_1/L$  is approximately equal to  $0.04$ .

Tank rotation speeds  $\Omega = 0.5\text{--}2.0\text{ rads}^{-1}$  and relative lid speeds  $\Omega_L = 0.0051\text{--}0.16\text{ rads}^{-1}$  (periods of  $1228\text{s}$  to  $40\text{s}$ ) gave Rossby numbers  $Ro = \Omega_L/\Omega$  from  $0.0026$  to  $0.16$ , Ekman numbers  $E = \nu/\Omega D^2$  from  $3 \times 10^{-5}$  to  $1.3 \times 10^{-4}$  and  $E^{1/4} \sim \tan(\alpha_1 + \alpha_2)$ . Only anticyclonic lid motion is used. Hence the boundary current flows from deep to shallower water. For two-layer cases a layer of salt solution is carefully filled beneath a layer of fresh water so as to establish a sharp density interface and left to approach solid body rotation before the lid motion is begun. A single density difference  $\delta\rho/\rho = 0.005$  has been used in order to reduce the number of variables. With  $d_1 = 4\text{cm}$  and  $\Omega = 1\text{rads}^{-1}$  the baroclinic deformation radius is  $2.2\text{cm}$ .

A particularly effective but simple method of flow visualisation in these experiments is to bleed narrow streams of dye into the flow from 1mm diameter syringe tubes positioned at strategic points in the tank. The most effective positions for these continuous dye sources were found to be within the boundary current. Hence they are positioned near the 'west', from where the dye lines are passively advected 'poleward' with the current. The dye lines enter the interior where the current separates from the wall, continue 'equatorward' through the interior of the basin, and eventually re-enter the western boundary current in the 'southern' region (using northern hemisphere directions). Throughout this circuit the tracer reveals the mean flow, any unsteadiness in the velocity field, eddy shedding, stirring in the interior, and mixing between layers. Dye reveals more information on the flow field than other techniques, such as streak photography, because the flow is unsteady and involves a large range of velocities ( $10^{-2}$  to  $1\text{cm s}^{-1}$ ). The advection of dye was recorded on still film and time-lapse video tapes. In addition, measurements were made of velocity profiles in the boundary current and the interior by using a solution of Bromothymol blue PH indicator and electrode wires stretched from the centre of the tank to the 'west' wall.

### 3. Results for homogeneous flow

Although new results for the homogeneous case are of intrinsic interest, only a few are given here for comparison with the two-layer flows. As in earlier  $\beta$ -plane experiments, a fast, narrow boundary current develops on the 'western' side of the tank, flowing 'poleward' when the surface stress distribution imparts anticyclonic vorticity. For very small Rossby numbers circulation is centred to the 'west' of the basin and streamlines diverge from the boundary current at all 'latitudes' in a manner consistent with linear theory (Pedlosky & Greenspan, 1967; Beardsley, 1969) and numerical solutions (Beardsley & Robbins, 1975; Becker & Page, 1990). However, in contrast to previous assumptions, the laboratory flow is never completely steady. Even at  $Ro < 0.005$  a small-amplitude oscillation persists indefinitely: each dye line leaves the boundary current at a point that fluctuates along the wall and the dye line is stirred across a broad region of the interior return flow.

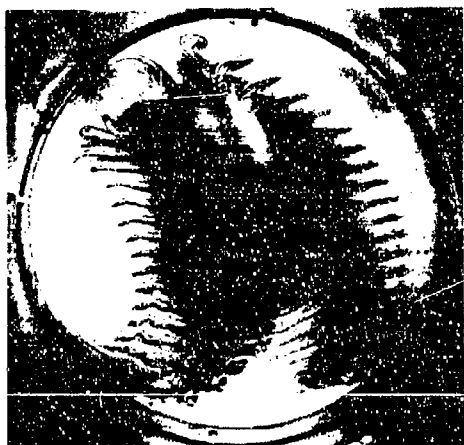


Figure 1. Circulation in an unstable homogeneous flow as revealed by dye advection (Northern hemisphere orientation -  $\Omega$  ant-clockwise,  $\Omega_L$  anticyclonic, water deepest at bottom of picture and shallowest at the top, which is 'north' or 'poleward'). Dye is injected at the 'west' and at the centre of the cylinder.  $Ro = 0.053$ ,  $E = 6.3 \times 10^{-5}$ ,  $Re_E = 6.7$ . Eddy shedding is periodic. Photograph at 350 rotations after beginning of dye release.

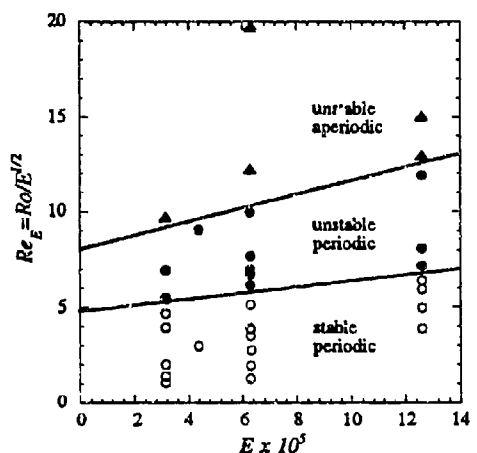


Figure 2. Stability transitions in one-layer flow. No steady flow was found.

For sufficiently large forcing the flow structure changes significantly. The current separates from the western wall as a narrow jet in which two streamlines initially 2 cm apart show no significant divergence. The jet penetrates a short distance 'southeastward' into the interior before looping 'northward' to supply the 'eastern' part of the basin. Increasing the forcing slightly farther causes the flow to become unstable in the region where the separated boundary current enters the interior (fig.1). The transition (fig.2) is well described by a critical value  $Re_c$  of the Ekman layer Reynolds number  $Re_E = Ro/E^{1/2}$ :  $Re_c \approx 4.9 + 1.5 \times 10^4 E$ . We have defined instability here as the formation and shedding of cyclonic eddies. (Anticyclonic eddies are shed to the 'northeast' at still greater values of  $Re_E$ .) Instability is associated with rapid divergence of the flow from the narrow separated jet to fill the full width of the interior of the basin. As this divergence occurs in an unsteady fashion, there is very extensive stirring of the passive tracer. Beardsley (1969) and Beardsley & Robbins (1975) reported a similar instability, but placed the threshold under their experimental conditions at larger values of  $Re_E$ . Another new observation is that there is a further transition from periodic flow at  $Re_E > Re_c$  to aperiodic eddy shedding at  $Re_E > Re^*$ , where  $Re^* \approx 8.2 + 3.5 \times 10^4 E$ .

The position of separation of the boundary jet is of particular interest for comparison with two-layer flows. Separation is meaningful only under conditions for which the current leaves the wall as a narrow jet. In these cases its position has been estimated from the path of a dyed streamline as close as possible to the wall and a region of reversed flow 'north' of separation. Separation occurs at  $\theta = 35^\circ \pm 3^\circ$  west of the shallowest point (fig.3) and is insensitive to conditions, showing only a possible small shift in the upstream direction ('equatorward') for larger forcing. This finding is inconsistent with the computations and experimental observations of Becker & Page (1990), whose results are for a cyclonic surface stress and show a region of reversed flow on the 'southeast' boundary, some distance east of the deepest point rather than  $35^\circ$  to the west as observed here. The difference may be a result of the smaller aspect ratio and relatively large values of the  $\beta$ -parameter  $S = L\beta/2\Omega = L\tan(\alpha_1 + \alpha_2)/D$  in our experiments.

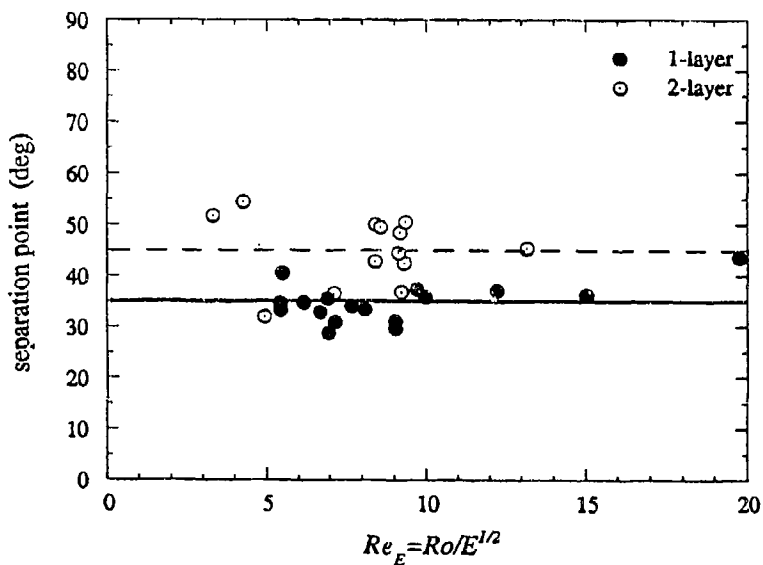


Figure 3. Separation position (in degrees west of the shallowest point, 'north') as a function of the Ekman layer Reynolds number based on the mean depth of water. In one-layer runs separation is plotted for unstable cases only. Two-layer runs with zero lid slope are omitted.

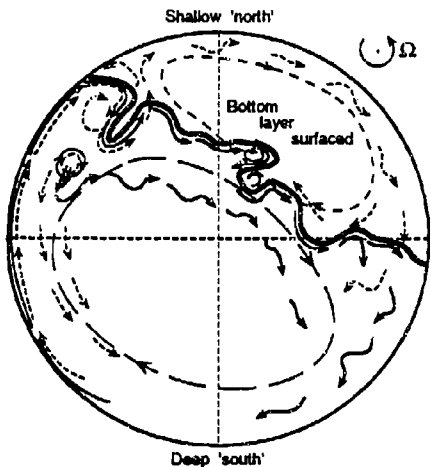


Figure 4. Circulation in a two-layer case (Southern hemisphere orientation -  $\Omega$  clockwise,  $\Omega_L$  anticyclonic, water shallowest at bottom of picture). Dye is injected in both layers at the west. Red dye in the upper layer leaves the wall at the outcropping and travels eastward in an energetic frontal stream. Blue dye in the weaker lower layer current passes under the outcropping and along the 'poleward' boundary. Mixing between layers occurs mainly in the east.  $Ro = 0.0565$ ,  $\lambda = 0.34$ ,  $S_1 = 1.22$ .

Figure 5. Sketch illustrating the main aspects of the two-layer flow (in Northern hemisphere orientation). Heavy line indicates outcropping of the interface; solid lines show upper layer flow, broken lines the lower layer.

#### 4. Two-layer flows

In our two-layer experiments an intense boundary current again develops on the 'western' side of the tank. The current extends throughout the depth, but velocities are smaller in the lower layer. The current separates from the western wall under all conditions that have been used, and forms a jet flowing into the interior (fig.4 & 5). Separation always coincides with outcropping of the lower layer to the surface at the wall. However, contrary to Parsons hypothesis separation and outcropping occurs in an approximately fixed location (on average at  $45^\circ - 7^\circ$  instead of  $35^\circ \pm 3^\circ$  from 'north'), with only weak dependence on conditions (fig.6). In fact, the data show a slight trend in the opposite direction to that expected: separation occurs farther downstream ('poleward') for *larger* values of the ratio  $\lambda$  of surface to buoyancy forces. Separation is also not sensitive to lid slope or upper layer depth (fig.7) when  $S_1 = L \tan \alpha_1 / d_1 > 1$  (i.e. in wide basins). In addition, the lower layer boundary current follows the separated upper layer jet into the interior. Thus, although separation occurs at slightly 'lower latitudes' than in the homogeneous case, the results indicate a primarily barotropic process.

A qualitative similarity between the one- and two-layer flows can also be seen downstream of separation (fig.4 & 5). The jet loops first anticyclonically to smaller 'latitude' and then cyclonically, in a relatively sharp turn, to flow 'poleward' again. The anticyclonic loop follows the perimeter of an anticyclonic gyre close to the western boundary. Cyclonic eddies are shed periodically from the tip of the cyclonic loop, move westward around the 'southeast' of the anticyclonic gyre, and then (as in the one-layer case) dissipate as they are advected 'equatorward'.

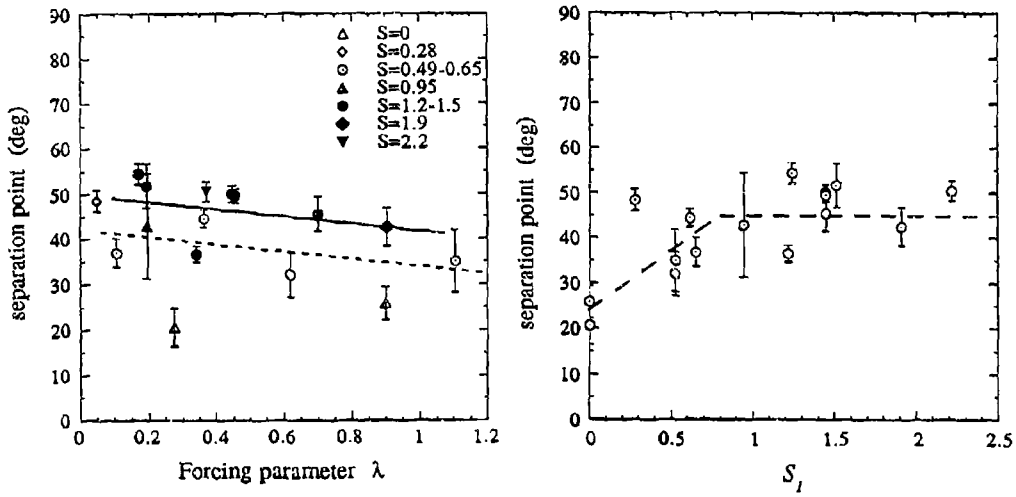


Figure 6. Separation position in two-layer runs (in degrees west of the shallowest, or ‘poleward’, point of the basin) as a function of surface stress/buoyancy. Symbols indicate values of dimensionless upper layer  $\beta$ -effect,  $S_1 = L \tan \alpha_1 / d_1$ . Solid line fits  $S_1 > 0.95$ , broken line fits data for  $0.49 < S_1 < 0.65$ .

Figure 7. Separation position of fig.6 but as a function of  $S_1$ , the magnitude of the topographic  $\beta$ -effect.

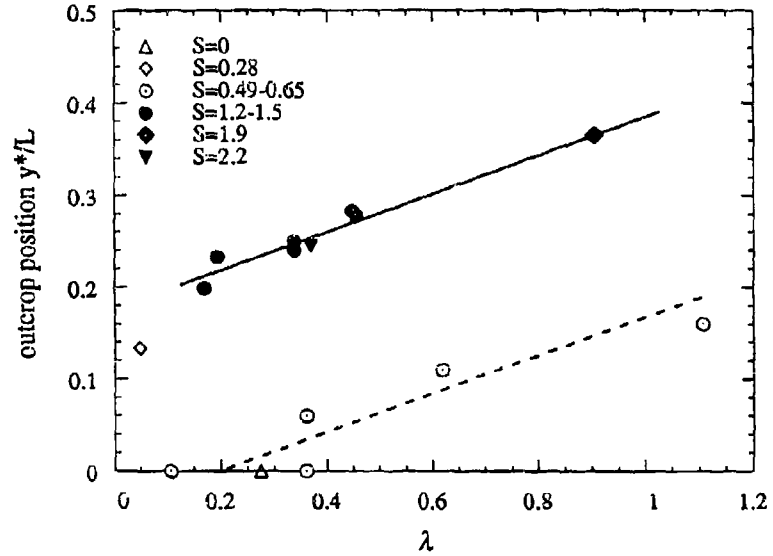


Figure 8. ‘Latitude’ of the outcropping front in two-layer runs as a function of forcing parameter and  $S_1$ , the dimensionless  $\beta$ -effect. (Latitude is measured as the ‘north-south’ distance  $y^*$  from the shallowest point of the basin, normalised by basin width  $L$ ).

The interior flow, on the other hand, is greatly altered by the effects of stratification. In the one-layer case the unsteadiness of the loop serves to spread the transport from the narrow separated jet across the full width of the interior Sverdrup flow. In the two-layer case (summarised in fig.5) eddy shedding divides the upper layer jet transport between, on the one hand, a return eddy flux 'equatorward' and to the west, and on the other hand, a narrow stream flowing across the interior. This is a frontal stream coincident with outcropping of the density interface. It is unstable, with meanders continually developing into eddies as they move eastward. The front divides the upper-layer warm pool on the 'equatorward' side from a region on the 'poleward' side in which unstratified lower-layer water is in contact with the lid. The water carried by the cyclonic eddies does not continue to drift 'equatorward' in the western part of the basin as it does in one-layer experiments, but instead is advected *eastward* some distance 'equatorward' of the outcropping front. Both branches of the upper layer transport join a broad eastern boundary current that returns water 'equatorward', where it is again taken into the western boundary current.

The lower layer boundary current, too, divides between a branch flowing round the anticyclonic gyre near separation and then meandering 'equatorward', and a branch that crosses beneath the outcropping line to return to the western wall and flow 'poleward'. The latter branch continues along the wall past the shallowest point and into the 'east' of the basin. In the eastern half of the basin there is a small flux of lower layer water into the upper layer as a result of the surface Ekman layer transport across the outcropping front in the manner discussed by Pedlosky (1987). This water is gravitationally unstable, mixes, and slowly adds to the upper layer volume. For instance, in one experiment the volume of the upper layer increased by 40% (inferred from density measurements) over 5 hours of forcing. It is not yet clear to what extent this mixing contributes to the observed circulation.

The latitude of the outcropping front in the interior, unlike the separation position, does vary with surface stress, lid slope and upper layer depth: increasing either  $\lambda$  or  $S_1$  shifts the front and its stream to deeper water ('lower latitudes') (fig.8). For small lid stresses, small lid slopes and large upper layer depths ( $\lambda < 0.4$  and  $S_1 < 0.6$ ) the boundary current separates but, after looping a small distance 'equatorward', it returns all the way to the 'northwest' boundary. There is no extended region of outcropping, only a small area against the 'west' wall beyond the separation point. However, for  $S_1 > 0.65$  and  $\lambda > 0.2$  the jet does not return to the boundary and the outcropping front extends across the interior to the eastern boundary. Thus the cyclonic loop and eddy-shedding represent a flow adjustment between the largely barotropic jet emerging from the fixed separation point and the strongly baroclinic, forcing-dependent interior flow.

For sufficiently large forcing ( $\lambda > 0.8$ ) the upper layer also separates from the eastern boundary and the outcropping front curves around to the 'south' (northern hemisphere again). The upper layer is then confined to a 'low-latitude' western pool, as in the numerical solutions of Huang and Flierl (1987). We note that the critical values of  $\lambda$ , first for extension of outcropping beyond the neighbourhood of the separation point and secondly for confinement of the upper layer pool to the 'southwest', in the laboratory model are not expected to coincide with the theoretical predictions based on a cosine zonal wind stress in a rectangular basin with a stationary lower layer.

## 5. Conclusions

Having demonstrated that a laboratory two-layer  $\beta$ -plane model reproduces many of the features of mid-latitude circulation and theoretical  $1\frac{1}{2}$ -layer models, there are a number of aspects which must now be investigated in greater detail before Parsons' model or its modifications can be compared quantitatively with the experiments. Those models did not include the effects of non-zonal surface stresses, a mobile lower layer of finite depth, or surface stress applied directly to the outcropped lower layer at 'high latitudes'. All of these are unavoidably present in the experiment. Comparison of theory and experiment will also need to take into account the water mass conversion from lower to upper layer at the outcropping line. Further experiments are being carried out also, using a broader

range of conditions (including a deeper lower layer), along with more detailed investigation of the lower layer motion and effects of a sloping side wall.

The experiments model an isolated sub-tropical gyre, neglecting effects of a reversal of the wind stress curl and interaction with a cyclonic sub-polar gyre. However, Parsons' analytic model of the anticyclonic gyre captured so much of the important dynamics that it should prove profitable to explore similar laboratory models, including additional, more realistic, factors. Particular attention needs to be given the mechanism for barotropic separation and the process of adjustment to a baroclinic interior flow.

### References

Beardsley, R. C. A laboratory model of the wind-driven ocean circulation. *J. Fluid Mech.*, 32, 255-271, 1969.

Beardsley, R. C. and K. Robbins The 'sliced-cylinder' laboratory model of the wind-driven ocean circulation. Part 1. Steady forcing and topographic Rossby wave instability. *J. Fluid Mech.*, 69, 27-40, 1975.

Becker, A. and Page, M.A. Flow separation and unsteadiness in a rotating sliced cylinder. *Geophys. Astrophys. Fluid Dyn.*, 55, 89-115, 1990.

Huang, R.X. and Flierl, G.R. Two-layer models for the thermocline and current structure in subtropical/subpolar gyres. *J. Phys. Oceanography*, 17, 872-884, 1987.

Krishnamurti, R. and Na, J. Y. Experiments in ocean circulation modeling. *Geophys. Astrophys. Fluid Dyn.*, 11, 13-21, 1978.

Parsons, A. T. A two-layer model of the Gulf Stream separation. *J. Fluid Mech.*, 39, 511-528, 1969.

Pedlosky, J. On Parsons' model of the ocean circulation. *J. Phys. Oceanography*, 17, 1571-1582, 1987.

Pedlosky, J. and Greenspan, H.P. A simple laboratory model for the oceanic circulation. *J. Fluid Mech.*, 27, 291-304, 1967.

Veronis, G. Model of world ocean circulation: I. Wind-driven, two-layer. *J. Marine Res.*, 31, 228-288, 1973.

# MANIFESTATIONS OF BOTTOM TOPOGRAPHY ON THE OCEAN SURFACE: THE PHYSICAL MECHANISM AND SOLUTION OF DIRECT AND INVERSE PROBLEMS ON A BETA-PLANE

By Victor I. Shrira and Sergei Yu. Annenkov

*P.P. Shirshov Institute of Oceanology, Russian Academy of Sciences,  
Krasikova 23, 117218 Moscow, Russia*

**1. Introduction.** The shape of oceanic basin, among many other factors, controls the formation of surface and subsurface fields of oceanographic characteristics, but it is generally admitted that the small- and medium-scale (i.e.  $10^1$  -  $10^3$  km) bottom relief features neither are directly portrayed on the surface nor bring out meaningful correlations with the surface fields of density and current.

However, a large number of observations, coming from two main sources, contradict to this viewpoint. First, during the last two decades there have been repeated reports of 'underwater mountains' visually observed from space. These very unusual observations were initially discarded as impossible, due to the lack of documentary evidence and information on the conditions of observation. Nevertheless, such strange reports, repeated independently by different people with persistence and certainty, eventually attracted serious attention. The analysis in Solomakha & Fedorov (1983) showed that the bottom topography cannot be directly visible from space as it seems to be. Indeed, it is well-known that an underwater object can be very rarely seen beneath the 50 meters depth; but the actual thickness of the water layer above the mountains so 'observed' sometimes exceeded several kilometers! On the other hand, the possibility that changes in the geoid height due to bottom topography can be observed visually was also disproved, since the corresponding tilts of the surface were found to be at least an order of magnitude smaller than those that could be observed. Solomakha & Fedorov supposed that the plankton or mud redistribution due to the topographically-caused disturbances in the surface and sub-surface flow fields may be observable, as well as surface waves modulations, and specified the optimal visibility conditions, but did not point out any mechanism responsible for the formation of such disturbances.

Meanwhile, observations of another kind appeared several years ago, and yet did not get attention they merit. It was discovered that there are bands in the one-dimensional spatial spectrum where surface temperature has surprisingly high correlations with bottom topography. The most thorough investigation was done by Ilyin & Melnikov (1988) who found out two spectral bands of high correlations - 4-40 km and  $> 200$  km. They also supposed that certain global mechanisms connecting bottom processes with those in the near-surface layer must exist, and suggested that the appearance of the correlations at shorter scales might be due to the fact that the process of the baroclinic tide formation is dominated by topography. However, in this paper we concentrate on another spectral band, corresponding to wavelengths of  $10^2$  -  $10^3$  km, though the ideas can also be applied to somewhat shorter scales.

Thus, the observations described above require a hydrodynamic theory providing a distinct pattern of surface or near-surface flow characteristics closely related to the shape of bottom relief features. This 'hydrodynamic image' then could be transformed into observable features on the surface by a number of mechanisms well-known from the study of internal wave manifestations (e.g. Pelinovsky 1982). In order to explain the observed phenomena, the theory must (i) provide an effective mechanism of penetration of the near-bottom perturbations to the upper layer, and (ii) this mechanism should give *local* or near-local relations between topography and surface. These conditions ensure that the topographic image be visible (easily observable), and preserve

similarity to the real topography shape.

Our attention will be focused on the *steady patterns*, since they seem more likely to be observed, and it is natural to postulate *a priori* that the mechanism can be found within the stationary model. The scales involved suggest making use of the quasigeostrophic  $\beta$ -plane approximation; smaller scales will be considered elsewhere.

The problem of steady horizontally uniform zonal quasigeostrophic flow over low-rise one-dimensional or axisymmetric topography is linear, and it is natural to present the solution in the form of a convolution of the corresponding Green's function  $G$  and any topography, which is assumed localized. The separation of variables leads to the expression for the horizontal part of  $G$  via Bessel functions, in the case of eastward flow supplemented by infinite Fourier-Bessel series representing the wake of stationary Rossby waves behind an obstacle. The explicit solution for the case of an unsheared incoming zonal current over axisymmetric infinitesimal topography shows that the disturbance has the form of a 'Taylor-Hogg cone' (the term proposed by Zyryanov 1985), its amplitude decaying exponentially with the distance from the bottom. The real ocean is rather strongly stratified, and the cone usually cannot reach the surface unless the barotropic current has the speed of 5-10 cm/s, which is too high for the time- and vertically averaged currents in the ocean.

The new element in the present work changing the situation qualitatively is taking into account the specific vertical structure of the flow, viz., the surface and bottom boundary layers. Indeed, the surface layer usually has the current velocity much higher than that of inner layers and is characterized by large gradients of current and stratification; the same, though to a lesser extent, is true for the bottom layer. The latter statement is supported by recent observations (see, e.g., Dickson, Gould, Muller & Maillard 1985, Klein 1987) and some theoretical models (e.g., Barenblatt, Galerkina & Lebedev, 1992). We demonstrate that if the vertical flow shear is taken into account, then the 'transmission' of the disturbance from bottom to surface is found to be considerably higher than in the equivalent barotropic case (we term the measure of this difference as an '*enhancement coefficient*'). For a three-layer model, which is the simplest one implementing the vertical structure described above, we show that even in the case of relatively low topography the free surface deflection turns out to be of the order 10' cm/100 km, the variations of the surface current are comparable with the undisturbed values, and the pycnocline displacements can be up to dozens of meters and may be observed visually under certain conditions.

Provided that the mechanism connecting processes at the oceanic bottom and the fields of surface characteristics exists, then the next question naturally arises: is it possible to get any information on the near-bottom structure or currents when the surface fields are given, and the topography known? This question constitutes the statement of the inverse problem. The positive answer would open the alluring perspective, since now we have no methods for determination of currents in the near-bottom layer besides very expensive direct observations. We show, within the multi-layer model, that partial information on the vertical structure can be obtained, though its large part is lost. If the stratification is assumed known, then the inverse problem is well-posed and can be solved by inverse methods known in geophysics, but the solution in general is not unique. For a three-layer model certain additional geophysically relevant conditions are specified, which allow us to obtain the unique solution.

**2. Problem statement.** The problem is treated here within the framework of the quasigeostrophic approximation. Let  $L$  and  $U_0$  be the length and velocity scales,  $H$  - the vertical scale, equal to the depth of the fluid,  $f_0$  and  $\beta_0 = df_0/dy$  - the Coriolis parameters, while  $\beta = \beta_0 L^2/U_0$ . The motion depends

in general on four nondimensional parameters: the length scales ratio  $\delta = H/L$ , the Rossby numbers  $\varepsilon = U_0/f_0 L$ ,  $\varepsilon_T = 1/T f_0$ , and the Burger number  $B = N_0^2 \delta^2/f_0^2 = g H \Delta \rho / f_0^2 L^2 \rho_0$ , where  $T$  is a timescale,  $N_0$  is some reference value of Brunt-Väisälä frequency,  $\rho(z)$  is a vertical density profile in the undisturbed state,  $\rho_0$  and  $\Delta \rho$  are the characteristics of this undisturbed profile, namely the Boussinesque reference density and a measure of vertical changes.

We are concerned with quasi-stationary disturbances of large ( $\delta = 10^{-1} - 10^{-2}$ ) horizontal scale caused by topography to a steady incoming zonal flow with vertical shear  $U(z)$  (see figure 1) and assume that the quasigeostrophic approximation is valid. The velocity  $\mathbf{q} = \{u, v, w\}$ , pressure  $p$  and density  $\rho$  are assumed to be dimensionless, while their dimensional counterparts (denoted by an asterisk) may be obtained as

$$\{x^*, y^*, z^*\} = L\{x, y, z\}, \quad \{u^*, v^*, w^*\} = U_0\{u, v, \delta w\},$$

$$p^* = \rho_0 U_0 f_0 L p(x, y, z), \quad \rho^* = [\rho(z) + \frac{\varepsilon}{B} \rho(x, y, z)] \Delta \rho$$

and the function which comprises the stratification effects  $S(z) = -B d\rho/dz$  is introduced. Expansion of the dependent variables in powers of  $\varepsilon$  leads to the vorticity equation

$$\left( \frac{\varepsilon_T}{\varepsilon} \frac{\partial}{\partial t} + \frac{\partial p}{\partial x} \frac{\partial}{\partial y} - \frac{\partial p}{\partial y} \frac{\partial}{\partial x} \right) \left( \nabla^2 p + \frac{\partial}{\partial z} \frac{1}{S} \frac{\partial p}{\partial z} + \beta y \right) = 0 \quad (1)$$

with the boundary conditions

$$\begin{aligned} J(p, \frac{\partial p}{\partial z}) &= 0, \quad z = 1, \\ J(p, \frac{\partial p}{\partial z}) + SJ(p, \frac{h}{\varepsilon}) &= 0, \quad z = h(x, y), \end{aligned} \quad (2)$$

where  $J(a, b) = a \frac{\partial b}{\partial y} - b \frac{\partial a}{\partial y}$ .

**3. Analysis of the vorticity equation.** The problem (1), (2) can be linearized about the upstream conditions, assuming  $\varepsilon_T/\varepsilon = O(1)$ . Then, search of the solutions with periodicity

$$\psi = \text{Re}\{\phi(z) \exp[i(kx + ly + \omega t)]\},$$

where  $\psi$  denotes the perturbation streamfunction,  $p(x, y, z) = -U(z)y + \psi(x, y, z)$ , yields the linearized vorticity equation

$$\sigma \left[ -k^2 \phi + \left( \frac{\phi'}{S} \right)' \right] - \left( \frac{\sigma'}{S} \right)' \phi + \beta \phi = 0 \quad (3)$$

with the boundary conditions

$$\begin{aligned} \phi' - \frac{\sigma' \phi}{\sigma} &= 0, \quad z = 1, \\ \phi' - \frac{\sigma' \phi}{\sigma} &= -\frac{Sh}{\varepsilon}, \quad z = 0. \end{aligned} \quad (4)$$

Here the prime denotes  $d/dz$ ,  $c = \omega/k$ ,  $\sigma = U - c$ , and the lower boundary condition has been transferred onto the undisturbed bottom.

On the other hand, it is easy to see that the problem is naturally linearized just by omitting its non-steady part. Since we are interested mainly in quasi-stationary disturbances caused by topography, we may put  $\varepsilon_T \ll \varepsilon$  in (1), and integrate it along streamlines, assuming the absence of closed streamlines above topography. Again denoting the perturbation streamfunction by  $\psi$ , we easily obtain

$$\nabla^2 \psi + \frac{\partial}{\partial z} \frac{1}{S} \frac{\partial \psi}{\partial z} + \frac{\beta - \frac{d}{dz} \frac{1}{S} \frac{dU}{dz}}{U} = 0 \quad (5)$$

with the boundary conditions

$$\begin{aligned} \frac{\partial \psi}{\partial z} - \frac{\psi}{U} \frac{\partial U}{\partial z} &= 0, \quad z = 1, \\ \frac{\partial \psi}{\partial z} - \frac{\psi}{U} \frac{\partial U}{\partial z} &= -\frac{Sh}{\epsilon}, \quad z = h(x, y), \end{aligned} \quad (6)$$

and the Long's condition of no upstream influence is also required.

The solution of the problem (5) - (6) may then be written as

$$\psi(x, y, z) = \int_{-\infty}^{+\infty} \int_{-\infty}^{+\infty} G(x-\xi, y-\eta, z) h(\xi, \eta) d\xi d\eta \quad (7)$$

where the Green's function  $G(x, y, z)$  is obtained via the decomposition over the normal modes of the corresponding homogeneous problem. The latter can be solved numerically for arbitrary  $S(z)$ ,  $U(z)$  (note however that we exclude the cases with  $U = 0$  at some  $z$ ); the solution for  $S = \text{const}$ ,  $U = \text{const}$  can be found in Johnson (1977), Zyryanov (1985). We assume here that the lower boundary condition may be applied at  $z = 0$ ; it is possible to take into account the exact boundary condition as well, but this would hardly help to win much accuracy within the quasigeostrophic approximation (see Schar & Davies 1988 for thorough comparison in a somewhat different context).

Thus, the solution of the nonlinear forced quasigeostrophic problem (1), (2) consists of stationary Rossby waves represented by the  $c = 0$  solutions of the homogeneous linearized problem, and the nonlinear terms vanish identically provided that the time-dependence and the horizontal non-uniformity of the incoming flow are neglected.

**4. Boundary-layer type asymptotics.** Here we consider the homogeneous counterpart of the problem (3), (4) for the case when the functions  $U(z)$ ,  $S(z)$  vary slowly over the entire fluid depth except for narrow layers (of dimensionless depths  $\delta_1$ ,  $\delta_2$ ) near the boundaries  $z = 0, 1$  respectively, where the gradients of these functions are localized. It is convenient to write

$$U(z) = U^* \left( \frac{1-z}{\delta_2} \right) U_* \left( \frac{z}{\delta_1} \right) U(\mu z), \quad S(z) = S^* \left( \frac{1-z}{\delta_2} \right) S_* \left( \frac{z}{\delta_1} \right) S(\mu z), \quad (8)$$

where  $\delta_1 = k_h \Delta_1$ ,  $\delta_2 = k_h \Delta_2$ ,  $\mu \ll \min(\delta_1, \delta_2)$ , indices '\*' and '\*\*' correspond to lower and upper boundary layers, respectively, and we assume, without loss of generality, that  $U(z) = U_*$ ,  $S(z) = S_*$  outside the boundary layers.

Two boundary layers are treated separately, with the asymptotic technique analogous to that of Shriram (1989). Here we will just summarize the results (see Shriram & Annenkov (1994) for details):

(i) The leading-order solution has the form

$$\phi(z) = \phi^* \left( \frac{1-z}{\delta_2} \right) \phi_* \left( \frac{z}{\delta_1} \right) \phi_i(z), \quad (9)$$

where  $\phi^* \left( \frac{1-z}{\delta_2} \right) = [U^* \left( \frac{1-z}{\delta_2} \right) - c]/(1 - c)$ ,  $\phi_* \left( \frac{z}{\delta_1} \right) = [U_* \left( \frac{z}{\delta_1} \right) - c]/(1 - c)$ ,

so that  $\phi(z) \rightarrow \phi_i(z)$  while  $\delta_1 \rightarrow 0$ ,  $\delta_2 \rightarrow 0$ ;

(ii)  $\phi_i(z)$  is simply the familiar trigonometric solution for the case when  $U$  and  $S$  are constants.

(iii) The dispersion properties of the solution are completely determined by its 'interior' part and unaffected by the boundary layers, to the second order in  $\delta_1, \delta_2$ .

Thus the problem considered differs from the analogous boundary-layer problem for the Rayleigh equation, due to the specific form of boundary conditions. Indeed, no solution of the 'vorticity wave' type appears. Moreover, the only consequence of a boundary layer imposed on slowly-varying current and density profiles is that the vertical mode gets attached to inner sides of the boundary layers as if they were solid (satisfying the boundary condition  $d\phi_i/dz = 0$ ), the solution within the layers being proportional to  $(U-c)$ , to the leading order, thus forming 'tails' affixed to either end of a slowly-varying function.

**5. The forced problem.** Here the result obtained is applied to the problem (5), (6). Provided that the functions  $U(z)$ ,  $S(z)$  can be presented in the form considered in the preceding paragraph, the Green's function is calculated directly. It is obvious that, in order to be effectively forced by topography, a natural mode of the system must have non-zero amplitude in the vicinity of the bottom, and the degree of the forcing depends directly on this amplitude. On the other hand, the modes that have maximum at or near the surface are most easily observed, providing the basis for the bottom topography manifestations in the surface field.

If the complete orthonormalized set of normal modes  $\phi_i(z)$  with the corresponding eigenvalues  $\kappa_i$  is known, then the Green's function has the form

$$G(R, z) = \frac{1}{2\pi\epsilon} \left[ -\frac{\pi}{2} \sum_{i=0}^N Y_0(\kappa_i R) \phi_i(0) \phi_i(z) + \sum_{i=N+1}^{\infty} K_0(\kappa_i R) \phi_i(0) \phi_i(z) \right] + F(R, \theta, z)$$

where  $(x, y) = R(\cos\theta, \sin\theta)$ ,  $N$  is the number of highest wavelike mode,  $Y_0$  and  $K_0$  are Bessel functions, and  $F(R, \theta, z)$  - part of the Green's function corresponding to the wake behind the obstacle. Since the functions  $Y_0$ ,  $K_0$  are both strongly localized near the origin, the surface disturbance will roughly preserve the form of the bottom relief. Certainly, in the presence of wavelike modes the disturbance will be distorted by the wake; however, the wakes of different seamounts must nearly compensate each other and are unlikely to be observed above a real corrugated topography.

Considering the interaction of a single normal mode with topography of unit height comprising one Fourier mode in each horizontal direction

$$h(x, y) = \cos(k_1 x) \cos(k_2 y)$$

and calculating the convolution in (7), we easily obtain that the response for  $i$ th mode is proportional to  $\cos(k_1 x) \cos(k_2 y) / (k_1^2 + k_2^2 - \kappa_i^2)$ , where  $\kappa_i^2 > 0$  for wavelike modes and  $< 0$  for decaying ones. We define this as the '*transmission coefficient*'. It is seen that the large-scale topography is better transmitted, while the shorter scales are suppressed.

In order to evaluate the degree of the response enhancement due to the mechanism described, the amplitude of the disturbance caused by an axisymmetric isolated topography to the flow with boundary layers was compared with that for the equivalent barotropic flow. The upper boundary layer thickness was taken to be about 150 m, while the thickness and velocity of the lower boundary layer were equal to 1/2 and 1/3 of the corresponding surface values. The maximal amplitude of the disturbance was computed, both asymptotically and numerically; the ratios to the disturbance value in the equivalent barotropic current (enhancement coefficients) are shown on fig. 2 for 4 values of westward flow average. The enhancement can exceed an order of magnitude, though

the averaged current should not approach to zero, since the link between two boundary layers becomes weak and the mechanism ceases to work.

**6. The multi-layer model.** In order to check and go over the results outlined, we performed a set of computations on the basis of a three-layer model. This model is characterized by a modest number of parameters, being able to represent the type of vertical structure described above. The results of computations are analyzed in Shrim & Annenkov 1994, and only a brief summary is presented here.

The topography has been chosen to have the form of a cylindrical cap 400 m height. Most of the computations were performed for the case of a thick and almost stagnant lower layer, while the thin surface and bottom layers had an order of magnitude quicker current. Though the velocities were moderate ( $< 10$  cm/s) and confined to the thin layers (2-10% of the total depth), images of the topography were well-pronounced on the surface, both for westward and eastward currents, in the latter case being considerably distorted by the wake behind the obstacle. In general, the stratification prevented the disturbance from reaching the surface in the equivalent barotropic flow; moreover, the disturbance diminished when simply the middle-layer current was enlarged! Other parameters important for the enhancement mechanism were the velocity values within the boundary layers, both of them being important for the surface disturbance, and the boundary layers thickness. It is important to note that the intense bottom current is not crucial for the mechanism to work, since the only prerequisite here is the normal mode increase towards the bottom, which can be provided by a moderate density jump.

We finish this paragraph with the remark on the validity of the quasigeostrophic approximation. In fact, the regimes involved in the present study require the lower interface to be significantly strayed from its undisturbed position, thus formally breaking the assumption that this distortion remains small in comparison with the thickness of the lower layer. However, we expect that the error still remains small and is associated with the mere underestimate of the disturbance amplitude, this judgement being in fact based on the assumption of minor influence of the thick and slow middle layer upon the much more intensive bottom one.

**7. The inverse problem.** In this paragraph we attempt to use the theory outlined above as the basis for reconstruction of the vertical structure of large-scale quasigeostrophic flows. Our attention will be confined to the multi-layer case. Apart from the evident gain in simplicity, we are motivated by the fact that multi-layer models are the main tool of the numerical simulation of ocean dynamics, the answer to the formulated question thus being especially important in view of the data assimilation problem. Here we will only sketch the main ideas.

According to the solution (7), the problem consists in the evaluation of the model parameters from observable functions  $h(x,y)$ ,  $\psi(x,y)$ . The information on the  $n$ -layer model that we need enters the streamfunction of the uppermost layer through  $n$  eigenvalues  $\kappa_i^2$ , these eigenvalues being the object to be determined empirically. However, the model is completely described by  $3n-2$  parameters. This means that the major part of information is inevitably lost.

In order to make the problem well-posed, it can be reformulated as the problem with only  $n$  unknowns - the velocities in each layer, while the stratification parameters are assumed fixed. This assumption is partially supported by the fact that the oceanic stratification is much easily observed and far better known than the velocity field. Thus, the solution of the inverse problem consists of three steps: (i) determination of the eigenvalues by numerical inversion of the formula (7), the corresponding numerical techniques being well-known in geophysics (Tarantola & Valette 1982), (ii) computation of the set of  $n$  integral parameters by solution of the system of  $n$  nonlinear equations, and (iii) provided that the stratification is given, the velocities

in each layer are found as roots of a linear matrix problem.

It is obvious that, the second step is the most complicated, since it can be shown that, in general, the system of nonlinear equations has  $n!$  solutions; though some of them may be complex or unphysical, it is still essential to make use of the *a priori* information for the elimination of the superfluous roots. We use the fact that the occurrence of the disturbance in the surface fields is possible under the special conditions, in particular for the special form of the current velocity profile. For the three-layer model, the simplest one of the type specified, two roots (of the total 6) are shown to satisfy the requirement, and the unique solution can be singled out if the surface velocity value is available.

**8. Discussion.** We have pointed out an effective mechanism responsible for the transmission of large-scale (with the length scales of the order  $10^2$  km) disturbances from the oceanic bottom to the surface. This mechanism is based upon the existence of the shear currents with the well-pronounced near-surface and near-bottom layers. This structure appears to be really observed in the ocean, though the information on the bottom currents is still fairly incomplete. However, the value of the current in the lowest 50-100 m about 2-3 cm/s seems to be sufficient for the mechanism to work, provided that the bottom layer is separated by a certain density jump. Now we are to discuss briefly the consequences of the result and the limiting factors associated with the approximations involved.

In this paper we have confined our attention to the investigation of the hydrodynamic transformation of the surface layer. However, within the slightly more complicated model it is easy to convert these disturbances into the surface temperature anomalies. The mechanisms of the transformation of the hydrodynamic disturbance into the optical radiation properties of the sea surface are much more complicated and diverse. The review of these mechanisms in application to the surface manifestations of internal waves can be found in Pelinovsky (1982), the analysis of their effectiveness for the scales involved being a non-trivial but realizable problem. Here we just mention the fact that the surface disturbances produced by bottom relief features with the height of several hundreds of meters beneath the water layer of several kilometers, according to our estimates, can be well-represented in the averaged characteristics of the sea surface radiation in the visible and infrared spectral bands.

The most important potential applications of the results are associated with the sensitivity of the surface disturbance to the vertical structure of the current. This fact allows to formulate the inverse problem - that of reconstruction of the undisturbed current as a function of depth given the surface disturbance and the bottom relief. The unique solution of the problem requires certain additional assumptions. First, the density structure must be specified *a priori*. This requirement appears to be only slightly limiting, since the stratification parameters of the ocean are much better known and less alterable than the current structure. Second, the current profile itself must be explicitly stated as belonging to the 'boundary-layer' type described above, the requirement being naturally connected with the existence of the aforementioned mechanism.

It is clear that these results are still far from the practical application. First, the surface streamfunction cannot be easily estimated: despite the high accuracy of modern altimetry measurements, their use is not possible due to the uncertainty of the geoid relief. However, the possibility to obtain the information on the deep and bottom currents using the surface measurements only appears to be potentially very important. At least, it can be used in data assimilation schemes in the numerical ocean modeling.

### References

Barenblatt G.I., Galerkina N.G., Lebedev I.A. Mathematical model of lower quasi-homogeneous oceanic boundary-layer - general concepts and model of sealing. *FAO*, 1992, 28, p. 91-100. (in Russian)

Dickson R.R., Gould W.S., Müller T.J., Maillard C. Estimates of the main circulation in the deep (> 2000 m) layer of the eastern North Atlantic. *Prog. Oceanogr.*, 1985, 14, p. 103-127.

Ilyin M.B., Melnikov V.A. On the link between spatial temperature changes and the ocean depth. In: *Hydrophysical investigations in the 'Mesopolygon' program*. Moscow, 1988, p. 152-159. (in Russian)

Johnson E.R. Stratified Taylor columns on a beta-plane. *Geophys. Astrophys. Fluid Dyn.*, 1977, 9, p. 159-177.

Klein H. Benthic storms, vortices, and particle dispersion in the deep West European basin. *Deutsche Hydr. Zeitschrift*, 1987, 40, s. 87-139.

Pelinovsky E.N. (ed.) *Large-scale internal waves effect on the sea surface*. Gorky, 1982. 251 pp. (in Russian)

Schar C., Davies H.C. Quasi-geostrophic stratified flow over isolated finite-amplitude topography. *Dyn. Atmos. Oceans*, 1988, 11, p. 287-306.

Shirra V.I. On the subsurface waves in the oceanic upper mixed layer. *Doklady AN*, 1989, 308, p. 732-736.

Shirra V.I., Annenkov S.Yu. Manifestations of bottom topography on the ocean surface: the physical mechanism and solution of direct and inverse problems on a beta-plane. *J. Fluid Mech.*, 1994 (Submitted).

Solomakha V.L., Fedorov K.N. On possibilities of feature observations of the deep ocean bottom topography from space. *Earth Research from Space*, 1983, 6, p. 13-21. (in Russian)

Tarantola A., Valette B. Inverse problems - Quest for information. *J. Geophys.*, 1982, 50, p. 159-170.

Zyryanov V.N. *The Steady Ocean Currents Theory*. Leningrad, 1985. 248 pp. (in Russian)

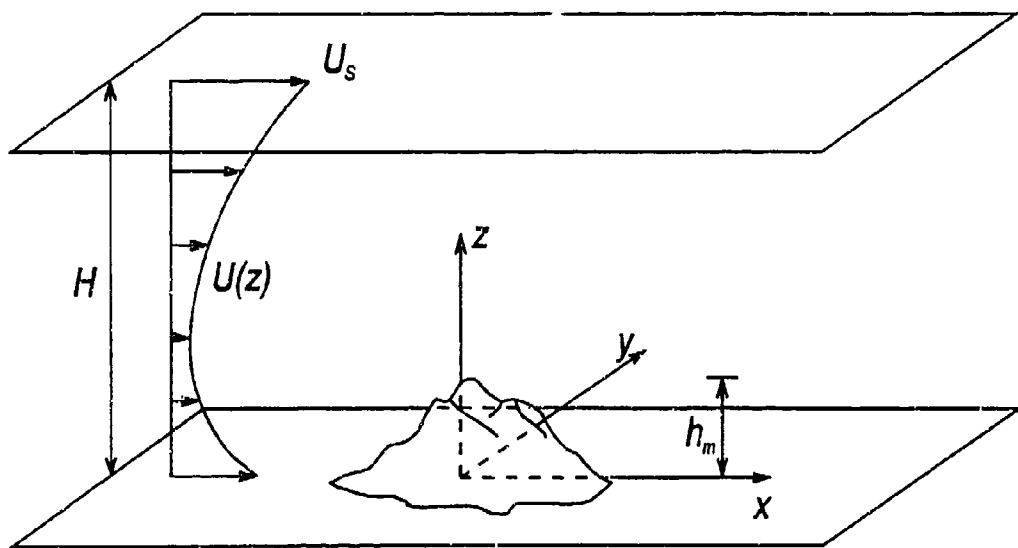


Figure 1. Coordinate system and basic notations.

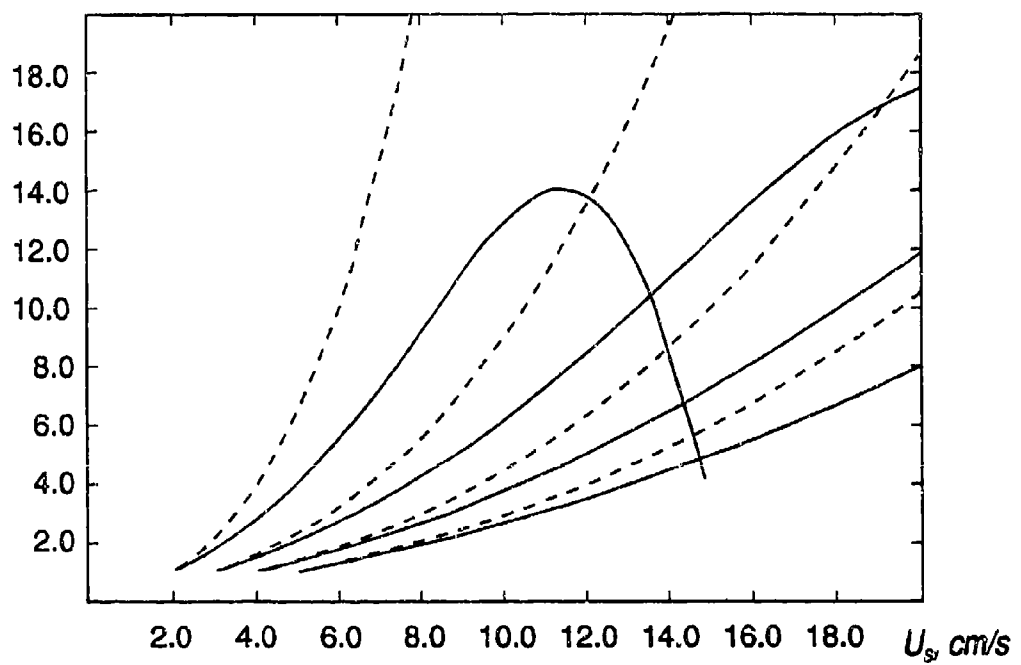


Figure 2. Enhancement coefficients for the disturbance caused by an axysymmetric isolated obstacle as functions of the velocity in the surface boundary layer. The lowest point of each curve corresponds to unsheared flow. Asymptotic curves are dashed; numerical curves are solid.

## CYLINDRICAL CO-ORDINATE SYSTEM AND LARGE SCALE OCEAN CIRCULATION

R. Schopp and R. Colin de Verdière

Laboratoire de Physique des Océans - UMR 127 Université-CNRS-Ifremer  
Université de Bretagne Occidentale - B.P. 809 - BREST 29285 Cedex - France

It is well known that the widely used, powerful geostrophic equations that single out the vertical component of the Earth rotation, cease to be valid near the equator. Through a vorticity and an angular momentum analysis on the sphere, equatorial dynamics must include the effect of the horizontal component of the Earth rotation if the flow varies on a horizontal scale  $L$  smaller than  $(H a)^{1/2}$ , (where  $H$  is a vertical scale of motion and  $a$  the Earth radius). In equatorial regions, where the horizontal plane aligns with the Earth rotation axis, latitudinal variations of planetary angular momentum over such scales become small and approach the magnitude of its radial variations proscribing, therefore, vertical displacements to be freed from rotational constraints. Two equatorial cases, including the effect of the vertical component of the Earth rotation will be presented: the slow geostrophic forced flow case ( $\varepsilon = U/(2\Omega H) \ll 1$ ) and the strong zonal flow case where  $\varepsilon \sim O(1)$  and  $L_\theta \ll L_\phi$  ( $L_\theta$  and  $L_\phi$  are respectively meridional and zonal length scales).

### I Small Rossby number regime

For slow geostrophic motions in a rotating container, the Taylor-Proudman-theorem-Poincaré (TPP in what follows) applies and the motion of fluid parcels occurs as fluid columns of constant length parallel to the axis of rotation. When the density of the fluid changes, the fluid columns still preserve their character within layers of constant density but velocity shear is possible at the interface between layers.

Within an oceanographic context, the steady geostrophic regimes associated with the works of Sverdrup (1947), Stommel and Arons (1960), are believed to apply to the large scale interior ocean circulation. With the assumption of hydrostatic pressure, such flows respond to stretching or compression of the vertical projection of the Earth rotation vector (caused by Ekman pumping or internal mixing) by moving poleward or equatorward according to the so called  $\beta$  effect where  $\beta$  is  $2\Omega \cos(\text{latitude})/R_{\text{Earth}}$ . However these flows which are geostrophic obey the Taylor-Proudman-Poincaré theorem and therefore evolve as columns parallel to  $\Omega$ . Reconciling these two views and extending the scope of these works in the equatorial regions is one of the objectives of the present study.

The full "geostrophic" balance:

$$2\Omega v = -\frac{1}{\rho_0} \frac{\partial P}{r \partial \phi} \quad -2\Omega u = -\frac{1}{\rho_0} \frac{\partial P}{\partial r} - \frac{\rho}{\rho_0} g \cos(\theta) \quad 0 = -\frac{1}{\rho_0} \frac{\partial P}{\partial z} - \frac{\rho}{\rho_0} g \sin(\theta)$$

(where  $(r, \phi, z)$  are radial distance from the rotation axis, azimuthal angle (longitude) and distance from equatorial plane along the rotation axis and where  $(u, v, w)$  are zonal, radial and  $\Omega$ -directed velocities) has been used to discuss slow, large scale fluid motions between two concentric spherical surfaces. When keeping all Coriolis terms in the momentum equations the fluid is rigid in the direction of the rotation axis, a constraint which forces shearing and no-stretching effects to be performed along this axis, rendering the spherical co-ordinates inappropriate. The change from spherical to cylindrical co-ordinates, favouring the planetary rotation  $\Omega$ , allows us to solve exactly the slow large scale motions at mid and low latitudes. The solution of the problem is made possible by working at the vorticity levels with the thermal wind equations

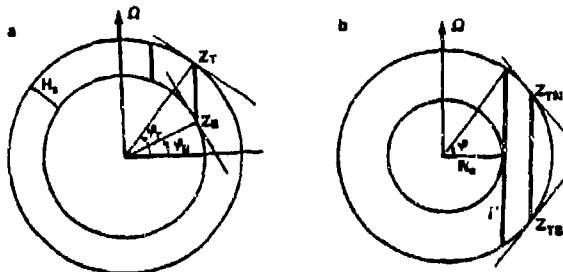
$$\frac{\partial u}{\partial z} = \frac{-g}{2\Omega\rho_0} \left( \sin(\theta) \frac{\partial \rho}{\partial r} - \cos(\theta) \frac{\partial \rho}{\partial z} \right) \quad \frac{\partial v}{\partial z} = +\frac{g \sin(\theta)}{2\Omega\rho_0} \frac{\partial \rho}{r \partial \phi} \quad \frac{\partial w}{\partial z} = -\frac{g \cos(\theta)}{2\Omega\rho_0} \frac{\partial \rho}{r \partial \phi}$$

The combination of the vorticity equations in the meridional plane shows that shearing and stretching along  $\Omega$  are tightly connected by relation  $\sin(\theta) \frac{\partial w}{\partial z} + \cos(\theta) \frac{\partial v}{\partial z} = 0$  which can easily be integrated along  $\Omega$ . At mid-latitude the integration is performed between the solid inner spherical surface and the spherical outer surface, while in the equatorial band, where the solid inner bounding surface vanishes, integration is performed between the southern and northern hemispheric free surfaces (Figure 1).

Illustration of the length of the fluid column between two concentric spherical surfaces along the rotation axis. a) Mid-latitude case. b) Equatorial band.

The positive radial variation of this length at mid-latitude undergoes a dramatic change (jump to a finite negative value) when crossing the cylinder tangent to the solid inner surface ( $r = R_s$ ).

Figure 1



This integration leads to an extension of the Sverdrup relation

$$\frac{Q_T}{\sin(\theta_T)} + \frac{Q_s}{\sin(\theta_s)} = \int_{z_s}^{z_T} v \frac{\partial(\cot(\theta))}{\partial z} dz = - \int_{z_s}^{z_T} \frac{vr}{z^2} dz$$

or

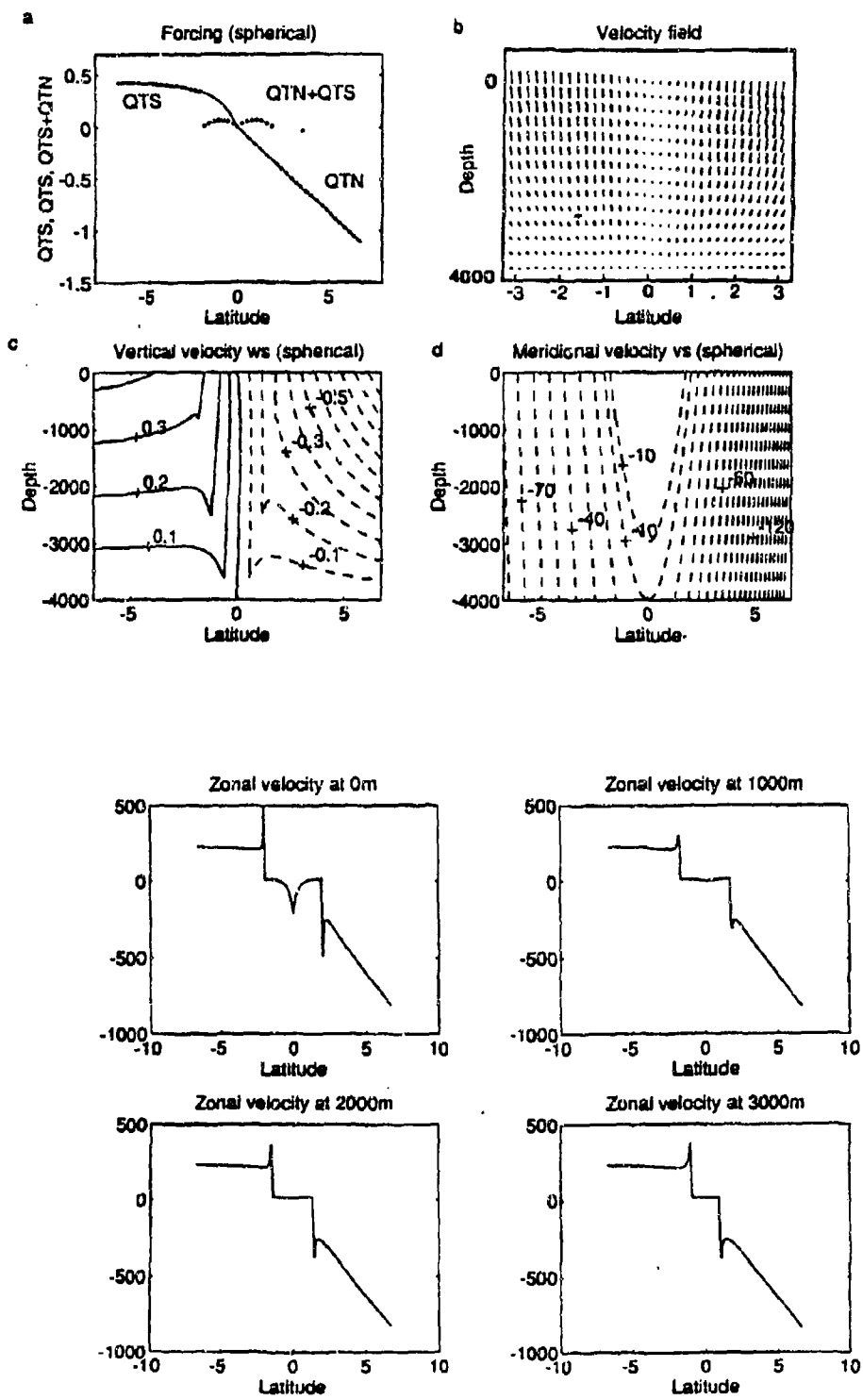
$$\frac{Q_T}{\cos(\theta_T)} + \frac{Q_s}{\cos(\theta_s)} = \int_{z_s}^{z_T} w \frac{\partial(\tan(\theta))}{\partial z} dz = \frac{1}{r} \int_{z_s}^{z_T} wdz$$

(where  $Q_T(\theta_T)$  and  $Q_s(\theta_s)$  are source or sink terms at the inner and outer spherical shells) valid both at mid-latitude and in equatorial regions. In those relations, the beta effect reduces to a purely topographic effect and expresses the varying meridional tilt of the tangent to the spherical shells along  $\Omega$  which in the homogeneous case becomes the radial variation of fluid layer thickness parallel to  $\Omega$ . It is further shown that the column height undergoes rapid variations when approaching the cylinder  $\Gamma$  tangent to the solid inner bounding surface followed by a drastic change at  $\Gamma$  and in its radial variation in the equatorial band (sign reversal of the beta effect). It remains to see whether this cylinder  $\Gamma$  plays an important role in geophysics. Its intersection with the free surface separate mid-latitude dynamics from equatorial dynamics in the simple theory presented here.

When source-sink forcing is included, it is shown that fluid can easily move along  $\Omega$  and can therefore cross the equator (Figure 2). But the TPP dynamics prevent fluid to move across the cylinder  $\Gamma$  outside boundary layers and therefore do not allow for fluid exchange from northern to southern hemisphere. For exchange to occur, zonal vorticity neglected in the above dynamics is needed. Nevertheless, these dynamics show the singular behaviour of the equatorial region in locating the cylinder  $\Gamma$  acting as a wall for meridional fluid motions and promoting the existence of jet like features. Such jets happen to appear each time density interfaces align with  $\Omega$  which, in general, arises in the equatorial plane. The dynamics studied here, need highly restrictive conditions to be applied (small Rossby number regimes) but may influence the behaviour of equatorial zonal jets. Higher order dynamics, instabilities and convection processes should play a major role in reshaping the flow structure in these jet regions located by this linear analysis.

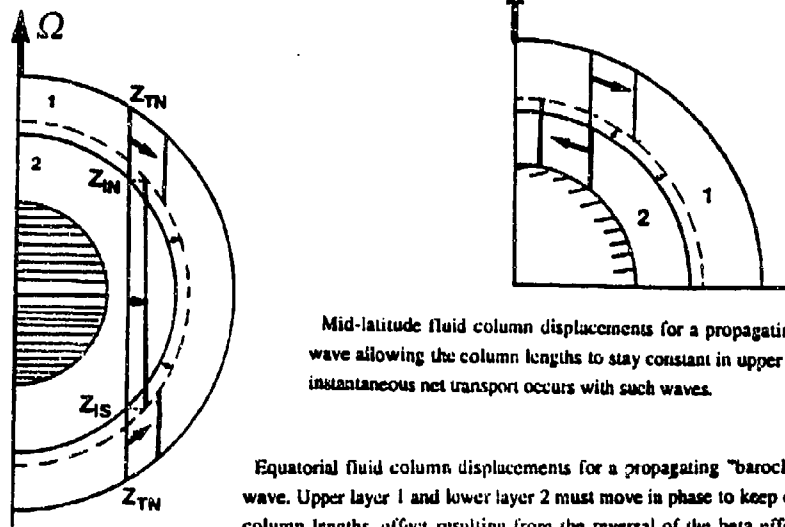
Example of fluid motions convected into spherical co-ordinates at low latitudes compatible with slow flow dynamics. a) gives the meridional structure of the antisymmetric forcing used (sources of fluid in the northern hemisphere and sinks in the southern one). Crosses indicate the forcing to be used for the fluid columns

Figure 2.



It has also been possible to extend and solve exactly for non dispersive Rossby wave dynamics up to the equator. The TPP constraint not only shows that these waves with non divergent character are possible over all the sphere contrary to the traditional view but also shows that baroclinic waves, in the equatorial band, are accompanied by an oscillating net transport. It is the sign reversal of the beta effect along  $\Omega$  which produces this result (Figure 3). It is necessary to emphasize that the high wave phase speeds found for this equatorial mode, need very shallow upper layers to reduce their speeds to realistic values.

Figure 3.



Mid-latitude fluid column displacements for a propagating baroclinic Rossby wave allowing the column lengths to stay constant in upper and lower layers. No instantaneous net transport occurs with such waves.

Equatorial fluid column displacements for a propagating "baroclinic" Rossby wave. Upper layer 1 and lower layer 2 must move in phase to keep constant their column lengths, effect resulting from the reversal of the beta effect along the rotation axis positive in the upper layer and negative in the lower layer. The baroclinic Rossby wave is therefore accompanied with a net radial transport, the upper velocity being more intense than the deeper one.

## II Strong zonal flows

When the zonal flow is strong compared to the meridional one, the above zonal component of the vorticity equation written in spherical co-ordinates becomes  $(2\Omega \cdot \nabla)u = g/\rho_0 \partial \rho / \partial \theta$  and is still valid since the  $O(1)$  non-linear relative vorticity terms cancel out remarkably in case zonal length scales are much larger than meridional ones. This equation, where  $\theta$  is latitude, expresses a balance between the buoyancy torque and the twisting of the full Earth vorticity by the zonal flow  $u$ . This generalization of the mid latitude thermal wind relation to the equatorial case shows that  $u$  may be obtained up to a constant by integrating the "observed" density field *along the Earth rotation axis* and not along gravity as in common mid latitude practice. The simplicity of this result valid in the finite amplitude regime is not shared however by the other velocity components.

Vorticity and momentum equations appropriate to low frequency and predominantly zonal flows are given on the equatorial  $\beta$  plane. These equatorial results and the mid latitude geostrophic approximation are shown to stem from an exact generalized relation that relates the variation of dynamic pressure along absolute vortex lines to the buoyancy field. The usual hydrostatic equation follows when the aspect ratio  $\delta = H/L$  is such that  $\tan \theta_\delta$  is much larger than one. Within a boundary layer region of width  $(H_\delta)^{1/2}$  and centered at the equator, the analysis shows that the usually neglected Coriolis terms associated with the horizontal component of the Earth rotation must be kept. If small, it removes the singular equatorial behaviour.

Figure 4 shows the good agreement of the thermal wind balance for an observed zonal velocity field in the equatorial ocean.

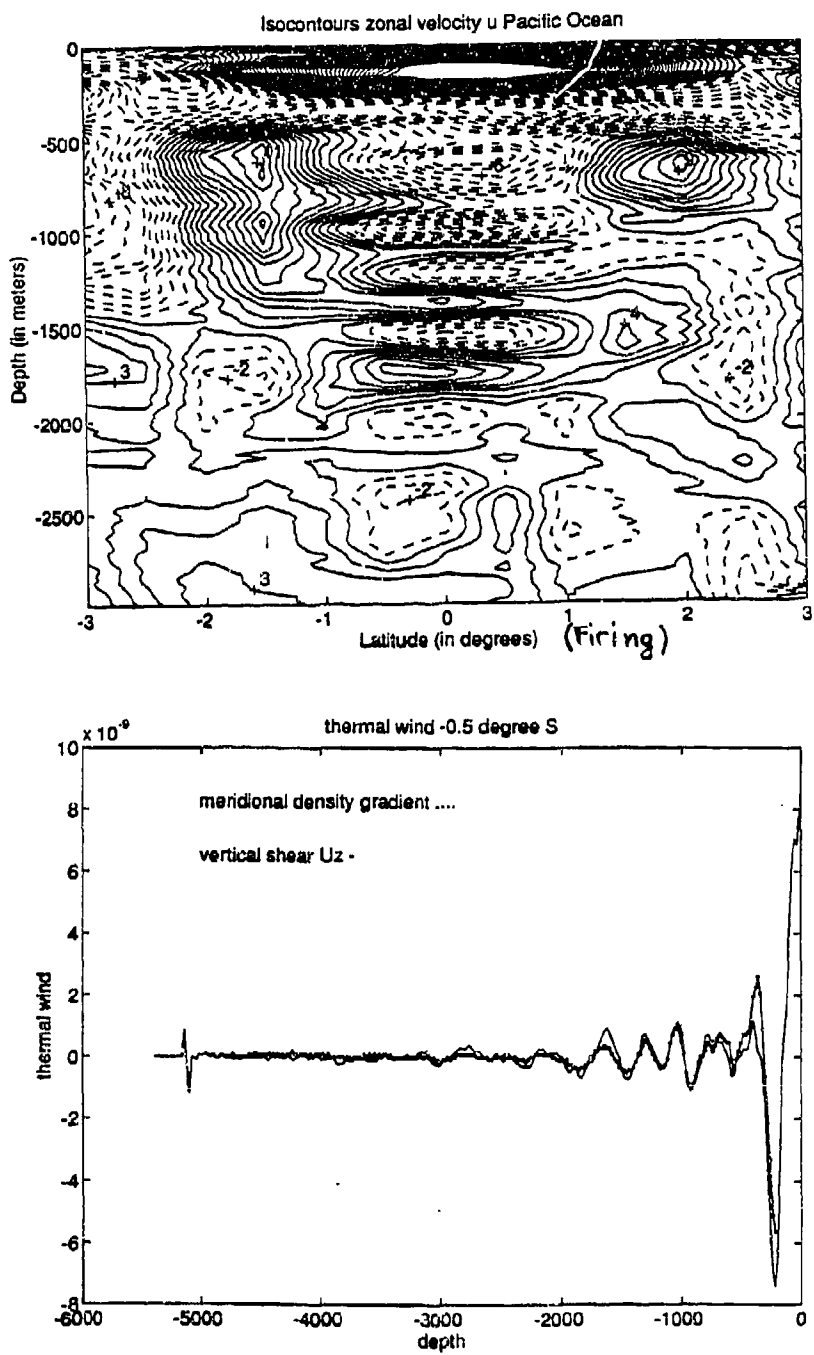
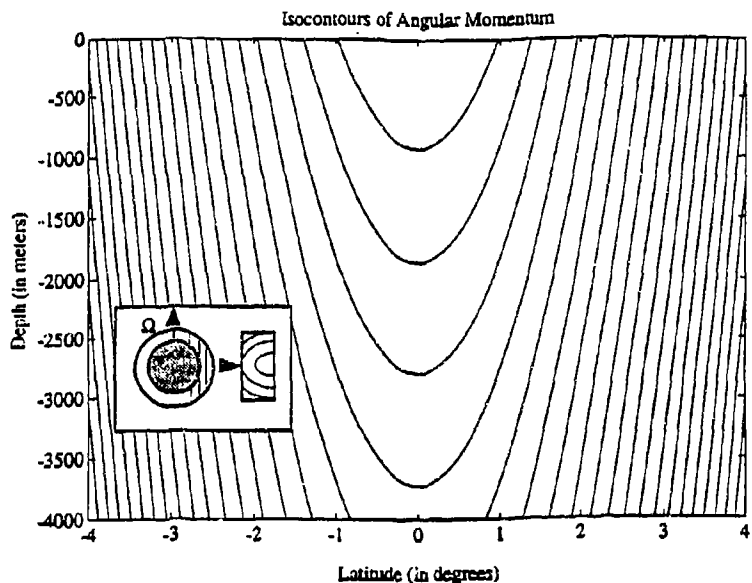


Figure 4.

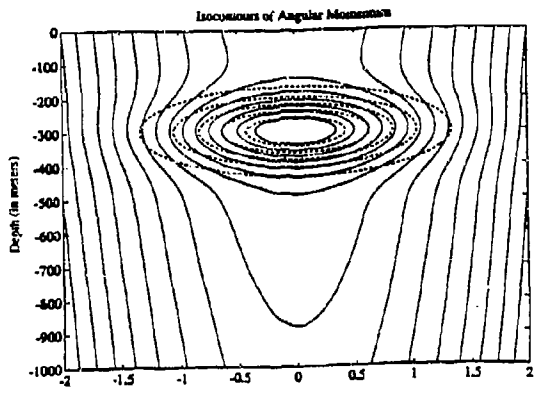
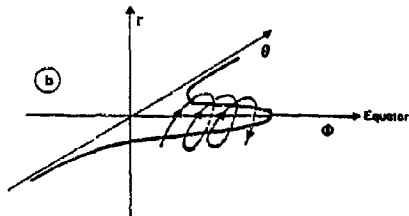
Finally, some solutions of zonally homogeneous, steady, equatorial inertial jets are presented in which the Earth vorticity is easily turned upside down by the shear flow and the correct angular momentum: " $\Omega^2 \cos^2(\theta) + u_r r \cos(\theta)$ " contour lines close in the vertical-meridional plane (Figure 5). Figure 6 illustrates the angular momentum contour lines deduced from the above observed velocity field. They close in the equatorial band.

Figure 5.



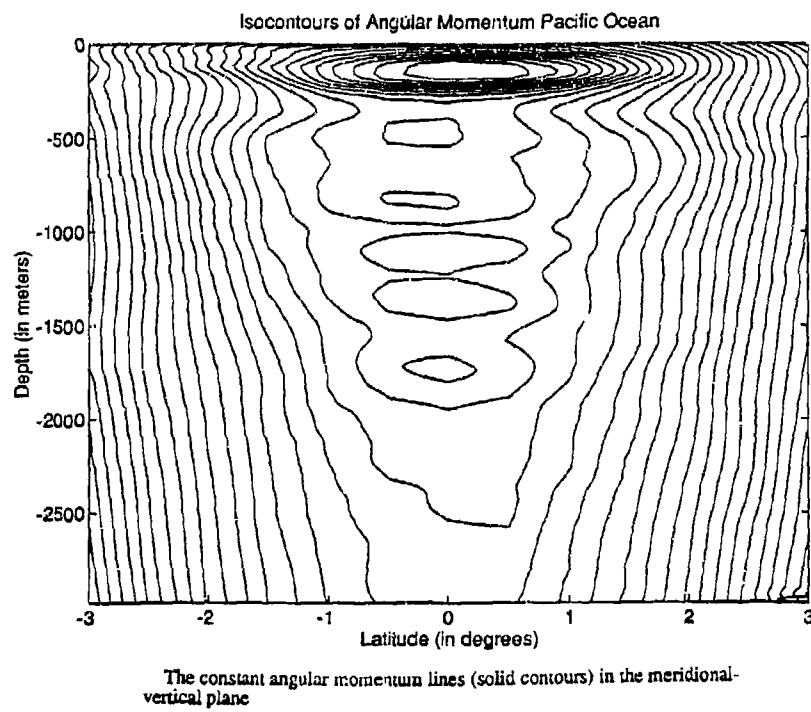
Lines of constant angular momentum  $\Omega[r \cos(\theta)]^2$  in the equatorial region in case the zonal velocity vanishes. These lines are just parallel to the rotation axis. Small figure sketches the way these lines are deformed when cartesian co-ordinates are used.

b) The trajectory of the fluid parcels are helices with generators parallel to the equator, winding themselves around the jet.



a) The constant angular momentum lines (solid contours) in the meridional-vertical plane, between 0 and 1000 meters depth, are pictured for the case of an oceanic eastward, zonal jet centered at the equator. The jet normal to the plane (stippled lines: constant zonal velocity lines) has maximum speeds of  $0.5 \text{ m s}^{-1}$  around 300 m and e-folds over  $1^\circ$  in latitude and 100 m in the vertical. With such shears, well into the geophysical range, the relative vorticity can exceed and turn around the Earth vorticity. When the absolute vortex lines are closed in the vicinity of the jet a steady inertial flow parallel to these solid contours is a solution of the equation of motions.

Figure 6.



**Colin de Verdier, A., and R. Schopp.** 1994: Flows in a Rotating Spherical Shell: the Equatorial Case. *Journal of Fluid Mechanics* (in Press).

**Schopp, R. and A. Colin de Verdier.** 1994: Taylor Columns between two concentric spheres. *Geophys. Astrophys. Fluid Dynam.* (Submitted)

# TURBULENCE DECAY IN STRATIFIED AND HOMOGENEOUS MARINE LAYERS

Iossif D. Lozovatski

*P.P.Shirshov Institute of Oceanology Russian Academy of Sciences, Krasikova  
St.23, Moscow 117851, Russia, fax:(095)-124-5983, j.lozovatsky/ownet*

## 1. Introduction

Important problems in studies of stratified ocean turbulence center around the generation processes on the one hand and regularities of the energy decay in the different patches and layers on the other, depending on background conditions. Marine turbulence is strong intermittent in time and space, so the mean turbulent exchange through stratified layers should be estimated by use of empirical and/or theoretical probability distribution functions of the main turbulence parameters. However space-time averaging evidently leads to underestimating of mixing efficiency because of energy dissipation in the different patches are measured at the various time intervals from patch infancy, i.e. at the different stage of decay. Therefore the probability description of turbulent decay parameters for a set of intermittent patches and layers may significantly improve the estimates of vertical global transport in the ocean.

But at the first stage of marine turbulence decay study it is important to understand the regularities of energy decay in the individual turbulent patch. Laboratory experiments [Hopfinger and Toly, 1976; Flierl et al., 1983; Stillinger et al., 1983; Itsweir et al., 1986; Lienhard and Van Atta, 1990; Gibson, 1991; De Silva and Fernando, 1992] allowed to examine turbulence evolution at the different stage of decay depending on the distances from the energy source (grid or jet turbulence). But it is extremely difficult or even impossible to detect both in time and space the initial stage of turbulent patch origin and to follow the evolution of turbulent energy in the deep ocean pycnocline by using of the traditional methods i.e., vertical microstructure profiling or towing turbulent measurements. Considerably easier to study some aspects of these processes in the marine boundary layers where the sources of turbulent energy can be identified and controlled over a period of time. Turbulence propagates into the water column by diffusion and horizontal or vertical advection from the solid borders or from the air-sea interface. So we can expect to find various turbulent decay phases at the different distances as the turbulence recedes from the boundaries. From this point of view oceanic coastal zone is one of the best natural laboratory for marine turbulence decay study.

Such measurements have been carried out in the Equatorial Pacific [Lilover et al., 1993]. The analysis of turbulence activity variations in the wake of the Equatorial Surface Current (ESC) and in the Pacific Equatorial Undercurrent (EUC) west of the Baker Island ( $0^{\circ}11.7'N$ ,  $176^{\circ}28.7'W$ ) are presented in section 3 to revealed the distinctions between turbulence evolution in the marine boundary layers and in the stratified internal layers.

Some theoretical speculations on a spectral structure of decaying turbulence in a stratified flow is proposed (section 2). It is conceivable that our consideration can help to eliminate a discrepancy between active [Dillon, 1982, 1984; Gregg, 1987] and fossil [Gibson, 1987] turbulence conceptions of oceanic mixing processes.

## 2. Different energy sources and turbulence decay: A spectral model

### 2.1 Active and fossil turbulence approaches

Turbulent cascade and corresponding energy decay in a stable stratified fluid can be described by various spectral models [Lozovatsky, 1986, 1987], in accordance with the relation of the overturn Thorpe scale,  $L_{Th}$ , to the local buoyancy scale  $L_N = c_N(\varepsilon/N^3)^{1/2}$ , where  $\varepsilon$  is the rate of turbulent energy generation,  $N$  is the local Vaisala frequency,  $c_N$  is the nondimensional constant. For the "external" sources of turbulent vorticity like, for example, as high amplitude internal wave breaking,  $L_{Th} > L_N$ . On the other hand, the small scale local shear can generate turbulence with energy containing eddies which maximum size  $L_{Th}$  is under the  $L_N$ , so called "internal" energy source.

According to Gibson's fossil turbulence model, decrease of ratio  $L_{Th}/L_N$  during turbulence decay in the laboratory experiments [Stillinger et al., 1983; Itsweir et al., 1986;] means that the  $L_N$  scale should decrease while  $L_{Th}$  remains constant. This leads to assumption of a "turbulence memory", i.e. the initial overturn scale  $L_{Th}$  is saved in scalar fluctuations. However Dillon [1982, 1984], Gregg [1987], Peters et al. [1988], based on field dissipation measurements presented a lot of examples around of the permanent value of  $L_{Th}/L_N$  ratio. In other words, in a shear turbulence the eddies scales adapt to the changing of local buoyancy, so called active turbulence model, and therefore the concept of "turbulent memory" is open to question.

In this reason we would like to consider how small scale velocity and temperature spectra vary in shape follow to the type of energy source and how the spectral approach reflects the concepts of active and fossil turbulence.

### 2.2 Active turbulence regime

An increasing of the local shear at the vertical scales less than  $L_{IW} = b_{IW}/N^2$  can produce the local ("internal") source of turbulent energy. Here  $L_{IW}$  is the external scale of weak internal waves turbulence [Lozovatsky, 1987] (herein referred to as L87) and  $b_{IW}$  is the total internal wave energy. For the Garrett-Munk standard model parameters  $b_{IW} = 34 \text{ cm}^2/\text{s}^2$ ,  $N = 5.3 \cdot 10^{-3} \text{ s}^{-1}$  [Garrett and Munk, 1975]  $L_{IW}$  is found to be equal to 9.7 m. So, the transition point,  $L_c = 2\pi/k_c$ , between the familiar  $k^{-2}$  and  $k^{-3}$  subranges in the vertical internal wave spectra for the deep ocean locates as usual in the vicinity of  $L_{IW}$ . Therefore, if in a relatively thin layer shear enhance is accompanied by significant decreasing of the Richardson number, a new additional fluxes of turbulent energy  $P_t = -\langle u'w' \rangle U_z$  and buoyancy  $B = -(\rho/g)\langle \rho'w' \rangle$  are generated. The main size of energy containing eddies,  $L_{Th}$ , in such turbulent patch has to be determine by the parameters of the energy source, i.e. the local momentum flux  $\langle u'w' \rangle$ , and the local shear  $U_z$ :  $L_{Th} = L_{U_z} = c_{U_z} \langle u'w' \rangle / U_z$ , were the spectral constant  $c_{U_z}$  will be introduce bellow. Notice that the same definition for the Thorpe scale were used by Dillon [1982]. It can be assumed that mean background shear is approximately constant at the time

where  $\alpha_2$  and  $\alpha_{2T}$  - the spectral constants that should be determined. The upper,  $k_{U_z}$ , and lower boundaries,  $k_R$ ,  $k_T$ , of these subranges are follow:

$$k_{U_z} = c_{U_z} U_z^{3/2} / \varepsilon^{1/2}, \quad (7)$$

$$k_R = c_R N / (\varepsilon / U_z)^{1/2}, \quad k_T = c_T (\varepsilon / U_z)^{1/2} T_z^2 / \varepsilon_T, \quad (8), (9)$$

where  $c_{U_z}$ ,  $c_R$  and  $c_T$  are expressed by use of  $\alpha_2$ ,  $\alpha_{2T}$  and  $\mu_T$ . We would like to emphasize that the transition points between production and inertial-convective subranges in spectra of velocity as well as of temperature fluctuations are located at the common wavenumber (7). By this is meant that typical sizes of main energy containing eddies (overturns) are equal to the vertical sizes of high amplitude temperature inhomogeneities (density inversions), that commonly is expressed in terms of rms Thorpe scale or Elision scale:  $L_E = 2\text{rmsp}' / \rho_z$ . So, the scale  $L_{U_z} = 2\pi / k_{U_z}$  is a unique spectral scale that is uniform up to the constant values for ever hydrophysical fields. Appear to be the spectral scale  $L_{U_z}$  do represents the

Thorpe scale  $L_{th}^{rms}$  for the active turbulence model.

If mean shear are kept reasonable time in stationary state by external background processes (drift currents, equatorial undercurrents, near bottom flows, etc.), the spectral scale  $L_R = 2\pi / k_R$  should coincide with vertical size of mixing layer (or patch). According to (7), (8) the ratio

$$\frac{L_R}{L_{U_z}} = \left( \frac{Ri_{cr}}{Ri} \right)^{1/2}, \quad (10)$$

where  $Ri = N^2 / U_z^2$ , is characterized the width of production subrange. We introduced a critical Richardson number  $Ri_{cr}$  equal to  $\alpha_1^3 / \alpha_2^2 \mu = 0.11\alpha_2$ . If  $Ri \geq Ri_{cr}$  the production interval can not exist or disappears. In such situation the scales  $L_R$  and  $L_{U_z}$  both transfer to the buoyancy scale  $L_N$ . (For  $Ri_{cr} = 0.25$ , the spectral constant  $\alpha_2$ , that had to be determined, is equal to 0.67 and for  $Ri_{cr} = 0.1$ ,  $\alpha_2 \approx 1$ ).

In scalar fields like temperature the end of active turbulence phase is defined by equivalence  $L_T / L_{U_z} = 1$ , where  $L_T = 2\pi / k_T$  from (9). It is easy

$$\frac{L_T}{L_{U_z}} = \frac{c_{U_z} \chi_T U_z^2}{c_T T_z^2 \varepsilon} = \alpha_{TR} \gamma \frac{Ri_{cr}}{Ri} \frac{K_T}{K_N}, \quad (11)$$

where  $\alpha_{TR} \approx 4.9$  and  $\gamma$  is a mixing efficiency,  $\gamma = Rf / (1 - Rf)$ ,  $Rf = Pr_c Ri$  is a flux Richardson number. The ratio of turbulent diffusivities in Eq.(11) can be defined in terms of activity parameter,  $A_G$ , introduced by Gibson, namely:

$$\frac{K_N}{K_T} = 13\gamma \left( A_G \right)^{-2} \quad (12)$$

intervals long enough relative to the typical time of turbulence generation. In this case the local momentum flux in the patch, affecting against this mean shear, may already produce the permanent energy source with the rate of kinetic energy generation equal to  $P_t$ . Owing to initial destroy of stratification by local overturn, the following energy generation goes on in a patch with negligible density gradient. Therefore the rate of turbulent temperature generation is controlled by temperature flux  $\langle T_w \rangle$  that acts against "large scale components" of turbulent gradients,  $GR_T(k)$ , rather than against mean gradient  $T_z$ . Following [Monin

and Yaglom, 1975]  $GR_T^2(k) = \int_{k_{U_z}}^k k^2 E_T(k) dk$ , were  $E_T(k)$  is a temperature

spectral density. Turbulence spectra in the vicinity of the local shear scale  $L_{U_z}$  can be found by use of a system of the spectral balance equations in follows form:

$$\varepsilon = -U_z \int_{k_{U_z}}^k E_{uw}(k) dk + W(k), \quad \chi_T = -GR_T(k) \int_{k_{U_z}}^k E_{Tw}(k) dk + W_T(k), \quad (1), (2)$$

where  $E_{uw}(k)$  and  $E_{Tw}(k)$  are spectra of turbulent momentum and heat fluxes,  $W(k)$  and  $W_T(k)$  are spectral transfers of turbulent energy and temperature inhomogeneities,  $\varepsilon$  and  $\chi_T$  are kinetic energy and temperature dissipation rates. Following Kovaschnay [1948] we introduce the simplest hypothesis to parameterize spectral gradients and transfers, i.e. to express  $E_{uw}(k)$ ,  $E_{Tw}(k)$ ,  $W(k)$  and  $W_T(k)$  in terms of wave number  $k$ , velocity spectrum  $E(k)$ , and temperature spectrum  $E_T(k)$ . For the nondimensional variables

$$x = \varepsilon^{1/2} U_z^{3/2} k, \quad \psi_E = \varepsilon^{-3/2} U_z^{5/2} E(k), \quad \psi_T = \chi_T^{-1} \varepsilon^{-1/2} U_z^{5/2} E_T(k)$$

the Eqs.(1) and (2) are represented as:

$$1 = \alpha x \psi_E (1 + \alpha_0 x^{3/2} \psi_E^{1/2}), \quad 1 = \alpha_T \Pr_t^{-1} x^{5/2} \psi_T^{1/2}, \quad (3), (4)$$

where  $\alpha$ ,  $\alpha_0$ , and  $\alpha_T$  are the universal spectral constants and  $\Pr_t = K_T/K_M$  is the turbulent Prandtl number,  $K_M$  is a turbulent momentum diffusivity. The asymptotic solution of Eqs.(3), (4) for  $\alpha_0 x^{3/2} \psi_E^{1/2} \gg 1$  provides well known inertial-convective intervals,  $\psi_E = \alpha_1 x^{-5/3}$ ,  $\psi_T = \alpha_T x^{-5/3}$ , were  $\alpha_1 = 0.48$  and  $\alpha_T = 0.7$  are the corresponding spectral constants. At the lower wave numbers,  $x \ll \alpha_0^{-2/3} \psi_E^{-1/3}$ , between the inertial-convective interval ( $E(k) = \alpha_1 \varepsilon^{2/3} k^{-5/3}$ ,  $E_T(k) = \alpha_T \chi_T \varepsilon^{-1/3} k^{-5/3}$ ) and the interval of "weak turbulence" ( $E(k) = \mu N^2 k^{-3}$ ,  $E_T(k) = \mu_T T_z^2 k^{-3}$ ,  $\mu \approx 1$ ,  $\mu_T \approx 0.3$ ) the additional narrow spectral intervals, so called "production" subranges, may appear. Velocity and temperature spectra for such intervals can be expressed in the dimensional variables as

$$E(k) = \alpha_2 (\varepsilon / U_z) k^{-1} \quad \text{and} \quad E_{2T}(k) = \alpha_{2T} (U_z / \varepsilon)^{1/2} k^{-2}, \quad (5), (6)$$

When Eq.(12) is compared with that of Eq(11), it is apparent that  $A_G$  takes the constant value if  $Ri = Ri_{cr}$ :  $A_G = 0.61$  for our set of the values for universal spectral constants.

So, if the turbulent patches are generated at the background of the permanent mean shear, the linear relation between the Thorpe scale,  $L_{th}$ , and the Ozmidov scale,  $L_N$ , should exist, i.e. the Dillon's conception on turbulence evolution in the "active regime" is confirmed. But, if external shear decreases ( $Ri \rightarrow Ri_{cr}$ ), the spectral scales  $L_R$ ,  $L_T$ , and  $L_{U_2}$  give way to  $L_N$ . For the higher values of Richardson number inertial-convective subrange disappears and  $L_N$  approaches to the Kolmogorov scale  $L_K = (\nu^3/\epsilon)^{1/4}$ . When  $L_N$  decreases to  $8L_K$  it converts to  $L_G = c_G(\nu/N)^{1/2}$ , where  $\nu$  is molecular viscosity and  $L_G$  is named by Gibson [1987] as the fossil Kolmogorov length scale,  $c_G = 21$ . From this point on turbulence decay is follows the fossil turbulence regime. Such type of turbulence evolution when an internal source of turbulent energy appears at the background of an external stratification, i.e. when  $L_R$ ,  $L_T$ , and  $L_{U_2}$  are smaller than  $L_N$ , was named in L87 as the regime of week internal stability. Turbulence decay in the conditions of week internal stability is characterized in L87 by the following limit on the Richardson number values:  $Ri < R_* \approx (c_{R_*} P_t / Ri_{cr})^{1/2}$ , where  $c_{R_*} \approx 0.1$ , and moreover  $Ri_{cr} < 0.13/P_t$ . It is known that turbulent Prandtl number in a stable stratified fluid is in excess of 1, so it is clear that  $Ri_{cr}$  must be less than 0.13, i.e. is close to 0.1. On the other hand, it is a matter of general experience that  $Ri_{cr}$  does close to 0.1, so  $P_t$  should be greater but close to 1 also. As a consequence, in the turbulent regime of week internal stability the turbulent coefficients of heat (buoyancy) and momentum exchange are approximately the same while  $K_t < K_m$ . It seems to be the common situation, when  $P_t = K_m/K_t \gg 1$ , relates to turbulence decay under strong internal stability, i.e. if  $Ri > R_*$ .

### 2.3 Fossil turbulence regime

Transition from active to fossil turbulence that was analyzed in previous paragraph might be subjected to criticism because of someone can say that turbulent motions are simply cut off at the scales of the order of  $L_G$ , rather than transfers to a fossil state. But it will be shown that turbulence decay in condition of strong internal stability is reasonably described in terms of fossil turbulence, i.e. if  $Ri > R_*$ . In spectral consideration it means regime of buoyancy subrange [Monin and Yaglom, 1975]. On the assumption of buoyancy forces may highly exceed viscous dissipation for certain scales of velocity and temperature fluctuations, the turbulent spectra  $E(k)$  and  $E_t(k)$  must contain well known buoyancy subranges, namely  $E(k) \propto k^{-11/5}$  and  $E_t(k) \propto k^{-7/5}$ . At high wave numbers these subranges are bounded by the Boldgiano - Obukhov buoyancy scale  $L_* = c_* \epsilon^{5/4} \chi_T^{-3/4} (-a_T g)^{-3/2}$ , where  $a_T$  is the coefficient of thermal expansion,  $g$  is gravity,  $c_*$  is the spectral constant. In the course of decay the buoyancy subrange is expanded to lower as well as to higher wave numbers, connecting with the interval of week turbulence from the one side and with the viscous-convective subrange from the other. As the result two new

spectral scales are appeared:

$$L_*^{\nu} = c_*^{\nu} \frac{\chi_T^{1/2} (-a_T g) \nu^{5/4}}{\varepsilon^{5/4}} \quad \text{and} \quad L_{**} = c_{**} \frac{\chi_T^{1/2}}{(-a_T g)^{1/4} T_z^{5/4}}, \quad (13), (14)$$

with two constants  $c_*$  and  $c_{**}$ . If we determine the squared buoyancy frequency as  $N^2 = (-a_T g) T_z$ , the spectral scale  $L_{**}$  from Eq.(14) is equivalent to the Thorpe scale

$$L_{Th} = 3 \frac{\chi_T^{1/2}}{N^{1/2} T_z} \quad (15)$$

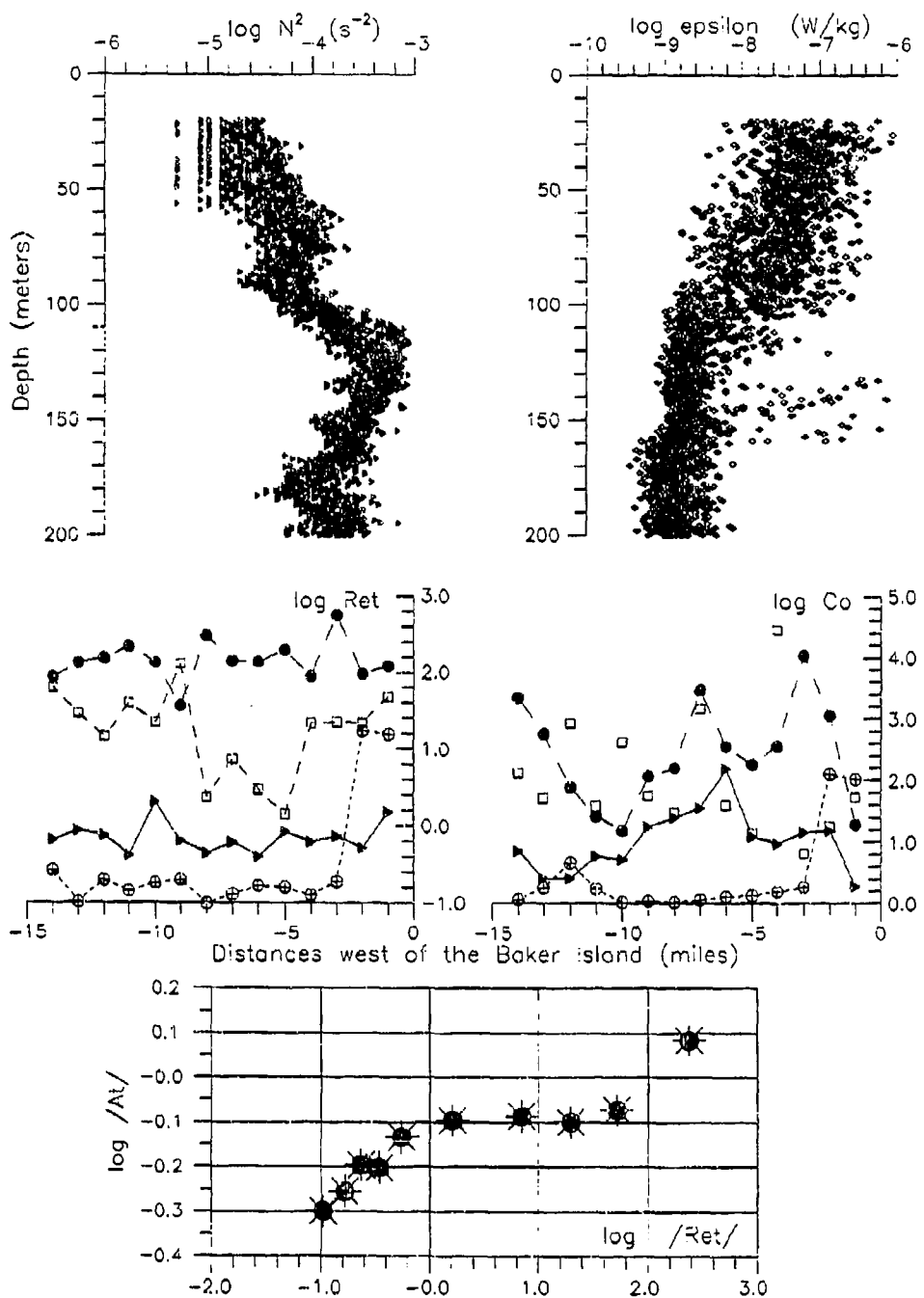
with accuracy to the value of constant. In such transition regime only, when viscous dissipation removes from the set of main turbulent parameters, the Thorpe scale, Eq.(15), does not correlate with Ozmidov scale and the fossil turbulence conception is truly realized. In the next section we will consider applicability of active and fossil models to decaying turbulence in the Pacific Equatorial Surface Current (ESC) and Equatorial Undercurrent (EUC) west of the small equatorial island.

### 3. Turbulence intensity variations: Pacific equatorial measurements

Dropsonde microstructure measurements were carried out in the equatorial Pacific near the Baker Island ( $0^{\circ}11.7'N$ ,  $176^{\circ}28.7'W$ ) in October 1990 from r/v *Akademik Kurchatov*. Diameter of the island is about 1 mile. Its presence produces a westward turbulent wake in the upper 100 m layer downstream of ESC and an eastward EUC wake about 50 m in thickness around the middle core depth  $\bar{z}_{core} = 210$  m. Moreover a turbulent band is appeared at the EUC depths in front of the island also. In addition to these island caused wakes and eddies the permanent vertical shear between ESC and EUC may produce turbulence in the depth range of 130 - 160 m. So we can analyze turbulence decay in such "natural laboratory" at the different depths and horizontal distances away from the generation sources.

Buoyancy frequency  $N^2(z)$  and energy dissipation rate  $\varepsilon(z)$  in the depth range of 20 - 200 m over a length of 13 miles are presented in the figure at the upper two panels. These data were obtained by microstructure dropsonde BAKLAN and standard NBIS CTD/ACM at 14 points each mile as the ship drifted directly westward from the island. Details of instruments, calibration and data processing technique as well as background hydrology can be found in Lilover et al.[1993]. ESC velocities were about of  $-50$  cm/s near the surface. In the EUC core zonal component  $\bar{u} \approx +70$  cm/s.

The thickness of relatively weak stratified upper layer close coincides with the lower boundary of the ESC turbulent wake,  $h_{wake}$ , which was marked by the epsilon level of  $\varepsilon \geq 4 \cdot 10^{-9}$  W/kg. So,  $h_{wake}$  decreased from 105 m near the island to 90 m at the distance of 9 - 14 miles downstream. In spite of mean exponential  $\varepsilon$  decreasing from the top down across the wake, horizontal  $\varepsilon$  variations along the wake achieved two orders in magnitude at all depths. Extremely high intermittence of the turbulent Reynolds number,  $Re_t = \gamma \varepsilon / N^2$ ,  $\gamma = 0.2$ , and Cox number,  $Co = \langle T_z'^2 \rangle / T_z^2$ , along the ESC are shown at the



At the upper panels: buoyancy frequency and epsilon vs depth for all casts. At the middle panels: the turbulent Reynolds number,  $Ret$ , and the Cox number,  $Co$ , variations at  $z = 25m$  (●),  $70m$  (□),  $140m$  (⊕),  $180m$  (▲). At the lower panel: phase diagram for total data set,  $|A|/|Ret|$  and  $|Ret|$  are equal probability averaged.

middle panels in the figure. The  $Re_t$  values even just under the entirely mixed surface layer ( $z = 25$  m) are in the range of 40 to 630, whereas  $Re_t$  variations at the lower wake depths ( $z = 70$  m, for instance) are in excess of two orders:  $1.3 \pm 120$ . Cox number variability is much higher:  $\log Co = 1.1 \pm 4.1$  at  $z_{25}$  and  $\log Co = 0.8 \pm 4.2$  at  $z_{70}$ .

In the pycnocline, below the upper SEC wake occupied layer,  $\epsilon(z)$  are mainly small and slightly varied except of depth range 130 - 160 m, that corresponds to the high shear zone between the SEC and EUC. But high  $\epsilon$  values in that zone consist of a small part of all  $\epsilon$  data in this layer. According to Reynolds number values at  $z = 140$  m, active turbulence are revealed in the first 2 casts only. Mixing activity, characterized by Cox number,  $Co = 100$ , is comparatively high at that depth within two miles band near the island. Beginning from the third mile west off the island turbulent as well as mixing disappear completely. Consequently, the interface shear is not sufficient to be an "internal energy source" that could generate small scale turbulence at the background of strong stratification ( $N > 15$  cph). However owing to mesoscale boundary layer mixing near the island, that leads to overall stratification weakening in the pycnocline, the interface shear can overcome buoyancy forces and produce shear turbulence. Such mechanism is bounded near the island and therefore turbulence decays rapidly at the distance of one mile.

In the EUC,  $z = 180$  m,  $Re_t$  are small and little affected,  $Re_t \approx 0.6$ , exceeding 1 twice only, whereas the  $Co$  values at that depth show an evident tendency to increasing from 2 to 160 at the first 6 miles west off the island with the following decreasing to the initial small values over a length of the next 6 miles upstream. Some similarity of  $Co$  horizontal variability in the EUC and ESC allows to assume that island generated boundary eddies, which are advected downstream in the upper layer, may exert some action on mixing enhance in the relatively weak stratified undercurrent core. But without support of "external" background shear active turbulence quickly converts to fossil state, that appear to be reflected in the figure.

Finally, let us consider the hydrodynamics phase diagram (lower panel) that was calculated for total data set (2620 samples in each row) by use of equal probability averaging. Every point,  $/At//Re_t/$ , corresponds to the arithmetic averaged activity parameter  $A_G$ , Eq.12, at the equal 10% intervals of the rearranged  $Re_t$  row. Thus, three turbulent regimes are clear revealed in this figure. First, in the wide range of the Reynolds numbers, from 100 to 1,  $/At/$  are constant, that means in accordance with Eqs. (10) - (12) the linear dependence between  $L_x$ ,  $L_y$ , and  $L_z$ , or in the other words - between

Thorpe scale and Ozmidov scale (active turbulence evolution regime). Secondly, for  $/Re_t/ < 1$   $/At/$  are dropped, so the tendency to achieve a fossil turbulence regime, Eqs. (13) - (14), is evident. And thirdly, we can identified a generation regime,  $/Re_t/ > 100$ . At such high Reynolds numbers turbulent activity is fast decreased to the stationary state,  $/At/ = \text{const}$ , and the following decay leads to the fossil turbulence,  $/Re_t/ < 1$ ,  $/At/ < 1$ .

**Acknowledgments.** I am indebted to Anatoly Erofeev, Valery Nabatov and Madis Lilover for assistance in the collection and processing of the data. I am grateful to Mark Baker from JHU and especially to Carl Gibson, who participated in the cruise, for useful discussions and for the help to receive the permission for measurements near the USA Baker Island. I wish to express my appreciations for Tom Dillon from OSU, who provided me by powerful Notebook computer in frame of our collaboration under ONR grant. This work was partially supported also by ISF ES2-2291-095 and RFFI 94-05-16371 grants.

## References

Gibson,C.H., Fossil turbulence and intermittency in sampling oceanic mixing processes, *J. Geoph. Res.*, 92, 5383-5404, 1987.

Gibson,C.H., Laboratory, numerical, and oceanic fossil turbulence in rotating and stratified flow, *J. Geoph. Res.*, 96, 12549-12566, 1991.

Gregg,M.C., Diapycnal mixing in the thermocline: A review, *J. Geophys. Res.*, 92, 5249-5286, 1987.

De Silva,I.P.B. and H.J.S.Fernando, Some aspects of mixing in a stratified turbulent patch, *J. Fluid Mech.*, 240, 601-625, 1992.

Dillon,T.R., Vertical overturns: A comparison of Thorpe and Ozmidov scales, *J. Geoph. Res.*, 87, 9601-9613, 1982.

Dillon,T.R., The energetic of overturning structures: Implication for the theory of fossil turbulence, *J. Phys. Oceanogr.*, 14, 541-549, 1982.

Flierl,G.R., M.E.Stern and J.A.Whitehead, The physical significance of modons: Laboratory experiments and general integral constraints, *Dynamics of Atmosphere and Oceans*, 7, 233-263, 1983.

Garrett,C. and W.Munk, Space-time scales of internal waves: a progress report, *J. Geoph. Res.*, 80, 291-297, 1975.

Hopfinger,E.J. and J.-A.Toly, Spatially decaying turbulence and its relation to mixing across density interface, *J. Fluid Mech.*, 78, 155-175, 1976.

Itsweir,E.C., K.N.Helland and C.W.Van Atta, The evolution of grid generated turbulence in a stable stratified fluid, *J. Fluid Mech.*, 162, 299-338, 1986.

Kovaszhnay,L.S.G., Spectrum of locally isotropic turbulence, *J. Aeronaut. Sci.*, 15, 745-753, 1948.

Lienhard,J.H. and C.W.Van Atta, The decay of turbulence in thermally stratified flow, *J. Fluid Mech.*, 210, 57-112, 1990.

Lilover,M.J., I.D.Lozovatsky, C.H.Gibson, and V.N.Nabatov, Turbulence exchange through the equatorial undercurrent core of the Central Pacific, *J. Marine Systems*, 4, 183-195, 1993.

Lozovatsky,I.D., Interpolation formulae for the spectra of small scale turbulence in a stable stratified ocean, *Atmosph. and Oceanic Phys.*, 22, 94-96, 1986, (in Russian).

Lozovatsky,I.D., A spectral model for vertical structure of the hydrophysical fields in the ocean, *Oceanological Res.*, No.40, 23-34, Moscow, 1987, (in Russian).

Stillinger,D.S., K.N.Helland and C.W.Van Atta, Experiments of the transition of homogeneous turbulence to internal waves in a stratified fluid, *J. Fluid Mech.*, 131, 91-122, 1983.

Monin,A.S. and A.M.Yaglom, *Statistical Fluid Mechanics: Mechanics of turbulence*, 2, The MIT Press, Cambridge, Massachusetts, 1975.

Peters,H., M.C.Gregg and J.M.Tool, On the parameterization of equatorial turbulence, *J. Geoph. Res.*, 93, 1199-1218, 1988.

## OBSERVATIONS OF INTERNAL WAVE REFLECTION AND MIXING AT A SEAMOUNT

Charles C. Eriksen

School of Oceanography WB-10, University of Washington, Seattle WA 98195  
USA

The spectrum of oceanic internal gravity waves is remarkably uniform except at sites where wave energy is suspected to be supplied to or drawn from the wave field, notably boundary regions such as the ocean surface, where wind stress generates near-inertial internal waves, and the ocean bottom, where waves reflect (Wunsch and Webb, 1979). For a smooth flat bottom, reflection does little to alter the frequency-wavenumber spectrum of internal waves. Reflection from a sloping boundary, however, quite generally requires waves to change wavenumber magnitude and orientation (Eriksen, 1982). Because group speed of internal waves is proportional to wavelength, waves reflected to shorter scale must have higher energy densities to conserve energy transport normal to a sloping bottom. Wave rays inclined at slopes matching bottom slopes will amplify most severely. Oceanic topography quite commonly includes slopes which match internal wave ray inclinations over a wide range of the band of frequencies for which free internal waves propagate. While linear theory predicts spectral enhancement over a sloped planar bottom to extend indefinitely, oceanic observations demonstrate that the effects of reflection decay away from the bottom over a few hundred meters. Within the region of wave enhancement, density overturns are commonly found, indicating mixing.

An advective-diffusive balance of oceanic properties on basin scales predicts an effective vertical diffusivity a decade or more higher than is found by in situ observations in the open deep ocean (Garrett, 1979a, Gregg, 1987). Munk (1966) suggested enhanced vertical mixing near the lateral boundaries but did not identify a plausible mechanism. Armi's (1978) suggestion that bottom boundary layer turbulence produced by quasi-geostrophic eddies was the mechanism was refuted by Garrett (1979b) as being not sufficiently energetic. Only a small fraction of the energy transfer that must be involved in internal wave reflection in order that the spectrum relax to its open deep ocean shape is sufficient for mixing at the boundaries to compensate for weak mixing in the ocean interior (Eriksen, 1985).

Detailed observations of the internal wave reflection process and boundary boundary mixing it produces have only recently been collected. The study presents the results of a moored array experiment on the steep flank of a seamount where current and temperature measurements were collected for more than a year, giving a very stable statistical description of the oceanic internal wave field and occurrence of mixing. The internal wave reflection process found on a seamount flank must also occur quite generally over any sloping topography in the ocean, from islands and mid-ocean ridges to continental margins.

We set a 3-mooring array on Fieberling Guyot (32° 25'N, 127° 48'W), a large seamount 1000 km west of San Diego in the eastern North Pacific Ocean, to observe internal wave reflection. The moorings were set roughly 300 m apart on a relatively smooth portion of the seamount's southwestern flank where bottom depths were in the range 1500-1650 m and the bottom slope was 45%. Two of the moorings extended 300m off the bottom and the

third had its top at 100m depth. The tall mooring was instrumented with current meters and temperature recorders closely spaced as closely as 5 m apart from 20 to 300 m off the bottom while the shorter moorings were more sparsely instrumented. The close spacing, both vertical and horizontal, insured that the instruments formed a coherent 3-dimensional array for motions across the entire internal wave band of frequencies. Buoyancy frequency was estimated from Conductivity-Temperature- Depth (CTD) casts made in two surveys by Roden(1994). Near the bottom at the moored array, buoyancy frequency was about 1.0 cph. The CTD casts verified that temperature and salinity were very well correlated so that temperature could reliably be used to estimate density.

The moored measurements indicate variance at free internal wave frequencies is dominated by waves reflected off the sloping seamount flank. In contrast to the vertically symmetric, horizontally isotropic, broadband open ocean internal wave field described by Garrett and Munk (Munk, 1981), current and temperature spectra at depths within several hundred meters of the bottom are peaked at the local critical frequency (the frequency for which internal wave rays are parallel to the local bottom slope). They carry signatures of waves having originated by reflection off the slope: horizontal currents are aligned across isobaths, phase propagates downward and toward shallow water at frequencies above the critical frequency and upward and toward deeper water at frequencies below the critical frequency. These signatures are the result of wavenumber amplification upon reflection, leading to horizontal turning of incident rays to directions normal to isobaths and increased energy density of reflected waves over incident ones.

The spectrum of reflected waves is dominated by a single wavenumber at each frequency, unlike the presumed broadband Garrett-Munk spectrum of incident waves. This single wavenumber is that which results from reflection of incident waves of the gravest open-ocean baroclinic mode. This narrowbandness is likely the result of the breaking and consequent loss of distinct identity of second and higher baroclinic mode incident waves. That these waves break can be expected from amplification of currents to levels that exceed phase speeds of reflected waves. Not only are Richardson numbers over 10m vertical scale less than unity roughly half the time near the sloping bottom, but temperature inversions are frequently observed. While the wavenumber slopes inferred from the phase structure of the dominant complex empirical orthogonal function describing current and vertical displacement variance are consistent with those predicted by linear internal wave theory, wavenumber magnitudes inferred from vertical displacement are roughly 3 times higher than those inferred from horizontal current. This discrepancy may be evidence that even the reflection of the lowest baroclinic mode is governed by nonlinear balances.

Since temperature is tightly correlated with salinity at the measurement depths, temperature inversions can be interpreted as density overturns. These appear and disappear with time scales of a few tens of minutes, comparable to the time scale associated with internal waves at the local critical frequency (about 2.5 hours) and are distributed nearly identically in records which have been low-pass filtered to remove tidal and lower frequency variance as in unfiltered records. They are taken to be a signature of internal wave breaking and a direct result of wave amplification from reflection. Calculating how much potential energy production is associated with unstable density differences observed over fixed vertical separations depends somewhat on assumptions of how overturns

relax. If we assume that unstable gradients relax to at least neutral stability, we find rate of potential energy production to be in the range 0.5 - 2.0 microwatts per cubic meter. This would require internal wave energy flux of roughly 0.2 milliwatts per square meter to maintain, an amount equivalent to about 1% of the incident wave energy flux.

The rate of reflection-induced internal wave breaking implies local equivalent turbulent buoyancy diffusivities of  $1.6 - 6.4 \times 10^{-4} \text{ m}^2/\text{s}$ . This level is two orders of magnitude above those found from microscale turbulence measurements in the ocean interior and about an order of magnitude above the level thought necessary to maintain thermocline structure on a global scale based on deep water renewal rates. Roughly speaking, mixing rates in the bottom tenth of the water column are an order of magnitude higher than those in the portion above. That is, mixing due to internal wave breaking concentrated near the ocean bottom is more intense roughly in inverse proportion to the fraction of the water column in which it occurs and at an intensity sufficient to explain much of the mixing required by basin scale property balances. The implication is that the deep ocean mixes substantially as a result of internal wave reflection at its boundaries.

Armi, L., 1978: Some evidence for boundary mixing in the deep ocean. *J. Geophys. Res.*, 83, 1971-1979.

Eriksen, C. C., 1982: Observations of internal wave reflection off sloping bottoms. *J. Geophys. Res.*, 87, 525-538.

Eriksen, C. C., 1985: Implications of ocean bottom reflection for internal wave spectra and mixing. *J. Phys. Oceanogr.*, 15, 1145-1156.

Garrett, C., 1979a: Mixing in the ocean interior. *Dyn. Atmos. Oceans*, 3, 239-265.

Garrett, C., 1979b: Comment on "Some evidence for boundary mixing in the deep ocean" by Laurence Armi. *J. Geophys. Res.*, 84, 5095.

Gregg, M. C., 1987: Diapycnal mixing in the thermocline: A review. *J. Geophys. Res.*, 92, 5249-5287.

Munk, W. H., 1966: Abyssal recipes. *Deep-Sea Res.*, 13, 207-230.

Munk, W. H., 1981: Internal waves and small scale processes. Evolution of Physical Oceanography Scientific Surveys in Honor of Henry Stommel. B. A. Warren and C. Wunsch, Eds., MIT Press, 264-291.

Wunsch, C. and S. Webb, 1979: The climatology of deep ocean internal waves. *J. Phys. Oceanogr.*, 9, 235-243.

# Numerical simulations of the flow of a stratified fluid over topography

By JAMES W. ROTTMAN<sup>1</sup>, DAVE BROUTMAN<sup>2</sup>

AND ROGER GRIMSHAW<sup>3</sup>

<sup>1</sup>College of Marine Studies, University of Delaware, Newark, DE 19716, USA

<sup>2</sup>School of Mathematics, University of New South Wales, Kensington, NSW 2033, Australia

<sup>3</sup>Department of Mathematics, Monash University, Clayton, VIC 3168, Australia

We use a high-resolution spectral numerical scheme to solve the equations of motion for the flow of a uniformly stratified Boussinesq fluid over long isolated bottom topography in a channel of finite depth. The results are compared with the existing theories: the nonresonant steady hydrostatic theory of Long (1955) *Tellus* 7, 341-357, resonant and nonresonant time-dependent long-wave theory, and the resonant fully nonlinear, weakly dispersive theory developed recently by Grimshaw and Yi (1991) *J. Fluid Mech.* 229, 603-628.

---

## 1. Introduction

The flow of a uniformly stratified inviscid Boussinesq fluid over two-dimensional localized bottom topography in a channel of finite depth has been the subject of extensive study since the pioneering work of Long (1955). For this special class of flows, Long was able to derive a linear field equation (often called Long's equation) that describes the fully nonlinear steady flow with the assumption that all the streamlines originate upstream (*i.e.*, no closed streamlines). Long found that with some restrictions on the amplitude of the topography solutions of this field equation that do not violate the no-closed-streamline assumption exist except when the flow conditions are such that one of the normal internal gravity wave modes of the channel is close to resonance. Near these resonance points the steady solutions exhibit closed streamlines no matter how small the amplitude of the topography. The appearance of closed streamlines in the steady solution presumably indicates the presence of wavebreaking and some as yet not fully determined type of unsteady flow.

Grimshaw & Yi (1991), hereafter referred to as GY, proposed an approximate theory for resonant flow in uniformly stratified flows. They derived a new evolution equation, which we will refer to as the finite-amplitude long-wave equation (or more simply, the FLW equation), which is in essence a small perturbation of the *time-dependent* form of Long's equation. They assumed that for topography of small amplitude and moderate slope that the upstream propagating component of the resonant mode has an amplitude that scales with the channel depth and that the nonlinearity comes in through the time dependence which scales with the 3/2 power of the height of the topography. Thus, small topography will produce a response on the order of the channel depth, but the smaller the topography the longer it will take for this large amplitude response to develop. The FLW equation has the property, shared with Long's equation, that its solutions are valid only up to the point where overturning streamlines appear somewhere in the flow. That is, the FLW equation can describe everything up to but not

including overturning internal waves, for sufficiently small topography sufficiently close to one of the resonant points.

Although there have been some recent studies, Hanazaki(1992, 1993) and Lamb (1994), that compare the results of numerical solutions of the fully nonlinear equations with the FLW equation, mostly near the first resonance point, there is as yet no thorough study of the range of validity of the FLW equation. In the present work we describe the results of a systematic study of this problem for long topography using a spectral method to solve the fully nonlinear inviscid equations. Our main focus is to explore the robustness of the GY equation near the first two resonance points.

## 2. Theory

### *Problem formulation*

The flow and coordinate system under consideration are sketched in figure 1. We use a Cartesian coordinate system with  $x$  as the horizontal and  $z$  as the vertical coordinate. A stratified, incompressible and inviscid fluid with constant buoyancy frequency  $N$  flows through a channel of total depth  $D$  that is bounded above by a horizontal rigid lid and below by a surface-mounted hill represented by the curve  $z = h(x)$ , where  $h(x) \rightarrow 0$  as  $x \rightarrow \pm \infty$ . The density variation of the fluid over the depth of the channel is assumed to be small compared to the mean density  $\bar{\rho}_0$  of the fluid. The hill is assumed to be two-dimensional, symmetric and streamlined, with a maximum height  $h(0) = a$  and has a horizontal length scale  $L$ . In all the simulations described in this paper the specific hill shape used was

$$h(x) = a e^{-(x/L)^2} \quad (1)$$

We consider the two-dimensional motion that results when the hill is towed through the fluid at some constant speed  $U$ . That is, at time  $t = 0$  surfaces of constant density are all horizontal and the fluid is at rest, and at time  $t = 0^+$  the hill is impulsively accelerated to speed  $U$ . We seek the solutions of this problem for  $t > 0$  in a reference frame in which the hill is at rest (as depicted in Fig. 1). Accordingly, we choose a background state to consist of a constant horizontal speed  $U$  and horizontally homogeneous density  $\rho_0(z)$  and pressure  $p_0(z)$  that satisfy the hydrostatic condition  $dp_0/dz = -g \rho_0$ , where  $g$  is the acceleration due to gravity.

In general, we will present our results in terms of the vertical displacement  $\zeta(x, z, t)$ , which is defined such that the total density  $\rho(x, z, t)$  at any given point and time is given by

$$\rho(x, z, t) = \rho_0(z - \zeta). \quad (2)$$

There are three nondimensional parameters that define this problem:

$$a/D, \quad L/D, \quad \text{and} \quad K = \frac{ND}{\pi U} \quad (3)$$

where  $K$  is the inverse of the Froude number (the ratio of the mean fluid speed  $U$  to the fastest linear internal gravity wave speed in the channel). The resonant points are where  $K = n$ , with  $n = 1, 2 \dots$

### Long's model

Long's model is derived based on the assumption that all streamlines originate upstream and therefore that there are no regions of the flow containing closed or overturning streamlines (regions of recirculating flow). Long showed that steady solutions that satisfy this assumption exist for all possible values of  $a/D$  if  $K < 1$  and for  $a/D$  that satisfy

$$K\pi a/D - |\sin[K\pi(1-a/D)]| \geq 0, \quad (4)$$

when  $K > 1$ . Apparently for the parameter regimes where (4) does not hold there are no steady solutions, since the solutions of Long's model implies statically unstable flows that presumably imply the existence of wave breaking and associated unsteadiness. Note from (4) that  $K a/D$  is a more natural scaling of the hill amplitude; in fact, with this scaling (4) becomes periodic in  $K$  with unit period for  $K > 1$ . Figure 2 is a parameter space plot that shows where steady solutions exist. Regions where no steady flow exists are shown shaded in the figure. Equation (4) and figure 2 are strictly valid when  $L/D \gg 1$ , but the curves are quite similar for smaller values of  $L/D$ . We have also plotted in figure 2 the numerical simulations we have performed for this paper.

### Grimshaw-Yi theory

If  $K \approx n$ , the resonant mode in terms of the vertical displacement is

$$\zeta(x, z, t) = A(x, t) \sin(n\pi z/D). \quad (5)$$

Grimshaw & Yi (1991) show that for small amplitude and moderately long hills the amplitude function  $A$  for the upstream propagating component of this resonant mode is governed by the following evolution equation (the FLW equation)

$$\int_{-\infty}^x G(A, A') \frac{\partial A'}{\partial t} dx' + D(U - c_n) A - \frac{1}{2} c_n^3 \frac{D}{N^2} \frac{\partial^2 A}{\partial x^2} - \frac{c_n^2}{N} \left(1 - \frac{N}{c_n} A\right) h = 0 \quad (6)$$

where  $A = A(x, t)$ ,  $A' = A(x', t)$ ,  $c_n = ND/(n\pi)$  is the linear long-wave internal gravity wave speed for mode  $n$ , and the kernel function  $G(A, A')$  is given by

$$G(A, A') = \int_0^D \left\{ \frac{\partial z}{\partial A} \frac{\partial z'}{\partial A'} - z \frac{\partial z}{\partial A} \frac{\partial^2 z'}{\partial A' \partial z} - z' \frac{\partial z'}{\partial A'} \frac{\partial^2 z}{\partial A \partial z} \right\} d\xi. \quad (7)$$

The variable  $\xi$  is defined as

$$\xi = z - A(x, t) \sin(n\pi z/D), \quad (8)$$

from which the inverse relationships  $z = z(\xi, A)$  and  $z' = z'(\xi, A')$  can be derived. For these inverse relationships to be single valued, we must require

$$|A| < \frac{D}{n\pi} = \frac{c_n}{N} \quad (9)$$

which is equivalent to requiring that there are no overturning streamlines in the flow, or that the perturbation horizontal fluid speed nowhere equals or exceeds the mean speed, which is the same restriction imposed on Long's model. It should be remembered that (9) is an approximate

criterion for overturning flow since it represents only the upstream propagating component of the resonant mode. For strongly nonlinear, strongly dispersive, or off-resonant flows, other modes may contribute which may cause overturning streamlines to occur earlier or later than predicted by (9).

It is possible to make (6) independent of the mode number  $n$  by rescaling the vertical length scales with  $D/n$  instead of  $D$ . This is analogous to the rescaling of Long's equation described above.

### 3. Numerical results

#### *Numerical methods*

We use a numerical collocation method to solve the full equations for the motion of a uniformly stratified, Boussinesq, inviscid fluid. The method solves the governing equations in their vorticity-streamfunction form. We impose the additional constraint that the motion be periodic in the horizontal direction with 'sponge' layers at both horizontal ends of the computational domain. For numerical convenience, the bottom topography is removed from the boundary conditions by transforming the equation to terrain-following coordinates. In our spectral method, the solutions of the governing equations are expanded in finite Fourier series in the horizontal direction and finite Chebyshev series in the vertical. Typically, for the calculations described here, 128 or 256 collocation points were used in the horizontal and 40 or 65 points in the vertical, depending on the size of the computational domain and the scale of the terrain. A third-order Runge-Kutta scheme is used to advance the vorticity and vertical displacement equations forward in time. We use a high-order high-wavenumber filter to eliminate noise in the calculation generated by some peculiarities of the initial conditions and to allow the calculation to continue past the point where wave overturning occurs.

The FLW equation was solved numerically using essentially the method described by GY and Yi & Warn (1987), except we chose to use third-order Runge-Kutta instead of leap-frog time stepping. We comment that the kernel function  $G(A, A')$  is singular near wave overturning amplitudes, when (9) is an equality, and must be treated very carefully as these amplitudes are approached. This aspect of the numerical solution of the FLW equation lead to an underestimate of the wavebreaking time in several cases reported by GY.

#### *Initial conditions*

Our initial conditions, which mimic what is done in laboratory tow-tank experiments, lead to some difficulties for an inviscid and nondiffusive calculation. Initially the isopycnal surfaces are horizontal and therefore several of them intersect the hill surface. Since the fluid particles initially on the hill surface cannot leave that surface, a small region with a horizontal density gradient is generated along the bottom boundary when the initial nonuniform distribution of density is swept over the hill crest after the flow is initiated. This small blob of nonuniform density is advected downstream by the mean flow and with time this density gradient sharpens as the heavier fluid advances into the lighter fluid forming a very sharp gravity current front. Such a front is very difficult to resolve numerically and eventually, if spectral filtering is not used, saturates the spectrum and leads to a breakdown of the calculation. This small abnormality can be seen propagating downstream at the mean flow speed in all of our spectral simulations.

### *The first resonance point ( $K = 1$ )*

We calculated the cases indicated by the  $\bullet$ 's in figure 2 near  $K = 1$ , for values of  $L/D$  ranging from 0.5 to 4.0, using both the fully nonlinear spectral model and the FLW equation. We do not have the space here to present all the results, so we show results in figures 3, 4 and 5 only for the case with  $K = 1$ ,  $a/D = 0.1$ , and  $L/D = 1.0$ .

Figure 3 shows the evolution in time of the amplitude function  $A(x, t)$  for the resonant mode as computed by the spectral model (the results from the FLW equation are identical). The conclusion that the FLW equation well represents the full calculation is reinforced by the drag (a sort of integral measure of the flow) calculated from the two methods and plotted in figure 4. Also, it appears that the drag is asymptotically approaching a small positive constant value. This is an indication that the flow in the neighborhood of the hill is approaching a permanent asymmetrical form with high pressure on the upstream surface and lower pressure on the downstream surface.

It is interesting that up to the time computed ( $t = 100 D/U$ ) there is no wave overturning although the first downstream trough is very close to overturning at the final time. Figure 5 is a plot of  $\max\{|A(x, t)| \pi\}$  as a function of time, showing that the approach to the overturning amplitude ( $|A(x, t)| \pi = 1$ ) is asymptotic in time.

For  $K > 1$ , wavebreaking occurs much sooner and the further from resonance the sooner wave breaking occurs, as long as the experiment is located in the shaded portion of the parameter space shown in figure 2 (otherwise no wavebreaking is ever observed). These wavebreaking times are comparable with Lamb's (1994) calculations. Also, the further from resonance the bigger the difference in the predicted time of wave overturning computed from the FLW equation as compared with that computed using the spectral model. However, in the cases we computed the difference in this overturning time was generally no greater than about 30%, and otherwise the FLW equation described the full calculations rather well. In general, these breaking times for fixed  $K$  scaled with  $L/a$ , for large enough  $L/D$  to be in the hydrostatic limit. So the larger  $L$  or the smaller  $a$  the longer the time scale of the developing flow. This is simply the long-wave linear resonant scaling.

### *The second resonance point ( $K = 2$ )*

Results for our representative calculation for the second resonant point are plotted in figures 6 and 7. The case we have chosen to show has  $K = 2$ ,  $a/D = 0.05$ , and  $L/D = 1.0$ . The time evolution of the amplitude function  $A(x, t)$  for the resonant mode as computed by the spectral method is plotted in figure 6 (and again the FLW equation produces a nearly identical plot). The more interesting feature of this calculation is the plot of the drag, plotted in figure 7, as computed by the two methods. The spectral model produces a drag that has the same mean time evolution as that computed by the FLW equation, but the spectral calculation shows a persistent oscillation with a nearly constant period and amplitude about this mean. Similar oscillations in the drag when  $1 < K \leq 2$  have been observed in the tow-tank experiments of Castro, et al. (1990) and the numerical simulations of Lamb (1994). We found that these oscillations did not appear when  $L/D = 2.0$ .

It appears that these oscillations in the drag are associated with the mode 1 wave that propagates upstream when  $K > 1$ . Since the GY theory neglects all other modes except the resonant mode, their theory cannot produce these oscillations. However, linear theory provides

an approximate explanation. The most persistent mode 1 wave when  $K > 1$  should be the one with the horizontal wavelength for which the group speed equals the mean flow speed. The wavenumber of this wave for mode 1 waves is  $k = (K^{2/3} - 1)^{1/2} \pi / D$ . The period of the oscillations of this wave is given by  $T = 2\pi/k (c - U)$  =  $2(K^{2/3} - 1)^{3/2}$ , where  $c$  is the phase speed. This theoretical result for the period of the drag oscillations is plotted in figure 8 along with the observed periods from the numerical simulations and tow tank experiments. The agreement is seen to be quite good. Also, note the wavelength of the most persistent wave decreases as  $K$  increases, so that if  $L$  is so large such that very little energy is put into the horizontal spectrum at the most persistent wavelength, then the oscillations will not be observable, as we saw in our simulations with  $L/D \approx 2.0$ .

We acknowledge helpful discussions with Simon Clarke about the self-similar properties of the FLW equation. We are grateful to Marina De Gabriele for her help with the numerical simulations and with the preparation of the figures.

#### REFERENCES

CASTRO, I.P., SNYDER, W.H. & BAINES, P.G. 1990 Obstacle drag in stratified flow. *Proc. Roy. Soc. Lond. A* 429, 119-140.

GRIMSHAW, R.H.J. & YI, ZENGXIN. 1991 Resonant generation of finite-amplitude waves by the flow of a uniformly stratified fluid over topography. *J. Fluid Mech.* 229, 603-628.

HANAZAKI, H. 1992 A numerical study of nonlinear waves in a transcritical flow of stratified fluid past an obstacle. *Phys. Fluids A* 4, 2230-2243.

HANAZAKI, H. 1993 On the nonlinear internal waves excited in the flow of a linearly stratified Boussinesq fluid. *Phys. Fluids A* 5, 1201-1205.

LAMB, K.G. 1994 Numerical simulations of stratified, inviscid flow over a smooth obstacle. (to appear in *J. Fluid Mech.*).

LONG, R.R. 1955 Some aspects of the flow of stratified fluid. III. Continuous density gradients. *Tellus* 7, 341-357.

YI, ZENGXIN & WARN, T. 1987 A numerical method for solving the evolution equation of solitary Rossby waves on a weak shear. *Adv. Atmos. Sci.* 4, 43-54.

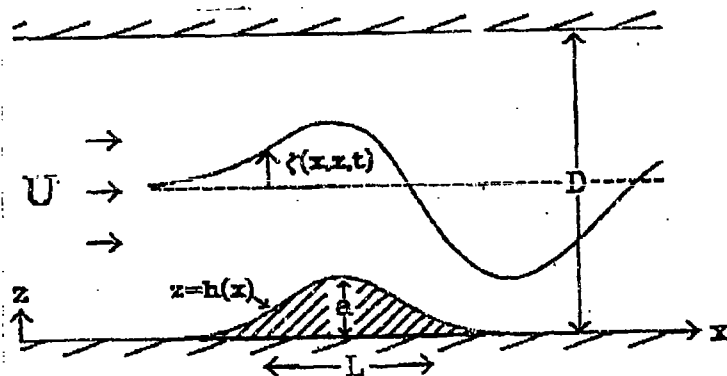


Figure 1. A schematic diagram of uniformly stratified flow over bottom mounted topography in a channel of finite depth.

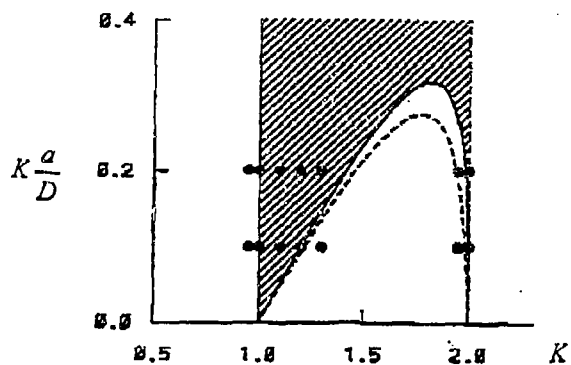


FIGURE 2. The parameter space diagram for the hydrostatic Long's model solution of flow over a two-dimensional hill. The white areas are regions of the parameter space for which the solution satisfies the assumptions used in deriving Long's model and the shaded regions are where the solution contains closed recirculating cells (which violate the assumptions used in deriving the model). The plot is periodic in  $K$  with unit period for  $K > 1$ . The regions between the dashed lines and the solid lines are where the Richardson number of the steady flow is less than unity. The •'s represent the numerical experiments done for this study.

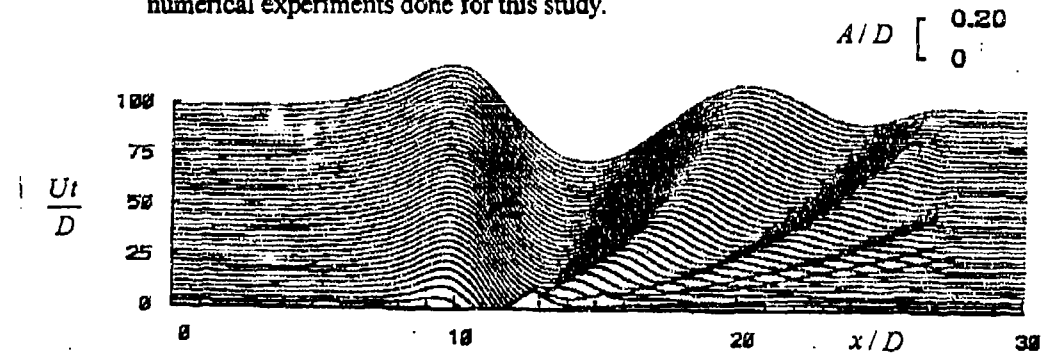


FIGURE 3. The function  $A(x, t)$  for the resonant mode as computed by the spectral model for the case with  $K = 1$ ,  $a/D = 0.1$ , and  $L/D = 1.0$ . The hill is located at  $x/D = 10$ .

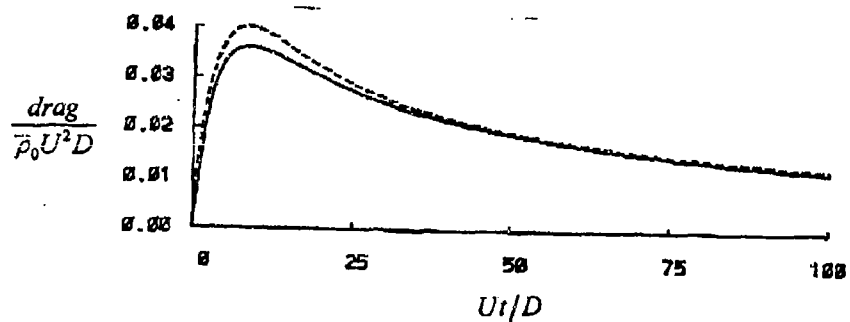


FIGURE 4. The drag for the simulations shown in figure 3: ---, spectral model; —, FLW equation.

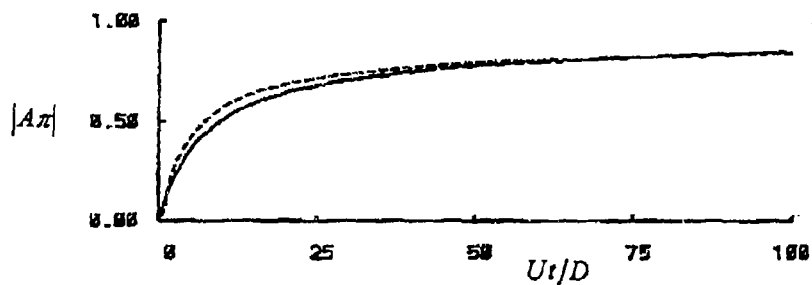


FIGURE 5. The value of  $\max\{|A(x, t)|/\pi\}$  as a function of time for  $A(x, t)$  shown in figure 3: ---, spectral model; —, FLW equation. A value of  $A(x, t)/\pi \geq 1$  indicates wave overturning.

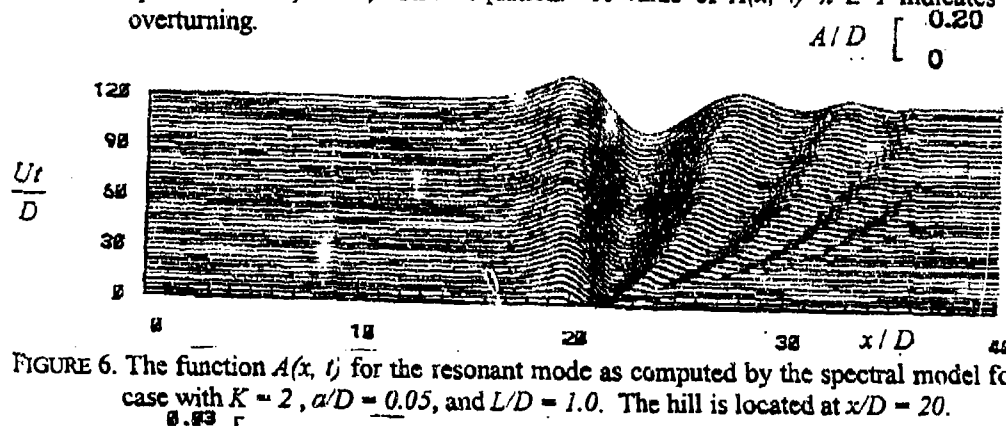


FIGURE 6. The function  $A(x, t)$  for the resonant mode as computed by the spectral model for the case with  $K = 2$ ,  $a/D = 0.05$ , and  $L/D = 1.0$ . The hill is located at  $x/D = 20$ .

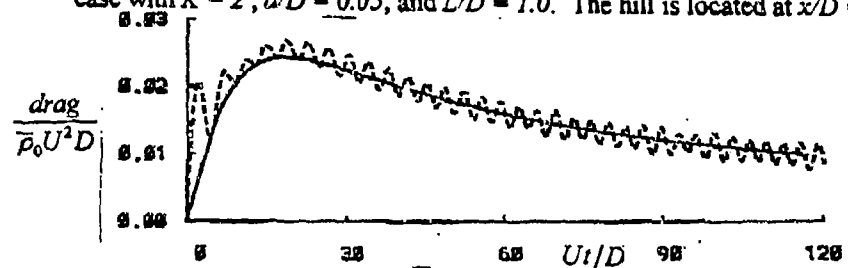


FIGURE 7. The drag for the simulations shown in figure 6: ---, spectral model; —, FLW equation.

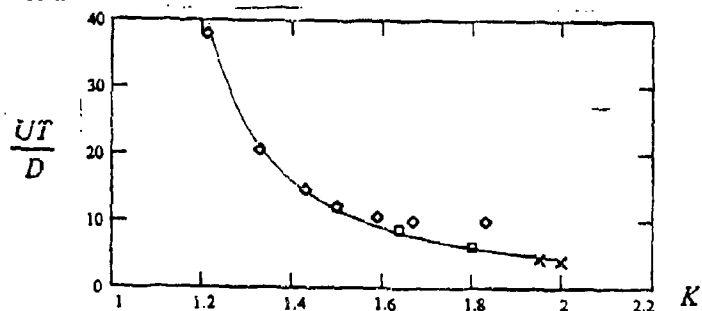


FIGURE 8. The period of the most persistent upstream propagating mode I wave for  $1 < K < 2$ : —, linear theory;  $\square$ , Castro, et al. (1990);  $\diamond$ , Lamb (1994);  $\times$ , present spectral model.

## PROCESSES IN THE SURFACE MIXED LAYER OF THE OCEAN

Chris Garrett  
Department of Physics and Astronomy  
University of Victoria  
P.O. Box 3055  
Victoria, British Columbia V8W 3P6  
Canada

### ABSTRACT

Models for the evolution of the surface mixed layer need to be improved to include dominant processes such as Langmuir circulation. It is shown that the wave forcing in Langmuir circulation models is much stronger than that due to a surface buoyancy loss, and beginning studies of the erosion by the cells of a pre-existing stratification are described. Mixed layer models will also need to allow for horizontal inhomogeneity; for example, it is shown that the horizontal buoyancy gradient that may be left behind after a storm produces restratification that can be significant. The nonlinearity of the equation of state is another real-world factor; it gives rise to an annual average surface buoyancy that is misleading as it is compensated by interior cabbeling. Current work linking the mixed layer to water mass formation is also introduced.

### 1. INTRODUCTION

The upper ocean typically exhibits a surface mixed layer, with a thickness of a few metres to several hundred metres, in which the density stratification is weak due to mixing by turbulence that is driven by surface flows of momentum and buoyancy, and possibly also by shear across the base of the layer. The physics of this surface mixed layer presents a variety of fascinating fluid dynamical problems, and is of great importance for a wide variety of problems arising in studies of climate, biological productivity and marine pollution.

In questions of climate, an elementary and common remark is that the heat capacity of the top 2.5 m of the ocean equals that of the whole column of air above it, so that, with turbulent mixing typically extending to a depth many times this in both summer and winter, the ocean essentially acts as a "thermal flywheel" for the climate system, smoothing out both temporal (seasonal) temperature changes and, through advection, meridional gradients. Of course heat exchange between ocean and atmosphere involves more than just the turbulent near surface layer of the ocean, with the subduction of surface layer water into the interior being a topic of great current interest.

Sea surface and mixed layer processes also play a vital role in the exchange between the atmosphere and ocean of gases, such as oxygen and carbon dioxide, by diffusion across the

sea surface and across the surfaces of bubbles created by breaking waves. Carbon dioxide is then taken up in the surface layers of the ocean by growing phytoplankton, with the growth rate depending on the availability of nutrients that are entrained from below the base of the surface mixed layer. The average light intensity to which the phytoplankton are exposed is also critical and this becomes insufficient for further growth if the depth over which the phytoplankton are mixed becomes too great.

Many models for the evolution of the surface mixed layer have been developed. These are usually one-dimensional (although possibly allowing for local convergence by prescription of a vertical velocity at the base of the layer). The simplest models parameterise the changes in average properties of the layer, and of its depth, in terms of the surface buoyancy flux and wind stress and/or the difference between the average buoyancy and average velocity of the mixed layer and the buoyancy and velocity of the water just below it. These models are based on plausible physical arguments and can, to some extent, be tuned to match data, but they are clearly incomplete. Various more complicated models, based on turbulence closure schemes at different levels, have thus been developed. These are often expected to be effective in view of the success of similar schemes in other boundary layer situations, though weaknesses in closure assumptions in the strongly stratified region at the base of the layer are admitted and sometimes compensated for by assumptions as *ad hoc* as those of the bulk models.

These models will be reviewed briefly in Section 2, but I believe that their most important shortcoming is that they ignore some of the real physical processes that are unique to the oceanic surface mixed layer. Breaking surface waves are clearly one phenomenon of great importance for the generation of turbulence near the surface, but the most important process appears to be Langmuir circulation. This refers to the helical circulation cells in the upper ocean, with axes generally oriented downwind, which appear to be generated by a mechanism involving the Stokes drift of surface waves; the cells are thus very different from coherent longitudinal vortices that may occur in other boundary layers. The physics of Langmuir circulation, and beginning studies of the role it plays in eroding the stratification at the base of the mixed layer and so deepening it, will be discussed in Section 3.

Increasing attention is also being paid to the effect on the surface mixed layer of horizontal gradients in its properties. Simple advection of these properties by a prescribed current is frequently allowed for in locally one-dimensional models, if only to balance the heat budget, but recent work points also to the possible importance of dynamical effects of a horizontal buoyancy gradient. This will be reviewed in Section 4.

Interesting physical effects can sometimes arise from the nonlinearity of the equation of state. One example, an annual average buoyancy flux in spite of zero annual average heat flux, will be described in Section 5. Recent consideration of water mass formation associated with a horizontal gradient of surface buoyancy flux will be mentioned in Section 6. The paper concludes in Section 7 with a discussion.

## 2. EXISTING MODELS

### 2.1 Forcing functions

The surface of the ocean is forced by wind stress  $\tau$ , with a corresponding friction velocity  $u_* = (|\tau|/\rho_w)^{1/2}$  where  $\rho_w$  is the density of water, and by a surface buoyancy flux  $B_0$  per unit area, given by

$$B_0 = -C_p^{-1} g \alpha \rho_0^{-1} Q + g \beta s \rho_0^{-1} (E - P) \quad (2.1)$$

where  $C_p$  is the specific heat of water,  $\alpha = -\rho^{-1}(\partial \rho / \partial T)_{p,s}$  is the coefficient of expansion of water at fixed pressure  $p$  and salinity  $s$ ,  $Q$  is the net heat flux into the water,  $\beta = \rho^{-1}(\partial \rho / \partial s)_{p,T}$ ,  $E$  is the evaporation rate and  $P$  is the rainfall rate (Gill, 1982). Here positive  $B_0$  corresponds to loss of buoyancy from the sea. The net heat flux into the sea is made up of insolation  $Q_s$ , which is distributed over an attenuation depth, minus longwave back radiation and latent and sensible heat loss rates which act at the surface.

The wind stress, at least in part, goes first into surface waves. In a wave field that is growing downwind, part of the momentum flux goes into the downwind increase of the wave momentum (associated with the Stokes drift of the irrotational waves) but for typical growth rates this fraction is only 3% or so (e.g. Richman and Garrett, 1977) so that it is reasonable to assume that all of  $\tau$  is available to drive the mean rotational flow of the mixed layer.

The energy budget is more complicated. Some energy can be advected away in a growing wave field, but the more important question concerns the energy input. Is it  $|\tau|$  times the surface drift of the water, or  $|\tau|$  times the phase velocity of the longest and fastest travelling waves in the surface wave spectrum? Gemmrich et al. (1994) have examined the energy budget of the mixed layer and conclude that the momentum goes mainly into rather short waves, with a wavelength of about 0.25 m and a phase speed of about 0.6 m s<sup>-1</sup> so that the energy input is  $|\tau|$  times this. This has important consequences for turbulence levels near the surface. In fact, Gemmrich et al. (1994) based their conclusion largely on recent measurements reported by Agrawal et al. (1992), Anis and Moum (1992) and Osborn et al. (1992) which show an energy dissipation rate much more than the value  $u_*^3/\kappa z$ , for von Karman's constant  $\kappa$  and distance  $z$  from the surface, which would apply for a conventional wall layer, but with a depth integral that is still much less than  $|\tau|$  times the wind speed (corresponding to the phase speed of the fastest wave for a fully developed sea). The result of Gemmrich et al. (1994) is in keeping with Thorpe's (1993) finding, from the observed frequency of wave breaking and the energy dissipation in a breaking event as a function of wave speed, that the breaking waves must be much shorter than the dominant waves.

The observed turbulent dissipation rate  $\epsilon$  greater than  $u_*^3/\kappa z$  means that in a convective situation the buoyancy flux does not dominate in the turbulent kinetic energy equation until it is rather deeper than the modulus  $u_*^3/\kappa B_0$  of the Monin-Obukhov length defined as minus this. Nonetheless, there are clearly times when the deepening of the mixed layer is largely determined by surface buoyancy loss (e.g. Lombardo and Gregg, 1989), with the main question being whether there is a significant buoyancy jump at the base of the mixed layer and, if so, whether it is a consequence of penetrative convection or is caused by something other than the surface buoyancy flux.

## 2.2 Bulk models

Simple models of the surface mixed layer envisage a sharp jump  $\Delta b$  in buoyancy  $b$  (given by  $b = -g(\rho - \rho_0)/\rho_0$ , with  $\rho_0$  a reference density) at the base of the layer of depth  $h$ , and prescribe the entrainment velocity across this. As reviewed by Phillips (1977), one class of models parameterises this entrainment rate as

$$w_e = u_* F(h\Delta b/u_*^2) \quad (2.2)$$

where  $Rb = h\Delta b/u_*^2$  is a bulk Richardson number based on  $u_*$  and  $\Delta b$ , and is the only dimensionless parameter if  $u_*$  is the only relevant velocity scale. The function  $F$  in (2.2) is presumably a decreasing function of  $Rb$ ; if the rate of energy input to the mixed layer is assumed proportional to  $u_*^3$  and a fixed fraction of this input is assumed to go into the increasing potential energy of the layer as a dense fluid is entrained upwards,  $F \propto Rb^{-1}$  (Turner, 1973). Models based on this formulation include those of Denman and Miyake (1973), Nüller and Kraus (1977) and Garwood (1977).

However, another possible velocity scale is the magnitude  $\Delta u$  of the difference between the average velocity of the surface mixed layer and the velocity of the underlying fluid. Various models for  $F(Rb)$ , with  $\Delta u$  replacing  $u_*$  in (2.2), are discussed by Phillips (1977) and generally have a rapid decrease with increasing  $Rb$ . A particularly simple form, suggested by Pollard et al. (1973), has  $F = \infty$  for  $Rb < 1$  and  $F = 0$  for  $Rb > 1$ , so that the mixed layer depth adjusts to have  $Rb$  always equal to 1 during a deepening phase, though it is assumed not to "unmix" if  $\Delta u$  decreases.

Of course  $\Delta u$  is a function of the history of  $u_*$  and the mixed layer depth, so that the two types of bulk model may predict somewhat similar behaviour, but there can also be major differences. For example, in the case of a mixed layer developing in response to an abrupt onset of wind above a stratified ocean, the first model will show a continued deepening of the layer whereas the second will give a mixed layer depth of no more than  $2^{3/4}u_*/(Nf)^{1/2}$  due to the rotation of the mixed layer velocity by the Coriolis force (Pollard et al., 1973), with  $N$  the buoyancy frequency of the underlying fluid, and  $f$  the Coriolis frequency.

The second type of bulk model, based on  $\Delta u$ , has perhaps become more common than the first in recent years, particularly with the popular model of Price et al. (1986) that stops the entrainment at  $Rb = 0.65$  instead of 1 and also smooths the interface at the base of the layer to give it a gradient Richardson number of 0.25.

A reasonable reaction to this uncertainty is to argue that in reality the entrainment depends on the behaviour of turbulence in a stratified fluid and cannot be simply represented in terms of either  $u_*$  or  $\Delta u$ , though possibly some simple parameterisation in terms of both of these can be extracted from more thorough studies.

## 2.3 Higher order models

The success of turbulence closure models in other boundary layer situations has led to the development of a variety of models for application to the surface mixed layer of the ocean. The simplest of these assume simple profiles of eddy viscosity and diffusivity, as in the recent model of Large et al. (1994). This has been used for successful simulation of various oceanic data sets, though success on seasonal time scales, rather than daily or for

individual storms, depends on allowing for advection of water with different properties. The model also maintains an eddy viscosity of  $10^{-4} \text{ m}^2 \text{ s}^{-1}$  and an eddy diffusivity of  $10^{-5} \text{ m}^2 \text{ s}^{-1}$  below the base of the mixed layer. Moreover, for this as for all other models, comparison with data is made difficult by uncertainty in the surface heat and water fluxes.

Many other mixed layer models are based on various closure schemes proposed by Mellor and Yamada (1974, 1982). However, as reviewed by Gaspar et al. (1990), the commonly used versions suffer from uncertainty in the prescription, or computation, of the "master length". Gaspar et al. (1990) adopt a scheme with eddy viscosity and diffusivity determined by the turbulent kinetic energy (TKE) and a length scale. The TKE satisfies a prognostic equation involving production, dissipation and diffusion, but the length scale is given by simple consideration of the vertical distance a particle could travel up or down in converting its TKE to potential energy (Bougeault and André, 1986). Blanke and Delecluse (1993) find that this scheme produces better simulations for the tropical Atlantic Ocean than that of Philander and Pacanowski (1986) in which mixing coefficients are given prescribed values that are reduced by some function of the local Richardson number, but some discrepancies still occur. More recently, Kantha and Clayson (1994) have extended the modified Mellor-Yamada second moment closure scheme of Galperin et al. (1988), but at the base of the mixed layer they use the same *ad hoc* Richardson number dependent mixing formulae as employed by Large et al. (1994) in the transition zone.

Further development and use of these models, whether bulk or higher order, is justified by the need for adequate simulation and prediction in a variety of situations. One might, however, question the value of some of the more elaborate schemes described above, and of the third moment closure scheme of André and Lacarrère (1985), in view of the fact that they do not explicitly incorporate the unique processes occurring in the oceanic surface layer. The most important of these processes is probably Langmuir circulation, which we turn to next.

### 3. LANGMUIR CIRCULATION

Lines of surface convergence, parallel to the wind, are frequently marked by "windrows" of foam and other flotsam. The Nobel prize winning chemist Irving Langmuir was the first to describe the associated subsurface pattern of vortices, of alternating sign, that now bears his name, and suggested that they are the key mechanism in producing the mixed layer. Pollard (1977) presented a schematic diagram of Langmuir circulation (Figure 1) based on observations up till then. More detailed observations by Weller and Price (1988) have shown larger downwelling speeds, up to  $0.2 \text{ m s}^{-1}$ , beneath the surface convergences, and associated downwind jet speeds of comparable magnitude.

Pollard's (1977) review of theories of Langmuir circulation up until 1976 provoked Craik and Leibovich (1976) to revise an unsatisfactory earlier theory and present an elegant dynamical model, reviewed by Leibovich (1983), that has been accepted since then. The basic physics is an instability mechanism in which an infinitesimal downwind jet has its vertical vorticity, with opposite sign on the two sides of the jet, tilted by the Stokes drift of the surface waves to produce longitudinal rolls. These produce the surface convergence at the jet, and this is in turn reinforced due to the acceleration, by the wind stress, of the water moving towards the surface convergence.

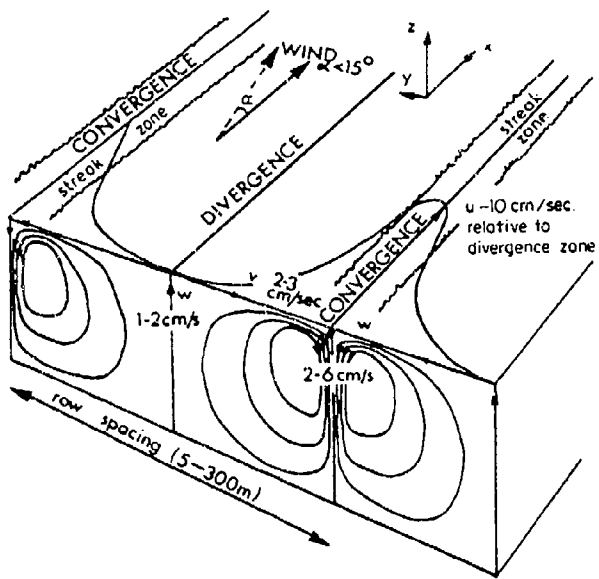


Figure 1: Pollard's (1977) schematic of Langmuir circulation.

Li and Garrett (1993) have examined the Craik-Leibovich (CL) model further and find that, for plausible values of the eddy viscosity in the model, the predicted downwelling speed is comparable to that measured, but the jet is weaker than observed. This suggests the need for more refined parameterisation of the turbulence or, possibly, the importance of other physical processes such as the interaction of the surface waves with the circulation pattern.

Nonetheless, the vortex force associated with the Stokes drift does seem to be powerful, making Langmuir circulation different from longitudinal rolls in other boundary layer situations. For example, Li and Garrett (1994, henceforth LG) recently investigated whether Langmuir circulation could be just convective rolls in a shear flow, given that, even under conditions of net heat input to the sea, insolation is penetrative and the sea surface is likely to be losing heat.

In their extension of the two-dimensional CL model, LG numerically solved the equations

$$\frac{\partial u}{\partial t} + v \frac{\partial u}{\partial y} + w \frac{\partial u}{\partial z} = \nu \nabla^2 u \quad (3.1)$$

$$\frac{\partial \Omega}{\partial t} + v \frac{\partial \Omega}{\partial y} + w \frac{\partial \Omega}{\partial z} = \nu \nabla^2 \Omega - \frac{du_s}{dz} \frac{\partial u}{\partial y} + \alpha g \frac{\partial \theta}{\partial y} \quad (3.2)$$

$$\frac{\partial \theta}{\partial t} + v \frac{\partial \theta}{\partial y} + w \frac{\partial \theta}{\partial z} = \kappa \nabla^2 \theta \quad (3.3)$$

where  $u$  is the downwind current,  $\Omega = \partial w / \partial y - \partial u / \partial z$  the downwind component of the vorticity and  $\theta$  the temperature. Turbulence is represented simply by eddy viscosity  $\nu$  and eddy diffusivity  $\kappa$ . The CL vortex force, associated with the Stokes drift  $u_s(z)$ , is given by the second term on the right hand side of (3.2). If there is surface cooling, streamwise

vorticity can also be generated by the buoyancy torque given by the last term in (3.2), with  $\alpha$  the expansion coefficient and  $g$  gravity. Internal heating is neglected here but can be added to (3.3).

LG show that this problem is characterised by three non-dimensional numbers. The first is the Langmuir number introduced by Leibovich (1977) and given by

$$La = \left( \frac{\nu \beta}{u_*} \right)^{3/2} \left( \frac{u_*}{S_0} \right)^{1/2} \quad (3.4)$$

where the Stokes drift is  $u_*(z) = 2S_0 \exp(2\beta z)$ . The second is the eddy Prandtl number  $Pr = \nu/\kappa$  and the third, which they term the Hoenikker number in honour of the distinguished ocean thermodynamicist Dr. Felix Hoenikker (Vonnegut, 1963), is

$$Ho = \frac{-\alpha g Q}{C_p \rho_w S_0 \beta u_*^2}. \quad (3.5)$$

In this problem  $HoPr$  represents the ratio of convective forcing by surface heat loss  $-Q$ , with  $C_p$  the specific heat of water, to wave forcing. From numerical solutions and scale analysis, LG show that, for  $Pr = 1$ ,  $Ho$  must be as big as about 3 for convective forcing to compare with wave forcing at appropriately small values of  $La$ . Realistic values for the surface heat flux, Stokes drift and wind stress, however, give  $Ho$  significantly less than 0.1. It thus appears that the surface heat flux is unimportant to the dynamics of the cells, a conclusion that also holds for other values of  $Pr$ , for net heating ( $Ho < 0$ ) and for depth-distributed heating. The temperature then behaves as a passive scalar in these numerical experiments in which a heat flux is applied to previously homogeneous water.

Figure 2 shows the non-dimensional fields obtained in a steady-state solution for  $La = 0.02$ ,  $Ho = 0.05$  and  $Pr = 1$ . In fact, with surface heat flux only, the  $u$  and  $\theta$  fields are proportional for  $Pr = 1$ . For plausible values of the heat loss and other parameters, the predicted surface temperature difference  $\delta\theta$  from divergence to convergence is  $O(10^{-2})K$ , comparable to values reported by Thorpe and Hall (1982) and Weiler and Price (1988). Scale analysis, supported by numerical solutions, shows that  $\delta\theta \propto HoPr^{1/2} La^{-1/6}$ . This implies weak dependence ( $\nu^{-1/4}$ ) on the eddy viscosity  $\nu$ , but more dependence on  $Pr$ . Doubts also remain, of course, about the validity of the simple parameterisations of turbulence.

Figure 3a shows, for the same parameters as Figure 2, the non-dimensionalised vertical profiles of the cross-stream average temperature ( $\theta$ ), made up of the conductive solution  $T$  and a change  $\langle \theta' \rangle$  due to the Langmuir cells. The cells homogenise the temperature below a thin conductive surface layer and Figure 3b shows that the total vertical heat flux  $Q_t$  is largely associated with the advective heat flux  $Q_a$  due to the cells, rather than the conductive heat flux  $Q_c$ . We conclude that Langmuir circulation is a powerful stirring agent of passive scalars in the surface mixed layer, and that temperature is indeed passive if realistic cooling or heating is applied to homogeneous water.

A more important question, however, concerns the interaction between the circulation and pre-existing stratification. Ming Li (personal communication, 1994) is using the same model to investigate this. Preliminary results show the expected result that, if wind stress is applied to a density-stratified ocean, Langmuir circulation quickly develops near the surface and, while the cells are small with a shallow penetration depth, tends to "engulf"

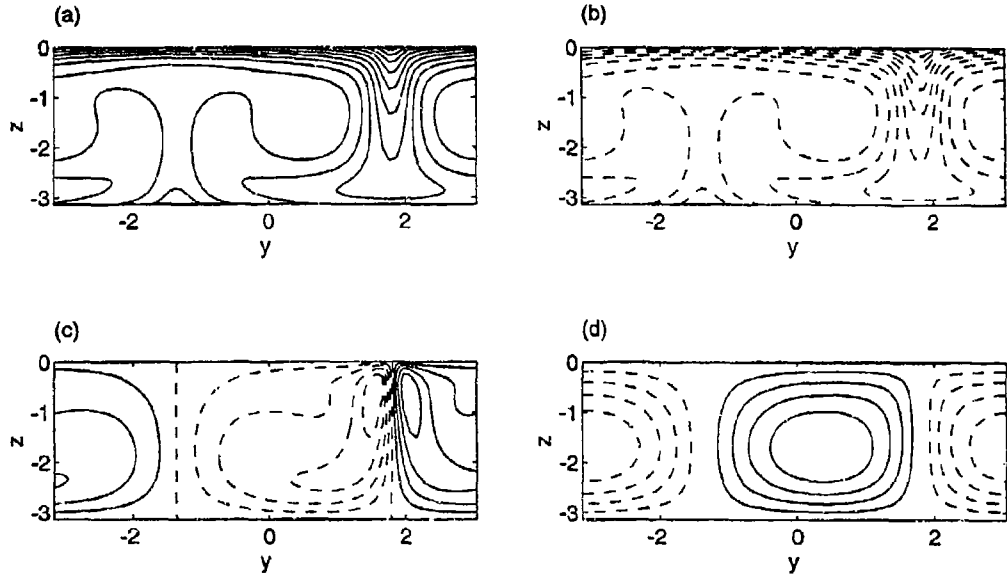


Figure 2: Quasi-steady Langmuir cells at  $La = 0.02$ ,  $Ho = 0.05$  and  $Pr = 1$ . Contours of (a) downwind current, (b) temperature, (c) streamwise vorticity, (d) streamfunction. (From Li and Garrett, 1994.)

and homogenise the temperature as if it were a passive scalar. As the cells merge and grow in scale, however, they do not penetrate as deeply as in homogeneous water and give instead a well mixed layer above a jump in buoyancy to the stratified ocean beneath. Attempts are being made to understand the depths of this layer in terms of the Froude number based on the downwelling speed in the cells and to characterise it in terms of external parameters. Preliminary results suggest that the mixed layer stops its rapid growth into a stratified fluid when its depth is about  $10u_*/N$ . However, the downwind velocity field is also fairly well homogenised in the mixed layer by the cells, leading to small values of the Richardson number at the base of the layer. This would presumably lead to shear instability (not possible in the present model due to its independence of the downwind coordinate  $x$ ) with the possibility that the mixed fluid would then be picked up by the cells and stirred throughout the upper layer, though this is probably a slower process than the initial rapid engulfment.

It is hoped that this work, and extensions to include three-dimensional effects and more realistic treatment of subgrid-scale turbulence, will lead to a plausible blend of bulk parameterisations of entrainment in terms of  $u_*$  (as for the initial engulfment) and  $\Delta u$  across the base of the layer (as for the later shear instability and stirring). Our expectations are that allowance for Langmuir circulation will mainly reduce the occurrence of some of the very shallow mixed layers which can occur with other schemes.

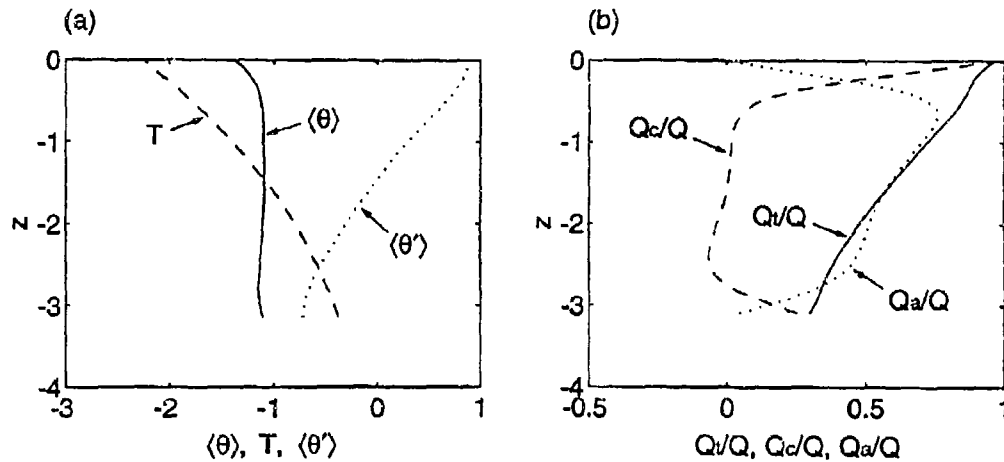


Figure 3: Vertical profiles at  $La = 0.02$ ,  $Ho = 0.05$  and  $Pr = 1$  for (a) nondimensionalised temperature and (b) heat fluxes. (From Li and Garrett, 1994.)

#### 4. THE ROLE OF HORIZONTAL BUOYANCY GRADIENTS

Most of the emphasis in mixed layer modelling has been on the parameterisation of mixing in one-dimensional models. This is clearly still the key problem, but there are increasing attempts to assess the importance of the frequently observed horizontal variations in mixed layer parameters. De Szeoke (1980) and de Ruijter (1983) have shown that the depth-varying advection of horizontal temperature variations by wind-driven shear currents can be important, and this effect has been included in the model of Lascaratos et al. (1993). Recent observations (Brainerd and Gregg, 1993a,b) have suggested that restratifying currents may be driven by the horizontal buoyancy gradients themselves rather than just by the wind, and this is providing impetus for a number of theoretical studies.

The simplest possible problem, reviewed by Tandon and Garrett (1994a), is of the adjustment of a constant horizontal buoyancy gradient  $b_x = -(g/\rho_0)(\partial\rho/\partial x)$  in a vertically well mixed layer of depth  $h$  initially at rest. The geostrophically adjusted state has a vertical buoyancy gradient with  $N^2 = -(g/\rho_0)(\partial\rho/\partial z)$  given by the simple formula

$$N^2 = M^4/f^2 \quad (4.1)$$

where  $M^2 = |b_x|$ . This restratification can be significant in some frontal situations in the deep ocean, at low latitudes and on the continental shelf. The adjustment occurs on a time scale comparable with the inertial period and is accompanied by inertial oscillations which cause the stratification to oscillate between zero and twice the value given by (4.1).

An interesting question concerns the shear stability of the solution to this problem; the development of stratification is accompanied by sheared currents in the direction of the buoyancy gradient and normal to it due to the action of the Coriolis force. In fact, the steady geostrophically adjusted state would have  $Ri = 1$  whereas the full time-dependent solution has  $Ri = \frac{1}{2}$  for all  $z$  and  $t$ , implying stability. Ou (1984) has examined the adjustment when  $b_x$  is not constant; Tandon and Garrett (1994a) find that  $Ri < \frac{1}{4}$  is possible if the frontal region is sharp enough.

These models are, however, limited by the assumption of a horizontally constant mixed layer depth that does not vary with time. A more plausible starting point (Figure 4) has horizontal variation in both buoyancy and mixed layer depth, as might be caused by spatially varying mixing of an ocean that was initially uniformly stratified. Tandon and Garrett (1994b) show that in this and related problems, with a plausible "wide front" approximation, there is a slight flattening of the interface slope but restratification given by (4.1) is still achieved locally. This holds promise for extensions of a general subinertial mixed layer model developed by Young (1994) but hitherto limited by the assumption of a large density jump across the base of the mixed layer which rules out changes in the interface.

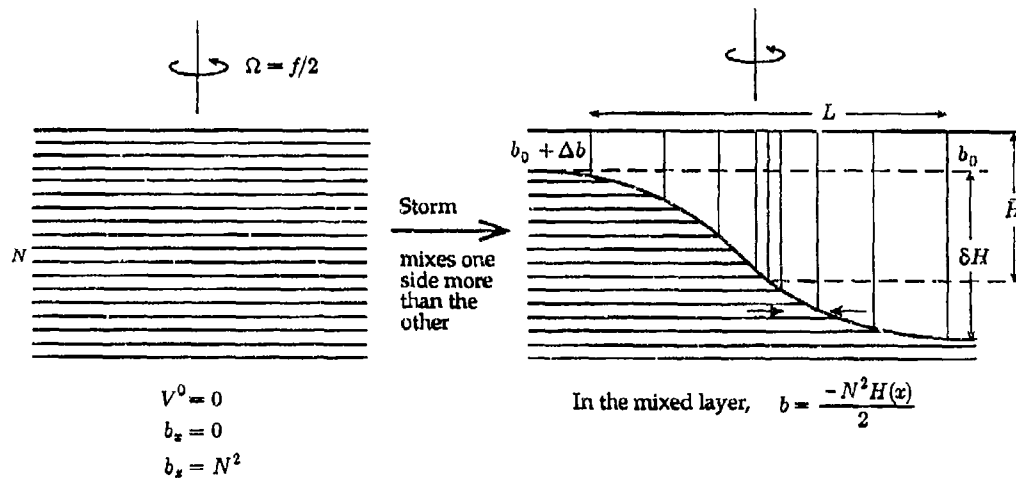


Figure 4: Horizontal buoyancy gradient in the surface mixed layer due to variable mixing. (From Tandon and Garrett, 1994b.)

## 5. IS THE NONLINEARITY OF THE EQUATION OF STATE IMPORTANT?

The density of seawater depends in a nonlinear way on the pressure and on the temperature and salinity of the water. For the surface mixed layer the temperature dependence is the most important and can give rise to the interesting and potentially misleading existence of a net annual buoyancy flux into the sea even in a situation where the net annual heat flux is zero!

This is easily seen by inspection of (2.1). The relevant nonlinearity in the equation of state corresponds to a temperature dependence of the expansion coefficient  $\alpha$  and the annual average buoyancy flux has a term  $-C_p^{-1} \rho_0^{-1} g \alpha' \bar{Q}'$  where  $\alpha'$ ,  $\bar{Q}'$  are the departures of the expansion coefficient and the total heat flux away from their annual means. We shall ignore the depth dependence of the insulation, or assume that it is distributed over a depth in which the temperature does not change from its surface value. Hence we may write  $\alpha' = (\partial \alpha / \partial T) T'$  with  $T'$  the departure of the surface temperature from its annual average  $\bar{T}$ , and so we are interested in evaluating the annual average  $\bar{T}' \bar{Q}'$ . Now if  $H$

represents the total heat content of the ocean (down to the greatest depth affected by the annual cycle) we have

$$\frac{dH}{dt} = (\rho_0 C_p)^{-1} Q. \quad (5.1)$$

If the mixed layer were well mixed of constant depth, (5.1) would give  $(dT'/dt) \propto Q'$  and hence  $T'Q' = 0$  as  $T', Q'$  would be in quadrature. In general, however, (5.1) gives (for  $\bar{Q} = 0$ )

$$T'Q' = \bar{T}\bar{Q} = \rho_0 C_p \bar{T} \frac{dH}{dt} \quad (5.2)$$

$$= \rho_0 C_p t_0^{-1} \oint T dH \quad (5.3)$$

where  $t_0 = 1$  year and  $\oint T dH$  is the area enclosed by the curve of  $T$  versus  $H$ , proceeding clockwise (Figure 5).

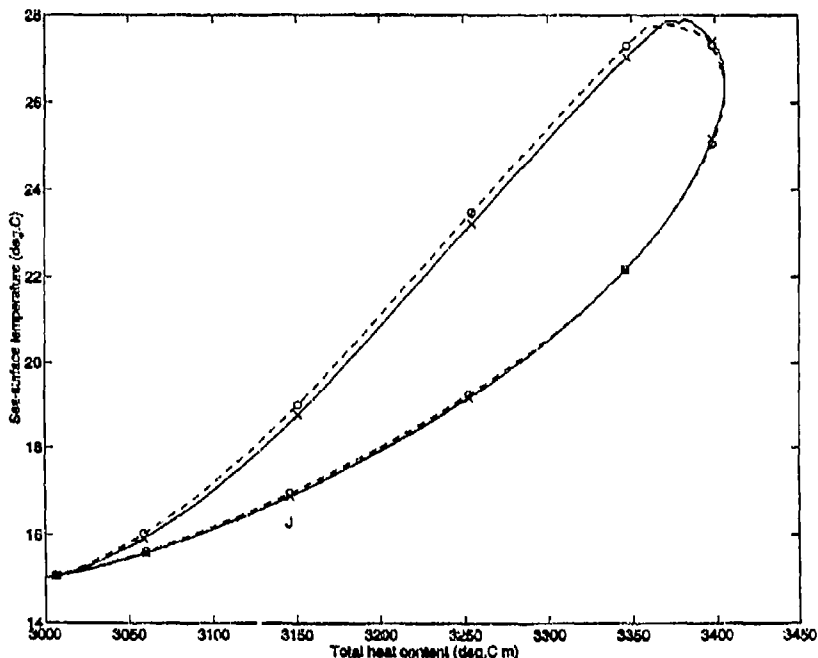


Figure 5: Temperature versus heat content of the surface mixed layer over an annual cycle which proceeds clockwise, with J marking 15 January. (From Zahariev and Garrett, 1994.)

Data and models (Gill and Turner, 1976; Zahariev and Garrett, 1994) show a tendency for this area to be positive (with increasing time corresponding to clockwise rather than anticlockwise circulation around the curve in Figure 5). Equivalently, there is a tendency for the heating of warm water and cooling of cold water, with the former expanding more than the latter contracts. The effect can be significant; for the Mediterranean Sea the associated buoyancy flux is comparable with other terms and equivalent to a heat input of  $6 \text{ W m}^{-2}$  (Garrett et al., 1993).

This possibility of a net surface buoyancy input for no net heat input does not mean that the ocean becomes steadily less dense. As discussed by Zahariev and Garrett (1994) there is a compensating loss of buoyancy due to cabbeling, or densification on mixing, whenever the mixed layer entrains colder water from below. The effect does, however, emphasize the need for care in evaluating the thermodynamics as well as the dynamics of the surface mixed layer.

## 6. WATER MASS FORMATION

The exchange of water between the surface mixed layer and the underlying ocean is a topic of great current interest, with particular attention being paid to the quantity and properties of water that is subducted into the main thermocline (e.g. Marshall et al., 1993). One approach (Walin, 1982; Speer and Tziperman, 1992) starts from consideration of the buoyancy flux, across the sea surface, between the surface outcroppings of neighbouring isopycnals. This buoyancy flux must be balanced by a diapycnal buoyancy flux, but with contributions from both diapycnal advection (related to water mass formation) and diapycnal mixing. Garrett et al. (1994) point out that it is hard to separate the relative contributions of advection and mixing, though the diapycnal buoyancy flux may all be advective in the special case of a well-mixed surface layer and an adiabatic interior. This result does, however, ignore the seasonal cycle in the properties of the surface layer and the horizontal diapycnal eddy fluxes in the surface mixed layer due to mesoscale eddies.

## 7. DISCUSSION

One-dimensional models remain the backbone of studies of the surface mixed layer, and improved observations and greater computer power now make it possible to conduct serious investigations of dominant physical processes such as Langmuir circulation which have hitherto been bypassed in bulk models or ignored in higher-order models and may give more rapid initial deepening of a layer than predicted by current models. Most investigations of fully nonlinear Langmuir circulation are still two-dimensional, but will eventually be supported and extended by three-dimensional "large eddy simulations". It is important, however, that the detailed results of these investigations be interpreted in ways that lead to simple parameterisations suitable for operational use.

Internal waves are a process that I have not discussed in this brief review, although the oscillatory vertical displacements and vertical shears of horizontal currents that they produce may well affect the average behaviour of the surface mixed layer and need to be parameterised (Mellor, 1989).

Horizontal inhomogeneities of mixed layer properties also give rise to interesting physical effects that may need to be incorporated better into mixed layer models, especially if they are being used as part of a study of larger-scale issues of ocean circulation and climate. There are still many exciting observational, theoretical, computational and practical questions awaiting solution.

### Acknowledgements

This limited review has referred, perhaps excessively, to my current interests and to joint work with colleagues whose papers are cited and whom I thank for their contributions. The

support of Canada's Natural Sciences and Engineering Research Council and Department of Fisheries and Oceans, and of the U.S. Office of Naval Research, is also gratefully acknowledged.

## REFERENCES

Agrawal, Y.C., E.A. Terray, M.A. Donelan, P.A. Hwang, A.J. Williams III, W.M. Drennan, K.K. Kalma, and S.A. Kitaigorodskii. 1992. Enhanced dissipation of kinetic energy beneath surface waves. *Nature*, **359**, 219-220.

André, J.C. and P. Lacarrère. 1985. Mean and turbulent structures of the oceanic surface layer as determined from one-dimensional, third order simulations. *J. Phys. Oceanogr.*, **15**, 121-132.

Anis, A. and J.N. Moum. 1992. The superadiabatic surface layer of the ocean during convection. *J. Phys. Oceanogr.*, **22**, 1221-1227.

Blanck, B. and P. Delecluse. 1993. Variability of the tropical Atlantic Ocean simulated by a general circulation model with two different mixed-layer physics. *J. Phys. Oceanogr.*, **23**, 1363-1388.

Bougeault, P. and P. André. 1986. On the stability of the third-order turbulence closure for the modeling of the stratocumulus-topped boundary boundary layer. *J. Atmos. Sci.*, **43**, 1574-1581.

Brainerd, K.E. and M.C. Gregg. 1993a. Diurnal restratification and turbulence in the oceanic surface mixed layer, 1, observations. *J. Geophys. Res.*, **98**, 22,645-22,656.

Brainerd, K.E. and M.C. Gregg. 1993b. Diurnal restratification and turbulence in the oceanic surface mixed layer, 2, modeling. *J. Geophys. Res.*, **98**, 22,657-22,664.

Craik, A.D.D. and S. Leibovich. 1976. A rational model for Langmuir circulations. *J. Fluid Mech.*, **73**, 401-426.

Demian, K.L. and M. Miyake. 1973. Upper layer modification at ocean station Papa: Observations and simulations. *J. Phys. Oceanogr.*, **3**, 185-196.

de Ruijter, W.P.M. 1983. Effects of velocity shear in advective mixed-layer models. *J. Phys. Oceanogr.*, **13**, 1589-1599.

de Szoeke, R.A. 1980. On the effects of horizontal variability of wind stress on the dynamics of the ocean mixed layer. *J. Phys. Oceanogr.*, **10**, 1439-1454.

Galperin, B., L.H. Kantha, S. Hassid, and A. Rosati. 1988. A quasi-equilibrium turbulent energy model for geophysical flows. *J. Atmos. Sci.*, **45**, 55-62.

Garrett, C., K. Speer, and E. Tragou. 1994. The relationship between water mass formation and the surface buoyancy flux, with application to Phillips' Red Sea model. *J. Phys. Oceanogr.*, submitted.

Garrett, C., R. Outerbridge, and K. Thompson. 1993. Interannual variability in Mediterranean heat and buoyancy fluxes. *J. Climate*, **6**, 900-910.

Garwood, R.W., Jr. 1977. An oceanic mixed layer model capable of simulating cyclic states. *J. Phys. Oceanogr.*, **7**, 455-468.

Gaspar, P., Y. Grégoris, and J.-M. Lefevre. 1990. A simple eddy kinetic energy model for simulations of the oceanic vertical mixing: Tests at station Papa and long-term upper ocean study site. *J. Geophys. Res.*, **95**, 16,179-16,193.

Gemmrich, J.R., T.D. Mudge, and V.D. Polonichko. 1994. On the energy input from the wind into the surface wave field. *J. Phys. Oceanogr.*, in press.

Gill, A.E. 1982. *Atmosphere-Ocean Dynamics*. Academic Press, New York, 662 pp.

Gill, A.E. and J.S. Turner. 1976. A comparison of seasonal thermocline models with observations. *Deep-Sea Res.*, **23**, 391-401.

Kantha, L. and C. Clayson. 1994. An improved mixed layer model for geophysical applications. *J. Geophys. Res.*, submitted.

Large, W.G., J.C. McWilliams, and S. Doney. 1994. A vertical mixing scheme for momentum and buoyancy in an ocean model with a K-profile boundary layer. *Rev. Geophys.*, submitted.

Lascaratos, A., R.G. Williams, and E. Tragou. 1993. A mixed-layer study of the formation of Levantine Intermediate Water. *J. Geophys. Res.*, **98**, 14,739-14,749.

Leibovich, S. 1977. On the evolution of the system of wind drift currents and Langmuir circulations in the ocean. Part 1. Theory and averaged current. *J. Fluid Mech.*, **79**, 715-743.

Leibovich, S. 1983. The form and dynamics of Langmuir circulations. *Ann. Rev. Fluid Mech.*, **15**, 391-427.

Li, M. and C. Garrett. 1993. Cell merging and jet/downwelling ratio in Langmuir circulation. *J. Mar. Res.*, **51**, 737-769.

Li, M. and C. Garrett. 1994. Is Langmuir circulation driven by surface waves or surface cooling? *J. Phys. Oceanogr.*, in press.

Lombardo, C.P. and M.C. Gregg. 1989. Similarity scaling of viscous and thermal dissipation in a convecting surface boundary layer. *J. Geophys. Res.*, **94**, 6273-6284.

Marshall, J.C., A.J.G. Nurser, and R.G. Williams. 1993. Inferring the subduction rate and period over the North Atlantic. *J. Phys. Oceanogr.*, **23**, 1315-1329.

Mellor, G.L. 1989. Retrospect on ocean boundary layer modelling and second moment closure. Proceedings of the Fifth 'Aha Huliko'a Hawaiian Winter Workshop, 251-272.

Mellor, G.L. and T. Yamada. 1974. A hierarchy of turbulence closure models for planetary boundary layers. *J. Atmos. Sci.*, **31**, 1791-1806.

Mellor, G.L. and T. Yamada. 1982. Development of a turbulence closure model for geophysical fluid problems. *Rev. Geophys. Space Phys.*, **20**, 851-875.

Niiler, P.P. and E.B. Kraus. 1977. One-dimensional models of the upper ocean. In: *Modelling and Prediction of the Upper Layers of the Ocean*, E.B. Kraus, ed., Pergamon, New York, 143-172.

Osborn, T., D.M. Farmer, S. Vagle, S.A. Thorpe, and M. Curé. 1992. Measurements of bubble plumes and turbulence from a submarine. *Atmos.-Ocean*, **30**, 419-440.

Ou, H.W. 1984. Geostrophic adjustment: A mechanism for frontogenesis. *J. Phys. Oceanogr.*, **14**, 994-1000.

Philander, S.G.H. and R.C. Pacanowski. 1986. The generation of equatorial currents. *J. Geophys. Res.*, **85**, 1123-1136.

Phillips, O.M. 1977. *The Dynamics of the Upper Ocean*. Cambridge University Press, 336 pp.

Pollard, R.T. 1977. Observations and theories of Langmuir circulations and their role in the near surface mixing. In: *A Voyage of Discovery: George Deacon 70th Anniversary Volume*, M. Angel, ed., Pergamon Press, New York, 235-251.

Pollard, R.T., P.B. Rhines, and R.O.R.Y. Thompson. 1973. The deepening of the wind-mixed layer. *Geophys. Fluid Dyn.*, **3**, 381-404.

Price, J.F., R.A. Weller, and R.P. Pinkel. 1986. Diurnal cycling: Observations and models of the upper ocean response to diurnal heating, cooling and wind mixing. *J. Geophys. Res.*, **91**, 8411-8427.

Richman, J. and C. Garrett. 1977. The transfer of energy and momentum by the wind to the surface mixed layer. *J. Phys. Oceanogr.*, **7**, 876-881.

Speer, K.G. and E. Tziperman, 1992. Rates of water mass formation in the North Atlantic Ocean. *J. Phys. Oceanogr.*, **22**, 93-104.

Tandon, A. and C. Garrett. 1994a. Mixed layer restratification due to a horizontal density gradient, *J. Phys. Oceanogr.*, **24**, 1419-1424.

Tandon, A. and C. Garrett. 1994b. Geostrophic adjustment and restratification of a mixed layer with horizontal gradients above a stratified layer. (In preparation).

Thorpe, S.A. 1993. Energy loss by breaking waves. *J. Phys. Oceanogr.*, **28**, 2498-2502.

Thorpe, S.A. and A.J. Hall. 1982. Observations of the thermal structure of Langmuir circulation. *J. Fluid Mech.*, **114**, 237-250.

Turner, J.S. 1973. *Buoyancy Effects in Fluids*. Cambridge University Press, Cambridge. 367 pp.

Vonnegut, K. 1963. *Cat's Cradle*. Gollancz, London.

Walsh, G. 1982. On the relation between sea-surface heat flow and thermal circulation in the ocean. *Tellus*, **34**, 187-195.

Weller, R.A. and J.F. Price, 1988. Langmuir circulation within the oceanic mixed layer. *Deep-Sea Res.*, **35**, 711-747.

Young, W.R. 1994. The subinertial mixed layer approximation. *J. Phys. Oceanogr.*, **24**, in press.

Zahariev, K. and C. Garrett. 1994. An apparent surface buoyancy flux associated with the nonlinearity of the equation of state. (In preparation).

SINGULARITY FORMATION IN A STRATIFIED  
FLUID SUBJECT TO OSCILLATORY FORCING.

Sergey T. Simakov

Department of Mathematics, Physical Faculty,  
Moscow State University, 119899 Moscow, Russia

Abstract

The paper considers singularity formation of a wave field from oscillatory sources in a density stratified fluid. Three kinds of forcing are studied: the monochromatic point source, monochromatic point sources distributed on a curve and sources distributed on a surface. In all the cases the frequency of the forcing is taken to belong to an interval over which the steady-oscillation equation is hyperbolic. We demonstrate that the solution diverges, as  $t \rightarrow \infty$ , on a characteristic manifold whose configuration is determined by the amplitude distribution of the forcing. Asymptotic formulae obtained show how the rate of the divergence at a point of that manifold depends on the power of the source and the way, in which the characteristic cone emanating from the point touches the source.

SINGULARITY FORMATION IN A STRATIFIED  
FLUID SUBJECT TO OSCILLATORY FORCING.

Sergey T. Simakov

Department of Mathematics, Physical Faculty  
Moscow State University

1. Introduction

We consider the large time behaviour of solutions of the problem

$$(\partial^2/\partial t^2)\nabla^2 u + N^2(x_3)\hat{\nabla}^2 u = f(x, t) \quad (1.1a)$$

$$u|_{t=0} = u_t|_{t=0} = 0; |u| \rightarrow 0, |x| \rightarrow \infty; \quad (1.1b)$$

where  $x = (\hat{x}, x_3)$ ,  $\hat{x} = (x_1, x_2)$ ,  $\nabla = (\partial/\partial x_1, \partial/\partial x_2, \partial/\partial x_3)$ ,  $\hat{\nabla}^2 = \nabla^2 - \partial^2/\partial x_3^2$ .

Equation (1.1a) governs waves in a density stratified fluid in the Boussinesq approximation and  $N(x_3)$  is the buoyancy frequency [1, 2, 3]. The following types of the forcing are discussed:

$$f(x, t) = \delta(x - x_0) e^{i\sigma t}, \quad x_0 = (\hat{x}_0, h); \quad (1.2)$$

$$f(x, t) = \int_{\gamma} \delta(x - \xi) d\ell_{\xi} e^{i\sigma t}; \quad (1.3)$$

$$f(x, t) = \frac{\partial^3 Q(x, t)}{\partial t^2 \partial x_3}, \quad Q(x, t) = \int_S \delta(x - \xi) d^2 S_{\xi} e^{i\sigma t} \quad (1.4)$$

Here  $\delta(x)$  denotes Dirac's delta-function,  $\gamma$  is a curve and  $S$  is a surface. When  $f(x, t)$  is given by (1.2) or (1.3) we assume that  $u$  is the vertical component of the velocity field. In that case  $f(x, t)$  is related to the volume density  $\vec{F} = F(x, t) \vec{e}_3$  of the real force as  $\rho_0^{-1} \hat{\nabla}^2 \vec{F}_t = f$ , where  $\rho_0$  is the rest density of the fluid. When the forcing is given by (1.4) we assume that  $u$  is the vertical component of the mass flow [1].

Throughout  $\sigma$  is taken to belong to the interval over which the steady-oscillation operator  $\mathcal{L}^0 = -\sigma^2 \nabla^2 + N^2(x_3) \hat{\nabla}^2$  is hyperbolic everywhere, i.e.  $\sigma \in (0, \inf N(x_3))$ , and the term "characteristic" is used only regarding  $\mathcal{L}^0$ . The hyperbolicity

ty of  $\Sigma^\sigma$  guarantees that at any point there exist directions, forming the angle  $\alpha(x_3) = \arccos(\sigma/N(x_3))$  with respect to the vertical line, along which wave energy of frequency  $\sigma$  propagates. We show that on a characteristic manifold emanating from the support of the forcing (i.e. from  $\Sigma_0$ ,  $\gamma$  or  $S$ )  $|u| \rightarrow \infty$ , as  $t \rightarrow \infty$ , while at any fixed point outside that manifold and the support  $U$  remains bounded. Mathematically such behaviour can be regarded as formation of singularities of the limiting solution taking place by the hyperbolicity of the steady-oscillation equation.

## 2. Monochromatic point source.

Let  $f(x, t)$  be given by (1.2). The solution of (1.1) may be written as

$$u(x, t) = e^{i\sigma t} \int_0^t e^{-i\sigma\tau} \mathcal{E}^h(\hat{x} - \hat{x}_0, x_3, \tau) d\tau$$

where  $\mathcal{E}^h(\hat{x} - \hat{x}_0, x_3, t)$  denotes the solution of (1.1a) subject to  $f(x, t) = \delta(x - x_0, t)$  and the conditions:  $\mathcal{E}^h|_{t \leq 0} = 0$ ;  $\mathcal{E}^h \rightarrow 0$  as  $|x| \rightarrow \infty$ . We are going to describe the  $t \rightarrow \infty$  behaviour of  $u$  on the characteristic conoid  $K^\sigma(x_0) \equiv \{x / \Gamma(\sigma, x, x_0) = 0, x \neq x_0\}$  where  $\Gamma(\sigma, x, x_0)$  is the square of the geodesic distance between  $x$  and  $x_0$ :

$$\Gamma(\sigma, x, x_0) \equiv \left\{ \int_{-h}^{x_3} (N^2(z) - \sigma^2)^{-1/2} dz \right\}^2 - \sigma^2 |\hat{x} - \hat{x}_0|^2$$

Putting  $x \in K^\sigma(x_0)$  we represent  $u(x, t)$  through the Fourier transform of  $\mathcal{E}^h(\hat{x} - \hat{x}_0, x_3, t)$ :

$$u(x, t) = \frac{e^{i\sigma t}}{2\pi i} \int_{-\infty}^{+\infty} \frac{e^{i(\omega-\sigma)t} - 1}{(\omega - \sigma)} \hat{\mathcal{E}}^h(\hat{x} - \hat{x}_0, x_3, \omega) d\omega$$

When  $N(x_3) = \text{const} = N$  we have  $K^\sigma(x_3) = \{x / d(x - x_0) = \sigma\}$  and  $\hat{\mathcal{E}}^h(\hat{x} - \hat{x}_0, x_3, \omega) = \hat{E}(x - x_0, i\omega)$  where  $d(x) = N|x_3|/|x|$  and

$$\hat{E}(x, \rho) = -\frac{i}{4\pi|x|} (p^2 + N^2)^{-1/2} (p^2 + d^2(x))^{-1/2} \quad (2.1)$$

(see [4-8]). In (2.1) the branches of the square roots  $(p^2 + d^2)^{1/2}$  are taken so that they assume positive values on the real axis

3

of  $p$  and have cuts along the rays  $(-\infty i\alpha, +i\alpha]$ . Since  $x \in K^\sigma(x_0)$ ,  $\hat{E}(x, i\omega)$  behaves like  $(\omega - \sigma)^{-1/2}$  near  $\omega = \sigma$ . Straightforward calculations give [9]:

$$u(x, t) \sim \frac{i}{4\pi|x-x_0|} \frac{\sqrt{2} e^{i(\sigma t + 3\pi/4)}}{(\sigma\pi)^{1/2} (N^2 - \sigma^2)^{1/2}} t^{1/2}, \quad x \in K^\sigma(x_0)$$

When  $N(x_3) \neq \text{const}$  we take advantage of Hadamard's expansion of a fundamental solution of  $\mathcal{L}^\omega$  in powers of the geodesic distance [10]. The first term of the expansion of  $\hat{E}^h(\hat{x} - \hat{x}_0, x_3, \omega)$  in powers of  $\Gamma$  is

$$g^h(\hat{x} - \hat{x}_0, x_3, \omega) = -(4\pi)^{-1} (N^2(x_3) - \omega^2)^{-1/4} (N^2(h) - \omega^2)^{-1/4} \Gamma^{-1/2}(\omega, x, x_0)$$

the next term being proportional to  $\Gamma^{1/2}(\omega, x, x_0)$ . The argument of the complex number  $\Gamma^{1/2}$  is assumed to equal  $\pi/2$  when  $\Gamma < 0$ . The form of  $g^h$  shows that, when  $x$  belongs to  $K^\sigma(x_0)$ ,  $\hat{E}^h(\hat{x} - \hat{x}_0, x_3, \omega)$  behaves like  $(\omega - \sigma)^{-1/2}$  near  $\omega = \sigma$ , so we get [11]:

$$u(x, t) \sim \frac{\sqrt{2} e^{i(\sigma t + 3\pi/4)}}{4\pi(\sigma\pi)^{1/2} \chi(x, x_0, \sigma)} t^{1/2}, \quad x \in K^\sigma(x_0)$$

where

$$\begin{aligned} \chi(x, x_0, \sigma) &= (N^2(x_3) - \sigma^2)^{1/4} (N^2(h) - \sigma^2)^{1/4} \times \\ &\times \left\{ \int_h^{x_3} (N^2(z) - \sigma^2)^{-1/2} dz \int_h^{x_3} (N^2(\eta) - \sigma^2)^{-1/2} d\eta + |\hat{x} - \hat{x}_0|^2 \right\}^{1/2} \end{aligned}$$

We note that this result is in agreement with Borovikov's hypothesis about the asymptotic behaviour of  $\hat{E}^h(\hat{x}, x_3, t)$  at large times [12].

### 3. Sources distributed on a curve.

From now on we assume that  $N(x_3) = \text{const} = N$ . Let in (1.3)  $\gamma$  be the curve  $\xi = \xi(\omega) = (\chi(\theta), \eta(\theta), \mu(\theta))$ ,  $\theta \in [\alpha, \beta]$ , with analytic  $\chi(\theta), \eta(\theta), \mu(\theta)$  satisfying the conditions:

$$\chi'^2(\theta) + \eta'^2(\theta) + \mu'^2(\theta) \neq 0; \quad \xi(\theta_1) \neq \xi(\theta_2), \theta_1 \neq \theta_2 \quad (3.1)$$

The solution of (1.1) with  $f(x,t)$  given by (1.3) has the form:

$$u(x,t) = \frac{i}{2\pi i} \int_{\gamma} d\ell_{\xi} \int_{c-i\infty}^{c+i\infty} dp \hat{E}(x-\xi, p)(p-i\sigma)^{-1} e^{pt}$$

where  $c > 0$  and  $\hat{E}(x,p)$  is the same as in (2.1). We rewrite  $u(x,t)$  as

$$u(x,t) = \frac{1}{2\pi i} \int_a^b d\theta \varphi(\theta) \int_{c-i\infty}^{c+i\infty} dp (p^2 + N^2)^{-1/2} (p^2 + d^2(\theta))^{-1/2} (p-i\sigma)^{-1} e^{pt} \quad (3.2)$$

Here  $d(\theta) = N|x_3 - \mu(\theta)|/|x - \xi(\theta)|$  and  $\varphi(\theta)$  is a smooth function whose form depends on  $\chi, \eta, \mu$  and  $x$ . We note that, by (3.1),  $\varphi(\theta) \neq 0$  for any  $\theta \in [a, b]$ .

The following formula is valid [13]:

$$u(x,t) = P(t) e^{i\sigma t} + O(1) \quad (3.3)$$

where  $P(t) = P(a, b, t)$  and

$$P(\alpha, \beta, t) = \int_{\alpha}^{\beta} d\theta \psi(\theta) \int_0^t d\tau \tau^{-1/2} e^{i(d(\theta) - \sigma)\tau}, \quad a < \alpha < \beta < b$$

$$\psi(\theta) = e^{-i\pi/4} \varphi(\theta) (2\pi d(\theta) (N^2 - d^2(\theta)))^{-1/2}$$

In (3.3) we suppress the dependence on the spatial variable for  $x$  is assumed to be fixed.

By the analyticity  $d(\theta)$  can equal  $\sigma$  either at a finite number of points or everywhere on  $[a, b]$ . In the latter case

$$P(t) = 2t^{1/2} \int_a^b d\theta \psi(\theta)$$

so  $u \sim t^{1/2} e^{i\sigma t}$ , as  $t \rightarrow \infty$ . Let  $d(\theta) = \sigma$  at  $\theta_i$ ,  $i = 1, \dots, k$  and  $d(\theta) \neq \sigma$  for all  $\theta \in [a, b]$  and  $\theta \neq \theta_i$ . If  $[\alpha, \beta]$  does not contain any of  $\theta_i$  ( $i = 1, \dots, k$ ) then  $P(\alpha, \beta, t) = O(1)$ . It can be shown by passing to variable  $|d(\theta) - \sigma|/\tau$  in the integral over  $\tau$ .

Now let us consider the case when  $[\alpha, \beta]$  contains only one of the points  $\theta_i$ , say  $\theta_j$ , and does not contain  $\theta$  at which  $d(\theta)$  equals either zero or  $N$ . Since  $d(\theta)$  is analytic and  $d(\theta) \neq \text{const}$  there is  $n_j$  such that  $d^{(s)}(\theta_j) = 0$ ,  $0 < s < n_j$ , and  $d^{(n_j)}(\theta_j) \neq 0$ . Here  $d^{(s)}(\theta)$  is the  $s$ -th derivative of  $d(\theta)$ .

Differentiating  $P(\alpha, \beta, t)$  we get

$$\frac{d}{dt} P(\alpha, \beta, t) = t^{-1/2} \int_{\alpha}^{\beta} d\theta \psi(\theta) e^{i(d(\theta) - \sigma)t} \quad (3.4)$$

Applying the stationary phase method to the integral in (3.4) and integrating over  $t$  we find that  $P(\alpha, \beta, t)$  has the following behaviour as  $t \rightarrow \infty$ . If  $n_j = 1$ ,  $P(\alpha, \beta, t) \sim 0(1)$ ; if  $n_j = 2$ ,  $P(\alpha, \beta, t) \sim \ln t$ ; if  $n_j > 2$ ,  $P(\alpha, \beta, t) \sim t^{4/2 - 1/n_j}$ .

Appropriately dividing  $[a, b]$  into a finite number of segments we may formulate the final result of this section. For this purpose we introduce the set

$$K^\sigma(\gamma) \equiv \{x \mid \exists \theta \in [a, b], d(\theta) = \sigma, d'(\theta) = 0\}$$

When  $K^\sigma(\gamma)$  is empty and  $x \notin \gamma$ ,  $u(x, t) = 0(1)$  as  $t \rightarrow \infty$ . The same result is valid when  $K^\sigma(\gamma)$  is nonempty but  $x$  belongs neither to  $K^\sigma(\gamma)$  nor to  $\gamma$ . When  $K^\sigma(\gamma)$  is nonempty and  $x \in K^\sigma(\gamma)$ ,  $|u| \rightarrow \infty$ , as  $t \rightarrow \infty$ , and the asymptotic formulae are valid:

$$u(x, t) \sim e^{i\sigma t} \ln t, \text{ if } \nu_x = 2; u(x, t) \sim e^{i\sigma t} \frac{t^{4/2 - 1/\nu_x}}{t}, \text{ if } \nu_x > 2;$$

$$u(x, t) \sim e^{i\sigma t} t^{1/2}, \text{ if } d(\theta) \equiv \sigma \text{ on } [a, b]. \quad (3.5)$$

Here  $\nu_x = \frac{1}{t} \ln n_i$  for fixed  $x$ .

Thus,  $|u(x, t)| \rightarrow \infty$  as  $t \rightarrow \infty$  on  $K^\sigma(\gamma)$ . The rate of that process depends on the position of  $x$  on  $K^\sigma(\gamma)$  and is given by (3.5). At any fixed point outside  $K^\sigma(\gamma)$  and  $\gamma$  the solution remains bounded in time. Geometrically set  $K^\sigma(\gamma)$  can be defined as the set of all points  $x$  that satisfy the condition:  $\gamma$  is tangent to the characteristic cone emanating from  $x$  (i.e. to  $K^\sigma(x)$ ). Since the slope of a tangent vector on the cone varies within the limits determined by the inequality  $|\sin \alpha| \leq \frac{1}{N}$ , where  $\alpha$  is the angle between the tangent vector and the horizontal plane, set  $K^\sigma(\gamma)$  is empty if

$$|(\vec{e}_3 \vec{t}(\theta))| / |\vec{t}(\theta)| > \sigma/N \text{ for all } \theta \in [a, b],$$

where  $\vec{t}(\theta) = \vec{x}' \vec{e}_1 + \eta' \vec{e}_2 + \mu' \vec{e}_3$  and  $\vec{e}_i$  are the unit vectors of the

corresponding axes.

Number  $\nu_{\xi-i}$  is the order of contact between  $\gamma$  and  $K^{\sigma}(x)$ . Formulae (3.5) show that the greater this number is, the more rapidly  $|\mathcal{U}|$  tends to infinity. This dependence is reasonable, since the order of contact between  $\gamma$  and  $K^{\sigma}(x)$  reflects the degree of focusing of characteristic rays along which the energy of frequency  $\sigma$  propagates from  $\gamma$  to a neighbourhood of  $x$ .

#### 4. Sources distributed on surfaces.

In this section we consider problem (1.1) subject to forcing (1.4). Its solution has the form

$$\mathcal{U}(x, t) = (-\sigma^2) \int_{c-i\infty}^{c+i\infty} dp e^{pt} \int_S d^2 \xi \frac{\partial}{\partial x_3} \hat{E}(x-\xi, p) (p-i\sigma)^{-i}, \quad c > 0$$

We assume that  $S$  is a smooth closed surface and that, for any fixed  $x \notin S$ , this surface can be covered by a finite number of its subsurfaces  $g_\alpha$  parametrized by triples of functions

$$\Psi_\alpha(\theta, s) = (\psi_{\alpha 1}(\theta, s), \psi_{\alpha 2}(\theta, s), \psi_{\alpha 3}(\theta, s))$$

with  $(\theta, s)$  varying within open domains  $\Omega_\alpha \subset \mathbb{R}^2$  so as each of  $g_\alpha$  to satisfy one of the following conditions:

(a) There is no point belonging to  $g_\alpha$  at which the relation

$$\nabla_{\theta s} d(\theta, s) = (0, 0) \quad (4.1)$$

holds;

(b) There is a unique point  $\xi_0 = \Psi_\alpha(\theta_0, s_0)$ ,  $(\theta_0, s_0) \in \Omega_\alpha$ , at which (4.1) holds;

(c) Equality (4.1) holds along a curve lying on  $g_\alpha$ , for instance, along the curve  $\xi = \Psi_\alpha(\theta, \lambda(\theta))$ ,  $\theta \in (b, B)$ , and on that curve  $d(\theta, \lambda(\theta)) \neq 0$ .

Here we used the notations:  $\nabla_{\theta s} \equiv (\partial/\partial \theta, \partial/\partial s)$ ,  $d(\theta, s) \equiv d(x - \Psi_\alpha(\theta, s))$ .

We restrict ourselves to considering surfaces possessing the nondegeneracy property:

$$\left. \frac{\partial^2}{\partial \theta^2} d \frac{\partial^2}{\partial s^2} d - \left( \frac{\partial^2}{\partial \theta \partial s} d \right)^2 \right|_{(\theta_0, s_0)} \neq 0$$

for each  $g_\alpha$  satisfying (b) and

$$\left. \frac{\partial^2}{\partial s^2} d(\theta, s) \right|_{s=\lambda(\theta)} \geq h_\alpha(x) > 0$$

for each  $g_\alpha$  satisfying (c). Technically these properties enable us to apply the appropriate form of the stationary phase method.

Fixing  $x$  and using the partition of unity we represent  $u(x, t)$  as a finite sum of the integrals:

$$u_\alpha(x, t) = \frac{0^\alpha}{8\pi^2 i} \int_{g_\alpha} d^2 s \int_{\xi} \frac{\mu_\alpha(\xi)(\xi_3 - x_3)}{|x - \xi|^3} \int_{c-i\infty}^{c+i\infty} \frac{e^{pt}(p^2 + N^2)^{1/2}}{(p-i\sigma)(p^2 + d^2(x-\xi))^{3/2}} dp \quad (4.2)$$

where  $\mu_\alpha(\xi) \in C_0^\infty(g_\alpha)$ . First we consider  $g_\alpha$  for which  $d(x-\xi)$  is separated from  $N$  and zero. From the integrand in  $\sim$  in (4.2) we extract the singular terms which can result in an unbounded growth of  $|u_\alpha|$ . Here the main role is played by the term

$$(2id)^{-3/2} (N^2 - d^2)^{1/2} (p-i\sigma)^{-1} (p-id)^{-3/2} e^{pt}$$

Using the same procedure as in § 3 we get [13] that  $u_\alpha \sim t^{1/2} e^{i\sigma t}$  if  $g_\alpha$  satisfies (b) with  $(\theta_0, s_0)$  fulfilling  $d(\theta_0, s_0) = 0$ , and  $u_\alpha \sim t e^{i\sigma t}$ , if  $g_\alpha$  satisfies (c) with  $\lambda(\theta)$  fulfilling the relation  $d(\theta, \lambda(\theta)) = 0$ . In the other cases  $u_\alpha(x, t) = O(1)$  as  $t \rightarrow \infty$ .

Let us turn to the situation when  $g_\alpha$  contains point(s)  $\xi$  for which  $d(x-\xi) = N$ . It is clear that at such  $\xi$  (4.1) holds. If  $d(x-\xi)$  is separated from  $0$  on  $g_\alpha$  we can reduce (4.2) to the form:

$$u_\alpha(x, t) = t^{1/2} \int_{Q_\alpha} d\theta ds (N-d)^{1/2} (A^+ e^{+idt} + A^- e^{-idt}) + O(1)$$

where  $d = d(\theta, s)$  and  $A^\pm = A^\pm(\theta, s) \in C_0^\infty(Q_\alpha)$ . Hence we get that  $u_\alpha(x, t) = O(1)$  as  $t \rightarrow \infty$ .

When  $g_\alpha$  is such, that  $d(x-\xi)$  is separated from  $0$ , and contains point(s)  $\xi$  at which  $d(x-\xi) = 0$  we estimate (4.2) using the fact that  $(p^2 + d^2)^{-3/2}$  is the Laplace transform of the function  $t J_1(dt)/d$  where  $J_1$  is the Bessel function of order one.

From the boundedness of the functions

$$t \int_0^\delta d\rho \rho J_1(\rho^2 t) \quad \text{and} \quad t \int_0^\delta ds J_1(st)$$

it follows that  $U_\alpha(x, t) = 0$  as  $t \rightarrow \infty$ .

An example of the surfaces fulfilling the conditions above is the sphere. For monochromatic sources distributed on a spherical surface we get the following picture. The absolute value of the solution tends to infinity, as  $t \rightarrow \infty$ , on two characteristic cones touching the sphere along horizontal circumferences. At the apexes of the cones  $U(x, t)$  diverges as  $t e^{i\theta t}$ , while on the rest of the cones  $U(x, t)$  diverges as  $t^{1/2} e^{i\theta t}$ . Everywhere outside the cones and the sphere  $U(x, t)$  remains bounded in time, i.e.  $|U(x, t)| < C(x)$ . This picture is in agreement with the results of [14] and [15], where pulsations of a sphere in a stratified fluid were studied.

#### Concluding remarks.

Asymptotical analysis made above mainly concerns the unbounded growth of  $|U(x, t)|$  as  $t \rightarrow \infty$ . It takes place on a characteristic set related to the support of the forcing. At a point of that set the rate of the growth is determined by the way the characteristic cone emanating from the point touches the source, in other words, by the degree of focusing of characteristic rays along which energy of frequency  $\Omega$  propagates from the source to a neighbourhood of the point.

The agreement of the results of §4 with those of [14, 15] shows that this approach may be used for studying radiative properties of a wide class of pulsating bodies.

#### References

1. Lighthill, M.J. 1978 Waves in Fluids. Cambridge University Press.
2. Gill, A.E. 1982 Atmosphere-Ocean Dynamics. Academic Press.
3. Brekhovskikh, L. & Goncharov, V. 1985 Mechanics of Continua and Wave Dynamics. Springer. (Translation from Russian)

4. Dickinson, R.E. 1969 Propagators of atmospheric motions.
  1. Excitation by point impulses. *Rev. Geophys.* 7, 483-514.
5. Diky, L.A. 1969 Theory of Oscillations of the Earth's Atmosphere. Leningrad: Gidrometeoizdat (in Russian).
6. Sekerzh-Zen'kovich, S.Ya. 1979 A fundamental solution of the internal-wave operator. *Sov. Phys. Dokl.* 24, 347-348.
7. Gabov, S.A. & Sveshnikov, A.G. 1986 Problems of Dynamics of Stratified Fluids. Moscow: Nauka (in Russian).
8. Voisin, B. 1991 Internal wave generation in uniformly stratified fluids. Part 1. Green's function and point sources. *J. Fluid Mech.* 231, 439-480.
9. Makhortykh, S.A. & Rybak, S.A. 1990 Effect of the near field of a point source on the generation of internal waves. *Izv. Atmos. Ocean. Phys.* 26, 194-198.
10. Hadamard, J. 1932 *Le Problème de Cauchy et les Equations aux Dérivées Partielles Linéaires Hyperboliques*. Paris: Hermann et Cie.
11. Simakov, S.T. 1993 Initial and boundary value problems of internal gravity waves. *J. Fluid Mech.* 248, 55-65.
12. Borovikov, V.A. 1990  $\Theta \rightarrow \infty$  asymptotic behaviour of the Green's function of the equation of internal waves. *Sov. Phys. Dokl.* 35, 631-633.
13. Simakov, S.T. Formation of singularities of limiting amplitude in a density stratified fluid disturbed by an extended monochromatic forcing. *Wave Motion* (in press).
14. Hendershott, M.C. 1969 Impulsively started oscillations in rotating stratified fluid. *J. Fluid Mech.* 36, 513-527.
15. Appleby, J.C. & Crighton, D.G. 1987 Internal gravity waves generated by oscillations of a sphere. *J. Fluid Mech.* 183, 439-450.

# A study of fine structure in stratified wakes past a cylinder by optical, acoustic and probe methods.

V.E. Prokhorov

*The Institute for Problems in Mechanics RAS  
E-mail:chakin@ipm.msk.su Fax:7/095 9382048*

An echosounding is widely used to study the fine structure of ocean flows. On the other hand, the highly sensitive optical (Schlieren) methods are used in laboratory studies of stratified liquid. Efficiency of the Schlieren technique is mainly provided by a complex optical scheme and stabilization of the Schlieren image device. Besides, for the fine vertical structure to be resolved the influence of the background vertical gradient must be compensated, for which a special optical compensating scheme is needed. Therefore, the Schlieren image device is generally adjusted to be sensitive to horizontal gradients.

In this connection it could be useful to supplement a lab facility by ultrasonic echosounder with narrow sound beam directed vertically. In this case a pressure  $P_s$  of the sound scattered by liquid inhomogeneities is given by [1]

$$P_s = \frac{P_0 k^2}{2\pi} \int_V \left( \frac{2c'}{c} + \frac{\lambda}{\Lambda'} \right) \frac{e^{ikr}}{r} dV, \quad (1)$$

where  $P_0$  is a pressure of incident wave of length  $\lambda$ ,  $k = 2\pi/\lambda$ ;  $c, c'$  — sound velocity and its fluctuation, respectively,  $\Lambda'$  — local vertical scale of variability of density fluctuations  $\rho'$  given by  $\Lambda' = \rho' / (d\rho'/dz)$ ,  $V$  — scattering volume,  $r$  — distance from scattering volume to antenna,  $z$  — vertical coordinate.

According to (1) scattering may be conditioned by both local fluctuations of liquid features and their gradients. The first type of scattering (volume scattering) is produced by a great number of liquid particles placed onto the inequilibrium horizons due to vertical movements. The second type — surface scattering — is caused by surfaces of discontinuity generated by flow in stratified fluid.

The structures generated by typical currents scatter a sound with a high intensity and provide a value of scattered signal no less than average maximum of scattering in the ocean. Formerly it was shown in lab experiments [2-4], and now is confirmed in experiments where we studied a flow past a circular cylinder in salinity stratified liquid without discrete particles (gas bubbles, suspensions). The flow was observed by optical and acoustic methods. Stratification (profiles of buoyancy, frequency) and intensity of liquid parameters fluctuations were measured by a small conductivity probe. Besides, some parameters of the flow were measured by means of correlative processing of the acoustic data.

The experiments were carried out on the installation shown on the block-diagram (Fig.1). The installation consists of lab basin ( $240 \times 60 \times 40 \text{ cm}^3$ ), two supply tanks (with fresh and salt water, respectively), a control stand with a transference mechanism, a conductivity probe and the lab echosounder. The echosounder contains a control pulse generator, a sound frequency generator, a power amplifier and time-controlled amplifier which selects a initial distance sounded and a space interval observed. After amplification the echosignals are detected and fed into a special digital transducer (Interface) which provide a feed of digit data with a speed of  $1.2 \text{ bit/s}$  into computer (PC) memory.

One of the important parts of echosounder was the antenna made of piezoelectric ceramic disc placed into a special sound shade.

The regime of echosounder was selected as follows: radiated frequency —  $1 \text{ MHz}$  (sound wave length  $\lambda = 0.15 \text{ cm}$ ), period of sounding  $t_s = 0.16 \text{ s}$ , radiated pulse duration  $\tau = 50 \text{ mcs}$ . A time window selected by the time-controlled amplifier was  $268 \text{ mcs}$ ,

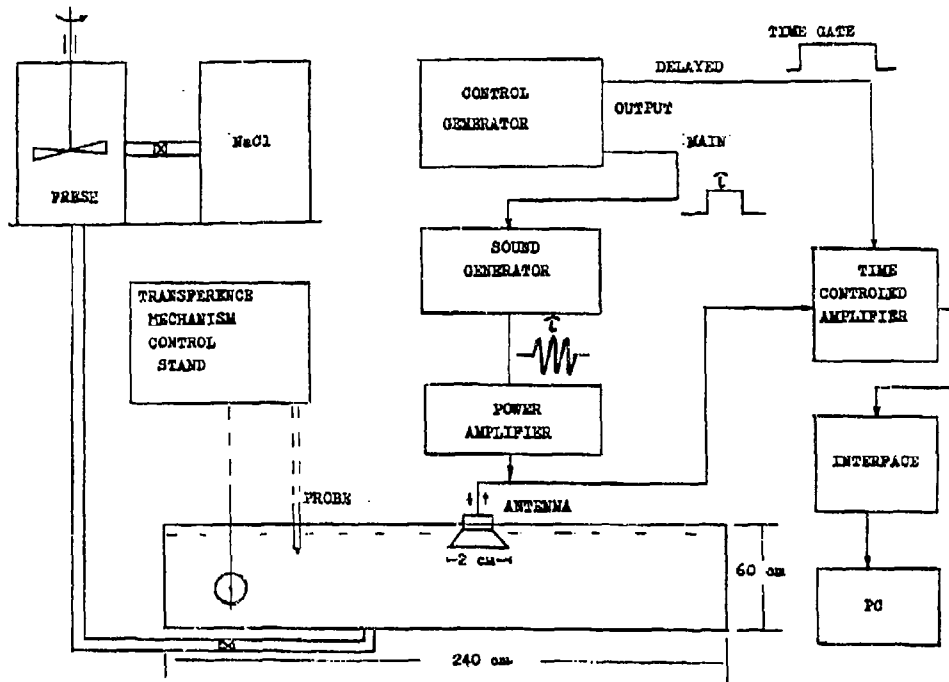


Fig. 1

that corresponds to total sounded depth of 20 cm centered to the axis of the moving cylinder.

To observe the picture of the flow the Shhlieren image device was used with horizontal thread shade which partly overlapped an image of a horizontal light gap. The axis of Shhlieren device was oriented horizontally and parallel to the axis of the moving cylinder, while the axis of the sound beam was oriented vertically. Both axes intersected in the centre of the basin.

The cylinder (diameter  $d = 7.5$  cm) was towed perpendicularly to its axis with a speed  $u = 0.5$  cm/s. The parameters of the flow past the cylinder were  $Re = ud/\nu = 350$ ,  $Fr = uT_b/2d = 0.11$ , where  $\nu = 0.01$  cm<sup>2</sup>/s,  $T_b = 10$  s are kinematic viscosity and buoyancy period.

Before the towage the vertical profile of specific conductivity was measured and used to calculate the profile of buoyancy frequency  $N(z) = 2\pi/T_b(z)$ . Besides, the amplitude of echo  $A_s$  from the bottom was measured and then used as a reference signal to calculate the coefficient of scattering according to

$$n = A_s/A_i = A_s/(A_b/\alpha), \quad (2)$$

where  $A_i, A_s$ —amplitudes of incident sound signals and signals scattered by fine structure of the flow, respectively,  $\alpha = 0.3$ —coefficient of sound reflection by the basin bottom.

To compare scattering features of the flow past the cylinder with the data of field measurements and to estimate similarity of the phenomena a dimensionless cross-section of volume backscattering was calculated

$$\sigma = m_w \lambda, \quad (3)$$

where  $m_v = n^2(cr/2)^{-1}$  is a coefficient of volume backscattering.

Prior to towage the cylinder was positioned closely to the end of the basin. During the towage the shadow picture of the flow was observed and photographed. Right after the cylinder left the sound beam zone (with the diameter of 2.5 cm) the echosounder switched on, and the backscattering profiles separated by period 0.16 s were obtained. During one towage the total number of scattering profiles equals to 800. The cylinder was stopped in the position  $x = 60$  cm from the sound beam axis that corresponds to  $x/d = 8$ . After that the cylinder approached the nearest end of the basin to be towed repeatedly in two hours.

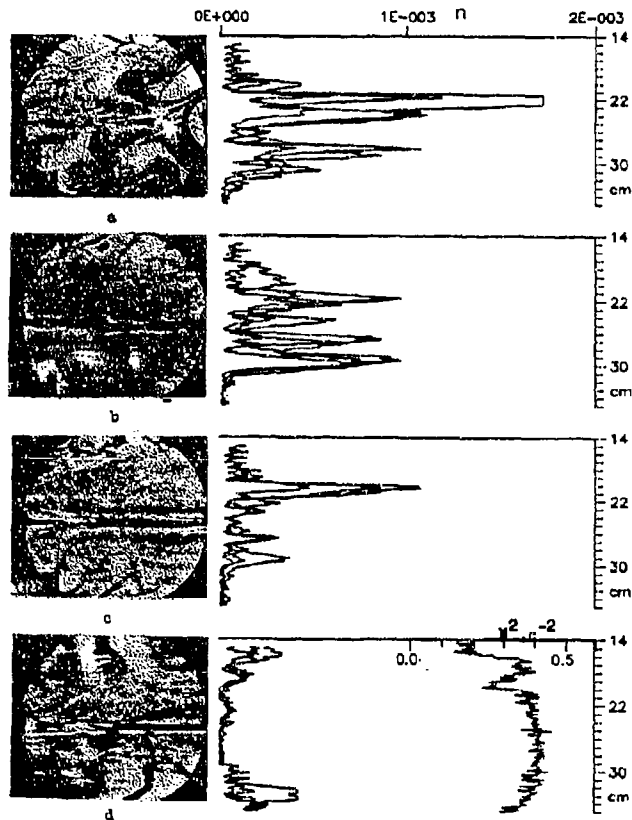


Fig. 2

Fig. 2,a-d show the shadowgraphs obtained for the values of age of the wake, respectively,  $T_b$ ,  $3.5T_b$ ,  $5.6T_b$ ,  $11T_b$ . Each shadowgraph is followed by a series of three vertical profiles (echograms) of the coefficient of backscattering according to (2). The echograms are separated by the time interval 0.32 s. In the right side of Fig. 2,d the profile of square of buoyancy frequency is shown.

At the initial stage the parameters of the flow ( $Re, Fr$ ) correspond to so called regime of chain of suspended rotors [5] which are clearly seen on the 30 cm depth. The rotors are placed in the nodes of the wake and separated from the central highly

gradient core by a wave-shaped layer of unstructured liquid. The dark inclined stripes mark the crests and the troughs of coupled internal waves.

With the age increase the following peculiarities are observed: the large scale vertical fluctuations fall into decay, the flow becomes nearly two-dimensional and the fine horizontally oriented laminations arise on the wake periphery. While the central highly gradient core appeared from the very beginning, the laminations on the boundaries are formed afterwards due to decaying of vertical movements.

At the final stage the gradients on the periphery become extremely high which can be identified by diffusive horizontal stripes outside the optical image region.

In the behavior of the profiles of backscattering the following features can be noted.

At the early age (Fig.2,a) the profiles are weakly correlated, however, they concentrate near the wave-shaped layers mentioned above (horizons of 21 and 28 cm). Likely enough, there is a case of scattering by sharp boundaries which separate these layers from the rest of the disturbed region of the wake.

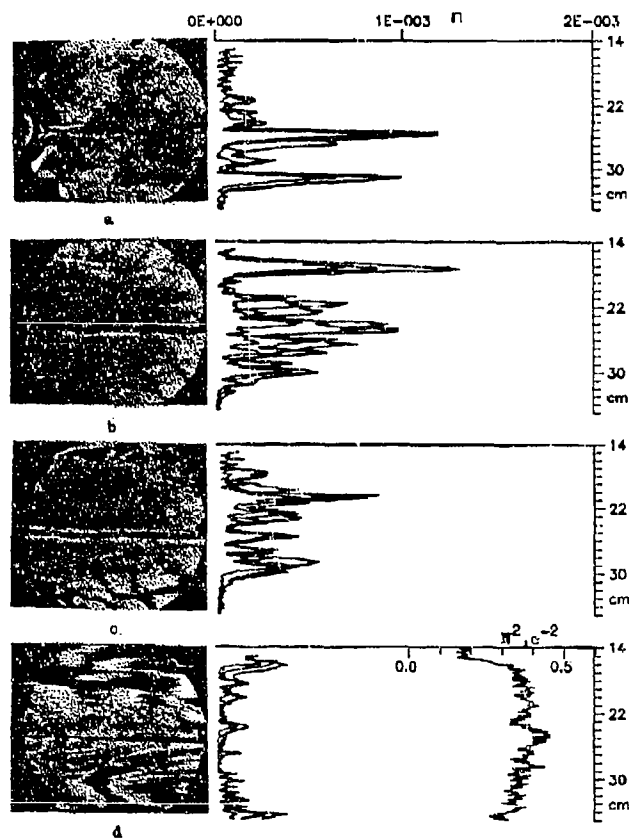


Fig. 3

With the age increase the rotors' chains dilapidate: at  $t = 3.5T$ , they are yet seen on the horizon 32 cm (Fig.2,b), but at  $t = 5.6T$ , they are absent (Fig.2,c). Accordingly, the location of the echograms stabilizes and at  $t = 5.6T$ , the echograms obtained for different time seem to be enclosed into each other.

This phenomenon is enhanced at  $t = 11T_b$  (Fig. 2, d) and followed by re-distribution of maxima of the coefficient of scattering to the wake periphery, where the extremely high gradients are indicated in the shadowgraphs.

The features mentioned above are conserved provided that the conditions of experiment are repeated. It is well seen in Fig. 3, where the results of the experiment with the same speed ( $u = 0.5 \text{ cm/s}$ ) of the towage in the opposite direction are presented.

The buoyancy frequency profile varied slightly but on the whole the regime of the flow ( $Re, Fr$ ) is conserved, and we can see the same peculiarities of backscattering.

A combined analysis of the shadowgraphs and the echograms shows that there are three main stages in the evolution of sound scattering according to the behaviour of the flow.

At the initial stage the scattering signal is induced by the whole vertical size of the wake, at the same time the shadowgraphs indicate intensive vertical movements.

At the intermediate stage the average value of the echosignals diminishes, and vertical movements decay. Then a tendency of displacement of the scattered signal maxima to periphery is observed.

At the final stage scattering from the boundaries dominates the rest region of the wake.

Durations of the stages are clearly seen in Fig. 4 where dependence of  $n$  on the dimensionless age  $t/T_b$  is shown for upper and lower boundaries of the wake. The boundaries are taken on the positions  $+3.5 \text{ cm}$  (upper) and  $-3.5 \text{ cm}$  (lower) from the axis of the cylinder.

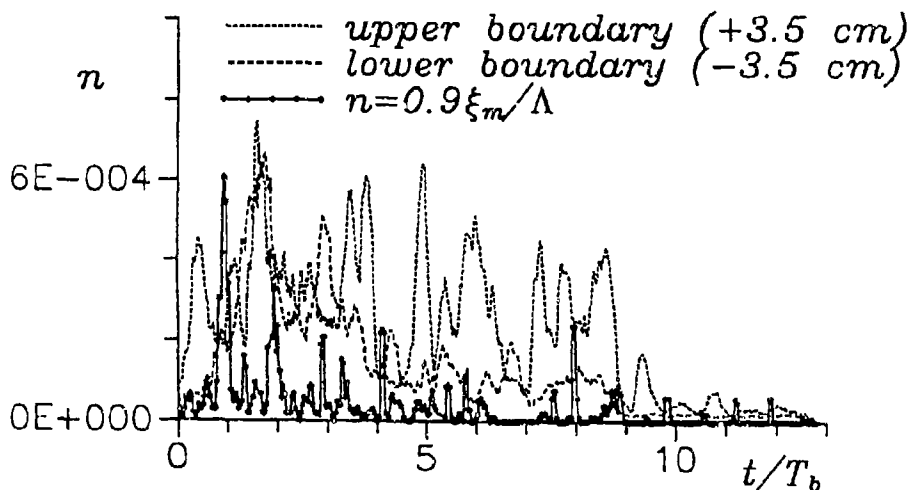


Fig. 4

The initial stage lasts from 0 to 2, the intermediate one - from 2 to 8. Between 3 and 8 the oscillations with periods of  $T_b$  and  $T_b/2$  are observed. They are induced by the scattering structure oscillating with the internal waves. Independent of the sign of the liquid particles displacement the scattered power is always positive, therefore we register the oscillations of both  $T_b$  and  $T_b/2$  periods.

Information about vertical displacement and module of vertical velocity  $|w|$  can be obtained from acoustic data using a relationship  $|w| = \xi_m/t_s$ , where  $\xi_m$  is a solution of empirical equation  $R(\xi_m, t) = \max\{R(\xi, t)\}$ , and  $R(\xi)$  is space correlation coefficient of two scattering profiles separated by time interval  $t_s$  (in this case  $t_s = 0.16 \text{ s}$ ).

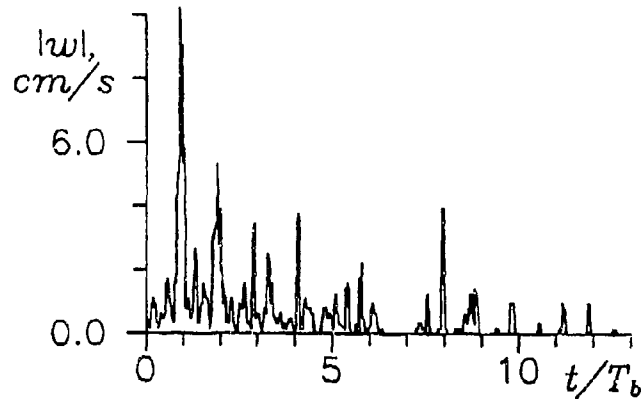


Fig. 5

In Fig.5 values  $|w|$  vs.  $t/T_b$  are shown which relate to the experimental data in Fig.1. To calculate  $|w|$  those  $\xi_m$  are taken valuable which correspond to  $R(\xi_m) > 0.7$ . A part of them is significant in the time interval  $0 < t/T_b < 6$ , therefore the dependence in Fig.5 seems to be continuous in that interval. However, in the range  $t/T_b < 7$  it is represented by sparse pulsations which indicates a sharp attenuation of the vertical movement.

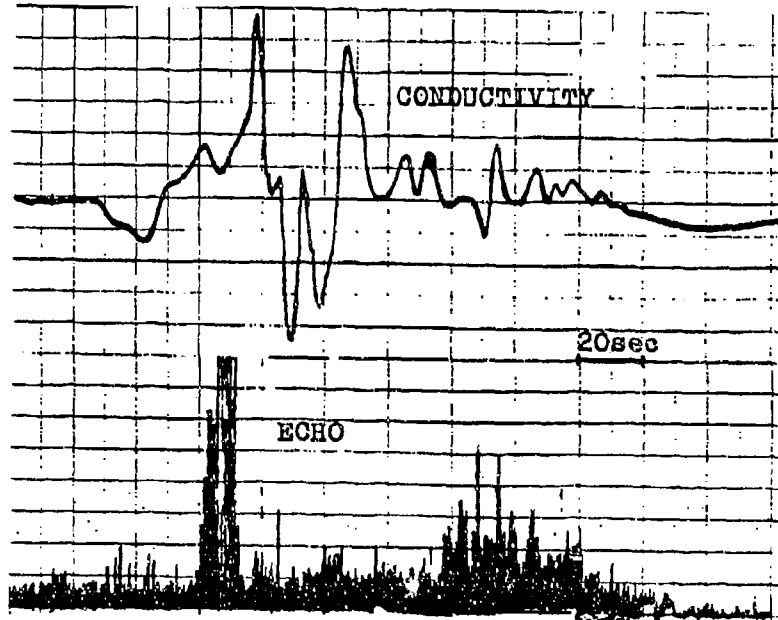


Fig. 6

Assuming the scattered signals to be formed by the surfaces of discontinuity moving at a vertical distance  $\xi_m$ , we can estimate the coefficient of backscattering  $n_a$  as [6]

$$n_a = \frac{(1 + \beta_c/\beta_p) N_a^2}{2g} \xi_m, \quad (4)$$

where  $N_a$  is a mean value of buoyancy frequency,  $\beta_c = c^{-1} \partial c / \partial S = 0.7 (\text{°}/\text{‰})^{-1}$ ,  $\beta_\rho = \rho^{-1} \partial \rho / \partial S = 0.8 (\text{°}/\text{‰})^{-1}$ ,  $S$ -salinity,  $\rho$ -density.

Substitution of these values in (4) gives  $n_a = 0.92 \xi_m / \Lambda$ , where  $\Lambda = g / N_a^2$ . The values of  $n_a$  calculated for  $N_a = N = 2\pi / T_b$  are essentially less than empirical values of  $n$  on the wake boundaries (Fig.4). It says that the surfaces of discontinuity play a second-rate role in the backscattering at the early stages of the wake.

In this connection the role of the volume scatterers of  $c'/c$  kind is more valuable. In Fig.6 the records of the conductivity probe and echosounder output are shown [6]. We see that pulsations of conductivity connected with microscale volume fluctuations correspond to more intensive sound scattering than high-amplitude large-scale conductivity fluctuations connected mainly with the motion of surfaces of discontinuity.

A monotonous variation of the flow regime leads to alternation both of microscale and large-scale structure [6].

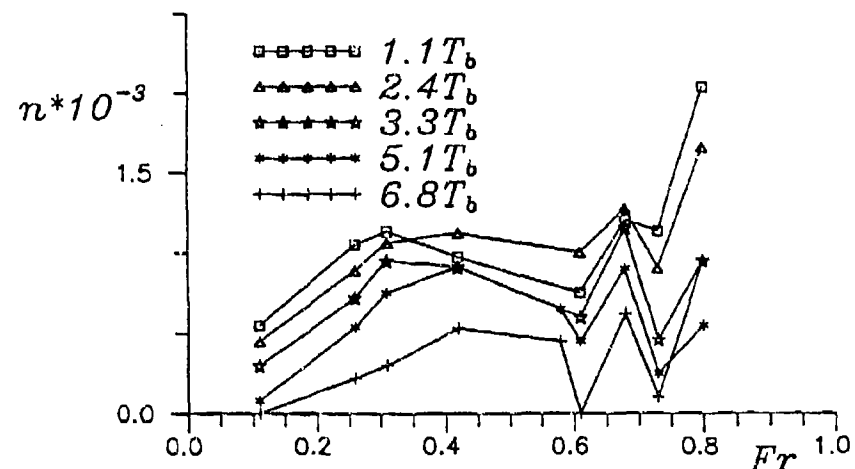


Fig. 7

Respectively, the parts of the volume and the surface scatterers vary as well as the intensity of scattering which is shown in Fig.7 for the different ages  $t/T_b$ . These data were obtained for the same cylinder and stratification but the different values of towage speed. A behaviour of scattering testifies an intermittency of large-scale and microscale structures on  $0 \div 1$  Froude number range. This fact is confirmed by shadowgraphs presented in [4,6]. It should be noted, that the mean value of dimensionless cross-section of backscattering (3) obtained in our experiments approximately equals those registered in the field measurements. It points to the fact, that the liquid inhomogeneities produce intensive scattered signals as well as the discrete particles (phyto-and zoo plankton) which are often considered to be the principal scatterers in the ocean.

#### REFERENCES

- [1] Goodman L. Acoustic scattering from ocean microstructure./J.Geoph.Res., 1990, 95, N C7, pp.11557-11573.
- [2] Brandt A. Acoustic return from density fluctuations in turbulent jets./IEEE Conf.Eng.Ocean Environ., San Diego, 1975, pp.8-13.
- [3] Prokhorov V.E. Remote measurements of dynamic inhomogeneities' parameters in stratified liquid./Izvestiya AS USSR, Atmospheric and Ocean Physics (USSR), 1989, 24, N 1, pp.90-94.

- [4] Prokhorov V.E., Chashechkin Y.D., Voeikov I.V. An observation of flow past a cylinder by optical and acoustic technique./Zhurnal Prikladnoi Mekhaniki i Tekhnicheskoi Fiziki (Russia), 1993, 34, N 3, pp.68-74.
- [5] Boyer D.I., Davies P.A., Fernando H., Zahng X. Linearly stratified flow past a horizontal circular cylinder./Phil.Trans.R.Soc. London, A.,1989,328, p.501.
- [6] Prokhorov V.E., Chashechkin Y.D. An ultrasonic sounding in fluid mechanics experiment./Preprint, Institute for Problem in Mechanics RAS, 1992, N 514, Moscow.

# MIXING AND BLOCKING EFFECTS IN TWO-LAYER FLOW OVER AN OBSTACLE

V.Yu.Liapidevskii

Lavrentyev Institute of Hydrodynamics  
Novosibirsk, 630090, RUSSIA  
E-mail: lde@hydro.nsk.su  
Fax: 383-2-35-40-50

A mathematical model of two-layer flow of mixible fluid is developed. An intermediate layer where turbulent mixing and generation of short waves takes place is included in the model as the third one. The governing equations consist of conservation laws and hence internal hydraulic jumps are uniquely determined. A new type of solutions describing an upstream steady-state blocked zone of finite length generated by a body towed in two-layer fluid at rest is obtained.

## Introduction.

Upstream disturbances of two-layer supercritical flow over a topography are nonlinear in character. For two-dimensional flows of immiscible fluids they were investigated experimentally and theoretically by Long (1954), Baines (1984), Armi (1986), Lawrence (1993). It was found that blocking effects in stratified flows over an obstacle may result in the increase of the shear between homogeneous layers and a substantial mixing may occur. Mixing is responsible for such phenomena as a formation of stationary upstream disturbance in supercritical flow over an obstacle and downstream control of amount of entrained fluid in mixing layers and buoyant jets (Wilkinson and Wood, 1971).

## Mathematical models.

A mathematical model taking into account mixing and generation of short waves at the interface is developed in (Liapidevskii, 1991). The basic idea of this work is to use the total conservation laws of mass, momentum and energy for determining such quantities as mean density, mean velocity and turbulence energy in the intermediate layer between homogeneous ones. A similar approach was used in (Liapidevskii, 1987) to simulate two-phase flows. The basic model and some more simple submodels are presented in this section.

*The basic model.* The equations of two-layer flow with an intermediate layer where entrainment of fluid from the homogeneous layers takes place, may be written in the form (Liapidevskii, 1991)

$$\begin{aligned} (h + 0.5\eta)_t + (hu + 0.5\eta v)_x &= 0, \\ u_t + (0.5u^2 + bh + \bar{b}\eta + p^*/\rho_0)_x &= 0, \\ w_t + (0.5w^2 + p^*/\rho_0)_x &= 0, \\ (bh + \bar{b}\eta)_t + (bhu + \bar{b}\eta v)_x &= 0, \end{aligned} \tag{1}$$

---

<sup>a</sup>The work was supported by Russian Foundation of Fundamental Research under grant No. 94-01-01210-a

$$\begin{aligned}
& ((H - h - \eta)w + \eta v + hu)_t + ((H - h - \eta)w^2 + \eta v^2 + \\
& + hu^2 + H p^*/\rho_0 + 0.5\bar{b}\eta^2 + \bar{b}\eta h + 0.5bh^2)_x = 0, \\
& ((H - h - \eta)w^2 + \eta(v^2 + e) + hu^2 + \bar{b}\eta^2 + 2\bar{b}\eta h + bh^2)_t + \\
& ((H - h - \eta)w^3 + \eta v(v^2 + e) + hv^3 + 2p^*Q/\rho_0 + 2\bar{b}\eta hu + \\
& + 2\bar{b}(h + \eta)\eta v + 2bh^2u)_x = 0. \\
& \eta_t + (\eta v)_x = 2\sigma q, \\
& (\eta q)_t + (\eta qv)_x = \sigma(0.5u^2 + 0.5w^2 + v^2 + e - v(u + w) - 0.5b\eta). \tag{2}
\end{aligned}$$

Here  $H$  is the channel depth,  $h$ ,  $\eta$  are the depths of the lower layer and the intermediate one, respectively,  $u$ ,  $v$ ,  $w$  are the mean horizontal velocities in the layers,  $b = (\rho^- - \rho_0)g/\rho_0 > 0$  is the given buoyancy of the lower layer,  $\bar{b} = (\bar{\rho} - \rho_0)g/\rho_0$  is the buoyancy in the intermediate layer,  $\rho^-$ ,  $\rho_0$  are the densities of the lower and upper layers,  $\bar{\rho}$  is the mean density of the intermediate layer,  $p^*$  is the pressure under the channel lid,  $Q = hu + \eta v + (H - \eta - h)w = Q(t)$  is the total flow rate,  $e$  is the specific kinetic energy of a small-scale motion,  $q$  is the velocity of "large eddies" in the intermediate layer. The only empirical coefficient  $\sigma \approx 0.15$  is determined by the analysis of mixing in shear flows of homogeneous and stratified fluids (Ovsyannikov et al. 1985). It is responsible for scaling horizontal and vertical motions and may be eliminated from the system by replacing independent variables.

The system (1)-(2) consists of the well-known shallow water equations for homogeneous layers and of the total conservation laws of mass, momentum and energy. The last equation in (2) is a differential consequence of the rest equations of (1),(2) when  $e \equiv q^2$ . For  $q^2 < e$  this equation is necessary to determine an entrainment rate of fluid from homogeneous layers. When a scale of flow is large enough comparing with length of waves generated in the intermediate layer, an equilibrium state ( $q \equiv 0$ ,  $e > 0$ ) may be achieved. If the entrainment may be neglected ( $\sigma = 0$ ) the equations (1),(2) are splitted into conventional three-layer shallow water equations and equations for  $e$ ,  $q$ . Therefore, the system (1)-(2) is hyperbolic when the shear is small enough. If the velocity difference between layers increases, the intermediate layer thickness grows and the entrainment process prevents the development of the long-wave instability in two-layer flow.

*Internal jump conditions.* The system (1)-(2) describes continuous as well as discontinuous solutions because it consists of the conservation laws. The jump conditions are uniquely determined by the system. Therefore, the well-known contradiction between the total momentum and energy in the two-layer shallow water theory may be overcome in the three-layer system since the energy  $e$  of small-scale motions in the intermediate layer is included into consideration. When the entrainment may be neglected ( $\sigma = 0$ ), the energy equation is not necessary to find continuous solutions of (1),(2). However, it gives an additional admissibility condition  $e \geq 0$  for internal jumps. When  $\eta \rightarrow 0$ , we have two-layer flow and the conservation laws are incompatible for flows with internal jumps. Nevertheless, it will be shown in the next section that there are travelling waves propagating through two-layer fluid at rest ( $w = 0$ ,  $p^* \equiv 0$ ,  $\eta_0 = 0$ ,  $h_0 \ll H$ ) with the

supercritical velocity  $D > \sqrt{bh_0}$  and containing no singularities. This new class of solutions of the system (1)-(2) will be applied to describe blocking effects in two-layer flow over an obstacle.

*Equilibrium model.* Equilibrium models may be used when a scale of the flow is much more than a length of waves generated in the intermediate layer. In this case the equations (2) should be replaced by

$$q = 0, \quad e = v(u + w) + 0.5b\eta - 0.5(u^2 + w^2) - v^2 \geq 0. \quad (3)$$

Equations (1),(3) describe equilibrium two-layer flows with a turbulent intermediate layer. Notice that in (1),(3) the total momentum and energy equations are included and the intermediate layer thickness  $\eta$  is derived from (3) and the energy equation. Jump conditions are uniquely determined by homogeneous conservation laws (1).

*Turbulent submerged jet.* The basic model (1)-(2) is rather complicated. It takes the more simple form when the intermediate layer reaches the bottom and the thicker upper layer is at rest ( $h \equiv 0$ ,  $\eta \ll H$ ,  $w \equiv 0$ ,  $p^* \equiv 0$ )

$$\begin{aligned} (\bar{b}\eta)_t + (\bar{b}\eta v)_x &= 0, \\ (\eta v)_t + (\eta v^2 + 0.5\bar{b}\eta^2)_x &= 0, \\ (\eta v)_t + (\eta v(v^2 + e + 2\bar{b}\eta))_x &= 0, \end{aligned} \quad (4)$$

$$\begin{aligned} \eta_t + (\eta v)_x &= \sigma q, \\ (\eta q)_t + (\eta q v)_x &= 0.5\sigma(v^2 + e - \bar{b}\eta). \end{aligned} \quad (5)$$

Equations (4),(5) are a version of the shallow water equations taking into account the entrainment from the upper layer. Main peculiarities of the basic model may be better understood by this model. Characteristics of (4),(5) are represented by

$$dx/dt = v \pm \sqrt{\bar{b}\eta}, \quad dx/dt = v.$$

The equilibrium conditions for the system take a form

$$q = 0, \quad v^2 + e = \bar{b}\eta \quad (6)$$

They can be fulfilled in subcritical flows only ( $v^2 < \bar{b}\eta$ ) since  $e \geq 0$  everywhere. For the equilibrium model (4),(6) characteristics are defined from

$$dx/dt = 1.5v \pm \sqrt{0.75(\bar{b}\eta - v^2)}, \quad dx/dt = v.$$

Hence, the equilibrium system is hyperbolic for subcritical flows where (6) can be satisfied. For supercritical flows the nonequilibrium model (4)-(5) is more adequate. In such flows the high entrainment rate caused by the right-hand part of (5) leads to fast towing of a turbulent layer thickness until a subcritical condition is reached. The system (4)-(5) has a variety of solutions. Among them there are continuous soliton-like structures and internal jumps followed by periodical waves. Travelling waves of (4),(5) propagating

through an equilibrium state ( $u_0 = 0, e_0 = \bar{b}_0 \eta_0$ ) are investigated in (Liapidevskii, 1989). It is shown that there is a "soliton" for  $\sqrt{0.75\bar{b}_0\eta_0} \leq D \leq \sqrt{\bar{b}_0\eta_0}$ , i.e. when the velocity  $D$  of a travelling wave lies between "equilibrium" and "frozen" speeds of disturbances, and a "jump-wave" configuration is realized for  $D > \sqrt{\bar{b}_0\eta_0}$ . Notice that for  $D = \sqrt{3\bar{b}_0\eta_0}$  there is a "smooth bore" connecting equilibrium states. In this case there are no waves generated downstream the bore.

#### Two-layer flow over an obstacle.

In this section we consider some applications of the mathematical models for describing mixing and blocking effects in two-layer flow of mixible fluids over a topography. The simplest case of the flow governed by single-layer shallow water equations may be realized when the two-dimensional body of maximal height  $h_m$  is towed along the bottom with the constant speed  $D$  in the thinner lower layer ( $h_0 \ll H, \eta_0 = 0$ ) of the two-layer fluid at rest (figure 1). The flow may be defined in terms of two dimensionless parameters

$$\delta = h_m/h_0, \quad \text{Fr} = D/\sqrt{bh_0}$$

A flow-regime diagram in the  $(\text{Fr}, \delta)$  - plane for mixible fluids differs considerably from that for immiscible fluids because mixing between layers results in a stationary blocked zone of the finite length upstream of the towed obstacle. A structure of such flows may be described by solutions of (1),(2).

*Steady-state solutions of (1),(2).* If a flow is steady in a frame of reference moving with the towed body the following relationships for continuous solutions of (1),(2) are satisfied ( $w \equiv 0, p^* \equiv 0, \eta_0 = 0$ )

$$\begin{aligned} \bar{b} &= 0.5b, \quad e \equiv q^2, \\ hu + 0.5\eta v - D(h + 0.5\eta) &= -Dh_0, \\ 0.5u^2 + 0.5b\eta + bh - Du &= bh_0 = J^-, \\ hu^2 + \eta v^2 - D(hu + \eta v) + 0.5b(h^2 + h\eta + 0.5\eta^2) &= 0.5bh_0^2, \\ \eta(v - D)(v^2 + q^2) + h(u - D)u^2 + b\eta hu + b(h + \eta)\eta v + \\ &+ 2bh^2u - bD(0.5\eta^2 + h\eta + h^2) = -bDh_0^2. \end{aligned} \tag{7}$$

All dependent variables may be expressed from (7) as functions of one variable, say,  $u$ . The relationship  $Q = \eta(D - v) = Q(u)$  is shown in figure 2 for  $\text{Fr} = 2$ . Along the curve  $A$  the energy  $e = e(u) < 0$  and this branch is not considered here. Along  $B$  we have  $\eta \rightarrow 0, h \rightarrow h_0, Q \rightarrow 0$  when  $u \rightarrow 0$ . The existence of limits  $v(u) \rightarrow D, e(u) \rightarrow D^2$  when  $u \rightarrow 0$  may be shown by differentiation of (7). The part of the curve  $B$  where  $e(u) > 0$  is shown in figure 2 by solid line. A dependence of variable  $\xi = x - Dt$  may be found from (7) and the following equation

$$dQ(u)/d\xi = 2\sigma q(u). \tag{8}$$

Solutions of (7),(8) are shown in figure 1 for  $\text{Fr} = 2$  (dotted line). Solutions of corresponding unsteady problem (1)-(2) are shown in figure 1 by solid line. The steady

upstream flow is determined by the parameters  $Fr$  and  $\delta$  since the flow is critical at crest (state "c") and supercritical downstream the body. Therefore, if the towed body is short enough comparing with the upstream blocked zone the entrainment over the body can be ignored and the relationships between the states "1" and "c" just upstream and at the crest, respectively, have a form

$$\left( \frac{(u_c - D)^2}{bh_c} - 1 \right) \left( \frac{(v_c - D)^2}{0.5b\eta_c} - 1 \right) - 0.5 = 0. \quad (9)$$

$$\begin{aligned} \eta_c(D - v_c) &= \eta_1(D - v_1) = Q_1 \\ h_c(D - u_c) &= h_1(D - u_1) = Dh_0 - 0.5Q_1 \\ 0.5u_c^2 - Du_c + b(0.5\eta_c + h_c + \delta) &= J^- \\ 0.5v_c^2 - Dv_c + 0.5b(\eta_c + h_c + \delta) &= \\ &= 0.5v_1^2 - Dv_1 + 0.5b(\eta_1 + h_1) = J_1^+ \\ q_c^2 &= q_1^2. \end{aligned} \quad (10)$$

The equation (9) is the regularity condition of the two-layer flow at the crest. A function  $\delta = \delta(Q_1)$  may be found from (9),(10) for every state "1" corresponding to the curve  $B$  for  $0 < Q_1 < Q_0$ . For  $Fr > Fr_*$  ( $Fr_* \approx 2.1$ ) the intermediate layer reaches the bottom ( $h_1 = 0$ ,  $Q_1 = 2h_0D$ ,  $\delta_1 = \delta(Q_1)$ ) and for  $\delta > \delta_1$  the flow is governed by (4),(5). The structure of travelling waves was investigated in this case in (Liapidevskii, 1989). It may be shown that for  $Fr > Fr^*$  ( $Fr^* \approx 2.6$ ) there is a steady upstream flow with the transition from a mixing layer to a submerged jet for all  $\delta > \delta_1$  in contrast to the flow-regime diagram for immiscible fluids (Baines, 1984).

*Mixing layer and submerged jet.* Further examples of simple turbulent shear flows, namely mixing layer and submerged jet, may be obtained by discharging a dense fluid along of the horizontal bottom in a quiescent light fluid ambient in a two-dimensional channel (figure 3). Such flows have been investigated theoretically and experimentally in a number of works, for example by Wilkinson and Wood (1971) and Chu and Baddour (1984). The system (7)-(8) may be used to describe a stationary mixing layer for  $D = 0$ ,  $\eta_0 = 0$ ,  $Fr = u_0/\sqrt{bh_0} > 1$ . The dependence  $Q = Q(u)$  from (7) is similar to that shown in figure 2. It is depicted in figure 4 for  $Fr < 5$  (the curve  $\Gamma_1$ ) and for  $Fr > 5$  (the curve  $\Gamma_2$ ). There are two branches  $A$  and  $B$  corresponding to subcritical and supercritical flows, respectively. If  $Fr > 5$  the mixing layer reaches the bottom and a submerged jet governed by the system (4),(5) is realized.

The distinctive feature of the mixing layer from the travelling wave considered above is that  $e > 0$  along the curves  $A$  and  $B$ . Hence a transition from the supercritical to subcritical flow by an internal hydraulic jump is possible. If the downstream control is absent ( $\delta = 0$ ) the critical flow with the maximal entrainment  $Q_{\max}$  is developed. When increasing the dimensionless height of the obstacle the transition "1" - "2" by a hydraulic jump occurs and the total entrainment in supercritical flow decreases. Notice that no additional hypothesis should be used to describe the maximal entrainment regime by (7),(8). Comparisons with experimental data presented in Chu and Baddour (1984) for

mixing layers and buoyant jets show that the system (1),(2) describes well the averaged flow dynamics.

#### Conclusions.

The three-layer flow model presented here is preferable to the two-layer one since mass,momentum and energy are conserved in the flow and the governing equations consist of conservation laws. Therefore, the well-known contradiction in the shallow water theory of two-layer flows may be overcome and internal hydraulic jumps are uniquely determined. It is shown that the mathematical model containing no essential empirical constants represents the main peculiarities of entrainment and downstream control in mixing layers and buoyant jets. In particular, the model explains an appreciable difference in the entrainment rate for subcritical and supercritical flows.

This model is used also for describing the mixing and blocking effects upstream an obstacle towed with a constant speed along the bottom in the two-layer mixible fluid at rest. It is shown that in contrast to the two-layer flow of immiscible fluid there is a steady-state zone of finite length just upstream the obstacle where the flow is blocked and mixing occurs. It is interesting to note that the transition from a supercritical external flow to a subcritical one is continuous and a mixing starts at the upstream boundary of the blocked flow with a finite entrainment rate. If the towed body is high enough a mixing layer may reach the bottom and a new type of flow would be established. The steady solution of (1),(2) considered above may be used as a good test in time-dependent calculations since the perturbated upstream subcritical flow has the finite length.

#### References

Armi,L. 1986 The hydraulics of two flowing layers with different densities. *J. Fluid Mech.* 163, 27-58.

Baines,P.G. 1984 A unified description of two-layer flow over topography, *J. Fluid Math.* 146, 127-167.

Chu,V.H. & Baddour,R.E. 1984 Turbulent gravity-stratified shear flows. *J. Fluid Mech.* 138, 353-378.

Lawrence,G.A. 1993 The hydraulics of steady two-layer flow over a fixed obstacle. *J. Fluid Mech.* 254, 605-634.

Liapidevskii, V.Yu. 1987 Hyperbolic two-phase flow models based on conservation laws. In *Problems of nonlinear acoustics*, Novosibirsk (ed.Kedrinskii,V.K.), 66-70.

Liapidevskii,V.Yu. 1989 The dynamics of a uniform turbulent layer in a stratified fluid. *Zhurnal Prikladnoi Mechaniki i Tekhnicheskoi Fisiki*, No.2, 235-238 (in Russian).

Liapidevskii,V.Yu. 1991 Two-layer shallow water equations with small-scale motions at the interfaces. In *Laboratornoe modelirovaniye dinamicheskikh processov v okeane*, Novosibirsk, (ed.Borisov,A.A.), 87-97 (in Russian).

Long,R.R. 1954 Some aspects of the flow of stratified fluids,II. Experiments with a two-fluid system. *Tellus* 6, 97-115.

Ovsyannikov,L.V.,Makarenko,N.I. et al. 1985 Nonlinear problems in a theory of surface and internal waves. *Nauka* (chap.4) (in Russian).

Wilkinson,D.L. & Wood,I.R. 1971 A rapidly varied flow phenomenon in a two-layer system. *J. Fluid Mech.* 47, 241-256.

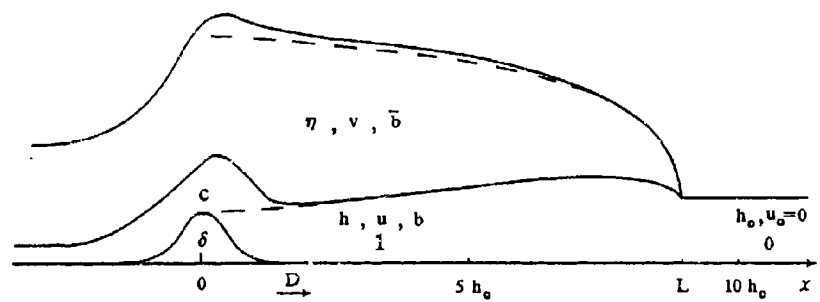


Fig.1

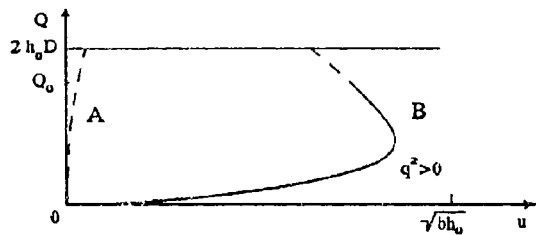


Fig.2

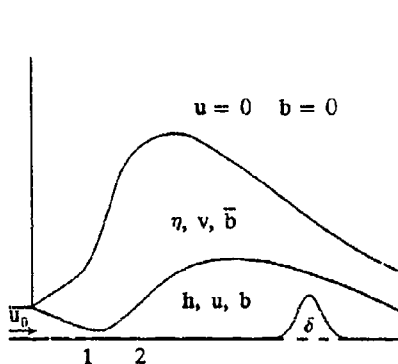


Fig.3

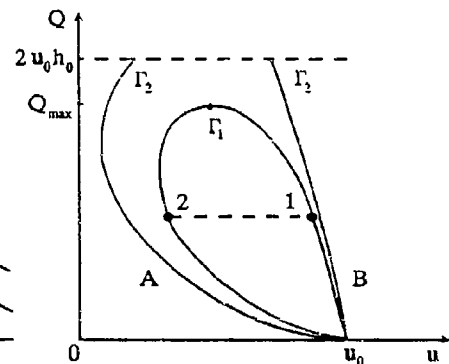


Fig.4

# Numerical Modelling of Heat Convection in a Stratified Laboratory Basin

S.A. Baranov, V.A. Brailovskaya, V.R. Kogan

Institute of Applied Physics Russian Academy of Science  
(IAP RAS)

## 1. Introduction

Mathematical simulation of the heat-mass transfer in the laboratory basin of IAP RAS designed for studying the dynamics of internal waves is based on the numerical solution of Navier-Stokes and energy equations. Unlike the two-dimensional models of small and intermediate basins considered before [1-3], the numerical simulation of stratification in the large basin is performed in three-dimensional formulation permitting to take into account volume fluid flow. This seems to be important for both to ascertain the possibility of creating and maintaining stable temperature stratification, which models the vertical density stratification in the upper ocean layer, and to study dynamics of internal waves appearing in the basin due to temperature and hydrodynamics fluctuations.

The first three-dimensional numerical investigations regarding natural convection were devoted to cavity flow [4,5]. In these studies the Navier-Stokes equations are expressed in terms of the vector potential and vorticity  $(\vec{\psi}, \vec{\omega})$ . This formulation has the advantage that the continuity equation is automatically satisfied and the pressure terms are eliminated. As an alternatives the formulation in terms of primitives variables-velocity and pressure  $(\vec{V}, P)$ , and the formulation in terms of velocity and vorticity  $(\vec{V}, \vec{\omega})$  [6] are used.

In the present paper to study hydrodynamics and heat exchange at the natural convection in the laboratory basin the flow field is calculated numerically using the variables  $(\vec{\psi}, \vec{\omega})$ .

## 2. Formulation of Problem

The model of the basin (Fig. 1) is a parallelepiped with the volume  $(d^*H^*)$ . Stratification in the basin is a result of the inhomogeneous temperature regime on the side walls (planes ABCO and  $A'B'C'D'$ ): the temperature at the height from  $H_0$  up to  $H_1$  is  $T_0$ , at the height from  $H_1$  up to surface is  $T_1$ . The rest part of the side walls lower  $H_0$ , face walls (the plane  $AB'B'A'$  and  $B'C'C'B$ ), and the bottom are heat isolated. On the surface heat exchange with surrounding takes place according to the formula  $q = \alpha(T_s - T_{\text{sur}})$ , where  $q$  is the density of the heat flow,  $T_{\text{sur}}$  is the temperature of the surrounding,  $T_s$  is the temperature of the surface,  $\alpha$ -heat exchange coefficient. Convection arises due to the violation of hydrostatic liquid equilibrium caused by the inhomogeneity of the temperature distribution in the field of mass forces.

In the dimensionless variables  $\vec{\omega}, \vec{\psi}, T$  (vortex, vector potential, temperature) the system of nonstationary Navier-Stokes and energy equations is written as

$$\begin{aligned}\frac{\partial \omega_x}{\partial t} &= -\nabla(\vec{V}\omega_x) + \nabla^2 \omega_x + \vec{\omega} \nabla U + Gr \cdot T_y \\ \frac{\partial \omega_y}{\partial t} &= -\nabla(\vec{V}\omega_y) + \nabla^2 \omega_y + \vec{\omega} \nabla V - Gr \cdot T_x \\ \frac{\partial \omega_z}{\partial t} &= -\nabla(\vec{V}\omega_z) + \nabla^2 \omega_z + \vec{\omega} \nabla W\end{aligned}\quad (1)$$

$$\frac{\partial T}{\partial t} = -\nabla(\vec{V}T) + \frac{1}{Pr} \nabla^2 T \quad (2)$$

$$\vec{\omega} = -\nabla^2 \vec{\psi} \quad (3)$$

where  $\vec{V}(U, V, W)$  is the velocity vector which define by the vector potential  $\vec{\psi}$  as  $\vec{V} = \Delta \vec{\psi}$ , i.e.  $U = \partial \psi_x / \partial y - \partial \psi_y / \partial z$ ,  $V = \partial \psi_x / \partial z - \partial \psi_z / \partial x$ ,  $W = \partial \psi_y / \partial x - \partial \psi_x / \partial y$ . On the solid walls and the bottom the condition of impermeability and sticking is fulfilled ( $\vec{\psi} = 0$ ,  $\partial \vec{\psi} / \partial n = 0$ ,  $n$  - is a normal to the boundary). The transition to dimensionless variables is made by means of following scales : the height of the side walls  $H$  is the characteristic length,  $H^2 / \nu$  is a time scale,  $\Delta T = (T_1 - T_0)$  is a temperature scale. The main similarity criteria are the Grashof number and the Prandtl number ( $Gr = g \beta H^3 \Delta T / \nu^2$ ,  $Pr = \nu / k$ , where  $\nu$ ,  $k$  and  $\beta$  are the kinematic viscosity, conductivity and thermal expansion coefficient respectively).

### 3. Method of Solution.

To solve the system of Navier-Stokes and energy equations numerically, the finite-difference method is used. For the transport equations of vorticity and energy the monotonous approximation of the convective terms of the second order accuracy with compensation of scheme viscosity by Samarsky method [7] is adopted. All these equations in time-dependent formulation are solved by applying an alternating direction implicit method. The assumption that the flows are solenoidal at  $\vec{\psi}$  makes it necessary to solve three three-dimensional Poisson equations for each time layer. The direct method with applying of Fast Fourier Transform is used providing a high accuracy of the solution the Poisson equations.

To solve eq.(1) numerically the boundary conditions for the vorticity are calculated by the method given in [8] for a two-dimensional case. Thus, the succession of the calculations at the every time step is as follows:

- Using the difference analog of the eq.(3) we calculate  $\vec{\omega}^{n+1}$  - the vorticity at  $(n+1)$ -th time layer at the boundary  $\gamma$  of the region of calculating  $\vec{\omega}$ , which is distant from the boundary of the main region by one spacing.
- Solving the system of equations (1) we find  $\vec{\omega}^{n+1}$  via  $\vec{\omega}^n$  inside the region, bounded by  $\gamma$ .
- We calculate  $\vec{\psi}^{n+1}$  from the eq.(3).
- Using the boundary condition  $\partial \vec{\psi} / \partial n = 0$ , we calculate the vector potential  $\vec{\psi}^{n+1}$  in the near-boundary node more exact taking into account the second condition  $\vec{\psi} = 0$  at the boundary.
- We calculate a new velocity vector  $\vec{V}^{n+1}$  using the definition  $\vec{V} = \Delta \vec{\psi}$ .
- Solving eq.(2) we find the temperature field in the all volume region.

The final temperature and fluid flow distribution are found in the process of stationary state establishing.

### 4. Results of Calculation

The numerical calculations were made in the half of the region with assumption about a symmetry relatively to the vertical symmetry plane  $SS'S''S'''$  of the basin (see Fig.1).

We use a grid which is inhomogeneous in  $y$ , with a considerable thickening of nodes in the boundary layer near the vertical side walls and homogeneous in the two other directions. These requirements should be met in order one may use FFT method for solving Poisson equation. The maximum number of the nodes to be computed by PC 486 equals  $33*60*33$  for the half of the volume, time spacing equals  $\tau = 10^{-6}$ . The particular calculation was performed for the model of the basin given in Fig.1:  $H_0 = 0.6m$ ,  $H_1 = 0.7m$ ,  $H = 2m$ ,  $d = 4m$ ,  $l = 20m$ ,  $T_0 = 6^0 C$ ,  $T_1 = 24^0 C$ ,  $T_{initial} = 20^0 C$ ,  $Gr = 1.4 * 10^{11}$ ,  $Pr = 7$ .

To make the computer time minimum the following way of transition to the stationary regime was used. Assuming that the temperature is practically homogeneous along the basin length and varies only near the side walls, the fields of temperature and flow were calculated at the first stage in a half of plane EFGR on the base of two-dimensional model, described in [1-3]. After the onset of the stationary regime of convection (see Fig.2) the fields of velocity and temperature were scattered along the basin length on all nodes of the three-dimensional grid. Then the calculation of the three-dimensional model (1-3) was performed till the stationary state established.

Fig.2 a,b shows the isolines of  $x$ -projection of the vector potential  $\vec{\psi}$  and isolines of the temperature on the plane E'F'F'E' (see Fig.1).

The analysis of these figures shows that the convective process at the rectangular basin induced by temperature profiling of the side walls leads to the formation of characteristic four-vortex structure of the global water circulation in the basin with various direction higher and lower the temperature jump. This structure maintains the stable vertical temperature stratification in the volume with a characteristic thermocline at the depth of the assigned temperature jump. Stratification in this case is practically homogeneous along the basin length except the boundary layers along the walls.

The calculated temperature profile in the middle vertical cross-section (Fig.2c) practically coincides rather well with the one measured in the experimental basin of IAP (designed by crosses on the plot), especially in the temperature jump region.

The conducted numerical simulation revealed the region of uniform thermal and hydrodynamics fields needed for investigation of internal waves in the basin. This region occupies almost the entire space along the basin length except for about two-meter parts off the end walls.

#### References

1. S.D. Bogatyrev, V.A. Brailovskaya, V.R. Kogan, F.A. Nikiforov and V.I. Talanov. Construction principles for laboratory model of stratified ocean, Preprint N.26, IAP RAS, Gorky, 1981.
2. S.D. Bogatyrev, V.A. Brailovskaya, S.A. Baranov, V.R. Kogan and V.I. Talanov. Numerical investigation of natural convection in basin with nonuniform lateral heating. Proceeding of X All-Union Seminar "Numerical methods for dynamics of viscous fluid", Novosibirsk, 62-68, 1983.
3. S.A. Baranov, S.D. Bogatyrev, V.A. Brailovskaya, A.V. Bune, V.R. Kogan, V.I. Polezhaev and V.I. Talanov. Convection and Heat Transfer in a Basin with Controlled Temperature Stratification, Izvestia, Atmospheric and Oceanic Physics, v.24, N.11, 879-885, 1988.
4. K. Aziz, J.D. Hellums. Numerical solution of the Three-dimensional equation of motion for laminar natural convection. Phys. Fluids, v.10, 1967, 314-324.
5. G.P. Mallinson, de Vahl Davis G. Three-dimensional natural convection in a box: a numerical study. J. Fluid Mech., v.83, 1-31, 1977.
6. O. Termina, A. Mortabi and B. Roux. A numerical procedure for Three-dimensional mixed convection developing flows in an axisymmetric geometry. Eur. J. Mech., B/Fluids, v.11, N.1, 21-38, 1992.

7. A.A Samarsky. Theory of difference schemes, Science, Moscow, 1977  
 8. V.I. Polezhaev and V.L. Gryaznov. Methods for calculating the boundary conditions  
 for the Navier-Stokes equations in the vortex and stream function variables. Dokl. Akad.  
 Nauk SSSR, 219, N 2, 301-304, 1974

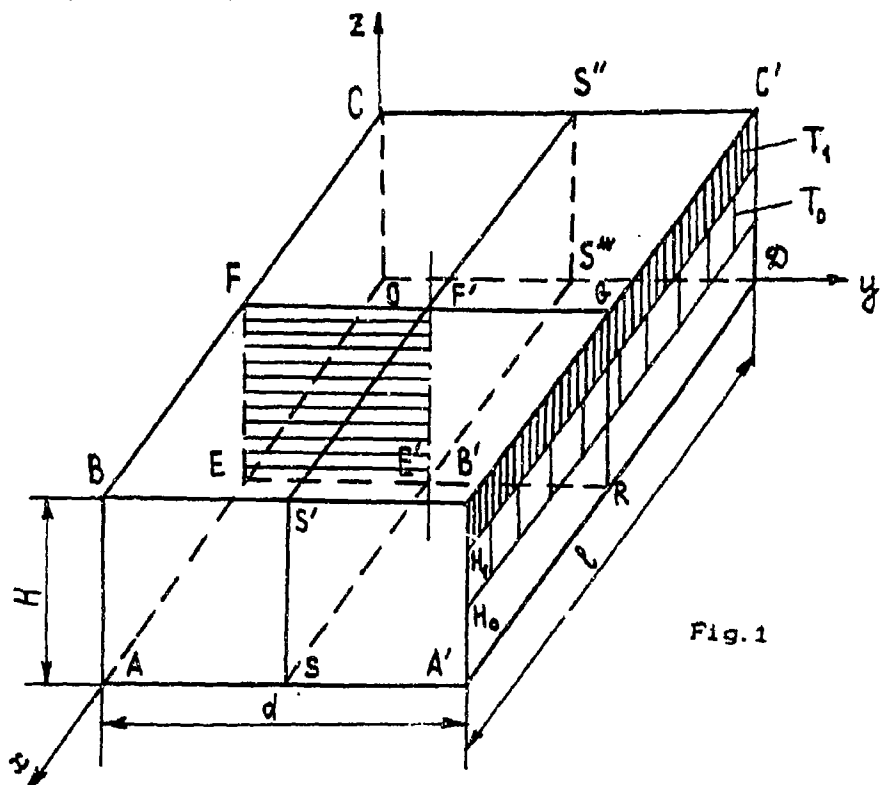


Fig. 1

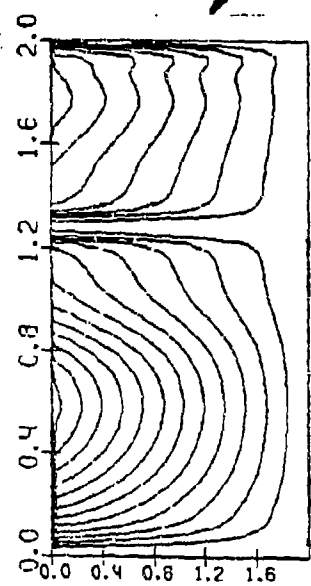
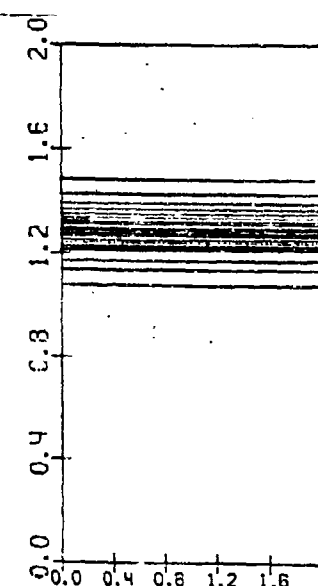
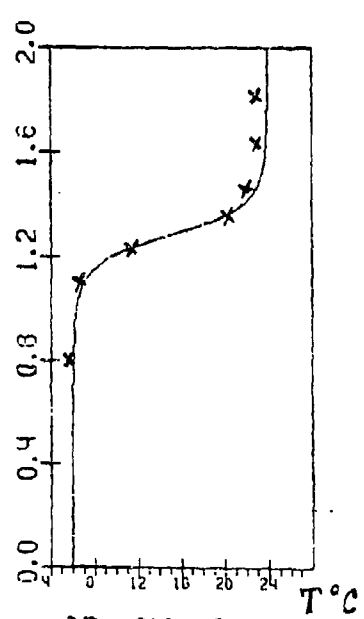


Fig. 2 a) Isolines  $\Psi_x$



b) Isothermes



c) Profile  $T(z)$

# Numerical Modelling of Heat Convection in a Stratified Laboratory Basin

S.A. Baranov, V.A. Pailovskaya, V.R. Kogan

Institute of Applied Physics Russian Academy of Science  
(IAP RAS)

## 1. Introduction

Mathematical simulation of the heat-mass transfer in the laboratory basin of IAP RAS designed for studying the dynamics of internal waves is based on the numerical solution of Navier-Stokes and energy equations. Unlike the two-dimensional models of small and intermediate basins considered before [1-3], the numerical simulation of stratification in the large basin is performed in three-dimensional formulation permitting to take into account volume fluid flow. This seems to be important for both to ascertain the possibility of creating and maintaining stable temperature stratification, which models the vertical density stratification in the upper ocean layer, and to study dynamics of internal waves appearing in the basin due to temperature and hydrodynamics fluctuations.

The first three-dimensional numerical investigations regarding natural convection were devoted to cavity flow [4,5]. In these studies the Navier-Stokes equations are expressed in terms of the vector potential and vorticity  $(\vec{\psi}, \vec{\omega})$ . This formulation has the advantage that the continuity equation is automatically satisfied and the pressure terms are eliminated. As an alternatives the formulation in terms of primitives variables - velocity and pressure  $(\vec{V}, P)$ , and the formulation in terms of velocity and vorticity  $(\vec{V}, \vec{\omega})$  [6] are used.

In the present paper to study hydrodynamics and heat exchange at the natural convection in the laboratory basin the flow field is calculated numerically using the variables  $(\vec{\psi}, \vec{\omega})$ .

## 2. Formulation of Problem

The model of the basin (Fig. 1) is a parallelepiped with the volume  $(d^*H^*)^3$ . Stratification in the basin is a result of the inhomogeneous temperature regime on the side walls (planes ABCO and  $A'B'C'D'$ ): the temperature at the height from  $H_0$  up to  $H_1$  is  $T_0$ , at the height from  $H_1$  up to surface is  $T_1$ . The rest part of the side walls lower  $H_0$ , face walls (the plane  $ABB'A'$  and  $B'CC'B$ ), and the bottom are heat isolated. On the surface heat exchange with surrounding takes place according to the formula  $q = \alpha(T_s - T_{\text{sur}})$ , where  $q$  is the density of the heat flow,  $T_{\text{sur}}$  is the temperature of the surrounding,  $T_s$  is the temperature of the surface,  $\alpha$ -heat exchange coefficient. Convection arises due to the violation of hydrostatic liquid equilibrium caused by the inhomogeneity of the temperature distribution in the field of mass forces.

In the dimensionless variables  $\vec{\omega}, \vec{\psi}, T$  (vortex, vector potential, temperature) the system of nonstationary Navier-Stokes and energy equations is written as

$$\frac{\partial \omega_x}{\partial t} = -\nabla(\vec{V}\omega_x) - \nabla^2\omega_x + \omega\nabla U + Gr T, \quad (1)$$

$$\frac{\partial \omega_y}{\partial t} = -\nabla(\vec{V}\omega_y) + \nabla^2\omega_y + \omega\nabla V - Gr T, \quad (1)$$

$$\frac{\partial \omega_z}{\partial t} = -\nabla(\vec{V}\omega_z) + \nabla^2\omega_z + \omega\nabla W \quad (1)$$

$$\frac{\partial T}{\partial t} = -\nabla(\vec{V}T) + \frac{1}{Pr} \nabla^2 T \quad (2)$$

$$\vec{V} = -\nabla^2 \vec{\psi} \quad (3)$$

where  $\vec{V}(U, V, W)$  is the velocity vector which define by the vector potential  $\vec{\psi}$  as  $\vec{V} = \Delta \vec{\psi}$ , i.e.  $U = \partial \psi_x / \partial y - \partial \psi_y / \partial z$ ,  $V = \partial \psi_x / \partial z - \partial \psi_z / \partial x$ ,  $W = \partial \psi_y / \partial z - \partial \psi_z / \partial y$ . On the solid walls and the bottom the condition of impermeability and sticking is fulfilled ( $\vec{\psi} = 0$ ,  $\partial \vec{\psi} / \partial n = 0$ ,  $n$  is a normal to the boundary). The transition to dimensionless variables is made by means of following scales: the height of the side walls  $H$  is the characteristic length,  $H^2/\nu$  is a time scale,  $\Delta T = (T_1 - T_0)$  is a temperature scale. The main similarity criteria are the Grashof number and the Prandtl number ( $Gr = g\beta H^3 \Delta T / \nu^2$ ,  $Pr = \nu/k$ , where  $\nu$ ,  $k$  and  $\beta$  are the kinematic viscosity, conductivity and thermal expansion coefficient respectively).

### 3. Method of Solution.

To solve the system of Navier-Stokes and energy equations numerically, the finite-difference method is used. For the transport equations of vorticity and energy the monotonous approximation of the convective terms of the second order accuracy with compensation of scheme viscosity by Samarsky method [7] is adopted. All these equations in time-dependent formulation are solved by applying an alternating direction implicit method. The assumption that the flows are solenoidal at  $\vec{\psi}$  makes it necessary to solve three three-dimensional Poisson equations for each time layer. The direct method with applying of Fast Fourier Transform is used providing a high accuracy of the solution the Poisson equations.

To solve eq.(1) numerically the boundary conditions for the vorticity are calculated by the method given in [8] for a two-dimensional case. Thus, the succession of the calculations at the every time step is as follows:

a). Using the difference analog of the eq.(3) we calculate  $\vec{\omega}^{n+1}$  - the vorticity at  $(n+1)$ -th time layer at the boundary  $\gamma$  of the region of calculating  $\vec{\omega}$ , which is distant from the boundary of the main region by one spacing.

b). Solving the system of equations (1) we find  $\vec{\omega}^{n+1}$  via  $\vec{\omega}^n$  inside the region, bounded by  $\gamma$ .

c). We calculate  $\vec{\psi}^{n+1}$  from the eq.(3).

d). Using the boundary condition  $\partial \vec{\psi} / \partial n = 0$ , we calculate the vector potential  $\vec{\psi}^{n+1}$  in the near-boundary node more exact taking into account the second condition  $\vec{\psi} = 0$  at the boundary.

e). We calculate a new velocity vector  $\vec{V}^{n+1}$  using the definition  $\vec{V} = \Delta \vec{\psi}$ .

f). Solving eq.(2) we find the temperature field in the all volume region.

The final temperature and fluid flow distribution are finded in the process of stationary state establishing.

### 4. Results of Calculation

The numerical calculations were made in the half of the region with assumption about a symmetry relatively to the vertical symmetry plane  $SS''S'''$  of the basin (see Fig.1).

We use a grid which is inhomogeneous in  $y$ , with a considerable thickening of nodes in the boundary layer near the vertical side walls and homogeneous in the two other directions. These requirements should be met in order one may use FFT method for solving Poisson equation. The maximum number of the nodes to be computed by PC 486 equals  $33*60*33$  for the half of the volume, time spacing equals  $\tau = 10^{-6}$ . The particular calculation was performed for the model of the basin given in Fig.1:  $H_0 = 0.6m$ ,  $H_1 = 0.7m$ ,  $H = 2m$ ,  $d = 4m$ ,  $l = 20m$ ,  $T_0 = 6^\circ C$ ,  $T_1 = 24^\circ C$ ,  $T_{initial} = 20^\circ C$ ,  $Gr = 1.4 * 10^{11}$ ,  $Pr = 7$ .

To make the computer time minimum the following way of transition to the stationary regime was used. Assuming that the temperature is practically homogeneous along the basin length and varies only near the side walls, the fields of temperature and flow were calculated at the first stage in a half of plane EFGR on the base of two-dimensional model, described in [1-3]. After the onset of the stationary regime of convection (see Fig.2) the fields of velocity and temperature were scattered along the basin length on all nodes of the three-dimensional grid. Then the calculation of the three-dimensional model (1-3) was performed till the stationary state established.

Fig.2 a,b shows the isolines of  $x$ -projection of the vector potential  $\vec{\psi}$  and isolines of the temperature on the plane EFFE' (see Fig.1).

The analysis of these figures shows that the convective process at the rectangular basin induced by temperature profiling of the side walls leads to the formation of characteristic four-vortex structure of the global water circulation in the basin with various direction higher and lower the temperature jump. This structure maintains the stable vertical temperature stratification in the volume with a characteristic thermocline at the depth of the assigned temperature jump. Stratification in this case is practically homogeneous along the basin length except the boundary layers along the walls.

The calculated temperature profile in the middle vertical cross-section (Fig.2c) practically coincides rather well with the one measured in the experimental basin of IAP (designed by crosses on the plot), especially in the temperature jump region.

The conducted numerical simulation revealed the region of uniform thermal and hydrodynamics fields needed for investigation of internal waves in the basin. This region occupies almost the entire space along the basin length except for about two-meter parts off the end walls.

#### References

1. S.D. Bogatyrev, V.A. Brailovskaya, V.R. Kogan, F.A. Nikiforov and V.I. Talanov. Construction principles for laboratory model of stratified ocean, Preprint N.26, IAP RAS, Gorky, 1981.
- 2.S.D. Bogatyrev, V.A. Brailovskaya, S.A. Baranov, V.R. Kogan and V.I. Talanov. Numerical investigation of natural convection in basin with nonuniform lateral heating. Proceeding of X All-Union Seminar "Numerical methods for dynamics of viscous fluid", Novosibirsk, 62-68, 1983.
3. S.A. Baranov, S.D. Bogatyrev, V.A. Brailovskaya, A.V. Bune, V.R. Kogan, V.I. Polezhaev and V.I. Talanov. Convection and Heat Transfer in a Basin with Controlled Temperature Stratification, Izvestia, Atmospheric and Oceanic Physics, v.24, N.11, 879-885, 1988.
4. K. Aziz, J.D. Hellums. Numerical solution of the Three-dimensional equation of motion for laminar natural convection. Phys. Fluids, v.10, 1967, 314-324.
5. G.P. Mallinson, de Vahl Davis G. Three-dimensional natural convection in a box: a numerical study. J. Fluid Mech., v.83, 1-31, 1977.
6. O. Termina, A. Mortabi and B. Roux. A numerical procedure for Three-dimensional mixed convection developing flows in an axisymmetric geometry. Eur. J. Mech., B/Fluids, v.11, N.1, 21-38, 1992.

7. A.A Samarsky. Theory of difference schemes, Science, Moscow, 1977  
 8. V.I. Polezhaev and V.L. Gryaznov. Methods for calculating the boundary conditions for the Navier-Stokes equations in the vortex and stream function variables. Dokl. Akad. Nauk SSSR, 219, N 2, 301-304, 1974

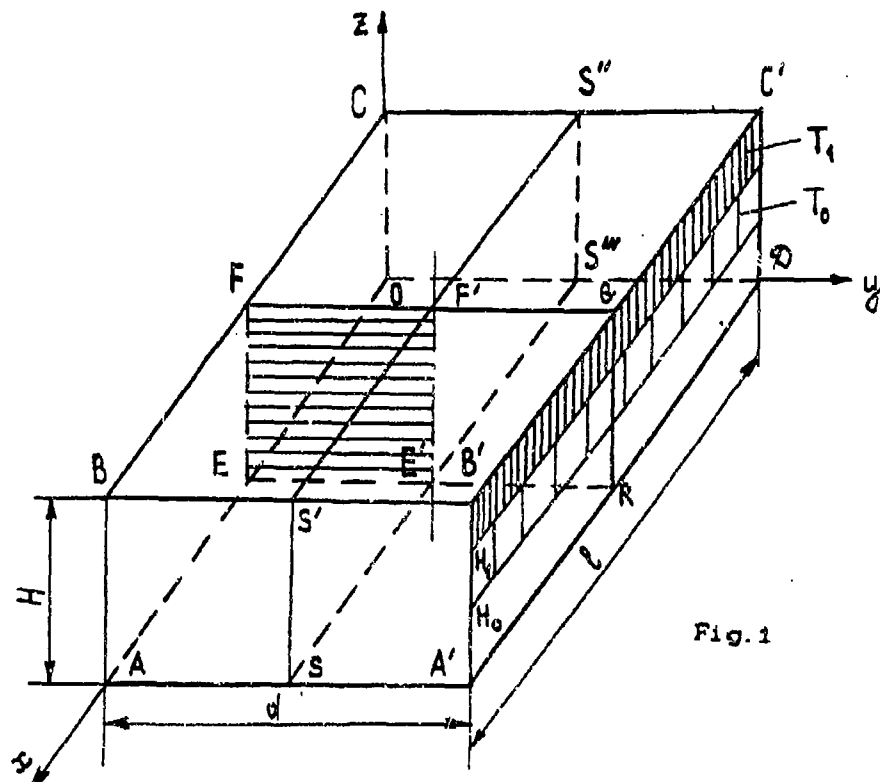


Fig. 1

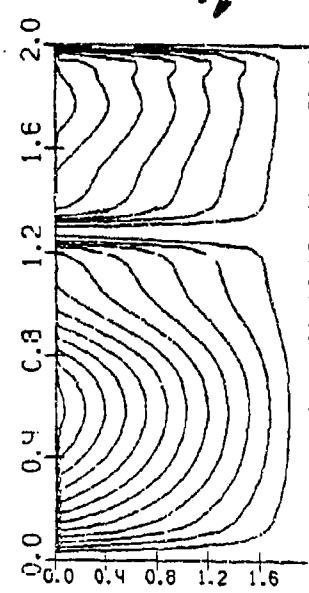


Fig. 2 a) Isolines  $\psi$

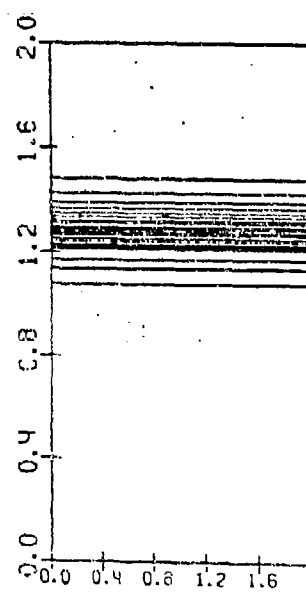


Fig. 2 b) Isolines  $\psi$

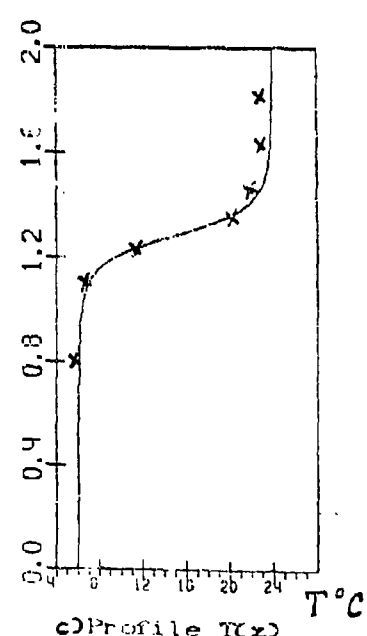


Fig. 2 c) Profile  $T^\circ C$